A NEW MF DOPPLER RADAR FOR UPPER ATMOSPHERIC RESEARCH

By

Brenton Vandepeer, B.Sc. (Hons)

Thesis

submitted for the degree of

DOCTOR OF PHILOSOPHY

at the

UNIVERSITY OF ADELAIDE

(Department of Physics and Mathematical Physics)

November 1993

Awarded 1994

This work contains no material which has been accepted for the award of any other degree or diploma in any university or other tertiary institution and, to the best of my knowledge and belief, contains no material previously published or written by another person, except where due reference has been made in the text.

I give consent to this copy of my thesis, when deposited in the University Library, being available for loan and photocopying.

Signed: ..... dated: 30/11/93

Brenton Vandepeer, B.Sc. (Hons)

Abstract

Partial construction of a new transmit/receive, medium–frequency Doppler radar has been completed and initial testing has been carried out at the University of Adelaide's Buckland Park field site. The electronic beam steering capabilities of the radar have been shown to be operative, and have been used to make preliminary measurements of atmospheric scatterer aspect sensitivities. D–region echoes down to altitudes of about 64 km have been observed with signal–to–noise ratios in excess of 15 dB.

An extensive study of the time–domain interferometric technique has been undertaken, with particular reference to contaminating effects. It has been found that both sea scatter and lower E–region totally–reflective "glints" give rise to anomalous interferometric results. In addition, contamination from some form of radio–frequency interference has been observed. Several methods of receiver phase–calibration have been tested, and it has been found that carefully–applied statistical corrections are necessary, at least at medium frequencies. In addition, it is shown that these phase corrections must be applied taking account of receiver gain setting and ambient temperature.

Various theoretical aspects of Doppler–sorted radar interferometry have been explored, and it is shown that in the case of volume scatter, imaging analyses utilizing smoothed cross–spectra must yield a wind velocity estimation which is equivalent to the full correlation analysis' apparent wind velocity. An IDI–like analysis is developed which, although ostensibly utilizing unsmoothed cross–spectra, is shown to yield wind velocities which in general agree best with the full correlation analysis' apparent velocity. A mechanism is proposed which may account for this curious result.

Acknowledgements

Over the duration of a PhD candidature one is given cause to be thankful to many people. Of all the pages in a dissertation such as this one, of all the figures, diagrams, tables and derivations, which page is eagerly perused before any other? Why, the acknowledgements page of course. Here it is where the author is allowed to express something of their own personality. No longer the dry, impersonal and objective tones of science, but perhaps the more poetic prose of a writer constrained no more. To business, then.

The first group of people to whom I must express my gratitude are the supervisors and other academics who have guided me for so long. To Dr. Iain Reid, my supervisor, whose patience, open–mindedness, and willingness to enter debate have led me thus far. To Dr. Basil Briggs, a man of almost legendary stature, whose conversations and advice over the last 5 years have been priceless, and who occasionally allowed me to be right. To Dr. Bob Vincent, who honed my appreciation of fine coffee and offered just the right amount of encouragement at just the right times. And lastly, my thanks go to Dr. Wayne Hocking who, before his departure to Canada, fulfilled his role as my supervisor for 2 years.

Often one of the most–remembered aspects of a PhD are the friendships forged and broken with one's fellow students. Some of those are now Doctors in their own right, while some are waiting on examiners, and still others are studying as I write. Of the first group, I would like to acknowledge Dr. Damien Muphry (oops, I mean Murphy) whose generous outlook on life, except where home–made pizza was concerned, was a shining ideal to which I aspired, yet never obtained. To Dr. Steven Eckerman, who put up with me in Oxford for a while, and supplied me with a role–model for laid–backness which I can never hope to achieve. To Dr. Drazen Lesicar, whose spelling and entrepreneurial skills gave me hope for the future. To Dr. Laurence Campbell, for showing me what not to do. To all of these I owe some measure of gratitude. Of those in the second group, I am indebted to Mr. Trevor Harris for his tireless help with both IDL, and LaTeX. When all else fails, "I have a procedure". To

the final group of colleagues on my list; Blowy Lowy, Spit, Mad Dog, Dot, Dippier, Ali, Scott, Bridget and that far–left radical, Simon, thanks for either drinking, arguing, philosophizing, discussing, wenching, partying or playing darts with me. Also worthy of mention here must be those friends who have left the world of science or study but have remained in contact with me over the years. I rather imagine that you are unaware of the support that you have lent me by allowing me to be who I am, and still being nice to me. Thanks.

One problem with spending such a long, continuous amount of time on one pursuit is that one's mind tends to become stale and bored. Luckily, in Adelaide there exist activities of a rather less cerebral quality to which one may turn one's attention and experience almost complete fulfillment. I therefore wish to express my sincerest gratitude to the Adelaide Football Club, without whose existence I would surely by now have perished. Good effort in '93, guys, let's do it better in '94! Also deserving of my thanks in this category is the Southwark brewing company of Thebarton, South Australia. You are the people who have blessed us with the mighty "green death", and given us cause to know and love it. I pray that your noble traditions will not be discarded in the wake of your new–found corporate identity.

The penultimate group of people who deserve mention in this self–serving piece of prose are those staff who have sometimes been of invaluable help to my work. To Lynn and Dallas, (how many acknowledgements have you guys been in?), Lesley, Alex, John Smith and Mike Shorthose; my sincerest thanks. (Especially those of you who have been silly enough to find yourself fixing antennae at Buckland Park in the middle of Summer!) A special mention must go to Shane and Brian, without whose technical expertise and assistance I would not yet have descended from the trees. Thanks also for maintaining my occasionally shaky perception of reality and providing me with some of the most memorable (?) evenings of my life.

And finally, what acknowledgement would be complete without mention of one's loved–ones? Those people who keep the home fires burning and have tea on the table at 6 every night. In my case, there are four of them to thank: my mother and father, whose support assistance during a sometimes difficult period has been unparalleled. Whether it be fences, clotheslines, gardens or banks, they seem to know their way around 'em pretty well. Thank you for your forbearance and understanding: I know that at times I've disappointed you. My undying gratitude must also be given to Tull; at least there was always one person at home who was glad to see me. And Lisa, what can I say? Thank you for supporting us through this extended period of time, and for not asking too often if I was going to finish

soon. Thank you for reminding me of my manners when it counted; at times it was hard to think of others, so I'm glad there was someone doing it for me.

So now I conclude this page of acknowledgements, and encourage the gentle reader to sally forth into the world of science. Research, as I have discovered first–hand, is not a discipline which may be directed by force of will alone, but rather an art which must be nurtured and coaxed. Most of us find, I suspect, that our initial path of research is quickly subverted into the highways and byways of the subject. Only rarely do we alight from the roller–coaster at the point at which we wished to arrive. Sometimes, nonetheless, we find something useful at our destination, and we grasp at it and pretend that this was what we wanted to find from the outset.

So now turn the page, enter my world and follow the twists and turns that the last 5 years have revealed to me. I bid you welcome to the magical mystery tour...

For Lisa and Tull — for all the good times.

Contents

List of Tables

List of Figures

Chapter 1

INTRODUCTION

1.1 Introduction

This thesis describes the design, construction and use of a beam–steerable, transmit/receive, medium–frequency Doppler radar. To a large extent, subject–specific introductions and surveys of the field of interest are presented at the beginning of each chapter in this thesis. Thus, this introduction is necessarily brief, and deals mainly with the nomenclature of both the various regions of the atmosphere and of partial–reflection radars themselves. The motivation for the project is also discussed, as is its pertinence to the field at large.

1.2 Atmospheric Nomenclature

1.2.1 Temperature structure

The Earth's atmosphere may be divided up and classified according to many criteria. One of the most prevalent used in the literature is that based on temperature (see, e.g., *Andrews et al.* [1987]). In Figure 1.1 a typical temperature profile of the atmosphere is displayed from the ground up to an altitude of 120 km. Note that all of the temperatures and altitudes discussed here are typical values only as both vary with season and latitude. The regions of interest are summarized in Table 1.1. The altitudes at which the slope of the temperature profile changes sign are given region–specific names such as the tropopause, the stratopause and the mesopause in order of increasing altitude. Thus, the tropopause is located just above the troposphere and is the altitude at which the temperature profile ceases to decrease with altitude, and begins to increase. The region above the thermosphere is known as the exosphere, and this extends upwards with ever decreasing density until it merges with the

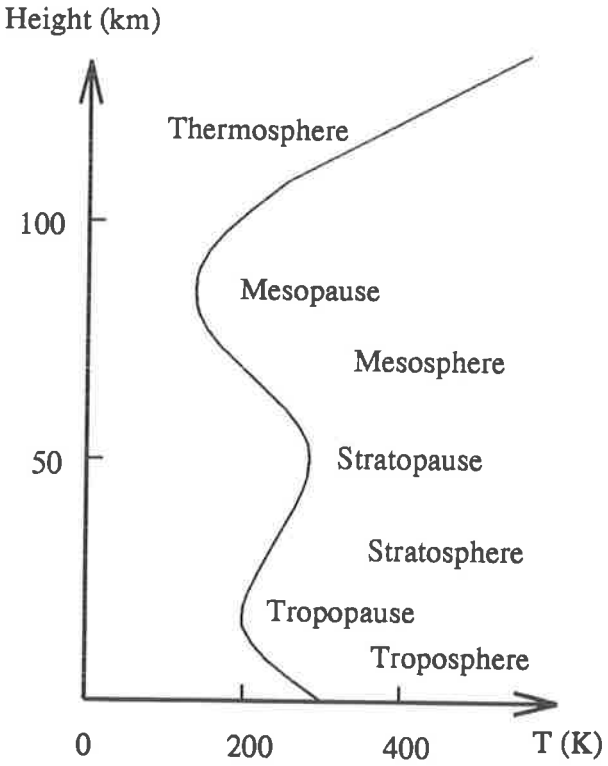

Figure 1.1: The Earth's atmospheric temperature profile and associated nomenclature.

Table 1.1: The temperature–derived nomenclature of the Earth's atmosphere

Region	Altitude range	Temperature range (K)
Troposphere	0 km → 15 km	300 → 215
Stratosphere	15 km → 50 km	215 → 270
Mesosphere	50 km → 85 km	270 → 180
Thermosphere	85 km → ∼500 km	180 → 1000+

background atomic number density present in the solar system. The temperature structure of the Earth's atmosphere is governed by a series of competing radiative and dynamical processes, each dominant in certain regions. For example, the rate of decrease of temperature with altitude in the troposphere is close to the (dry) adiabatic lapse rate (9.8 Kkm^{-1}); the rate at which a gas adiabatically cools as it is displaced upwards in a fluid governed by hydrostatic equilibrium. The rate of decrease of temperature in the troposphere is somewhat less than this due to the absorption of long–wave infra–red radiation from the Earth's surface by constituents such as carbon dioxide, methane and water vapour. The radiative and dynamical equilibrium established gives rise to cooling rates with altitude which vary with latitude, longitude and season, but has a typical value of about 6.6 Kkm^{-1}.

The rate of cooling decreases near the tropopause and eventually changes sign in the stratosphere as the concentration of ozone increases. Incoming ultra–violet solar radiation in the 200 nm to 300 nm range is absorbed by the ozone which has a peak abundance at around 45 km. The energy balance is preserved at these altitudes by re–radiation in the infra–red by carbon dioxide.

Above about 45 km, the ozone concentration decreases quite rapidly, and the temperature profile again changes slope as emission by carbon dioxide dominates. The cooling continues in the mesosphere until a temperature minimum occurs at about 85 km at the mesopause. It is observed that the temperature structure of the mesosphere often departs significantly from radiative equilibrium. Although unexplained for many years, this departure is now understood in terms of deposition of energy and momentum by breaking internal gravity waves.

Above the mesopause, both atomic and molecular oxygen absorb solar ultra–violet radiation, and the temperature again increases with altitude. Thermospheric temperatures may reach 1000 K to 2000 K depending on solar activity.

1.2.2 The Ionosphere

A second criterion for nomenclature is that of the local electron concentration (see, e.g., *Risbeth & Garriott* [1969]). Incoming short–wave solar radiation and cosmic rays ionize molecular oxygen and nitrogen and also nitrogen monoxide to create positive ions and free electrons. The recombination of the positive ions and electrons is governed by a complex series of reactions whose rates vary greatly with altitude and season. Electron density peaks during the day–time at about 5×10^6 cm^{-3} at altitudes around 280 km. This region is known for historical reasons as the F_2–region (see Figure 1.2). Below the F_2–region lies the F_1–region at an altitude of about 180 km, and then the E–region (100 km to 120 km). Finally, the D–region lies below about 86 km in altitude. Generally, the electron concentration present in these different regions (sometimes called layers) falls with decreasing altitude, with the D–region possessing the lowest electron concentration of about 10^3 cm^{-3}. The D–region is formed by the ionization of nitrous oxide by the 121.6 nm Lyman–α emission line. It is from the D–region that partial echoes are obtained by MF and VHF radars, and it is this region of the atmosphere which is of primary interest in this work. We note that the D–region of the ionosphere roughly corresponds to the mesospheric region in the temperature–derived

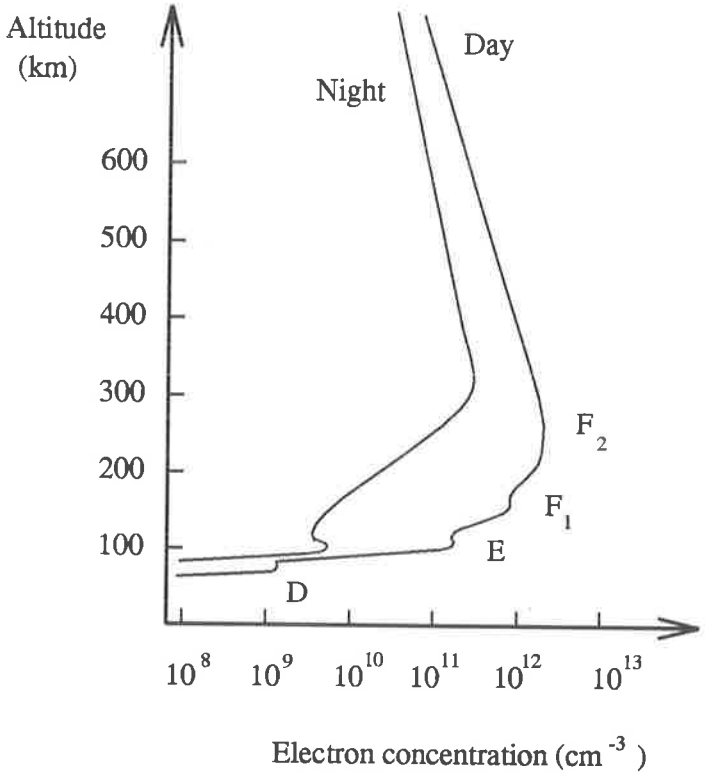

Figure 1.2: Average ion concentration profiles for both day–time and night–time ionospheres during periods of solar maxima (adapted from *Richmond* [1987]).

nomenclature. These two terms, except where explicitly stated, are used somewhat interchangeably throughout this work.

1.2.3 Turbulent mixing

A third possible system of nomenclature is that of the extent of the mixing of the different atmospheric constituents. Below about 100 km in altitude the atmosphere is relatively well mixed due to turbulent and wave motions. This lower region of the atmosphere is therefore known as the homosphere due to its homogeneous nature. Above 100 km the eddy and molecular viscosity coefficients become sufficiently large that turbulent motions are quickly suppressed, and the atmospheric constituents "settle out" according to their relative molecular masses. This region of the atmosphere is known as the heterosphere.

1.3 Measurement Techniques

Experimental techniques devised to study the atmosphere fall naturally into two groups; those techniques which sense the state of the atmosphere from a distance are known as

remote sensing techniques, while those experiments which are transported or situated in the region of the atmosphere of interest are known as in–situ techniques. Examples of the former include such devices as satellites, radars (Radio Detection And Ranging), lidars (Light Detection And Ranging) and other ground–based optical devices, while examples of the latter include balloon and rocket–borne experiments and those experiments mounted on towers or booms. In general, remote sensing techniques have a significant time resolution advantage over in–situ experiments, as the in–situ experiments can only take a "snap shot" of the condition of the atmosphere. Conversely, in–situ experiments have the advantage that they actually measure a parameter in a well–defined and predictable manner, while remote sensing techniques generally suffer from some uncertainty about either which parameter, or in what way the parameter is measured.

Of the remote sensing experiments, two further distinctions may be made; those experiments which simply receive or monitor some state or constituent of the atmosphere are known as passive experiments, while those which "sound" the atmosphere with some form of radiation are known as active experiments. Examples of passive experiments include spectrometers, photometers and most satellite–borne apparatus. Clearly both radar and lidar fall into the active category. Disadvantages of passive sensing techniques often include severe coverage restriction. For example, photometers must be tuned to a single emission line (presumably) emanating from a particular altitude range. The device can be retuned to another line emanating from a different altitude, but this, in general, precludes simultaneous measurements at multiple altitudes. Satellite measurements have the disadvantage of relatively poor height and time resolution and can not easily make measurements of the same area from one orbit to the next. They are able, however, to achieve excellent global coverage over latitudes between $\pm 80°$.

Atmospheric radars are able to make measurements with excellent time and height resolution, are relatively inexpensive and can operate at remote sites unattended for long periods. Disadvantages of radar include the inability to sample at more than a small number of spatially separated locations and, in general, a restriction of altitude coverage. Radars operating on different frequencies, however, are able to probe different regions of the atmosphere. The earliest observations of atmospheric partial reflections were reported in the literature by *Appleton* [1930]. These, however, were merely incidental to the observations of the heights of totally–reflective ionospheric layers. The first systematic investigations of D–region partial reflections appears to have been made by *Gardner & Pawsey* [1953] and later by *Gregory*

[1956]. Both of these studies utilized fixed–frequency pulsed systems operating at about 2 MHz. In terms of the middle atmosphere, (approximately that part of the atmosphere above the tropopause and below the turbopause), MF/HF radars are able to probe between about 60 km and 100 km. In general, MF/HF radars receive backscattered signals from those altitudes where both sufficient ionization and discontinuities exist in order to produce a change in the refractive index of the medium, and are most sensitive to discontinuities with vertical scales equal to one–half the radar wavelength. With the exception of some extremely powerful very high frequency radars operating with long integration times, MF/HF radars offer almost the only reliable radar coverage of this part of the middle atmosphere with high time resolution.

Very–high frequency (VHF) radars were first used for clear–air atmospheric research in the late 1960's and early 1970's [*Flock & Balsley*, 1967; *Woodman & Guillen*, 1974]. These radars usually operate at frequencies from about 40 MHz to 230 MHz, and offer good coverage from altitudes as low as 1 km, to about 20 km. In addition, VHF radars offer excellent height resolution which can be as small as 150 m when pulse–coding schemes are implemented.

In the last decade, a number of studies and reports have focussed on the mesosphere–stratosphere–troposphere (MST) radar concept, (see, e.g., *Harper & Gordon* [1980], *Balsley & Gage* [1980] and *Röttger* [1980*b*]) although routine observations above about 25 km remain difficult, especially at night. An exception to this range limit can be found in the enhanced backscatter returned from the polar Summer mesopause echo (PMSE) observed at high latitudes at altitudes between 80 km and 90 km [*Balsley et al.*, 1983; *Czechowsky et al.*, 1989a; *Czechowsky et al.*, 1989b; *Rüster et al.*, 1989]. Thus, VHF radars can provide reliable coverage only to about 25 km in altitude, with sporadic returns observed from the mesospheric region during the daylight hours. Although the exact nature of the reflection processes is as yet unknown, it is supposed that variations in humidity and temperature are the primary causes of the backscatter measured by VHF radars. *Hocking et al.* [1991] has proposed a viscosity wave mechanism which may explain the highly–specular returns often observed by VHF radars in the lower atmosphere.

Ultra–high frequency (UHF) radars usually operate on frequencies between 400 MHz and 900 MHz and are used primarily as boundary–layer radars. In addition, UHF radars at the lower end of this frequency range are operated as tropospheric radars and regularly obtain returns from as high as 15 km. UHF radars rely on backscatter from water vapour, precipitation echoes or aerosols, and are occasionally known as weather radars or pollution radars.

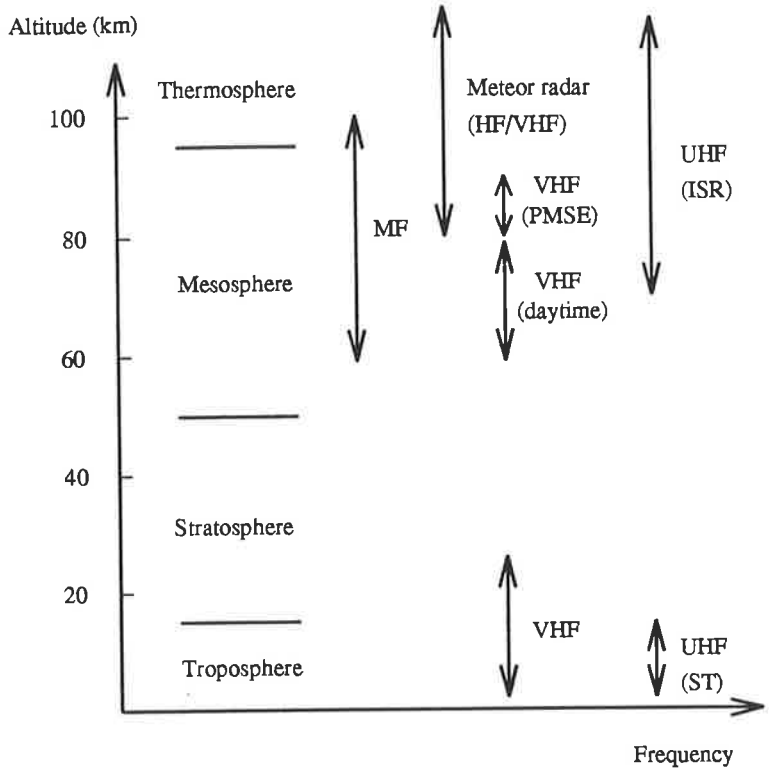

Figure 1.3: The regions of the atmosphere from which backscatter is regularly observed by MF and VHF radars.

In addition, UHF radars with comparatively large power–aperture products are operated as incoherent scatter radars (ISR) which observe scattering from the free electrons present in the medium due to their weak Thompson scattering cross section (see Subsection 1.4.5).

In Figure 1.3 the regions of the atmosphere from which backscatter is observed by MF, VHF and UHF radars are shown. Inspection of this figure shows that, except for the PMSE, MF radars offer almost exclusive routine coverage of the mesosphere, and that there exists a large gap in coverage by any radar type from 25 km to 55 km. This mostly stratospheric region is extremely difficult to observe using atmospheric radars as its density (and subsequent density fluctuations) is too low to provide VHF radars with sufficient backscatter, and the level of ionization present is insufficient to provide either type of radar with significant backscatter. In fact, this data–sparse region is difficult to observe with most remote–sensing techniques, lidar providing one of the few exceptions. In–situ measurements, of course, are quite feasible in this region, and rocket measurements provide the bulk of the experimental data available. Balloon–borne experiments are limited to altitudes below about 40 km.

1.4 Radar Scattering Mechanisms

1.4.1 Refactive index

The refractive index for radio waves propagating through the lower and middle atmosphere is given by *Gage & Balsley* [1980] as,

$$n - 1 = \frac{3.73 \times 10^{-1} e}{T^2} + \frac{77.6 \times 10^{-6} P}{T} - \frac{N_e}{2N_c}, \tag{1.1}$$

where e is the partial pressure of water vapour in mb, T is the absolute temperature, P is the atmospheric pressure also in mb, N_e is the number density of free electrons and N_c is the critical plasma density. The three terms on the right–hand–side of Equation 1.1 are known as the wet, dry and ionization terms respectively. The wet term dominates the refractive index equation when applied in the lower troposphere due to the relatively large amount of water vapour present. Its influence is, however, negligible when considered above the tropopause. The dry term begins to dominate from the mid–troposphere upwards into the stratosphere until ionization begins to become significant at about the stratopause. At these altitudes the third term, or ionization term dominates.

We now categorize the different types of scatter observed by atmospheric radars.

1.4.2 Bragg scatter

Bragg scatter, or turbulent scatter results from variations in the refractive index with scale projected along the line of sight of the radar equal to one–half the radar wavelength. In order for there to be Fourier components present in the turbulence with the correct scale, the radar wavelength must lie roughly between the inner scale, l_o and the outer scale, L_o of the turbulence present. More rigorously, the inequality $C_1 2\pi l_o < \lambda/2 < C_2 2\pi L_o$ must hold [*Balsley & Gage*, 1980], where C_1 and C_2 are constants with magnitudes empirically determined to be 0.94 and 0.75 respectively [*Megaw*, 1957].

1.4.3 Fresnel scatter

Fresnel scattering (see e.g., *Röttger* [1989]) occurs from collections of extended layers of vertical variation in refractive index. In the case of Bragg scatter, the scattering scales in the horizontal are less than the size of the first Fresnel zone[1] and many scatterers are

[1]The radius of the first Fresnel zone is given by $\sqrt{\frac{R\lambda}{2}}$, where R is the range of interest, and λ is the radar wavelength.

involved. Therefore the scatter produced tends to vary randomly in amplitude and phase and is relatively weak. Fresnel scatter, conversely, produces much stronger and more coherent scattered signals. Fresnel scatter, and to some extent, Fresnel reflections are also known as partial reflections.

1.4.4 Fresnel reflection

Fresnel reflection (see e.g., *Röttger* [1989]) is analogous to the Fresnel scattering model except than a single extended layer or sheet gives rise to the backscattered signals. In this case the returned signal may be quite strong and will be quite steady in amplitude and phase over relatively long periods. Fresnel reflections are responsible for "slow fading" of radio signals backscattered from the mesosphere at MF. Fresnel reflection is distinct from total reflection from mirror–like structures such as sporadic–E layers in that it is still a partial–reflection phenomenon.

1.4.5 Incoherent scatter

In all of the scattering processes outlined above, the electric field is scattered from a large number of coherent structures within the pulse volume and thus these processes are known as coherent–scatter processes. An alternative (and much weaker) form of scatter arises when the incident electro–magnetic field interacts directly with free electrons which are forced to oscillate with the electric field. The oscillating electrons re–radiate at a similar frequency to the incident radiation. If the wavelength of the incident radiation is sufficiently small, then the re–radiated signal is phase–incoherent. Since incoherent scatter relies on the Thompson scattering cross section of the electron it is extremely weak, and consequently incoherent scatter radars must possess relatively large power–aperture products in order to observe these backscattered signals. Incoherent scatter is also known as Thompson scatter, or thermal scatter.

1.5 Radar Measurement Techniques

In this section we briefly examine some of the more common radar techniques used to measure various atmospheric parameters in the troposphere, stratosphere and mesosphere. We begin by considering the initial signal processing stages common to many atmospheric radars and many radar techniques. Only fixed–frequency pulsed radar data processing is considered.

1.5.1 Initial radar signal processing

In a typical multi–receiver partial–reflection radar, the echoes amplified by each receiver are sampled every 6.7 μs for each kilometre between adjacent range gates. Sampled data are recorded as fixed–length time series for each range, each time series spaced by a small interval used to transfer the data to some form of storage device. These fixed–length records may vary in length from as short as a few seconds, to as long as several minutes, depending on the data rate, the parameter of interest and the amount of memory available to the radar during data acquisition. A data set, or data record consists of an equally–spaced sequence of samples taken from the amplified voltages generated in the antennae by the backscattered signals. In the case of a spaced antenna radar where different antennae must be sampled independently, one of two schemes is possible. Either a separate receiver and signal processor must be provided for each independent antenna, or one receiver and signal processor must be multiplexed between all antennae. The latter scheme requires that small time–delay corrections be applied to the sampled points.

The radar frequency as well as many other related frequencies are derived from a master oscillator, which is often kept in a temperature–controlled environment. In many radars, the carrier frequency of the transmitter pulse is mixed with a local oscillator frequency (locked in some way by the master oscillator to the carrier frequency) in the radar receivers yielding an intermediate frequency (IF), or beat frequency. In the case of the 8 channel Buckland Park MF radar used for this work, the intermediate frequency of 495 kHz is then further mixed in the signal processor with two quadrature phase references whose frequencies are equal to the IF beat frequency. Thus, for a constant–strength backscattered signal, only Doppler shifted signals will give rise to varying signals from the signal processor.

Since the IF is mixed with two quadrature signals, two pulse trains are produced by the signal processor. These are known as the in–phase voltage and the quadrature voltage. The in–phase and quadrature voltages are independently digitized for each range gate of interest and transferred to some form of temporary memory buffer. In most atmospheric radars, the pulse repetition interval is much smaller than the time taken for the atmosphere to change state. In these cases it is often assumed that a sequence of pulses actually represents a number of measurements of the same quantity. Thus, the pulses are often averaged to find the "best estimate" of the backscattered voltage over a short length of time. This process, if performed independently on both the in–phase and quadrature samples, is known as coherent

integration, and yields an improvement in the signal–to–noise ratio of a factor of N, where N is the number of pulses which are averaged. Coherent integration is often carried out by a micro–processor while the data are in the temporary memory buffer and before the data are transferred to the controlling computer or storage device. With the advent of more powerful computers, however, it has sometimes become possible to perform coherent integration in software once the raw data have been transferred to the controlling computer. This is now becoming a very attractive alternative for these types of radars as it eliminates much of the costly, custom–built hardware from the radar system. Software coherent integration also tends to offer more flexibility in the radar and subsequent experimental investigations. All of the data presented in this thesis were obtained using coherent integration performed in software.

Data obtained in the ways outlined above may be utilized in one of two ways. First, they may simply be stored on some form of magnetic device and analysed at leisure in the future, or second, some form of analysis may be performed immediately by the controlling computer and the results of this may be stored for later examination. Both approaches offer their own advantages and drawbacks. The advantages inherent in storing the raw (although possibly coherently averaged) samples include

- the data in raw form are available for analysis using whichever technique is desired,
- the data are available for further scrutiny should some problem become apparent with the radar hardware,
- the data may be reanalysed should some error in the analysis technique become apparent and
- no time need be wasted during data collection for an analysis to be performed.

The major drawback of the "off–line" analysis approach is that very large data files are produced and these must be stored. For example, the 8 channel MF radar used to collect the data presented in this dissertation accumulated some 120 kb of data every two minutes. This equates to almost 90 Mb per day. As more powerful computer hardware and larger storage devices become available these high data collection rates become less of an issue.

These data collection and pre–processing techniques are applicable to almost every analysis method commonly in use today. Some of these analyses are outlined below. In an

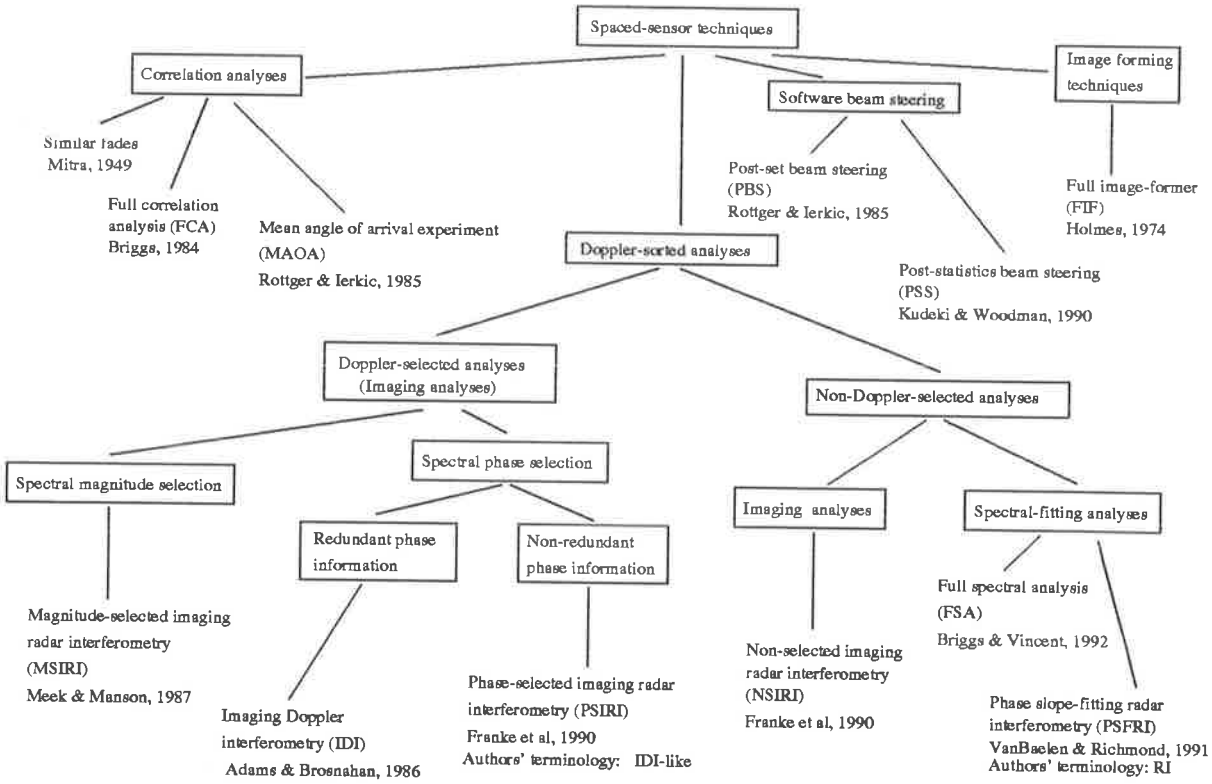

Figure 1.4: A taxonomy of spaced–sensor techniques.

attempt to unify the sometimes confusing nomenclature associated with different spaced–sensor techniques, a taxonomy of these appears in Figure 1.4. The following subsections briefly outline the techniques appearing in Figure 1.4, while those techniques most directly related to this work are covered in greater detail in Chapter 3.

1.5.2 Full correlation analysis

The full correlation analysis (FCA) makes use of at least three non–colinear, spatially separated antennae to measure the wind field above the radar, as well several other atmospheric parameters. The analysis calculates the auto– and cross–correlation functions for the three sampled time series and, taking account of the random change present in the diffraction pattern on the ground, extracts the background wind vector. This wind vector, corrected for random changes in the diffraction pattern is known as the true velocity. An intermediate wind vector calculated by the analysis is called the apparent velocity. This quantity does not take account of random change in the pattern and is, in general, an over–estimate of the background wind velocity. In the absence of random change in the diffraction pattern, the correction applied to the apparent velocity to yield the true velocity is zero.

An early and comparatively crude method designed to calculate the wind vector from time series sampled from spaced antennae was devised by *Mitra* [1949] and was known as the "method of similar fades". More sophisticated developments taking into account the random change in the diffraction pattern were reported by *Briggs et al.* [1950]. Anisometry of the pattern was considered by *Phillips & Spencer* [1955]. Many more modern discussions of the full correlation analysis in its current form and some of the computational difficulties involved in its implementation have also been written [*Meek*, 1980; *Briggs*, 1984; *Hocking et al.*, 1989]. Although more correctly referred to as the full correlation analysis, the technique is often called the spaced antenna analysis in the literature. This usage often occurs in the following chapters.

1.5.3 Doppler beam steering

Although not a spaced–sensor technique, the Doppler beam steering experiment (DBS) is often used in studies of the middle and lower atmosphere. It may also be synthesized in software using multiple spaced sensors. The DBS experiment utilizes at least one off–vertical radar beam from which the average radial velocity of the scatterers within the pulse volume is obtained. At least three non–coplanar Doppler beams are required if the full three–dimensional wind field is to be measured. Off–vertical Doppler beams may be formed either by inserting appropriate length phase–delay cables between successive rows of antennae in the array, or by electronically adjusting the phases of the intermediate frequency reference signals. Other parameters which may be measured with (multiple) Doppler beam radars include turbulence, wind shear and momentum fluxes.

1.5.4 Post–set and post–statistics beam steering

Both post–set and post–statistics beam steering utilize several independent groups of antennae and receiving channels in order to steer the direction of the radar beam on reception in software. In post–set beam steering (PBS) [*Röttger & Ierkic*, 1985], the complex time series are multiplied by an appropriate complex constant (which is in general different for each antenna group) and then summed to form a single time series. This time series is mathematically equivalent to one which would be measured if the corresponding cable delays had been used between antenna groups and a single receiver.

In post–statistics beam steering (PSS) [*Kudeki & Woodman*, 1990a], the complex auto– and cross–correlation functions (or power spectra and cross–spectra) are first calculated for

each antenna group and these are then multiplied by the appropriate complex constant. Note that post–set and post–statistics beam steering yield similar results. Post–statistics beam steering is computationally more efficient since in the PSS method auto– and cross–correlation functions (or spectra) must be calculated[2] only once. In the PBS formulation, the correlation functions (or spectra) must be recalculated for each beam direction.

1.5.5 Mean angle of arrival measurement

This, and the following three radar techniques, are in fact all spaced–sensor radar direction–finding techniques. For historical reasons, the nomenclature of these four experiments is somewhat confusing. The nomenclature presented here is that which is in reasonably common usage in the literature (except where specifically noted) and will be used throughout this work. More specific affixes are given to techniques such as "Radar interferometry" [*Van-Baelen & Richmond*, 1991a] in order to distinguish these from other similarly–named, yet distinct, techniques. The mean angle of arrival experiment is perhaps the simplest of these direction–finding experiments.

In the mean angle of arrival experiment, the complex temporal cross–correlation functions are calculated from at least three spaced antennae and the zero–lag phases are used to infer a mean angle of arrival for the incoming radiation [*Röttger & Ierkic*, 1985]. Note that frequency components from all parts of the spectrum are included in this measurement, and so Doppler–shifted backscattered signals from the entire illuminated region contribute to the mean angle of arrival estimate. This aspect of the measurement is distinct from the three Doppler–sorted spaced–antenna interferometer techniques described below.

1.5.6 Doppler–sorted analyses

In all Doppler–sorted analyses, the time series recorded at the spaced sensors are Fourier transformed to find the auto– and cross–spectra. Thus, the radiation arriving at the spaced sensors is ordered, or sorted into sequential, evenly–spaced frequency "bins". The exact nature of the information contained in the frequency spectra is currently somewhat uncertain, and different philosophies exist as to its interpretation. It is known that the characteristics of the scatterers and hence the frequency spectra vary with altitude, so it seems reasonable to alter the interpretation of the frequency–domain data as the region of the atmosphere of interest changes.

[2] An $O(n^2)$ operation.

Once the data have been Doppler sorted, two distinct techniques may be applied to the spectra. The analysis may either preferentially select a number of Doppler frequencies for further use, or all Doppler frequencies may be used at all times. The former type of analyses shall be termed "Doppler–selected" analyses in this work, while the latter shall be named "Non–Doppler–selected" analyses (see Figure 1.4).

Further to this, two distinct philosophies exist over the treatment of both the Doppler–selected and Non–Doppler–selected spectra. It is either assumed that each Doppler frequency used in the analysis (whether a selecting analysis or not) contains information about a single scattering point or, in the case of Non–Doppler–selecting analyses, it may be assumed that single Doppler frequencies do not contain information about discrete scatterers, and that information of a purely statistical nature regarding the mean and fluctuating motion within the radar beam is contained within the spectra. By their very nature, Doppler–selected analyses must find the angular position relative to the radar of one scatterer for each selected Doppler frequency and, with range–gating information, the three–dimensional coordinates of each "scattering point". This process has been named "imaging" by *Adams et al.* [1986], and shall be applied to all such analyses which image individual scatterers with unique Doppler frequencies. The alternative statistical approach involves fitting straight lines to the phases of cross–spectra and hence usually precludes any form of Doppler–selection. These analyses shall be termed "spectral–fitting" analyses in this work.

1.5.7 Doppler–selected analyses

Two main methods may be applied to Doppler–select certain "desirable" frequencies encompassed by the auto– and cross–spectra. First, cross– and/or auto–spectral magnitudes may be examined for large power levels, or simply a local peak in the power level in order to select an ensemble of frequencies. To date, the only researchers to have applied this technique have been *Meek & Manson* [1987]. Selection of Doppler frequencies on the basis of spectral magnitude shall be termed "Magnitude–selected imaging radar interferometry" (MSIRI) for the purposes of this work.

The alternative to frequency selection on the basis of spectral magnitude is that of frequency selection on the basis of spectral phase. If a single scatterer is responsible for the power contained at some Doppler frequency, then the backscattered radiation from that scatterer should appear on the ground as an approximate plane wave. Therefore, the cross–spectral phases around a closed ring of antennae on the ground should sum to zero. *Franke*

et al. [1990] used this condition with three antennae in order to locate scatterers and derive mean winds, and termed the technique "IDI–like" (see below). For those experiments where only three antennae are employed to determine the plane–wave radiation condition the term "Phase–selected imaging radar interferometry" (PSIRI) shall be used. Other experiments conducted along these lines have employed at least five independent antennae in order to gain extra degrees of freedom in the determination of the existence of plane–wave radiation at some Doppler frequency. In particular, *Adams et al.* [1986] have coined the name "imaging Doppler interferometry" (IDI), and this technique (which utilizes unsmoothed spectra) is now patented. Although somewhat arbitrary, the division shall be drawn in this work between those phase–selection techniques which use only three antennae (PSIRI), and those which use more than three antennae (IDI, or IDI–like). Many of these techniques are covered with greater specificity in Chapter 3.

1.5.8 Non–Doppler–selected analyses

In non–Doppler–selected analyses, all of the spectral information is used to derive the mean wind field and other atmospheric parameters. The technique used to find the wind field may be of the imaging type [*Franke et al.*, 1990][3], but is more usually of the statistical type. Probably the best–known of these statistical analyses is the "radar interferometer" (RI), or "spatial radar interferometer" (SI) [*Farley et al.*, 1981; *VanBaelen & Richmond*, 1991a; *VanBaelen et al.*, 1991b], although in this work the terms RI and SI will not be used. In this technique, linear fits against frequency are made to the phases of the cross–spectra calculated between the three antenna pairs. The slopes of these linear fits in frequency are simply related to the magnitude and direction of the FCA apparent wind velocity [*VanBaelen & Richmond*, 1991a; *Briggs & Vincent*, 1992]. Since the primary feature of this analysis is the linear fit to the cross–spectral phase, the term "phase slope–fitting radar interferometry" (PSFRI) shall be used in the remainder of this work.

Phase slope–fitting radar interferometry has recently been extended [*Briggs & Vincent*, 1992] to account for random pattern change and can now be applied in the form of "full spectral analysis" (FSA) as a Fourier counterpart to full correlation analysis. In fact, PSFRI is simply the first step in the FSA analysis which ultimately yields a wind velocity equivalent to the FCA true wind velocity.

[3] In the study reported by *Franke et al.* [1990], both Doppler selected and non–Doppler selected approaches were used

1.5.9 Image–forming techniques

If a large number of spaced sensors[4] are deployed in a regular grid then the diffraction pattern formed on the ground by the backscattered radiation can be sampled over a large area at each instant in time. Performing a two–dimensional spatial Fourier transform on the coherent signal obtained each spaced sensor then yields the complex aperture function of the diffracting screen above the radar. In this way the number, positions and sizes of the irregularities moving above the radar may be measured. Such an experiment was performed using E–region echoes by *Holmes* [1974] with the Buckland Park MF antenna array connected to 89 independent receivers and an ultra–sonic image–forming system. Image forming has also been attempted by *Brownlie et al.* [1973] with the large, steerable, MF crossed–array at Bribie Island in Queensland, Australia [*Mines*, 1969].

1.5.10 Frequency–domain interferometry

The term "frequency–domain interferometry" (FDI) was first coined by *Kudeki & Stitt* [1987], although the history of frequency–shift experiments extends as far back as *Appleton & Barnett* [1925]. *Appleton & Barnett* [1925] used a bi–static, continuous–wave radar system whose carrier frequency increased linearly with time. By counting the number of peaks of the beat frequency recorded at the remote receiving station per unit time, the apparent height of the ionospheric reflecting layer could be deduced. In this way, *Appleton & Barnett* [1925] obtained the first evidence for a strong reflecting layer in the ionosphere.

The next work with a frequency–shift experiment was that of *Briggs* [1951] who employed a frequency–swept vertical–incidence ionosonde to study the characteristics of signals reflected from various ionospheric layers at different frequencies. Subsequently, *Kudeki & Stitt* [1987] utilized the Urbana MST radar operating on two discrete frequencies of 40.82 MHz and 40.92 MHz to estimate heights and thicknesses of scattering layers. The MU[5] radar in Japan has also been utilized in a dual–frequency FDI experiment by *Palmer et al.* [1990]. *Brown* [1992] has performed FDI at medium frequencies with the Birdlings Flat radar in New Zealand with a total of five frequencies. This allowed explicit calculation of the frequency correlation function at a total of 10 frequency increments.

Frequency domain interferometry differs from most of the techniques discussed above in that it requires the use of frequency–agile radar systems. Due to the absence of this type of

[4] Of the order of 10^2 for radars operating at medium frequencies
[5] Middle and Upper atmosphere

equipment at Adelaide (at present), no such studies were undertaken. A brief history of FDI has been included for completeness, and in the expectation that such a facility will become available at Adelaide in future.

1.6 Motivation And Scope Of Thesis

As has been discussed, MF/HF radars are able to probe routinely at altitudes as low as 60 km. With a large increase in power–aperture product, it is possible that this coverage can be extended to lower altitudes, where lower free electron concentrations give rise to weaker backscatter. It is hoped that, with an increase of RMS pulse envelope power to at least 100 kW and an increase in aperture size of a factor of 150, the new Buckland Park radar will yield returns from lower altitudes.

The building of a new radar offered the opportunity to incorporate many modern features more commonly implemented in VHF radars. One of the most important of these was the ability to steer the transmitter beam electronically. The technical details of the new radar are discussed in Chapter 2.

Increasingly in the atmospheric physics literature, articles can be found which report various implementations of radar interferometric techniques. In Chapters 3, 4 and 5 different time– and frequency–domain radar interferometric techniques are used to measure winds and the mean angle of arrival of the backscattered radiation. It is hoped that these studies serve to illuminate some aspects of interferometric techniques which are presently poorly understood.

Chapter 2

THE NEW ADELAIDE MF DOPPLER RADAR

2.1 Introduction

Unlike most Doppler radars in use in the world today, [*Balsley & Ecklund*, 1972; *Balsley et al.*, 1980; *Folkestad et al.*, 1983; *Fukao et al.*, 1985a; *Fukao et al.*, 1985b; *Vincent et al.*, 1987; *Röttger et al.*, 1990] the large Buckland Park antenna array has hitherto been used only for reception. The Buckland Park array was originally designed to sample the spatial correlation function of the diffraction pattern produced by E– and F–region reflections. As such, it was necessary that the width of the transmitted beam be quite large, enabling as large a portion as possible of the "diffracting screen" to contribute to the diffraction pattern [*Felgate*, 1969]. In some more modern applications of medium frequency (MF) and very high frequency (VHF) radars, it is desirable to obtain as narrow a beam as possible for both transmission and reception. With very narrow, or, "pencil" beams, it is sometimes possible to ignore minor contamination of the atmospheric parameter of interest due to unwanted contributions from a finite range of angles.

Also possible with current technology is the ability to electronically steer a transmitter beam. This facility replaces the more cumbersome technique of inserting coaxial cable phase delays of varying length between the transmitters or receivers and the antenna array. With an increase in the number of the solid-state power amplification modules used to transmit on the large Buckland Park array, it is hoped that D–region echoes below 60 km may be obtained. In its final form, the new Buckland Park transmitter will have a total RMS peak

power output of 100 kW; some four times the power available with the current solid–state transmitter used for spaced antenna wind measurements. In fact, when compared with the original valve–driven transmitter installed at Buckland Park, the new transmitter and large array combination produces some 400 times more power per unit solid angle.

The Buckland Park antenna array offers a unique opportunity to implement an electronic beam steerable radar utilizing the largest filled–aperture HF array in the world in true transmit/receive mode. In the sections following, the design criteria considered in order to build this new radar are discussed in some detail. Some measurements taken with the first one–third of the new Doppler radar are presented and discussed in Chapter 4. The design process begins with a description of the current Buckland Park array and its modes of operation.

2.2 The Buckland Park Antenna Array

The Buckland Park Medium Frequency/High Frequency (MF/HF) Doppler Radar array occupies some 80 ha of land about 40 km North of Adelaide in the Port Gawler area [*Briggs et al.*, 1969]. Both the transmitting and receiving arrays are designed to utilize circularly polarized radiation and are optimized for a frequency of 1.98 MHz. A 5.94 MHz transmitting array is also available for use in conjunction with the 1.98 MHz receiving array (operating at its third harmonic) which, aside from certain design details, is not pertinent to this report.

The transmitting array consists of four centre–fed half–wave dipoles, arranged in a square and suspended some 27.4 m above the ground by four steel towers. The dipoles are formed from hard–drawn copper of 2 mm diameter, and are each 71.6 m long. Hung in the centre of each dipole is a balun matching the 75 Ω coaxial feeder cable to the (nominally) 75 Ω antenna. This small square transmitting array has a one–way power polar diagram of 40° half–power half–width and so can be regarded essentially as an isotropic radiator, at least as far as atmospheric partial reflections are concerned. In 1989, an obsolete valve–driven transmitter, with a nominal power of 50 kW, was de–commissioned and replaced with a solid–state modular transmitter with a RMS peak envelope power of 25 kW. In fact, the measured power output of the valve driven transmitter was only of the order of 10 kW, and so this represents a significant increase in radiated power. The solid–state transmitter is made up of 10 modules, each of 2.5 kW nominal power, and designed to produce amplitude modulated pulses of Gaussian shape. The exact shape and length of the pulse is adjustable,

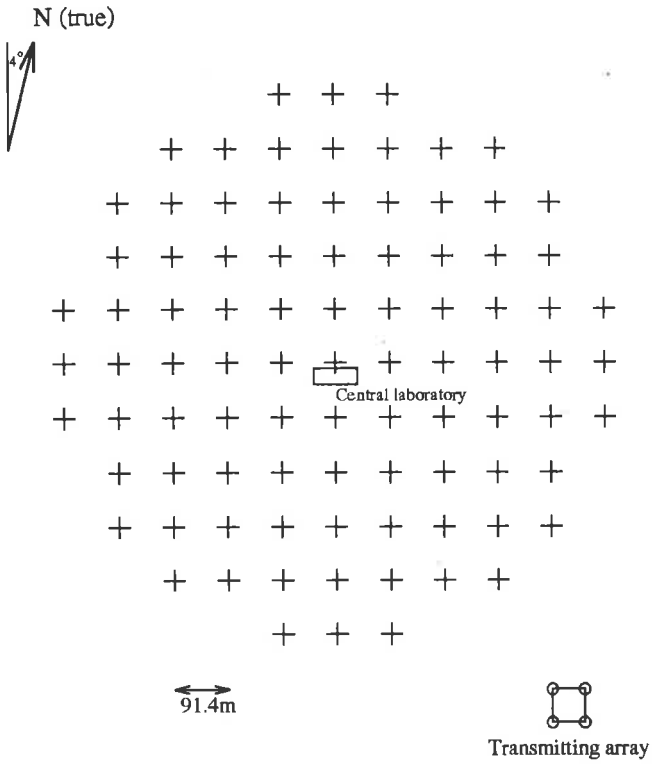

Figure 2.1: The Buckland Park field site array layout.

with an optimum pulse length of ~25 μs typical. In spatial terms the transmitted pulse was approximately 8 km in length with a resultant range resolution of 4 km (see *Röttger* [1984]). Operating at typical daytime pulse repetition frequencies (PRF) of 80 Hz, the transmitter duty cycle is less than 1% and thus transmits an average power of only 60 W RMS. Much of the experimental work reported in this thesis was conducted using this new solid–state transmitter.

The receiving array consists of 178 crossed half–wave dipoles arranged on the vertices of a rectangular grid to form a filled–in circle with a diameter of 915 m (see Figure 2.1). The orientation of the array is such that rows of antennae in the North–South direction are aligned with the bearing of magnetic North in 1967. This effectively means that the receiving array is rotated by 4° in an anticlockwise sense from true North. The field site is located on a (nearly) flat coastal plane which drops by only 1.6 m towards the South–West over the 915 m diameter of the array [*Reid*, 1984]. Each centre–fed dipole is suspended atop a 10 m high wooden pole and is cut to a resonant length of 71.6 m at 1.98 MHz. The resulting antenna impedance is nominally 28 Ω, although this may vary markedly on a day–to–day basis because of changing ground conditions. In order to match this 28 Ω antenna with the 75 Ω coaxial cable a balun is mounted on top of each wooden pole for each of

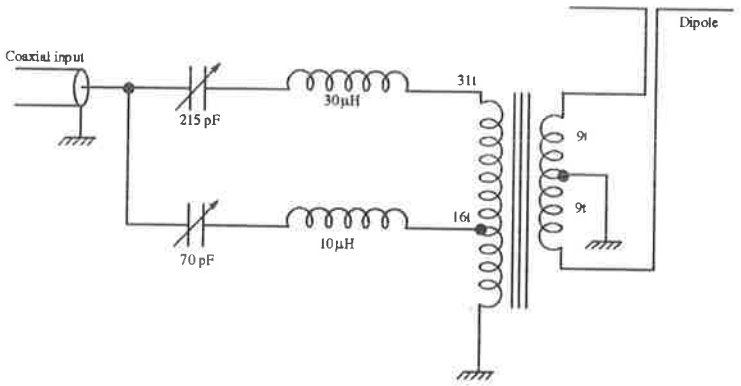

Figure 2.2: The old receiving antenna balun showing the two transformer taps for 1.98 MHz and 5.94 MHz operation.

the 2 antenna polarizations. In addition to its impedance matching role, each balun also serves as a passive switch between the 1.98 MHz and 5.94 MHz modes of operation. This is accomplished by a simple series tuned circuit for each frequency connected to one of two taps on the balun transformer (see Figure 2.2). The distance between adjacent dipoles is 91.4 m which, at a frequency of 1.98 MHz, is equivalent to a wavelength spacing of $\frac{3}{5}\lambda$. The full receiving array has a one–way half–power half–width of 4.5° and, due to this spacing, exhibits no grating lobes in its radiation pattern when used at its fundamental frequency. However, when the array is used in the 5.94 MHz mode, grating lobes are evident at off–vertical angles of ±35° (see Section 2.4). Each of the 178 dipoles is connected individually to the central laboratory by 75 Ω coaxial cable cut to electrical half–wavelengths at the operating frequency. Figure 2.3a shows the electrical length of each cable used in the array.

The shortest cables have an electrical length equal to one–half wavelength at 1.98 MHz with a resulting attenuation of 0.49 dB, while the longest cables are 4.5 wavelengths long and have an attenuation of 4.45 dB (see Table 2.1). In all, a total of 70 km of underground coaxial cable is used to connect the phased array, running in trenches dug in such a pattern as to minimize the total trench length (see Figure 2.3b).

In the central laboratory, each antenna is represented by a Belling–Lee coaxial socket on one of two "patch boards". One patch board contains the 89 dipoles aligned in the North–South direction (historically named the East, or "E" polarization) and the other contains the 89 dipoles aligned in the East–West direction; the "N" polarization. The connectors on the patch boards are arranged in such a way as to mirror the physical layout of the antenna array, thus allowing selection of individual dipoles or groups of dipoles for multiple receiver experiments. In addition to this remarkably flexible patch board arrangement, two

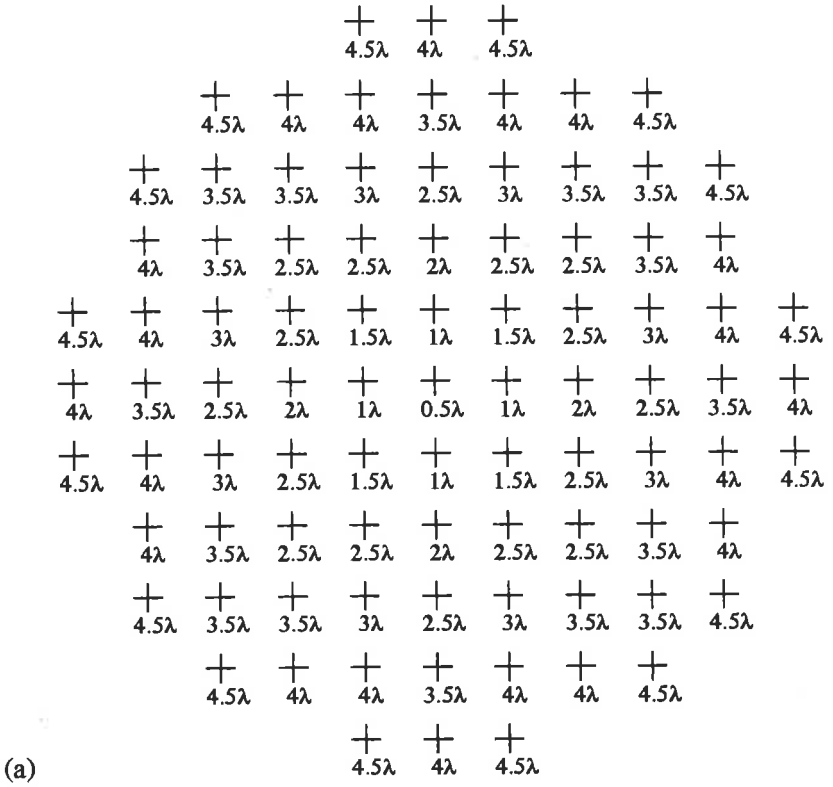

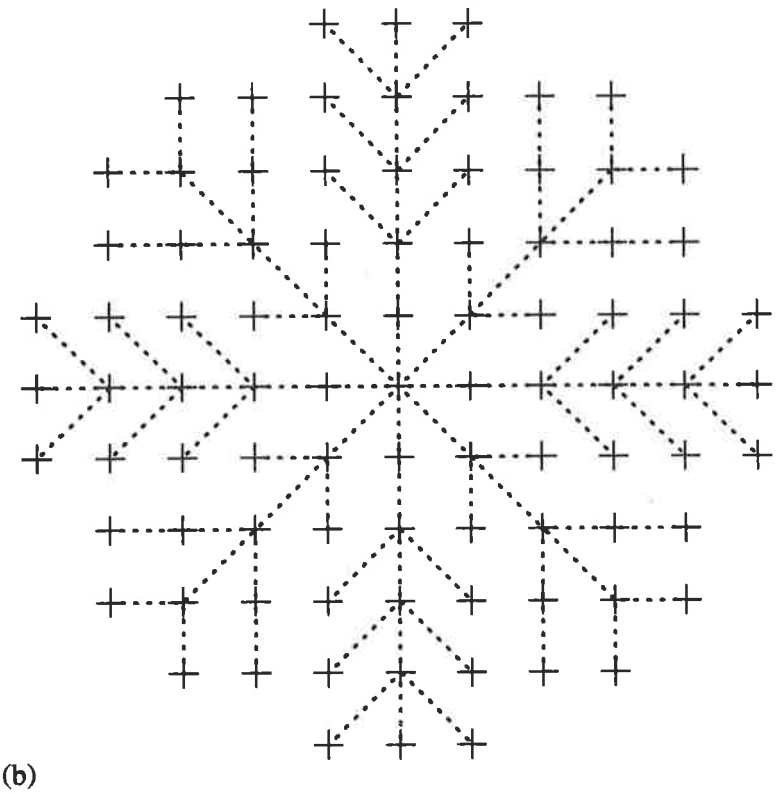

Figure 2.3: (a) The electrical length of each cable in the receiving array. (b) The physical layout of the underground cables.

Table 2.1: The attenuation of the Buckland Park underground coaxial cables.

Cable attenuation		
Cable length (λ at 1.98 MHz)	Attenuation (dB at 1.98 MHz)	Attenuation (dB at 5.94 MHz)
0.5	0.49	0.86
1.0	0.99	1.73
1.5	1.48	2.59
2.0	1.99	3.46
2.5	2.48	4.33
3.0	2.99	5.20
3.5	3.48	6.06
4.0	3.97	6.92
4.5	4.45	7.74

racks of ganged switches allow individual switching of each polarization between its patch board and a Doppler beam–forming rack. The "E" polarization may be switched to form two off–vertical Doppler beams comprising all 89 of the "E" dipoles. These two beams are directed 11.6° off–vertical in the North and South directions and are useful for conducting coplanar Doppler beam experiments such as the measurement of mesospheric momentum fluxes (see, e.g., *Reid & Vincent* [1987]). The "N" polarization may also be switched to form two off–vertical Doppler beams directed Eastward and Westward also at 11.6° to the zenith or, alternatively, an Eastwardly–directed off–vertical Doppler beam and a vertically–directed Doppler beam (see Figure 2.4).

From 1980 onwards, the radar consisted of a 5 channel coherent (ie: both in–phase and quadrature components) receiver system, coupled to 10 8–bit digitizers capable of sampling every 10 μs. This allowed coherent samples to be taken of the voltage present at each connected antenna corresponding to atmospheric partial echoes from every 2 km in altitude, thus oversampling the 4 km transmitter pulse volume by two times. In 1991, this author undertook an extensive refurbishment of the 5 channel Doppler radar which included an expansion of the radar from 5 to 8 channels. Although the receiving system had originally been designed to support 8 channels, the full 8 channel system had never been implemented due to computational limitations. Procuring and de–bugging the extra receivers and digitizers required for this expansion and updating the DMA computer interface and software were the main areas of labour. These endeavours are expanded upon in Section 2.6.

In 1989, it became possible to commence studies on the feasibility of upgrading the

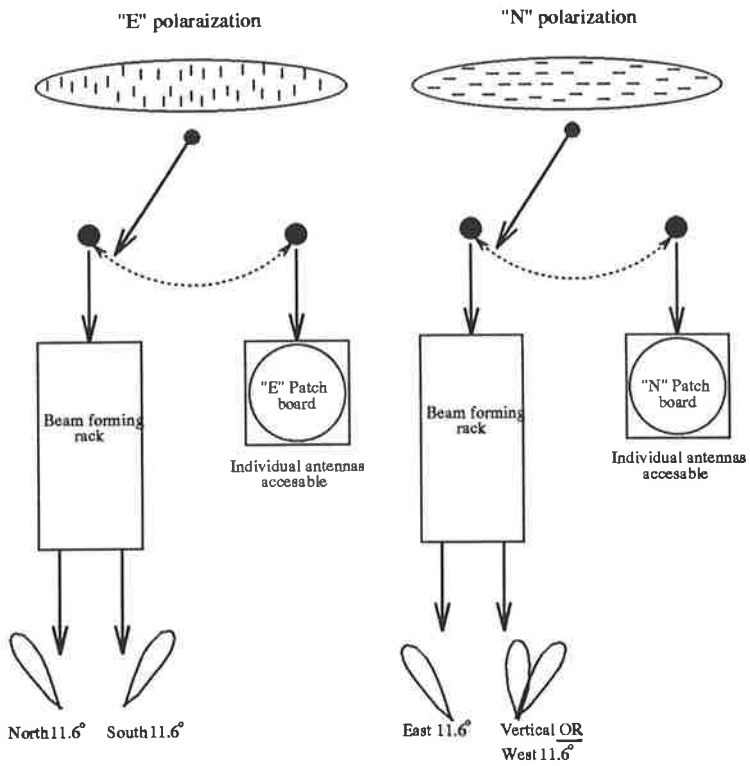

Figure 2.4: Schematic diagram of the beam configurations possible with the original beam forming racks and switches.

Buckland Park MF/HF array to a modern, beam steerable, transmit/receive Doppler radar, with the 1 km square array used for transmission as well as reception. Some of the design criteria considered in this upgrade are detailed in the following sections.

2.3 The Design Criteria For A True Doppler Radar

In order to plan the conversion of the Buckland Park radar facility into a true Doppler radar, the following points were first considered.

- The transmitted power losses in the underground coaxial cable,
- the power loss due to dipoles suspended less than $\frac{\lambda}{4}$ above a lossy ground plane,
- the ability of the existing baluns to cope with the new transmitter power,
- the ability of damaged underground cables to cope with the transmitter power,
- the number of solid–state transmitter modules and upgraded receivers affordable and the resulting groupings of antennae required,

- the beam steerability parameters and the resulting beam pointing accuracy,
- the experimental flexibility and future expandability, and
- the material durability used in array refurbishment and maintenance.

2.3.1 The power loss in the underground coaxial cables

As part of the initial feasibility study into the implementation of the full Doppler radar using existing assets at the Buckland Park field site, any power losses due to the underground coaxial cable were evaluated.

The cable in question is some 25 years old and originally selected for the radar on the basis of its high propagation constant, low radio–frequency (RF) impedance, light weight and low cost. Since the cable was to be used only for reception and thus be subjected to potentials of only microvolts, at no stage was its ability to conduct high instantaneous RF currents ($\geq$ 10 A) or to withstand relatively high RF voltages ($\geq$ 300 V RMS) considered. The final choice of cable was a single strand copper conductor surrounded by an air–cored dielectric. The copper earth braid included a continuous copper sheath between itself and the dielectric. The cable's nominal characteristic impedance was 70 Ω and its propagation constant was 80% (due to the air–cored dielectric). In practice, the characteristic impedance of the cable varied above 70 Ω, and for the purpose of impedance matching could be considered as standard 75 Ω cable. The choice of cable, although economically sound, led to some frustrating longer term problems, detailed in Subsection 2.3.4.

In order to evaluate the possible power loss problems, a prototype of the solid–state module to be used in the final transmitter system was connected via a suitable filter (see Section 2.5) to three of the array's half–wave dipoles (see Subsection 2.3.5) equipped with prototypes of the new transmitter baluns (see Section 2.5). The three antennae selected for this test were connected to the central laboratory with cables of average length (approximately two wavelengths at 1.98 MHz), and were considered to be representative of the entire array. The transmitter module was triggered at a PRF of 100 Hz and the power output at the baluns on top of the antenna poles observed. No discernible power loss could be detected (given the uncertainty of the exact impedance of the load being driven) and it was concluded that the coaxial cables in service would suffice.

2.3.2 The power loss due to dipoles suspended less than $\frac{\lambda}{4}$ above a lossy ground plane

For a half–wave dipole suspended Δh m above a lossy ground plane, the image dipole formed Δh m below the surface is imperfect. The radiation pattern of this imperfectly matched end–fire array of two dipoles will deviate from that expected in the case of an ideal ground plane, and some portion of the energy transmitted into the dipole antenna will not be radiated as desired. The amount of power absorbed by the lossy ground plane is minimized by setting the antenna height, Δh to be $\frac{\lambda}{4}$. It was for this reason that the original transmitter towers at Buckland Park were chosen to be as close to $\frac{\lambda}{4}$ above ground as possible while, since it was not possible to install 89 $\frac{\lambda}{4}$ high poles for the receiving array, the large array was only suspended 10 m above the ground.

In order to determine that significant power could be radiated by the receiving dipoles, the single module prototype transmitter was slaved to a standard three channel spaced antenna receiver system and attached to the three dipoles fitted with the new transmit/receive baluns. The three spaced antenna receivers were connected to three groups of four dipoles each on the opposite linear polarization to that used by the transmitter. Approximately 30 min of data were collected and saved as raw time series of the coherent voltage recorded at each antenna. The PRF was set to 80 Hz and since a 32 point coherent integration was used, successive data points were separated by 0.4 s. A total of 20 heights covering 40 km in altitude were recorded starting at 50 km and ending at 88 km. Examination of the variance of the signals recorded over the height region 70 km to 88 km revealed no great diminution from the variance recorded immediately before by the same receiving system when using the original 27 m high transmitting array and the 10 channel solid–state transmitter. Further analysis of the data revealed that usable power spectra and auto–covariance functions could be calculated to acceptably low altitudes. Due to the high returned signal levels and the acceptability of the data recovered, it was concluded that ground plane absorption when transmitting through the main array's modified receiving dipoles was satisfactorily low.

2.3.3 The ability of the existing baluns to cope with the new transmitter

The inadequacy of the existing receiver baluns to survive (let alone transmit) the high powers to be delivered to the dipoles was patently clear from the outset of the feasibility study. Consequently, design of the new transmit/receive baluns was one of the first tasks undertaken

in the construction of the upgraded radar (see Section 2.5).

2.3.4 The ability of damaged underground cables to cope with the transmitter power

With the aid of time–domain reflectometry (TDR) and physical inspection it was discovered that in some cases the integrity of the coaxial cable originally chosen to connect the phased receiving array had been compromised by the intrusion of water into the air–cored dielectric. In addition to this problem, mechanical fatigue had in nearly all cases damaged the outer sheath on the section of cable attached to the wooden antenna pole. In cases where the outer insulation had been breached, almost complete destruction of the copper earthing braid had ensued due to the extremely corrosive nature of the sea–side environment of the site. In order for these antennae to be used, it was necessary for these damaged upright sections of cable to be replaced, and this was done during replacement of the old receiving baluns with the new transmit/receive baluns. Since the relative permittivity of water ($\epsilon_r = 78.2$) is substantially higher than that of air ($\epsilon_r \approx 1.0$), sections of water lying in the coaxial cables caused the characteristic impedance of that section of cable to drop and the propagation constant to decrease. Thus, not only would some power be reflected from the water in the cable due to the impedance mismatch, but the electrical length of the cable would be increased. This would have had the effect of presenting loads with reactive components to the transmitter modules located at the other end of the no longer $\frac{n\lambda}{2}$ long cables. For this reason, all cables suffering from this problem had the water within their dielectric blown out by compressed air.

2.3.5 The number of solid–state transmitter modules and upgraded receivers affordable and the resulting groupings of antennae required

Since the cost of each transmitter/receiver channel was of the order of AUS$10000, it was not possible to build an ideal 89 channel transmit/receive radar. The first design settled upon was a 30 channel transmit/receive radar in which each solid–state transmitter module would drive three of the array's dipoles with a transmit/receive (TR) switch allowing the connection of one of the 30 receivers to the same three dipoles. The advantage of this arrangement is that it provides considerable flexibility in the choice of receiver antennae, and the potential for good image–forming capability. As a first stage, a 30 module transmitter system and a 10 channel receiving system was constructed. In reaching this decision much thought was

given to the ramifications of forcing groups of antennae to be phased together. While this enforced grouping has no effect on the radiation pattern of the full array when the beam is directed vertically, considerable distortions (including grating lobes) may occur in off–zenith beams. Antenna groupings of two, three and four dipoles were considered for transmission. Particular attention was given to polar diagram distortion and the magnitudes and angular positions of side lobes for beams directed at non–zero off–zenith angles. A final grouping of three dipoles was found to be satisfactory provided that flexibility was retained in selection of the antennae to be grouped. The antenna patterns considered during this process are described in Section 2.4.

2.3.6 Beam steerability parameters and pointing accuracy

One of the prime motivations for upgrading the Buckland Park radar to a modern Doppler radar was the possibility of rapid beam steering on transmission using digital techniques. Since dipoles (or groups of dipoles) were to be driven by independent transmitter modules, beam steering could be accomplished by progressively shifting the phase of each PA module connected to different antennae across the array. In order that the design of a phase–control module could begin, it was necessary for the minimum phase increment required, $\Delta\phi$ to be established. The logical choice for $\Delta\phi$ was such that the beam could be steered by as little as one–half of one beam–width in any direction. For a beam at angle θ to the zenith,

$$\Delta\phi = \frac{2\pi d}{\lambda} \sin\theta \ , \tag{2.1}$$

where d is the distance between adjacent antennae and λ is the radar wavelength. For the Buckland Park array operating at a frequency of 1.98 MHz it was found that the appropriate $\Delta\phi$ corresponded to a time delay of approximately 24 ns. The final time delay chosen was one–half of this value to allow for digitization errors in the phase–control module. Thus, the phase of each transmitter module could be controlled through a full range of 360° in steps of 8.5°, making a total of 42 independent phase steps. Since each transmitter module was to be independently phase controlled, the progressive phase shift across the array could be induced in any direction, and hence beams could be formed at non–cardinal azimuthal angles. This has not hitherto been possible with any large, filled–aperture, phased–array MF/HF radar.

2.3.7 Experimental flexibility and future expansion

A prime feature of the Buckland Park phased–array radar has been its extreme flexibility in experimental configuration. The array has repeatedly been utilized in ways unanticipated by its original designers. It was with this tradition of versatility in mind that the design of the new radar system was undertaken. To this end, the smallest possible number of "hard–wired" items of the design were tolerated. Thus transmitter modules may be connected to any antennae that an experimenter desires. The receivers may be connected to the same antennae as the transmitter modules, or different antennae as needed. Paradoxically, such flexibility may increa he risk of the mis–informed or inexperienced configuring the system in a nonsensical ma To minimize this possibility clearly defined and marked "default" settings were included as part of the experimental system. Thus, new users may immediately and without error begin to collect data while experienced experimenters may devise more complex configurations without hindrance from concessions to "user friendliness". The key to this versatility was the inclusion of a number of patch boards enabling the interconnection of transmitter modules, receivers and antennae in various permutations. Details of the design of these patch boards can be found in Section 2.5.

It was decided that the first stage of construction of the 30 channel transmitter/30 channel receiver radar system would be a 30 channel transmitter/10 channel receiver system. This smaller radar was designed to be upgradable to its full complement of 30 receivers and, although requiring much work, did not directly form a part of this research.

2.3.8 Material durability used in array refurbishment and maintenance

Due to the increased demands placed on the array by the new transmitting system, and the advanced age of the array, it was necessary to give careful thought to the materials used in refurbishment and routine repair of the antennae. The dipoles had originally been suspended by wooden poles at their centres and held aloft at their ends by a fully insulated steel wire spacer connected to the next co–linear dipole. Thus the 91.4 m between dipole centres was bridged by

1. one half of the half–wave dipole measuring 35.8 m,
2. a galvanized steel spacer insulated at both ends measuring 19.8 m and
3. half of the adjacent dipole also measuring 35.8 m.

As the array was 25 years old, the lifetime of the steel spacers in the rather corrosive environment had expired. Many dipoles were finding themselves "grounded" as steel spacers frequently gave way. To extend the lifetime of the new array beyond the next quarter century, it was decided to use glass fiber rope in place of the vulnerable steel spacers. The rope, known as "DB wire", had a tensile strength per unit cross section far in excess of that of steel, and did not suffer from corrosion. In addition, it was an excellent RF insulator and so ceramic insulators (prone to failure under compression) were not required.

Two other failure modes in the array were apparent. First, the copper dipoles themselves, although not as susceptible to corrosion as the steel spacers, were nonetheless weakened by corrosion and had also suffered a certain degree of stretching. Stresses sustained from breaking steel spacers also contributed to the failure of some dipoles. In order to remedy any similar future breakages, a larger diameter hard–drawn copper wire was purchased. The new wire was not heat treated and so remained work hardened from the extrusion process and was therefore less prone to stretching than the original wire. Second, the two wires connecting the dipole to the balun box (known as "feeders") were excessively susceptible to mechanical fatigue. This, along with a minimum of corrosion, would quickly cause the newest of feeders to fail. The method used to eliminate the feeders from the regular maintenance schedule was to replace them with a very large cross section, multistrand copper wire with heavy ultra–violet (UV) stabilized plastic insulation. In addition to this, all soldered joints connecting feeders to copper dipoles were sealed using waterproof self–polymerising tape.

2.4 Beam–Pattern Modeling

In order that the beam patterns of various combinations and groups of antennae could be predicted theoretically, a flexible computer program called "xsect" was developed. This mouse–driven program allowed the user to select any of the antennae in the Buckland Park array to make up any particular subset array. In addition, it was possible to phase–group sets of these antennae together in any desired manner to observe the effect on the off–vertical beam–pattern. Random phase errors could also be added to gauge the importance of cable length accuracy and nominal antenna impedance. We begin our exploration of antenna beam–patterns with the theoretical expressions for half–wave dipoles in free space.

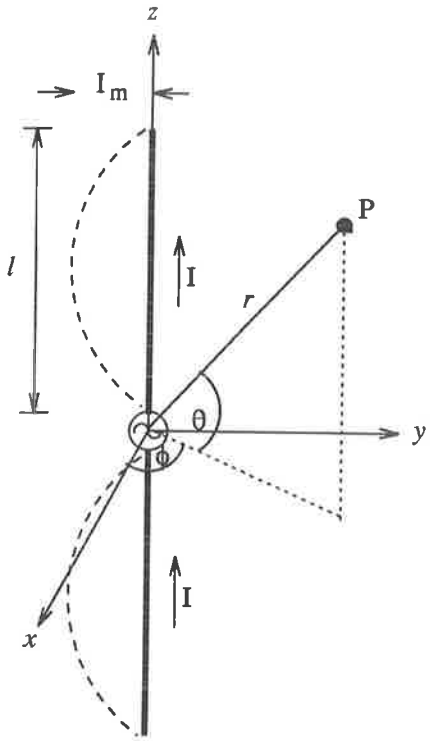

Figure 2.5: Long straight wire antenna showing rectangular and polar coordinate systems.

2.4.1 Radiation pattern for a half–wave dipole

Consider a long straight wire antenna of length 2ℓ, centred at the origin and aligned with the z–axis. Given the coordinate system displayed in Figure 2.5 and assuming a current distribution on the wire $\mathrm{I}(\zeta)$, the magnetic field pattern of such an antenna is given by

$$H_\phi = \frac{jk}{4\pi r} e^{-jkr} \sin\theta \int_{-\ell}^{+\ell} I(\zeta) e^{jk\zeta\cos\theta} d\zeta \ , \tag{2.2}$$

where k is the wavenumber of the driving oscillation, j is the square root of -1 and H_ϕ is the magnetic field which is everywhere aligned with the $\hat{\phi}$ unit vector. (see, e.g., *Ramo et al.* [1984], *Sander & Reed* [1986]). In the case of a half–wave dipole, we take the functional form of $\mathrm{I}(\zeta)$ to be

$$I(\zeta) = I_m \cos\left(\frac{\pi\zeta}{2\ell}\right) \ , \tag{2.3}$$

with $\ell = \frac{\lambda}{4}$, and Equation 2.2 reduces (after much manipulation) to

$$H_\phi = \frac{jI_m}{2\pi r} e^{-jkr} \left[\frac{\cos(\frac{\pi}{2}\cos\theta)}{\sin\theta}\right] \ . \tag{2.4}$$

The power radiation pattern of a half–wave dipole is found by dropping the dependence of Equation 2.4 on distance, ignoring constants and squaring to obtain

$$K(\theta) \propto \frac{\cos^2(\frac{\pi}{2}\cos\theta)}{\sin^2\theta} \ . \tag{2.5}$$

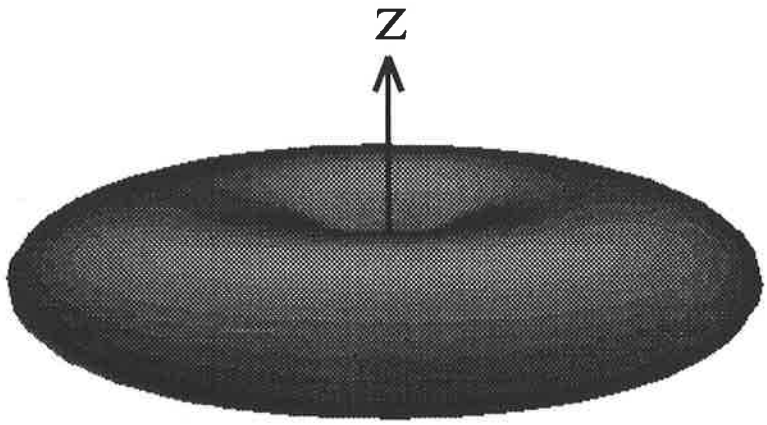

Figure 2.6: The radiation pattern of a half–wave dipole in free space aligned with the z–axis.

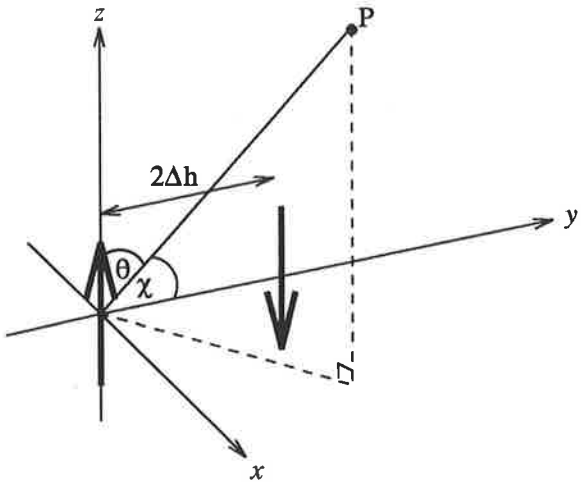

Figure 2.7: Dipole with image below ground plane showing polar coordinate system used in text.

Thus the power radiation pattern for a half–wave dipole in free space takes the form of a torus whose axis of symmetry is the z–axis as depicted in Figure 2.6.

In the more practical case of a horizontal half–wave dipole, Δh m above a perfectly conducting ground plane, we may replace the ground plane with the antenna's image situated Δh m below ground level (see Figure 2.7). The magnetic field pattern of such a combination of dipole and image separated by distance 2Δh m and arranged at the origin of the coordinate system shown is

$$|H_\phi| \propto \sin(k\Delta h \cos\chi)\frac{\cos(\frac{\pi}{2}\cos\theta)}{\sin\theta}\ , \tag{2.6}$$

which has a power radiation pattern

$$K(\theta,\chi) \propto \sin^2(k\Delta h \cos\chi)\frac{\cos^2(\frac{\pi}{2}\cos\theta)}{\sin^2\theta}\ . \tag{2.7}$$

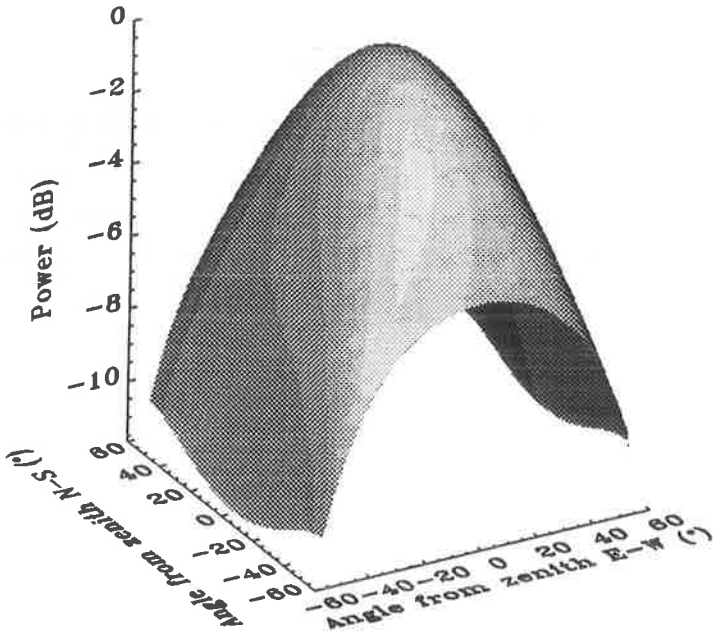

Figure 2.8: Power polar diagram of a single half–wave dipole above a perfect ground plane. The value of Δh selected is appropriate for that of an antenna at Buckland Park.

This is represented in Figure 2.8 as a three–dimensional surface in polar coordinates. This power polar diagram has a half–power half–width of 30° in the direction parallel to the dipole's axis, and 44° in the direction orthogonal to the dipole's axis.

We take Equation 2.7 as our standard individual radiating element which may be duplicated and arranged in any pattern to produce an array of half–wave dipoles.

2.4.2 Radiation patterns for arrays of dipoles

We now define our field pattern in terms of two separable functions representing the field pattern of a single radiating element and the layout of the array. This latter function is known as the array function, $M(\chi)$ (see *Sander & Reed* [1986]). Having defined the field pattern for a single element in Subsection 2.4.1 we follow the notation of *Sander & Reed* [1986] and label this as $F(\theta, \chi)$, and write

$$|H_\phi| \propto M(\chi)F(\theta, \chi) \,. \tag{2.8}$$

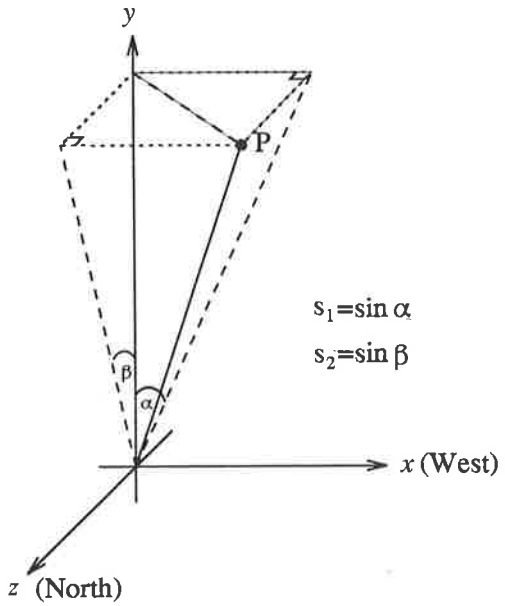

Figure 2.9: The coordinate system used for the calculation of the array function from the aperture function.

Following the coordinate system of Figure 2.7, we write the array function, $M(\chi)$ as the complex sum of the spatially separated currents, I_i present in each antenna, as

$$M(\chi) = \sum_{i=1}^{n} I_i \, exp(jka_i \cos\chi) \; . \tag{2.9}$$

As has been well established in optical diffraction theory, (see, e.g., *Hecht* [1987]) this is exactly equivalent to calculating the Fourier transform of the aperture function in two dimensions, $A(x, y)$. Thus

$$M(s_1, s_2) = \int_{-\infty}^{+\infty} \int_{-\infty}^{+\infty} A(x, y) e^{jk(s_1 x + s_2 y)} dy dx \; , \tag{2.10}$$

where s_1 and s_2 are the sines of the angles in aperture space defined in Figure 2.9.

The aperture function, $A(x, y)$ represents the amplitude and phase of radiation emitted from the aperture at each point, (x, y). For an aperture emitting a plane wave of constant amplitude, $A(x, y)$ is a constant which, for convenience, we will take to be unity. In the case of the Buckland Park array, $A(x, y)$ may take non–zero values only at certain discrete positions which, of course, correspond to the fixed antenna positions. For convenience we constrain x and y to be integers which results in $A(x, y)$ being defined in steps of antenna separation in wavelength units. The aperture function may also be used to model the varying amplitude of radiation across the array due to cable attenuation (see Table 2.1 and Figure 2.3). This is achieved by weighting the non–zero values of $A(x, y)$ with the varying signal levels emitted

by each antenna in the array. In this way the calculated beam pattern takes account of the "tapering" of signal across the array with the attenuation lowest in the centre, and increasing towards the fringes of the aperture. For non–plane–wave radiation emitted from the aperture, $A(x, y)$ is assigned complex values representing the in–phase (real) and quadrature (imaginary) part of the signal at each antenna. The modulus of $A(x, y)$ at some point in the aperture is interpreted as the amplitude of the transmitted signal, and the argument of $A(x, y)$ is then the phase angle of the radiation relative to some arbitrary zero. Using these definitions we can model the beam–pattern resulting when the beam is tilted from the zenith by use of progressive phase delays across the array. Phase uncertainties at each antenna may also be modeled using normally distributed phase errors to simulate errors in the electrical length of the coaxial cable connecting the centre of the array to each dipole.

In order that this new formulation may be utilized, it is necessary to transform Equation 2.7 into the coordinate system defined in Figure 2.9.

In Figure 2.10, the two different polar coordinate systems are labeled with their respective angles (θ, χ) and (α, β). Also depicted in this figure is the angle δ used for construction purposes, and the lengths A, B, C, D, E, R and Y. We begin the derivation by defining the first six lengths in terms of the angles χ and δ and the seventh length, Y, such that

$$\begin{aligned} A &= Y \tan\chi \,, \\ B &= Y \tan\chi \cos\delta \,, \\ C &= Y \tan\chi \sin\delta \,, \\ D &= Y\sqrt{1+\tan^2\chi \sin^2\delta} \,, \\ E &= Y\sqrt{1+\tan^2\chi \cos^2\delta} \end{aligned}$$

and

$$R = Y\sqrt{1+\tan^2\chi} \,. \tag{2.11}$$

Next we define the angles α and β in terms of the above lengths:

$$\begin{aligned} \tan\alpha &= \frac{C}{Y} \\ \tan\beta &= \frac{B}{Y} \,. \end{aligned} \tag{2.12}$$

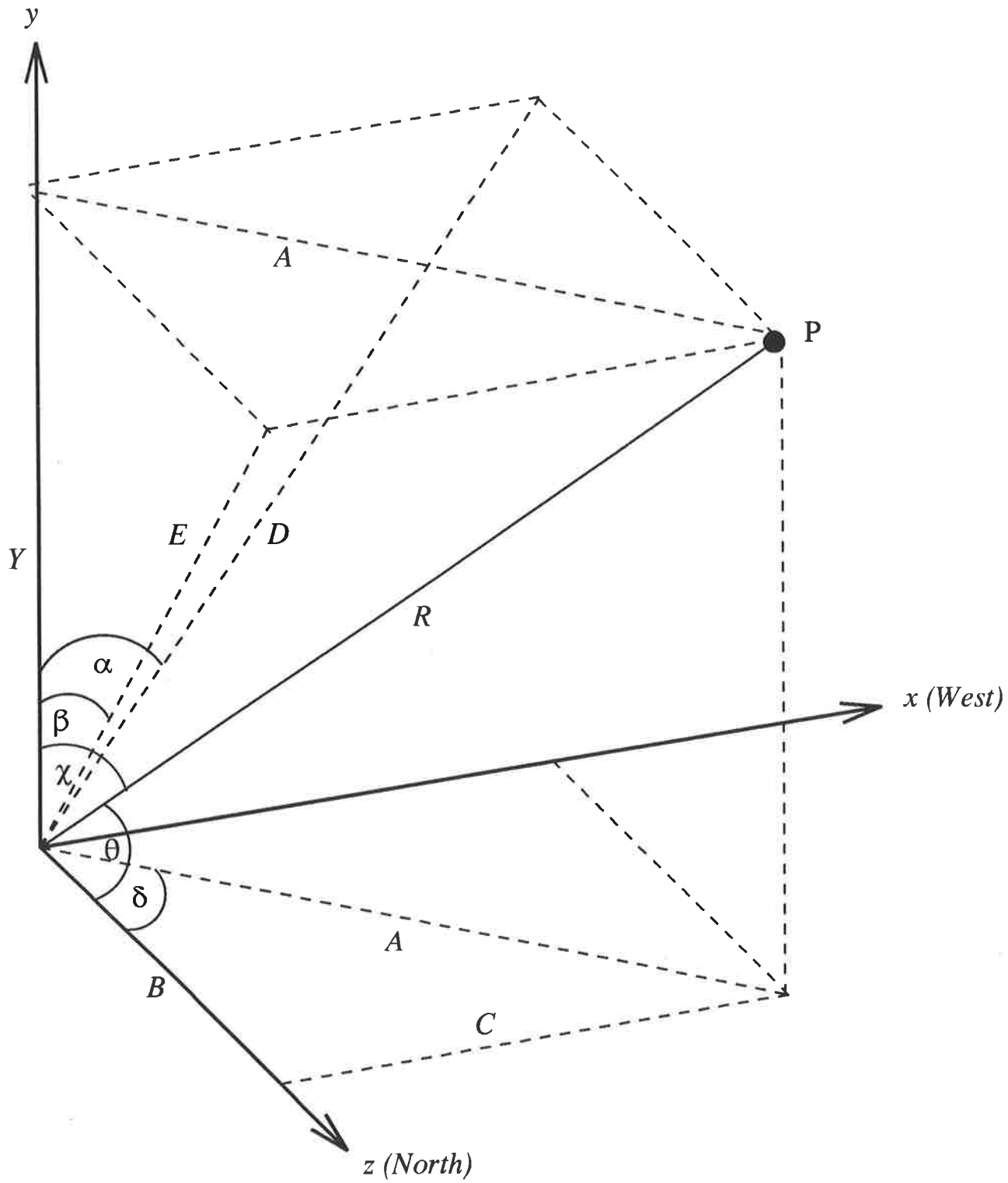

Figure 2.10: The two coordinate systems used for the calculation of the array function and for the radiation pattern of a single half–wave dipole above a ground plane. Also depicted is the construction used to transform between the two sets of coordinates.

Substituting for the appropriate lengths from Equations 2.11 yields

$$\begin{aligned} \tan\alpha &= \tan\chi\sin\delta \\ &\text{and} \\ \tan\beta &= \tan\chi\cos\delta\ . \end{aligned} \tag{2.13}$$

In order to eliminate δ, the angle used purely for construction, we square and add equations 2.13 to find

$$\tan^2\alpha + \tan^2\beta = \tan^2\chi\ . \tag{2.14}$$

Expressions for $\cos\chi$, $\sin\theta$ and $\cos\theta$ may now be derived using Equations 2.11, 2.13 and 2.14. Hence

$$\begin{aligned} \cos\chi &= \frac{Y}{R} \\ &= \frac{1}{\sqrt{1+\tan^2\chi}} \\ &= \frac{1}{\sqrt{1+\tan^2\alpha+\tan^2\beta}}\ , \\ \sin\theta &= \frac{D}{R} \\ &= \frac{\sqrt{1+\tan^2\chi\sin^2\delta}}{\sqrt{1+\tan^2\chi}} \\ &= \frac{\sqrt{1+\tan^2\alpha}}{\sqrt{1+\tan^2\alpha+\tan^2\beta}} \\ &\text{and} \\ \cos\theta &= \frac{B}{R} \\ &= \frac{\tan\chi\cos\delta}{\sqrt{1+\tan^2\chi}} \\ &= \frac{\tan\beta}{\sqrt{1+\tan^2\alpha+\tan^2\beta}}\ . \end{aligned} \tag{2.15}$$

The radiation pattern for a half–wave dipole Δh m above a perfect ground plane (Equation 2.7) can now be expressed as

$$\begin{aligned} K(\alpha,\beta) \propto\ & \sin^2\left(\frac{k\Delta h}{\sqrt{1+\tan^2\alpha+\tan^2\beta}}\right)\times \\ & \cos^2\left(\frac{\pi}{2}\frac{\tan\beta}{\sqrt{1+\tan^2\alpha+\tan^2\beta}}\right)\left(\frac{1+\tan^2\alpha+\tan^2\beta}{1+\tan^2\alpha}\right)\ . \end{aligned} \tag{2.16}$$

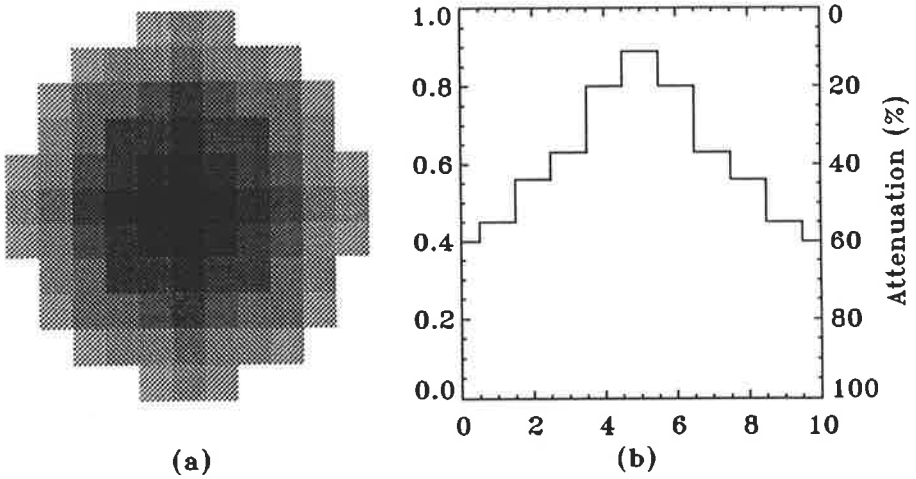

Figure 2.11: Graphical representation of the Buckland Park array's cable attenuation shown as (a) a grey–scale intensity map and (b) a cross–section through the centre of the array. The figures shown are gains scaled such that a value of one corresponds to zero attenuation. Note that even in the centre of the array the attenuation level is non–zero.

We are now able to write both the array function and the radiation pattern of an individual dipole in terms of the new coordinate system described by the angles α and β. By Fourier transforming suitable aperture functions and then multiplying by the single dipole radiation pattern we now investigate the beam–patterns of various relevant array configurations.

2.4.3 Radiation pattern: the full Buckland Park array

The full Buckland Park array's aperture function consists of an 11 by 11 array, 89 of whose 121 elements are non–zero. The real values assigned to the aperture function represent the varying attenuation of the coaxial cables connecting different antennae to the central laboratory. A graphical representation of the attenuation appears in Figure 2.11. The full Buckland Park antenna array's power polar diagram appears in Figure 2.12. As can be seen from the cross–sectional plot, the main lobe is quite symmetrical with a one–way half–power half–width of 4.8°. In fact, the differences between the East–West and North–South cross sections are negligible in the off–zenith angle range of ±40°. The main side lobes occur at about 17° and 30°, and are some -22 dB less than the maximum gain at the central peak. If the two–way radiation pattern is considered, the situation is much improved. We consider the situation where the full array is used for transmission and reception on opposite linear polarizations. The two–way radiation pattern can then be found by multiplying the array function of the full array by the same array function rotated through 90°. The two–way

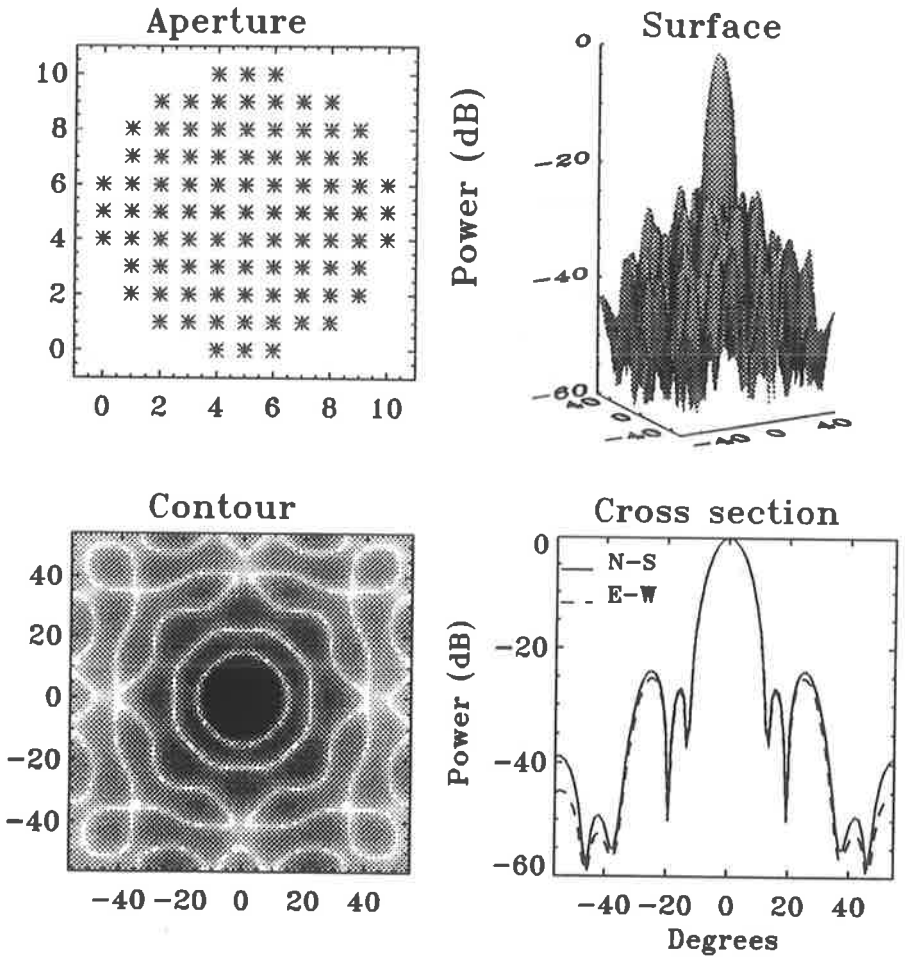

Figure 2.12: The full Buckland Park power polar diagram. Clockwise from top left, (a) The aperture function, (b) three–dimensional surface representation of the radiation pattern, (c) Grey scale intensity plot, (d) Two cross sections through the centre of the pattern at right angles. All off–zenith axis scalings are in degrees.

radiation pattern thus found is presented in Figure 2.13. Note that the main side lobes are now suppressed by at least 45 dB compared to the central beam. The two–way half–power half–width is reduced by approximately 1° to 3.8° and the circular symmetry of the central lobe is enhanced. The asymmetry in the main lobe of the one–way radiation pattern is due to the difference in curvature of the single element's orthogonal cross sections. As the full array's one–way radiation pattern is rotated by 90° before multiplication with the original pattern, this asymmetry is removed.

Casual inspection of Figures 2.12 and 2.13 reveals no evidence of higher "orders" of the radiation pattern at large off–zenith angles as might be expected by analogy to diffraction theory. Higher orders, or "grating lobes", do in fact occur at off–zenith angles less than

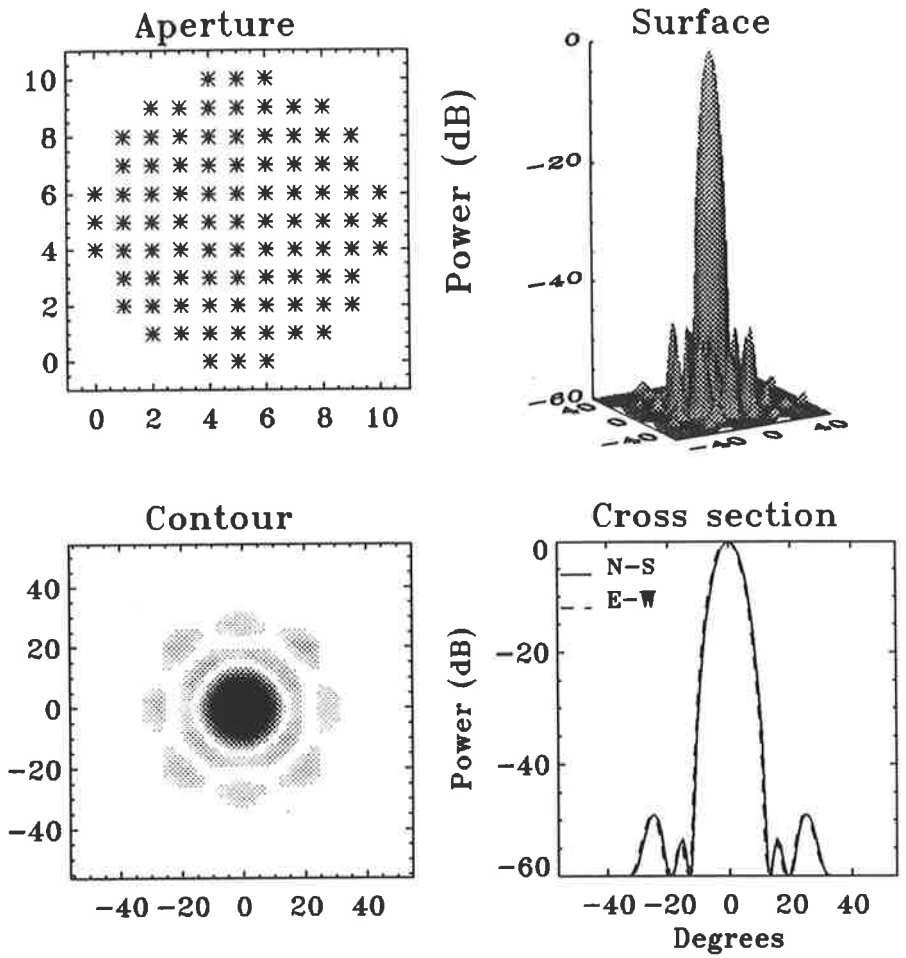

Figure 2.13: The full Buckland Park two-way power polar diagram. Panels are as indicated in Figure 2.12.

90° where the spacing between individual elements is larger than one wavelength. Although this is not the case for the Buckland Park array operating at 1.98 MHz, the effective array spacing is tripled to about $\frac{9}{5}\lambda$ when the array is used at 5.94 MHz. Although not central to this work, the operation of the array at 5.94 MHz is still of some interest, and the presence of grating lobes in the radiation pattern of the array at 5.94 MHz serves to illuminate some aspects of the radiation patterns displayed in later sections.

2.4.4 Radiation pattern: full Buckland Park array at 5.94 MHz

In order to begin calculating the radiation pattern of the Buckland Park array at 5.94 MHz, we first recognise that the radiation pattern of each element in the array is no longer that of a half-wave dipole. The elements in the array when used at their third harmonic are, of course, $\frac{3}{2}$-wave dipoles. For a derivation of the radiation pattern of a $\frac{3}{2}$-wave dipole similar

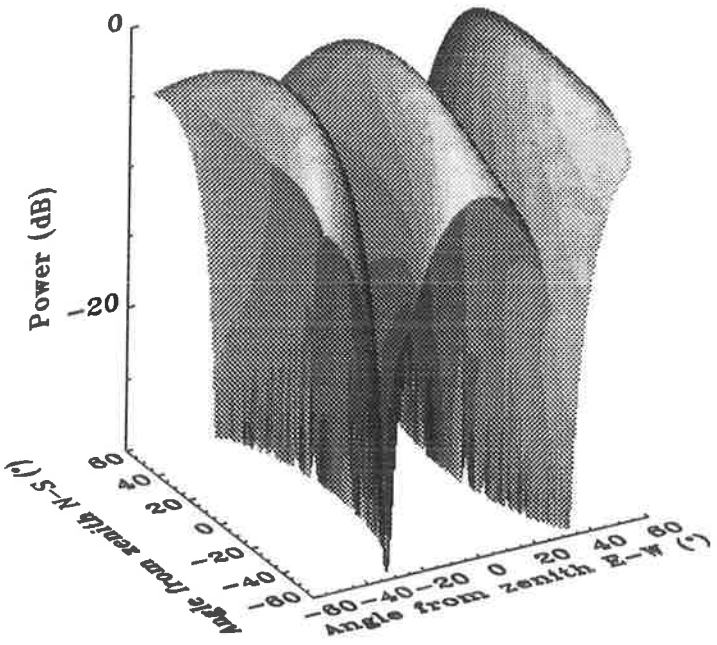

Figure 2.14: Power polar diagram of a single $\frac{3}{2}$–wave dipole above a perfect ground plane. The dipole is aligned with the East–West axis.

to Subsection 2.4.1, the reader is directed to Appendix A. Taking the result of Equation A.8 in Appendix A, we have

$$K(\alpha,\beta) \propto \sin^2\left(\frac{k\Delta h}{\sqrt{1+\tan^2\alpha+\tan^2\beta}}\right)\times \cos^2\left(\frac{3\pi}{2}\frac{\tan\beta}{\sqrt{1+\tan^2\alpha+\tan^2\beta}}\right)\left(\frac{1+\tan^2\alpha+\tan^2\beta}{1+\tan^2\alpha}\right)$$

(c.f. Equation 2.16). The radiation pattern described by Equation A.8 appears in Figure 2.14 and may be contrasted to the radiation pattern of the dipole at 1.98 MHz appearing in Figure 2.8. The half–power half–width of the dipole operating at 5.94 MHz is 10° in the direction aligned with its axis, and 44° in the orthogonal direction. This is quite similar to the dipole at 1.98 MHz where the two corresponding measurements are 30° half–power half–width in the parallel direction, and 44° in the orthogonal direction. Note especially that the $\frac{3}{2}$–wave dipole has not one, but three major radiation lobes located at 0° and ±45°. The two nulls in the pattern occur at about ±25° and manifest themselves quite clearly in the radiation pattern of the full array appearing in Figure 2.15. The nulls run through the pattern in the North–South plane starting some 40° from vertical in the East–West plane and approaching to within 25° of vertical at the pattern's mid point. The maximum depth

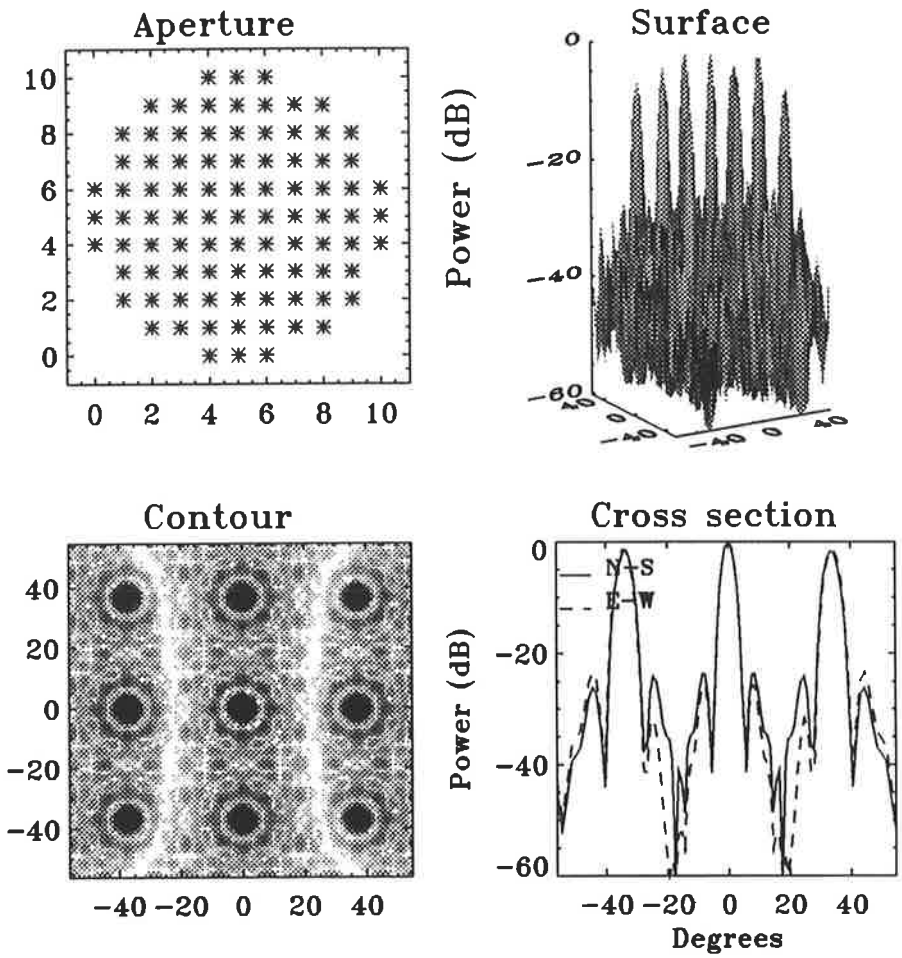

Figure 2.15: The full Buckland Park power polar diagram at 5.94 MHz. Panels are as indicated in Figure 2.12.

of the null is approximately -40 dB. The most obvious feature of the radiation pattern in Figure 2.15 is the presence of 8 grating lobes in addition to the main lobe. These occur at off–zenith angles, θ satisfying the relation

$$\theta = \arcsin\left(\frac{\lambda}{d}\right) , \tag{2.17}$$

where d is the separation between adjacent antennae. This is a simple consequence of diffraction theory, where higher orders appear when the optical path difference between rays from adjacent grating lines (in this case, antennae) is equal to $n\lambda$, where n is an integer. The calculated value of θ for $d = 91.4$ m and $\lambda = 50.5$ m is 33.5°, and inspection of Figure 2.15 reveals that this value agrees well with the numerical model.

Grating lobes in radiation patterns are easily recognised as distinct from side lobes due to (at least) two obvious differences.

Firstly, each position in the pattern at which a grating lobe appears will repeat the local pattern shape found at every other grating lobe. For a vertically–directed beam, the zeroth–order lobe will be in the centre of the pattern, and its local pattern can be used to locate the other grating lobes. In fact, the pattern repeated at off–zenith grating lobes will not be identical to that at the zenith since the projection of the aperture onto a plane normal to the off–zenith direction will have a smaller area than the aperture seen from above. Thus the pattern at off–zenith grating lobes will appear somewhat broader than at the centre due to the reciprocity of aperture area to diffraction pattern size.

The second distinctive feature of a grating lobe is that its gain should be roughly equal to the zeroth–order gain. Modulation of off–zenith grating lobe gains will, however, be produced by the radiation pattern of each element. This can be seen quite clearly in Figure 2.15. Side lobes, on the other hand, exhibit significantly less gain than the grating lobes and for symmetrical apertures are arranged with corresponding symmetry about each grating lobe.

As stated in Subsection 2.4.3, grating lobes are not observed in radiation patterns of the full array operating at 1.98 MHz. They are observed, however, when the dipoles in the array are grouped together in fours (four adjacent antennae are forced to radiate with the same phase) and the beam is tilted to an off–zenith angle of greater than about 10°. In fact the array, when grouped in fours, exhibits grating lobes at off–zenith angles of 55°. We examine this effect in Subsection 2.4.5.

2.4.5 Beam steering

In order to model the effects of beam steering on the power radiation pattern of the array, the phase of the field radiated from each element in the array is adjusted such that plane waves are emitted propagating at the desired off–zenith angle. This numerical technique is analogous to the practice of inserting cable delays between rows of antennae to produce off–vertical beams for transmission and reception.

For a beam directed at an angle of θ to the zenith, the fractional phase delay required between antennae separated by a distance ξ, is

$$\text{delay} = \frac{\xi}{\lambda} \sin\theta \ , \tag{2.18}$$

and the phase delay in radians is therefore

$$\phi = 2\pi \frac{\xi}{\lambda} \sin\theta \ . \tag{2.19}$$

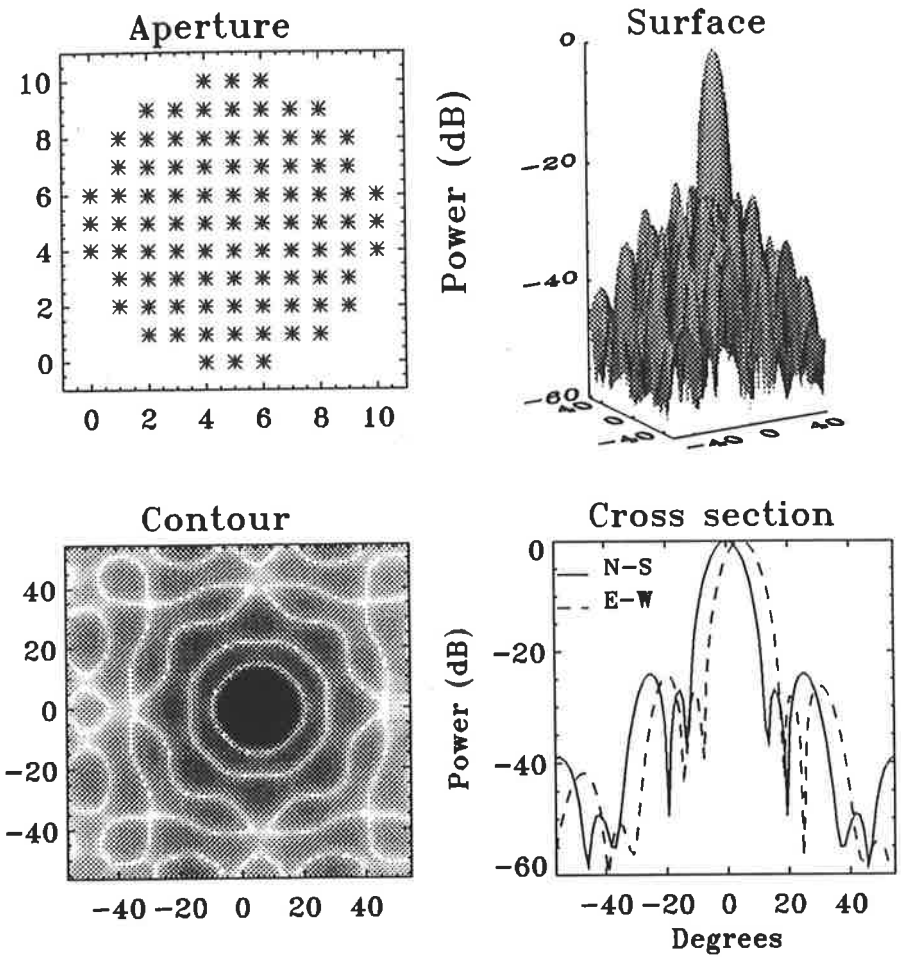

Figure 2.16: The full Buckland Park power polar diagram tilted 5° off–zenith in the Eastward direction. Panels are as indicated in Figure 2.12.

This delay is introduced to the model aperture function by multiplying the attenuation weight of each element, k, by $e^{j\phi_k}$ where ϕ_k is the phase delay in radians for that element. Since the absolute phase of the radiated signal is completely arbitrary we take zero phase delay to occur at the origin of our coordinate system.

Applying these principles of complex phase delay to the case of the full Buckland Park aperture, we tilt the beam 5° off–zenith in the Eastward direction in Figure 2.16.

We note firstly that the main lobe is indeed shifted 5° Eastwards and is marginally wider in the E–W plane as compared to the vertical beam case. This is due to the area of the aperture projected in the off–zenith direction being smaller than that of the full area of the aperture as viewed from above. The beam–width in the N–S plane remains unchanged, as does the position of the main lobe. The shape and amplitude of the side lobes appears unchanged, apart from the 5° shift Eastwards in the E–W cross section. Thus the radiation

pattern of the array is almost unchanged when shifted off–vertical, provided that each element in the array is free to radiate at the correct phase. The situation is somewhat different when groups of antennae are forced to radiate with a common phase.

If groupings of two antennae are forced to radiate with common phase, the actual phase chosen for the two antennae is that which an antenna placed at their midpoint would need to radiate to form a beam at the correct off–zenith position. For groupings of three and four antennae, the unweighted average of their geometrical positions is also used to calculate the necessary radiation phase. This, as will be demonstrated in Subsection 2.4.6, has the same effect as independently radiating antennae with random errors superimposed upon their phases. Recalling that only 30 solid–state transmitter modules were available to provide independent radiation phases for the array, groupings of two antennae per module resulted in only 60 of the possible 89 antennae being placed in service. Thus, in this case, the radiation pattern of the 60 antenna array when steered off–vertical would have smaller phase errors associated with each antenna pair than would larger groupings of antennae, but would entail using only 66% of the array in the aperture function. This smaller aperture, as we have seen, would result in a radiation pattern with a broader main lobe, but probably with side lobes somewhat more suppressed than would be the case with larger phase errors resulting from larger phased groupings of antennae. Figure 2.17a presents the radiation pattern of 60 antennae selected from the full array forced to radiate in phase groupings of two and tilted to an off–vertical angle of 5°.

As predicted, the half–power half–width of the 60 element array is larger than the full 89 element array, the increase being about 1°. The most distinctive feature of Figure 2.17a is the loss of symmetry apparent in the pattern distribution about the main lobe. This is a direct result of the introduction of radiation phase errors due to antenna grouping. The effect is enhanced in Figure 2.17a by the somewhat asymmetric aperture chosen to accommodate the use of only 60 antennae. Examination of Figures 2.17b and c also reveal the lessening of side–lobe symmetry about the main peak. The half–power half–widths of the radiation patterns in the second and third cases remain unchanged from the ungrouped case at 4.8°. The most undesirable feature of Figure 2.17a is the lessened attenuation of the major side lobes which is now -18 dB. This is an increase of 7 dB over the attenuation level of the side lobes in the ungrouped array which was about -25 dB. Figure 2.17b and c show minimum side lobe attenuations of at least -23 dB, an increase over the ungrouped array of only 2 dB.

The conclusion from the above must be that the use of all 89 dipoles for transmission

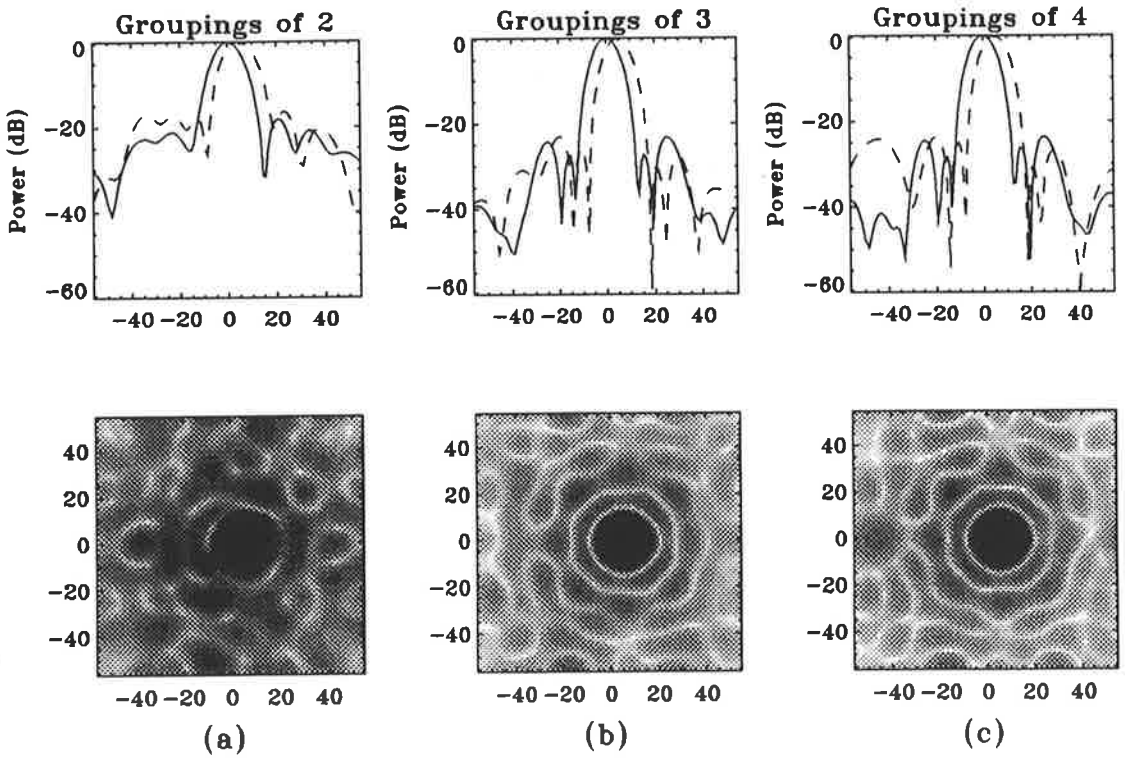

Figure 2.17: Radiation pattern of the Buckland Park array tilted off–vertical by 5° Eastward and forced to radiate with common phase in groups of (a) two, (b) three and (c) four antennae. The top three panels are orthogonal cross sections through the main lobe of the pattern while the bottom panels are grey scale intensity contour plots of the gain of each radiation pattern. Solid lines represent cross sections in the North–South direction whereas dashed lines are for the East–West plane. All unmarked axis are scaled in units of degrees off–zenith.

offers better beam–width characteristics and side–lobe suppression than does the use of only 60 antennae. In addition, phase errors caused by larger groupings do not cause excessive pattern distortion, at least for small off–vertical beam angles. Thus we reject the grouping of antennae in pairs in favour of groupings in threes or fours and now explore the relative advantages of the latter two groupings.

Although casual inspection of Figures 2.17b and c may reveal few significant differences in the radiation patterns of the two different antenna groupings, careful examination reveals an anomalous lobe at -50° in the East–West cross section of Figure 2.17c. This "side lobe" may at first appear as no more than part of the asymmetric arrangement of lobes about the main peak but is, in fact, a grating lobe (despite its low intensity). As previously stated, grating lobes appear in the radiation pattern when the spacing between adjacent elements in the aperture is larger than one wavelength of the radiation transmitted. Although the spacing between dipoles is significantly less than one wavelength at 1.98 MHz, when dipoles

are forced to radiate with the same phase the spacing relevant to the appearance of grating lobes is that between the centres of the common–phase radiating groups. Thus, when four antennae are grouped together, the spacing between the centres of adjacent groups of four becomes the critical parameter and is, of course, simply twice the spacing between ungrouped elements. In the case of the Buckland Park array, the spacing between centres of adjacent groups of four is roughly $\frac{6}{5}\lambda$. Recalling Equation 2.17, we expect grating lobes to appear at angles of 55° from the main lobe when the array is phased in groups of four and tilted away from the vertical. Thus, if the pattern is tilted 5° towards the East, then we should observe a grating lobe at -50° (towards the West) in the radiation pattern. This is indeed the case. As a result, we reject the use of groupings of four antennae for each transmitter module and conclude that the optimum use of resources is the use of 30 transmitter modules individually driving 30 groups of three antennae phased to produce a transmitter beam pointing in any direction.

2.4.6 Radiation patterns of imperfect arrays

In this subsection we examine the effect on the array's radiation pattern of varying antenna impedances and missing antenna elements. With an array as large as the Buckland Park MF/HF array, it is difficult to know and adjust the impedance of every element in the array to perfect resonance. Since the phase angles of the antenna impedances vary on a day–to–day basis by as much as five or ten degrees, it is, in fact, impossible to maintain the array in exact tune. Thus we now turn our attention towards the associated distortion in the power radiation pattern when antenna reactance is non–zero.

Firstly we must characterize the antenna impedance errors most likely to affect the array. Variables such as humidity and temperature are substantially constant across the whole array and so should produce a systematic biasing of the antenna reactances. As has been stated, the absolute phase of radiation from the array is not important, and so systematic phase errors will not affect the beam–pointing direction nor the beam–pattern. Several factors causing random phase errors can be identified. These include,

- varying coaxial cable electrical lengths,
- non–constant ground plane height due to varying water table levels,
- incorrectly tuned antenna baluns and

- slightly non–resonant antennae due to variations in dipole length.

Whatever the cause of eventual phase error, we model random phase errors with a normal distribution with adjustable standard deviation. The phase of the radiation at each element is adjusted by this random factor and the resulting radiation pattern determined. After examining different magnitudes of phase error, it became apparent that little or no effect is observed when the standard deviation of the normally distributed errors is less than about 20°. Even so, no asymmetry is observed in the main lobe of the pattern at the $\sigma = 20°$ level, although significant randomization of the side–lobe pattern is quite clear with the side–lobe attenuation also suffering by about 7 dB. In fact, the main lobe is unaffected to the extent that its half–power half–width remains unchanged at 4.8°. Figure 2.18 depicts the radiation pattern of the array with each element subjected to random phase errors distributed normally with a standard deviation of 20°. It should be noted that although the relative intensities of main beam and side lobes are only affected by a small amount, the absolute gain of the main lobe is also about 3 dB less than that of the array radiation pattern when free from random phase errors.

An equally unpleasant reality to the occurrence of random phase errors in the array is the tendency of elements to periodically break and remove themselves from the aperture function. In Figure 2.19, a total of 11 elements have been removed to simulate an array in a state of some disrepair. Although the side–lobe suppression has suffered by about 2 dB, it is apparent that the radiation pattern of the remaining elements in the array is quite satisfactory, with the main lobe's half–power half–width unaffected at 4.8°. Clearly, the only significant effect is the randomization of the side–lobe pattern as was the case with the random antenna phase errors above. We may therefore conclude that, although the existence of damaged or broken elements is undesirable, the presence of at least a few such antennae does not have a major deleterious effect upon the array's radiation pattern.

2.5 Hardware Required For Transmission

Although the transmitter modules to be used in the new 30 channel transmitter system only required minor modification from those used in previous spaced–antenna radar systems, certain unique sections of hardware were required to enable the new system to operate. Since in the spaced–antenna radar transmitter system all 10 modules transmit in phase, their outputs are brought together and combined in one filter/combiner unit. The module

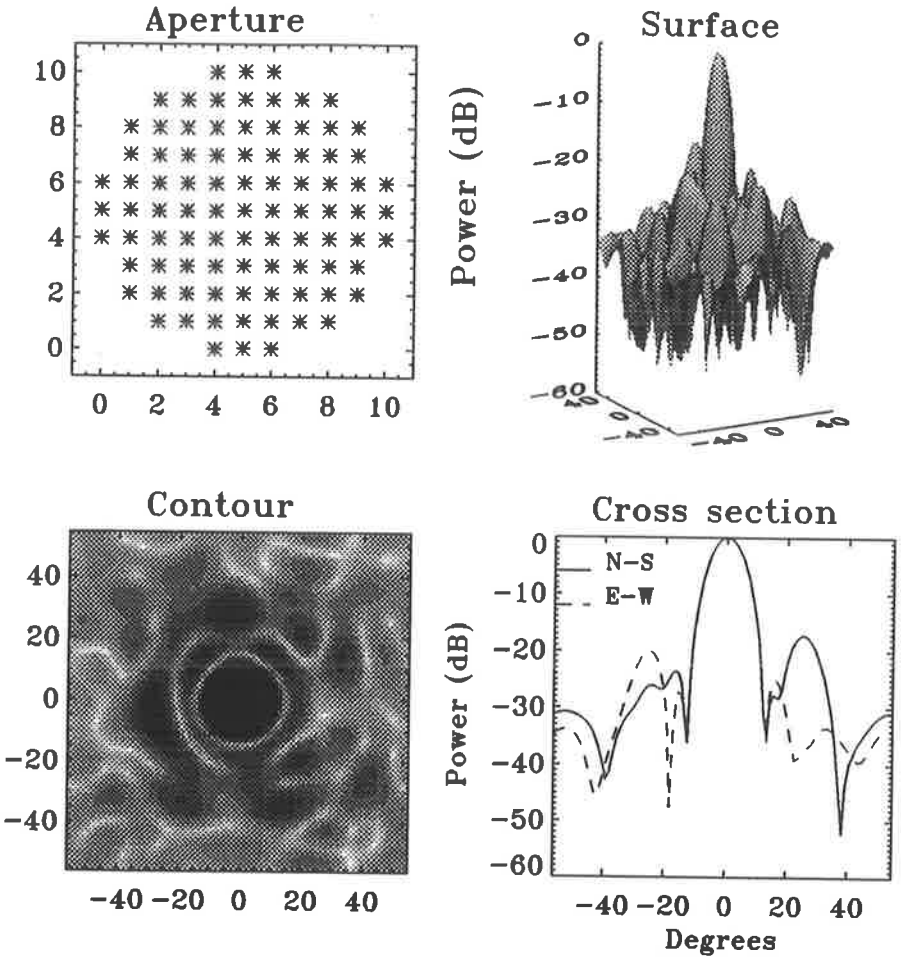

Figure 2.18: The full Buckland Park power polar diagram with normally distributed random phase errors with a standard deviation of 20°.

output, which is an amplitude–modulated square wave with Gaussian envelope shape (see Figure 2.20) and a carrier frequency of 1.98 MHz, must be filtered to remove the strong odd harmonics present. The third harmonic, in particular, must be attenuated by about 50 dB to 60 dB to minimize interference in other HF radio communication bands. In the spaced–antenna transmitter, one filter capable of processing a total of 25 kW is used for this purpose, but for the new Doppler radar a total of thirty 2.5 kW filters were needed. The following subsection details some of the design considerations of these new filters.

2.5.1 Filter design

Before any consideration can be given to filter design, certain parameters of the environment in which the filter is to operate must be specified. Many of these parameters are set by the power amplification (PA) module, while others are set by the load ultimately driven. We

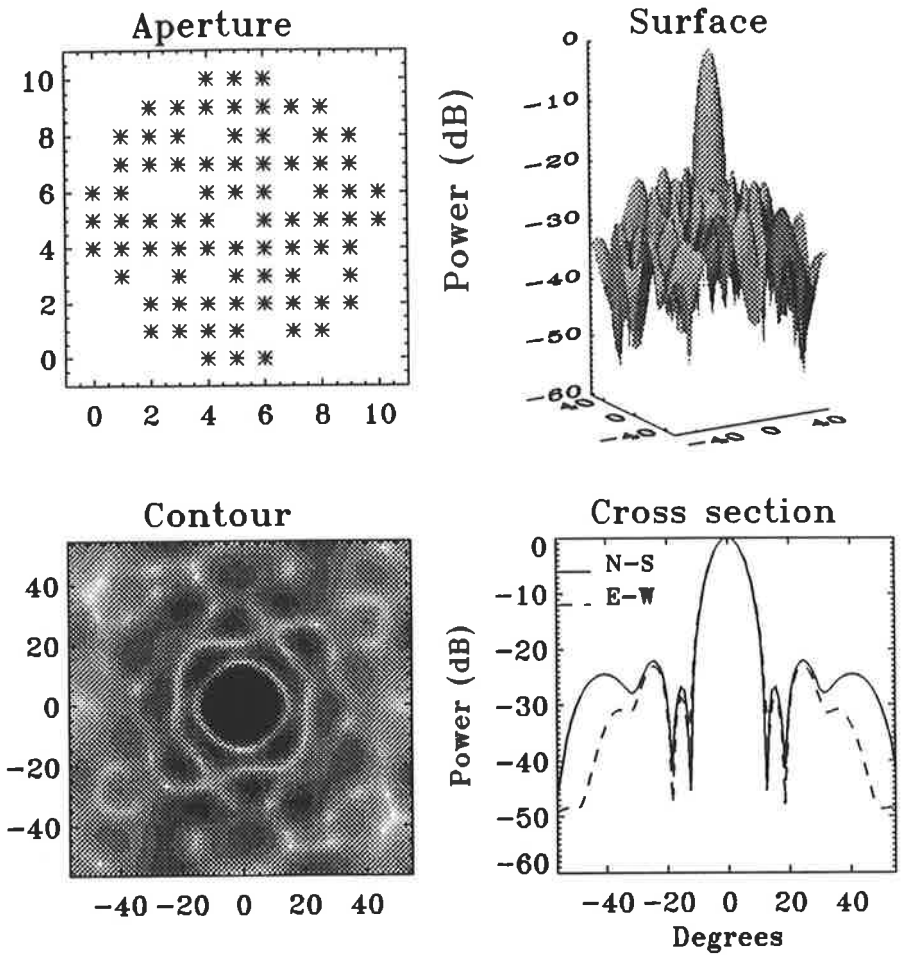

Figure 2.19: The full Buckland Park power polar diagram with 11 elements randomly omitted.

begin this subsection with an overview of the PA module characteristics.

The PA modules used were "class D" switching amplifiers utilizing state–of–the–art complementary power MOSFETs. As such, the PA modules are not linear amplifiers and simply provide an amplified and modulated square wave which must then be filtered. The modules are driven by a square–wave RF drive signal at a frequency of 1.98 MHz. The amplified pulse modulation is adjustable, and is usually modified to be as nearly Gaussian in shape as possible. The transmitted bandwidth is less than 200 kHz when the minimum pulse width of about 15 μs is used (see Figure 2.20). The output impedance of the modules is less than 10 Ω, while the best performance of the module is achieved with the PA driving a load of 50 Ω of pure resistance. The peak output of such a 2.5 kW amplifier driving a 50 Ω load is about 500 V. This is an important consideration in terms of component breakdown and nonlinearity of magnetic materials.

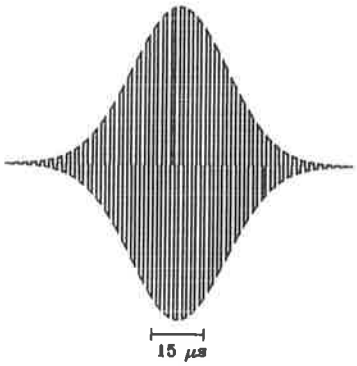

Figure 2.20: The solid–state PA module pulse shape.

Any filter considered for use with the new Buckland Park Doppler radar is required to fulfill 6 conditions. These are:

1. It must attenuate the 3rd harmonic of the 1.98 MHz square wave by a total of at least 50 dB.

2. It must achieve this attenuation with a bandwidth of about 200 kHz.

3. Its components must withstand the high RF voltages associated with resonant circuits.

4. Its electrical characteristics must be thermally stable to avoid phase and resonance drift.

5. Its input impedance must be 50 Ω.

6. It must match the impedance of the eventual load chosen to its 50 Ω input.

Three fundamentally different filter designs were considered and each appears in Figure 2.21. Note that all three contain only passive components and that the level of complexity of the filters is similar. We do note, however, that the filter depicted in Figure 2.21c utilizes the fewest components (especially wire–wound magnetic materials) and as such would be favoured given all other specifications being met. *Marshall* [1978] provides a more complete survey of filters suitable for this application. The first design considered appears in Figure 2.21a (excluding the components enclosed by the dotted–line rectangle) and is simply a series LC resonant circuit tuned to a frequency of 1.98 MHz followed by an impedance matching transformer. The filter was constructed, and although this design showed some

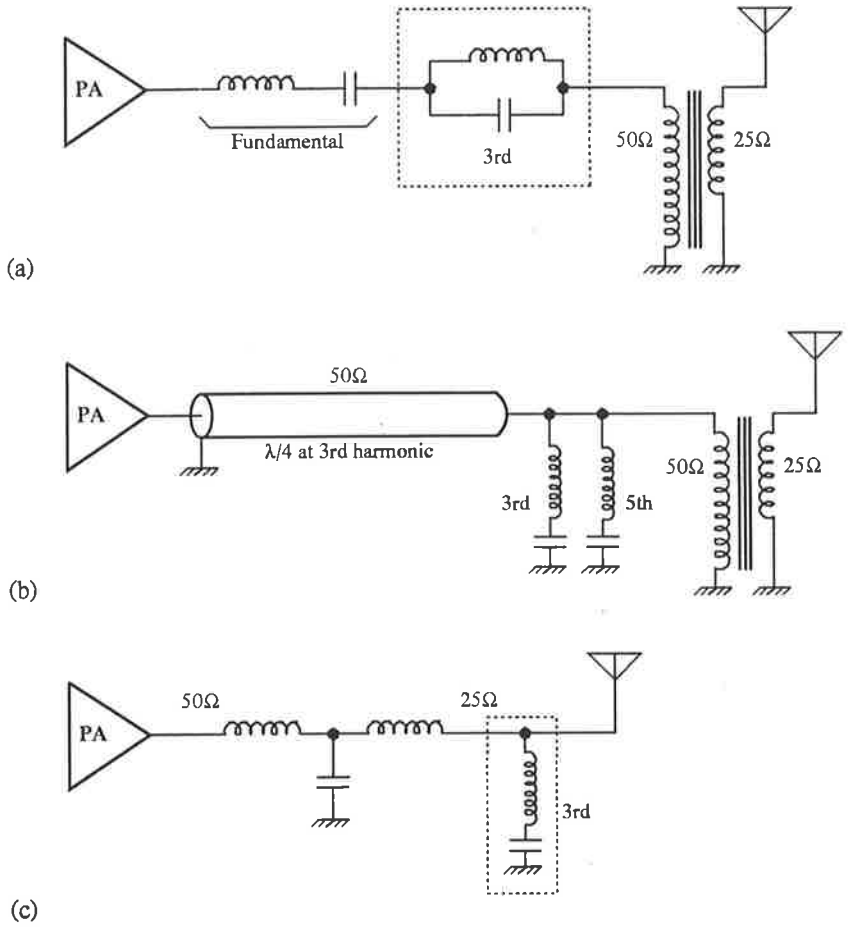

Figure 2.21: Filter types considered for the class–D PA modules. (a) Series LC circuit tuned to 1.98 MHz with a 50 Ω to 25 Ω impedance match. (b) Quarter wave line with series LC circuits to ground tuned to the 3rd and 5th harmonics and then matched to 25 Ω. (c) Inductor–capacitor–inductor "T" filter with built in matching. Note that the dotted boxes enclosing components denote later modifications tried with the filters.

promise, it soon became apparent that in order to achieve the attenuation of the 3rd harmonic required, the quality factor (Q) of the resonant circuit would have to be well in excess of 10.

A practical difficulty with circuits employing such high Q's is that they are extremely hard to tune. For example, minute changes in the placement of turns on the magnetic material alter the capacitive coupling between turns and hence influence the centre frequency of the resonant LC pair. In fact, the presence of a human hand near the inductor changes the magnetic permeability of the "free space" near the magnetic material making tuning impractical. It was decided to avoid these high Q circuits. The design was subsequently altered to include a parallel LC combination resonant at the 3rd harmonic and in series with the original series LC circuit. In contrast to the series resonance, the parallel resonant circuit

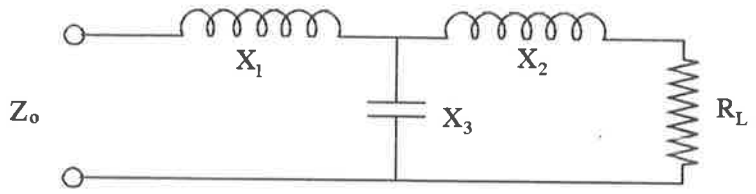

Figure 2.22: The equivalent circuit of the "T" filter.

presents a high impedance to the frequency components for which it is tuned. With both resonant circuits possessing a Q of 10, the total attenuation of the 3rd harmonic increased to about 36 dB. The main disadvantage with this design was the number of components required to transmit the full 10 A peak RF current without breakdown. In addition, the capacitors and inductors were required to withstand a potential of up to 5 kV without arcing or conducting. At this point the design was, at least temporarily, shelved.

The next filter considered is depicted in Figure 2.21b. In this case a 5.94 MHz quarter–wave transmission line is included in series with the output of the module. The quarter–wave line has the effect of presenting an impedance to the PA module which is the "reciprocal" of whatever impedance lies at its termination[1]. Thus, by placing a low impedance (for the 3rd harmonic) at its termination, the module will perceive a very high impedance at 5.94 MHz. Little power, then, will be transmitted at 5.94 MHz, allowing the fundamental frequency to dominate. The quarter–wave line at the 3rd harmonic becomes a $\frac{5}{4}$ wave line at the 5th harmonic and so on. Therefore similar tuned circuits to ground can be employed at each of the higher odd harmonics until the required attenuation is achieved. The filtered output is then impedance matched to 25 Ω using a 50 Ω to 25 Ω transformer. The design was abandoned without actual construction due to the large amount of coaxial cable (8.3 m for each filter) needed for the quarter–wave lines, and the relatively large number of resonant circuits required to be tuned to each odd harmonic.

The last filter design considered is shown in Figure 2.21c. Here a "T" type filter consisting of 2 inductors and a capacitor provides both attenuation and impedance matching. Although at first glance the circuit appears uncomplicated, it turns out to be reasonably difficult to analyse mathematically. Consideration of the equivalent circuit shown in Figure 2.22 yields two equations in two unknowns. These are

$$R_L X_3^2 = R_o R_L^2 + R_o(X_2 + X_3)^2$$

[1]The quarter–wave line is simply an impedance shifter which changes the impedance attached at one end to a different one at its other end as indicated by a Smith chart.

and

$$X_3(R_L^2 + X_2^2 + X_2X_3) = QR_o(R_L^2 + (X_2 + X_3)^2) , \tag{2.20}$$

where R_L, X_1, X_2 and X_3 are defined in Figure 2.22, R_o is the desired input resistance of the filter, and Q is the required Q of the filter. These, after some manipulation, yield two simultaneous equations in X_2 and X_3,

$$X_2 = -X_3 \pm R_L\sqrt{\frac{1}{R_LR_o}X_3^2 - 1}$$

and

$$X_2 = \frac{-(X_3^2 - 2QR_oX_3) \pm \sqrt{A}}{2(X_3 - QR_o)} , \tag{2.21}$$

where

$$A = (X_3^2 - 2QR_oX_3)^2 - 4(X_3 - QR_o)(R_L^2X_3 - QR_oR_L^2 - QR_oX_3^2) . \tag{2.22}$$

At this stage a numerical solution was employed taking into account the additional factor of the output impedance of the PA module. This was measured at approximately 10 Ω. Altering the input parameters Q, X_1, X_2 and X_3, and constraining the input impedance to be 50 Ω pure resistance at 1.98 MHz for a 25 Ω load, the attenuation of the 3rd harmonic for a bandwidth of 200 kHz was calculated to be 48 dB. The calculated reactances were

$$\begin{aligned} X_1 &= 250.0\,\Omega , \\ X_2 &= 178.5\,\Omega \\ &\text{and} \\ X_3 &= -107.1\,\Omega , \end{aligned} \tag{2.23}$$

with a resulting quality factor Q, of 5. The only negative reactance turns out to be X_3 which is, as assumed, a capacitor with X_1 and X_2 both being inductors. The component values, and the peak voltages appearing across them when the PA modules are active appear below:

$$\begin{aligned} L_1 &= 20.1\,\mu H \\ L_2 &= 14.3\,\mu H \\ C_3 &= 751\,pF \\ V_1 &= 2.06\,kV \\ V_2 &= 2.08\,kV \\ V_3 &= 2.10\,kV \end{aligned} \tag{2.24}$$

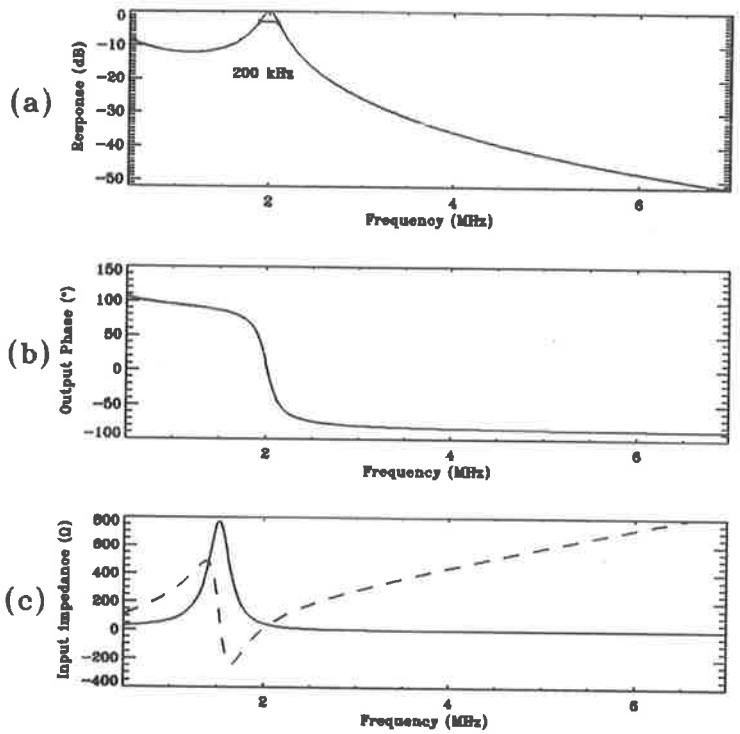

Figure 2.23: The response functions of the "T" filter showing (a) attenuation, (b) the output phase and (c) the input impedance. The solid line in (c) represents the resistive component of the input impedance while the dashed line represents the reactive component.

Given that the 3rd harmonic of a square wave is nearly 10 dB down on the fundamental frequency, a filter attenuation of 48 dB gives a total attenuation of almost 60 dB which is more than adequate for our application. Figure 2.23 displays the relevant filter characteristics from 500 kHz to 7 MHz including the 3 dB cutoff points of the filter and the 200 kHz bandwidth. Note that in Figure 2.23a, the 3 dB cutoff points of the filter almost exactly match the width of the horizontal line which spans 200 kHz of the frequency axis and is centred on 1.98 MHz.

The filter was constructed using the component values enumerated above with some consideration given to suppression of high voltage arcing and the resulting component breakdown. The 751 pF capacitor was composed of seven silvered–mica capacitors connected in series such that the peak voltage drop across each capacitor did not exceed that component's specification. The inductors were wound using 26 turns for L_1 and 31 turns for L_2 on two type 225A(2) iron powder toroidal cores with taps provided to ± 4 turns for fine tuning purposes. The toroids were covered with a triple layer of electrical insulation tape to prevent the 2 kV potential difference across the inductors from arcing through the iron powder cores. The critical factor to be considered when utilizing any magnetic material is the peak

magnetic flux density to which the material is expected to be subjected. Although magnetic materials have well defined saturation levels beyond which the core can be magnetized no further, some nonlinearity in their response is observed at much lower flux levels. For the particular iron powder toroids used, the percentage of initial permeability of the core at a magnetic flux density of 5×10^{-2} T is about 102%. Thus it is desirable for the purposes of the filter's linearity that the peak flux density within the cores is kept well below this level. The calculated peak flux density for the two toroids used in this filter design were 2.8×10^{-2} T and 3.3×10^{-2} T for L_1 and L_2 respectively. This was considered to be acceptable.

After construction the filter was loaded with a 25 Ω pure resistance and tuned by selecting the tap on L_1 which resulted in the smallest reactive component at the input of the filter. A signal generator operating at a frequency of 5.94 MHz was used in conjunction with a CRO to measure the attenuation of the filter at the 3rd harmonic. The result of 42 dB was within expectations and again considered acceptable.

The filter was then attached to the output of a single solid–state transmitter module triggered at a PRF of 80 Hz. The same 25 Ω dummy load was connected to the output of the filter and the filtered transmitter pulse monitored using a spectrum analyser. Careful measurement of the attenuation of the filter at the 3rd harmonic revealed that the signal level at 5.94 MHz was only 36 dB less than that measured at 1.98 MHz. This result was all the more puzzling given that the 3rd harmonic output from the module should have been approximately 10 dB less than the fundamental frequency before filtering, yielding a total attenuation of about 52 dB.

Eventually it was discovered that the PA module, driving a high impedance at 5.94 MHz, was no longer producing a square wave and the level of the 3rd harmonic was enhanced by about 20 dB. Thus the filter was, in fact, successfully attenuating the output level of the PA module at the 3rd harmonic by 42 dB, but the enhancement produced by the PA module was effectively negating some of this attenuation.

Several modifications to the "T" filter were tested before the design depicted in Figure 2.21c was found satisfactory. The series tuned circuit to ground effectively loads the 3rd harmonic sufficiently that the PA module does not enhance the signal at 5.94 MHz and the load is sufficiently small that little or no power is consumed at 5.94 MHz. The attenuation of the 3rd harmonic when measured relative to the fundamental frequency across the dummy load was found in this case to be 52 dB.

Although the basic design of the filter detailed above was found satisfactory, several small

changes were necessary in order that it could be included in the overall transmitter design. The easiest of these was the addition of a one turn secondary on the second inductor, L_2. The purpose of the secondary was to provide a voltage sample which was in phase with the current in the inductor, and hence was representative of the phase of the signal transmitted to the antenna. Using this sample, the phase of each individual module could be checked and suitable action taken to ensure that all 30 modules were transmitting in phase. This phase check would also compensate for the unpredictable phase propagation delay inherent in the filter. Design of the phase–control modules is detailed in Subsection 2.5.2.

A later addition to the filter boards was a transmit/receive (TR) switch. This ensures that the receiver inputs are isolated during the period that the pulse is transmitted and enables the receivers to remain unsaturated. The TR switch utilizes PIN diodes and lumped circuit quarter–wave lines to achieve the degree of isolation of the receiver inputs required while allowing the powerful transmitter pulse to reach the antenna. Inherent in the TR switch design is a quarter–wave line at 1.98 MHz to earth via two PIN diodes which, at 1.98 MHz, appears to the filter output as a high impedance, but at higher frequencies becomes a progressively lower impedance. This quarter–wave line obviates the need for the series LC circuit tuned to 5.94 MHz to ground included in the prototype, and has the advantage that higher harmonics than the 3rd are also affected. Although research was conducted into some early designs, the final form of the TR switches did not form a major part of this work and, as such, their design process is not included here. For completeness, a diagram of the final filter/TR design appears in Figure 2.24.

2.5.2 Phase–control modules

Of primary importance in the design of the new Adelaide MF/HF Doppler radar was the ability of the radar beam to be steered electronically off–zenith in any direction and at any angle. To achieve this steerability, electronic phase–control modules were required which would allow the transmitted phase of each individual PA module to be monitored and adjusted. The basic elements of the design were

- a means of driving the PA module at a specified phase,
- a means of sensing the phase of the PA module's output,
- a means of adjusting the phase of the PA module's output, and

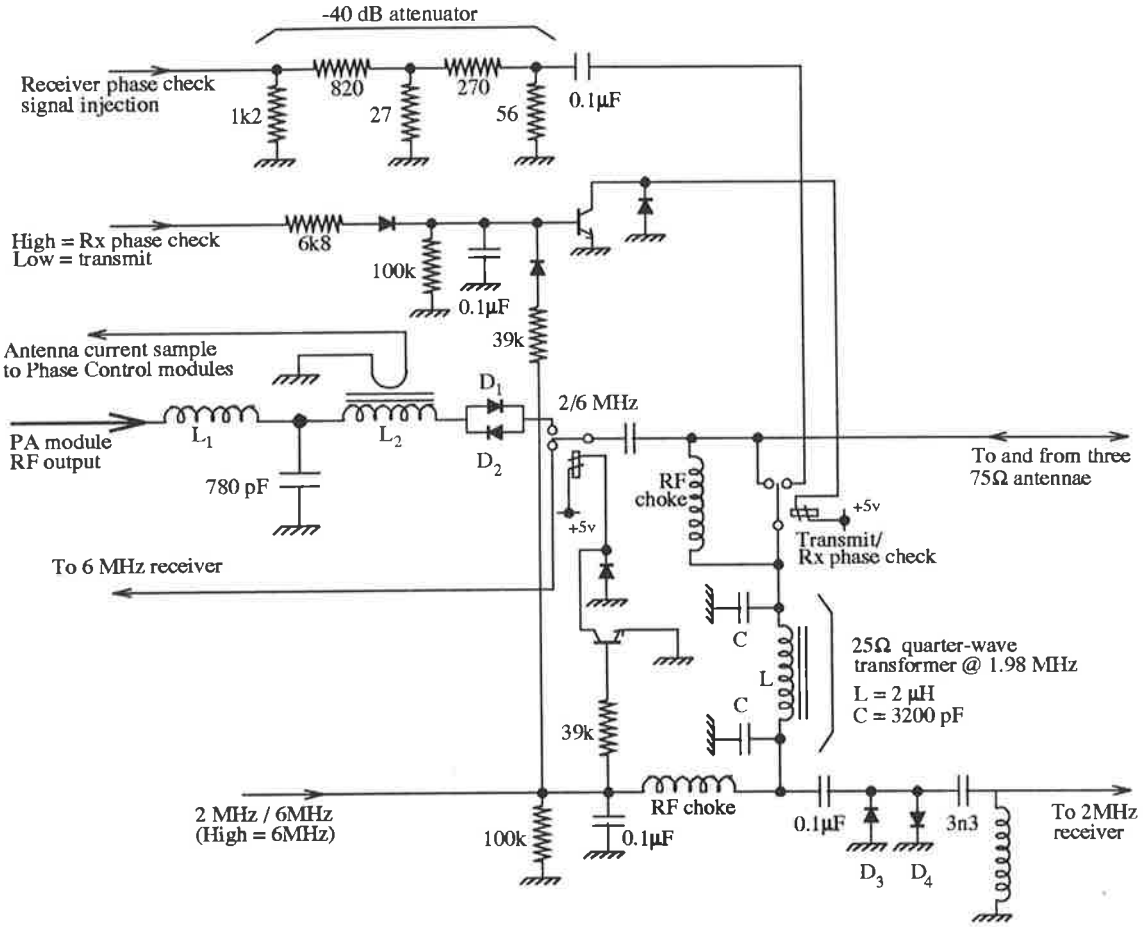

Figure 2.24: The final design of the filter/TR circuit as used in the 30 channel solid–state transmitter. Note that $D_1 \rightarrow D_4$ are 400 V ultra–fast diodes of type BYTO3–400.

- a means of comparing the phase produced by the PA module to the desired phase.

The PA modules are driven by a 15 V square–wave signal which is generated ultimately by the master oscillator in the receiving equipment. In the normal 10 channel spaced antenna transmitter arrangement, the drive signal is split a total of 10 ways and each PA module is therefore presented with a drive signal of identical phase. By changing the phase of each individual drive signal relative to the master reference's phase, the signals produced by each module can be adjusted such that they are all in phase or, alternatively, each module can be adjusted such that it has a specified phase lag relative to the master reference.

The three central components of the phase–control module are the delay circuitry, the phase comparator and the counting logic for the delay step. A block diagram of the phase–control module appears in Figure 2.25.

The phase–control (PC) modules were designed to operate in two modes. Firstly, a phase–zero check would be performed to ensure that the PA modules were radiating in phase with

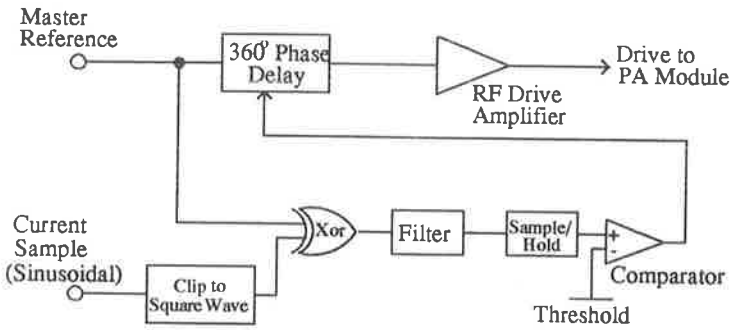

Figure 2.25: Block diagram of the phase–control module.

the master reference. Secondly, the PC module would accept a number of shift instructions from the interface control intended to move the phase produced by the PA module a certain number of radians $\Delta\phi$, away from the master reference. The procedure used for a phase–zero attempt was as follows; the PA module was triggered at 100 Hz and a sample of the current in the "T" filter (see Subsection 2.5.1) was supplied to the PC module and clamped between 0 V and +5 V using a total of six diodes. Since the amplitude of the current sample was about 80 V, the quality of the square wave produced was quite high, and the errors in the zero crossing were thought to be negligible. The "squared–up" current sample was then "Exclusive ORed" with a buffered sample of the master reference. The result was, in general, a square wave of variable mark–to–space ratio which would theoretically become a constant DC level at zero volts when the two signals were perfectly in–phase. In practice, of course, some noise contributed to the process and a constant DC level slightly above zero volts was observed. For phase differences of 180°, the output of the exclusive–or gate was a DC level of +5 V. This square wave was then low–pass filtered by a simple LCR combination to smooth each individual peak into a representative DC level. A sample–and–hold device gated for 10 μs in the centre of each transmitted pulse was used to store this representative DC level for comparison with a pre–set, adjustable threshold level. The output of the comparator was then high (+5 V) when the DC level was above the threshold, and low (0 V) when below. This "error state" was used to gate a logic pulse delayed from the falling edge of the trigger by 100 μs to the phase delay counting logic which would, if triggered, count to the next delay step for the next transmitter pulse. The phase delay selected by the counting logic was implemented by taking one of three references derived from the master phase reference, each separated by 60°. The particular reference selected was then delayed by between 8 ns and 84 ns by a three–bit programmable delay line with a total of 7 delay steps, and then fed to a series of gates designed to invert the signal if desired. Thus a total of 42 phase delay

steps were available, each separated approximately by 8.6° in phase (see Subsection 2.3.6).

The threshold level is set such that only the phase step which creates a (nearly) perfectly in–phase master reference signal and current sample will allow the error state line to fall low. Thus, in theory, a maximum of 42 pulses are required to achieve the "phase–zeroed" state. This, at a PRF of 100 Hz, takes less than one–half of one second, and as all 30 modules are phase–zeroed in parallel, the PC modules are then free to receive phase–shift information from the radar controller.

The phase–shifting information is in the form of a series of pulses equal to the desired number of phase steps to shift off phase–zero. These are transmitted by the radar controller to each module in order. Thus, if a PA module is to transmit pulses whose phases lag behind the master phase reference by 16°, then it will receive two pulses after it is phase–zeroed. The phase correction circuitry is not active during normal operation, and so the fact that the current sample from the PA module is no longer in phase with the master reference is of no consequence.

The eventual state of the phase delay counter after a phase–zero process is read back to the computer via the radar controller, as is a logic level which is set if the phase was successfully zeroed. This number is recorded for each module and enables any faults in the hardware to be quickly discovered. Such faults include damaged modules, de–tuned filters, and broken antennae. Since the phase of the current leaving the filter will depend partly on the impedance of the load driven (the antenna), any variation in this impedance can be detected by monitoring the phase step needed for the PC module to phase–zero. Therefore the system can be used in part to ensure that the antenna array is in complete working order.

A prototype of the phase–control module was built on a printed circuit board designed and constructed by the author and tested with a PA module driving a dummy load. The load's impedance was matched by a "T" filter with the current sample taken from the second inductor (see Subsection 2.5.1). First, the phase of the signal present across the dummy load was compared to that of the main reference signal and found to be some 120° out of phase. Second, the phase–zero enable input of the PC module was held high while the module was triggered at 80 Hz. The relative phases of the voltage across the dummy load and the master reference signal were compared and found to change on each pulse until the two were exactly in phase at which point the relative phase shift was observed to cease. Third, the phase zero enable input was taken low after which the phase step input was triggered while again the

relative phase of the load and reference voltages was observed. At each pulse the load signal was retarded by some 8° relative to the master reference. The testing of the prototype was considered to be successful.

As with the filter/TR switches some minor design changes were required to integrate the phase–control modules with the rest of the transmission system. In the case of the PC modules, it was decided to include the facility for the phase–delay step required to zero the phase of PC module to be recorded by the transmitter–computer interface. Many other "teething" problems were rectified before the design was finalized, but these have little direct bearing upon this work.

2.5.3 Baluns

As stated in Section 2.3, the original antenna baluns were not suitable for use with the high transmitter powers to be produced by the new radar system. An additional motivation for the redesign of the baluns for the new radar was the large number of maintenance problems associated with the old baluns. Due to poor sealing, inadequately mounted components and poorly selected components, malfunctioning baluns accounted for somewhere near 50% of antenna failures. To eliminate this acute problem, much time and thought was given to the new balun design. The following points were addressed:

- Problem: Water penetrating the metal balun boxes due to poor sealing corroded components and solder joints within the box and migrated into the air cored dielectric coaxial cable.

  Solution: The new balun boxes procured were of UV–stabilized plastic construction with rubber–gasketed tight–fitting lids providing a water proof seal. In the event of condensation forming inside the box two large holes (used for the entry of the coaxial cable) were left unsealed in the bottom of the box allowing for ample drainage. A solid–dielectric coaxial cable was used to replace the air–cored variety from the ground to the top of the antenna poles which prevented any water from entering the cables.

- Problem: The replacement of broken "feeder" wires from the balun to the antenna was a time consuming and difficult task.

  Solution: Larger diameter multi–cored feeder wires were used with eyelet type solder lug terminals attached to one end. These could be removed from, and reattached to the balun box quite quickly using a spanner. In addition the larger diameter feeders

were not as susceptible to mechanical fatigue.

- Problem: Poorly mounted components tended to fail with vibrational fatigue.
  Solution: All components within the balun box were securely mounted upon a purpose–built printed circuit board (PCB). The board layout included large conductive pads used to surface–mount various numbers of capacitors while the balun was in service to allow for tuning of each individual antenna.

- Problem: Baluns were becoming detached from the antenna poles due to inadequate mounting.
  Solution: The galvanized nails penetrating into the wooden antenna poles were replaced with stainless steel banding straps wrapped fully around the pole at top and bottom of each balun box.

- Problem: Coaxial cable entering the bottom of the balun box was difficult to disconnect for tuning purposes and required the use of a soldering iron.
  Solution: BNC plugs were used on the end of the coaxial cable with right–angle "elbow" BNC sockets mounted on the new balun PCB.

- Problem: Existing method of isolation between 1.98 MHz and 5.94 MHz operation was inadequate for use with high transmitted power.
  Solution: Incorporate high–current relays driven by DC voltages superimposed on the RF signal on one of the antenna polarizations to enable mechanical switching between 1.98 MHz and 5.94 MHz.

- Problem: Existing baluns would saturate and break down with the high transmitted power expected.
  Solution: Redesign balun with different magnetic materials and number of windings on the core.

As with all components designed or redesigned for use with the new transmitting system, several design options for the baluns were considered before a final prototype was constructed. The starting point for the design was (apart from those considerations listed above) that the antenna impedance was 26 Ω at 1.98 MHz with little or no reactive component, and that the balun must be capable of operating at both 1.98 MHz and 5.94 MHz.

The first design considered appears in Figure 2.26a. The motivation behind this design was the avoidance of any tuning capacitors in the balun. Most baluns possess a significant

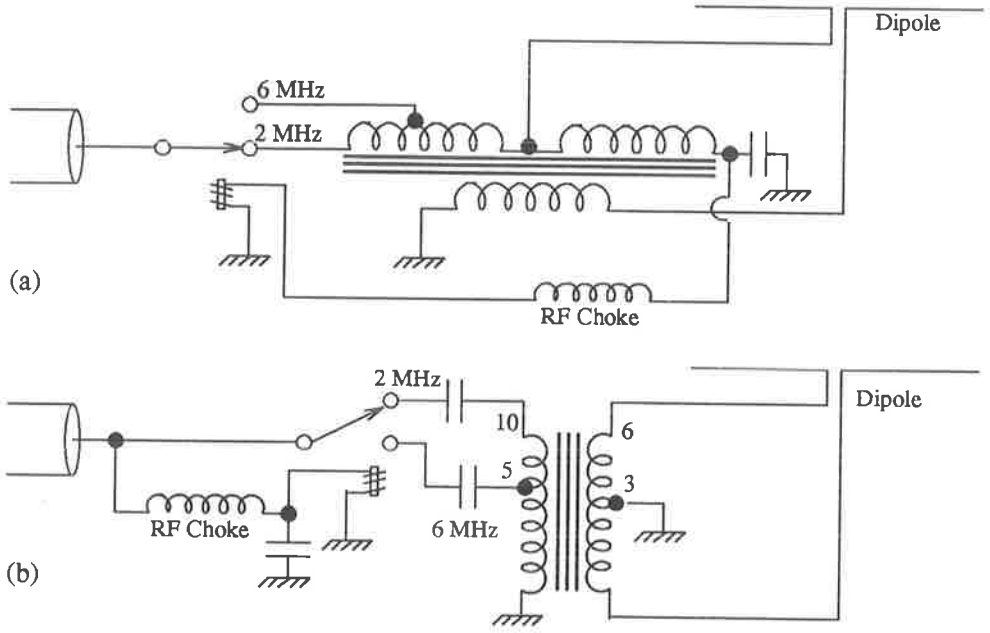

Figure 2.26: Two balun designs considered for use with the high transmission powers expected with the new PA modules.

amount of leakage inductance as a result of magnetic field lines produced by the primary winding not linking the secondary winding. The balun shown in Figure 2.26a does not share this problem, and for this reason the signal from the coaxial cable is fed directly into the primary winding via a relay. The relay is energized by placing a DC level of 24 V on the coaxial cable upon which the 300 V RF transmitter pulse is superimposed. The RF component is filtered out on the earthed side of the primary winding by use of a low–pass LC combination allowing the DC component to reach the relay coil. The relay is energized for 5.94 MHz operation, but is unenergized in its normal position for use at 1.98 MHz.

The design was abandoned relatively quickly due to two serious problems. First, in order for the leakage inductance to remain negligible it was only possible for the impedance transformation of the balun to take on certain values such as 1:1 or 4:1. Since the balun finally chosen needed to match impedances in the ratio 3:1 the design was unsuitable. The second problem related to the continuance of the DC current used for switching between the two primary taps for 1.98 MHz and 5.94 MHz operation. As the relay was energized and began to switch, a momentary interruption to the DC current would occur, possibly causing the relay to cease switching and return to its unenergized state. This, though, would restore the DC current to the relay coil, and cause to relay to begin switching again. Depending upon the mechanical inertia of the relay switching arm and the time constant of the circuit

Table 2.2: Some electrical characteristics of the balun design chosen for the new Buckland Park radar.

	1.98 MHz	5.94 MHz
Impedance transformation	28 Ω ∠ 0°→ 80 Ω ∠ 23°	97 Ω ∠ 0° → 76 Ω ∠ 34°
Leakage inductance	27 Ω ∠ 87°	46 Ω ∠ 87°
Magnetizing reactance	1.1k Ω ∠ 70°	600 Ω ∠ -11°
Balance	1.4% difference	1.4% difference
Tuned input impedance	73.6 Ω ∠ 0°	63 Ω ∠ 0°

including the balun windings, a relaxation oscillation may result.

The second design appears in Figure 2.26b. This balun design returns to that originally incorporated in the Buckland Park radar and abandons the aim of avoiding leakage inductance from the transformer. Thus, the design requires the use of tuning capacitors whose specifications permit relatively high RF currents and voltages. As was incorporated in the "T" filter, silvered–mica capacitors were used in the balun for tuning purposes. As with the older balun, a tapped primary winding provides for different impedance matching at 1.98 MHz and 5.94 MHz. The two major differences between the older balun and the new design are the change in the type of magnetic material used in the impedance transformer, and the use of a sealed mechanical relay to change between the taps on the primary winding.

The balun transformer was wound on an "E" core type EA–77–625 fitted with a 1 mm air gap. The "A_L" value[2] of the magnetic core with the air gap in place is 8000 μH per hundred turns. The transformer section of the balun was constructed ensuring that the secondary was wound bi–filar and several electrical characteristics measured. These appear in Table 2.2.

The most important figure of merit shown in Table 2.2 is the impedance transformation. As can be seen, the balun presents an impedance of about 74 Ω at 1.98 MHz after the effect of the leakage inductance is removed. This was considered entirely satisfactory. The leakage inductance of 27 Ω at 1.98 MHz was also considered small enough to have little or no effect on the balun's bandwidth for the purposes of a dual frequency Doppler radar. In all, 178 such baluns were wound (with considerable assistance from technical staff) and mounted in pairs in 89 plastic boxes containing the baluns, tuning capacitors and relays on a single printed–circuit board. The boxes were gradually installed at the Buckland Park field site where, at the time of writing, 30 antenna poles had been completed. The initial 30 antenna

[2]The "A_L" value of a magnetic material is a measure of the number of turns of wire around the material required to achieve a certain inductance value.

poles targeted for upgrading were selected in preparation for a pilot transmission experiment the results of which are reported in Chapter 4.

2.6 Interim 8 Channel Receiver System

In 1991, a large scale refurbishment and upgrading of the 5 channel Buckland Park receiver system was undertaken with the following points in mind:

- the extension of the 5 channel system to its full potential of 8 channels,
- the replacement of the master frequency synthesis unit with a modern, digitally–driven unit,
- realignment and tuning of the (now) 8 receivers with a new intermediate frequency (IF) of 495 kHz as opposed to the old IF of 450 kHz,
- matching the IF output levels of the 8 receivers to the 8 signal processor boards,
- matching the gain of the in–phase and quadrature amplifiers on the signal processor boards,
- incorporating a computer–controlled receiver phase check facility,
- tracing and eliminating anomalous signal voltage level variations related to earth loop problems,
- upgrading the computer interface to cope with the increased data rate,
- replacing the range marker hardware with a more modern version and
- rewriting and debugging the data acquisition software.

2.6.1 Extension to 8 channels

Although the original design of the 5 channel radar receiver system incorporated the facility to upgrade to 8 channels, many practical problems impeded such activity. The first task undertaken was to locate the additional three receivers and signal processors. This was accomplished with relative ease although the equipment recovered had in some cases never been tested, and in others had been constructed to operate at 5.94 MHz. Such was the age of the receiver design that capacitors used in tuned circuits had significant temperature

Table 2.3: Some measured characteristics of the old coherent receivers (With thanks to John Smith).

Parameter	Rx 1	Rx 2	Rx 3	Rx 4	Rx 5	Rx 6	Rx 7	Rx 8
Bandwidth (kHz)	31	29	28	29	28	31	28	30
Linearity	5%	2.5%	0%	5%	7.5%	5%	2.5%	2.5%
S/N at 1 μV (dB)	4	3	3.5	3	4	3	2.5	1.8
RF gain control ratio	13:1	13:1	13:1	13:1	16:1	6.5:1	6.5:1	16:1
IF gain control ratio	48:1	26:1	25:1	42:1	46:1	62:1	60:1	30:1
Input impedance (Ω)	66	58	58	58	58	58	42	66

coefficients. All capacitors used in tuned circuits on all 8 receivers were immediately replaced with zero temperature coefficient ceramic types. Such modifications necessitated the retuning of all 7 tuned circuits on each of the 8 receivers. The receivers were tested by feeding a swept frequency centred on 1.98 MHz into the RF input of the receiver with an externally generated local oscillator frequency (LO) of 2.75 MHz. The resulting IF output of 495 kHz was displayed on a CRO synchronised to the frequency sweep, which allowed the measurement of the bandwidth of the receiver and its realignment by trial–and–error adjustment of the 7 tuned circuits. After the retuning was completed the absolute gains of the 8 receivers were checked for various externally–controlled RF and IF gain settings. This measurement resulted in the replacement of several faulty FETs responsible for mixing and amplification in the receiver front–end. During this activity many faults and defects were discovered in the receivers ranging from hair–line breaks in tracks on the PCB's, to unshielded or ungrounded RF signals on small–diameter coaxial cable on the receiver board. Once all such faults were rectified, several aspects of the operational performance of the receivers were examined with the results appearing in Table 2.3.

2.6.2 Signal processors

Three extra signal–processor boards were located and a general inspection carried out. A block diagram of the signal processor design is included in Figure 2.27.

As the 8 signal–processor boards ranged in age over several design revisions it was necessary to bring the older boards up to current specification. As with the receivers, many faults were located and rectified ranging from the ubiquitous broken tracks on the PCB, to uncommitted inputs on CMOS logic integrated circuits.

The IF input amplitude had hitherto been matched to each individual receiver by different

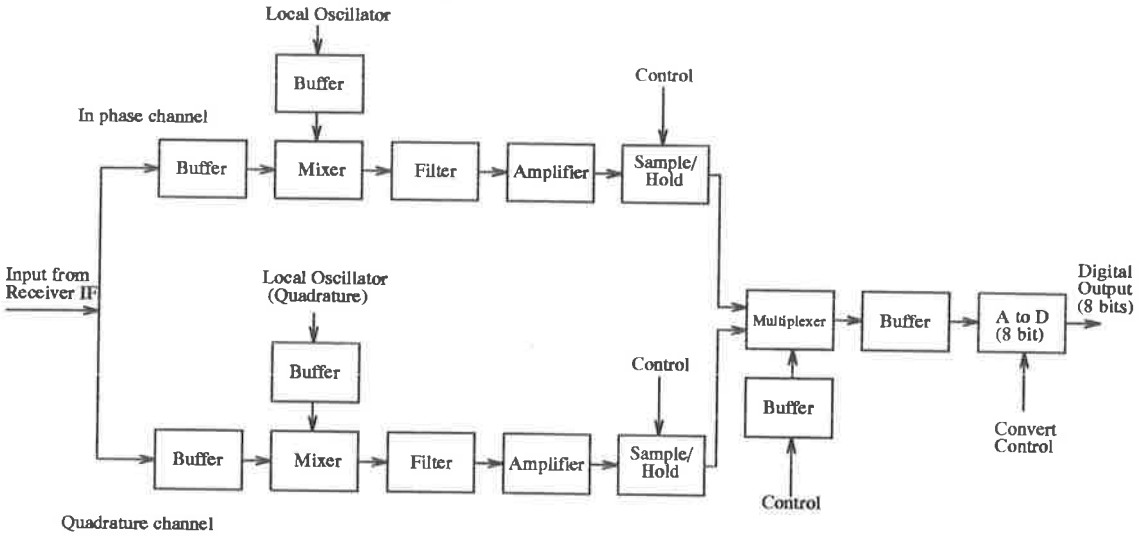

Figure 2.27: A block diagram of the receiver signal processing board. The centre frequency of the IF signal is 495 kHz and the gain of each channel is about 15 dB.

input signal attenuators on each signal–processor board. Since the refurbished receiver IF output levels did not vary substantially from receiver to receiver, it was decided in the interest of uniformity to use identical attenuators in each signal–processor board. The gains of the in–phase and quadrature amplifier channels were checked by using an externally–supplied, unlocked signal at approximately 495 kHz as an IF input, and monitoring the amplifier outputs on a CRO set in the x–y mode. The frequency difference between the input IF signal and a phase–locked signal caused constantly varying in–phase and quadrature signals which described sinusoids whose frequency was equal to that of the original frequency difference, and whose phase relationship was a constant 90°. For amplifiers of equal gain and phase delay (and for mixers of equal insertion loss) the two output signals should be of exactly equal magnitude, and when displayed using the orthogonal x–y mode should describe perfect circles. It was quite clear from this observation that the gains of the amplifiers in the two mixing channels were, in some cases, radically different, with ellipses of varying axial ratios displayed for the 8 digitizers. The problem was solved by trimming the gains on the amplifiers to yield equal RMS outputs from identical input voltages as measured by a highly accurate (1 in 10^6) digital volt–meter.

2.6.3 Phase check facility

To gain some knowledge of the phase propagation differences between receivers it was necessary to monitor the outputs of the signal–processor boards while a phase–locked, zero–beat–frequency signal was fed into the 8 receiver RF inputs. To make this possible, a new frequency synthesis unit capable of producing such a phase–locked signal was incorporated in the receiver system. To enable automatic phase–monitoring, additional hardware was required, including an 8–way power splitter and a means of remotely selecting the test signal level for different receiver gains. Significant modifications to the software were also required. The receiver phase check sequence occurs at the beginning of a data set and typically takes about one second to complete. The phase of the retarded output is read from the signal–processor boards and averaged over many samples to form a representative phase–delay figure. This figure is saved in the data "house keeping" information block as a two–byte integer which is actually ten times larger than the true phase angle to achieve a one decimal place accuracy. If required, the raw phase check information can be saved in a data block preceding the actual raw data itself. This facility is a valuable debugging tool for cases where input signals or reference signals are not satisfactory and cause the receivers' absolute phase to vary from data point to data point. Such a situation was observed during laboratory testing of the phase test hardware and led to significant fault finding work being carried out and eventually minimization, if not elimination, of several elusive earth loops. This work appears in the following subsection.

2.6.4 Earth loops

Once the receiver and signal processor problems had been addressed the radar receiver system was reassembled along with the new frequency synthesis unit, range marker and phase test hardware. Phase test data were taken over various lengths of time from periods of 2 min up to periods of 30 hr. By plotting the phase of the signal processor outputs for each data point sequentially in time it was quickly noticed that spurious and instantaneous changes in phase were occurring at apparently random time intervals. These "phase jumps" often occurred simultaneously in more than one receiver and sometimes occurred in all 8. At times, however, only one receiver was affected.

Eventually it was discovered that mechanical agitation of the equipment reproduced the phase jumps with some repeatability and, after the possibility of intermittent connector or

cable faults was eliminated, it was speculated that multiple earthing paths might exist within the chassis and equipment rack.

Precautionary measures were taken to eliminate any earth loops within the chassis by ensuring that all front panels were isolated from the electrical earth on the attached circuit board and were reliably connected to the earthed equipment rack. This was done by using countersunk conductive screws in specially routed holes in the anodised equipment chassis. In addition, individual chassis were securely grounded by the use of a large copper braided strap connected to the power supply earth. These measures resulted in a much reduced frequency and magnitude of spurious phase excursion.

Eventually the phase excursions were eliminated entirely by modifying a multiply–earthed signal shield between the front and back end of the receivers. The shield consisted of a plate projecting vertically from the surface of the receiver board to a height of 3 cm, and extending its entire width. The plate was grounded by conductive bolts anchored through the boards surface and in contact with the local electrical earth. In addition to this shield on the receiver board aluminium plates were mounted in the equipment chassis between each receiver in such a way that mechanical contact was made with the receiver's shield when the receiver board was inserted in the chassis. Since the chassis was earthed this additional contact created multiple paths to ground which were somewhat unreliable. By placing stress on the equipment rack slight movement would occur and the contact resistance between the two shielding plates could be affected. Signal voltage levels related to local earths could then change relative to earthing points elsewhere in the equipment and a change in the measured phase (which is simply the arctangent of the ratio of the quadrature to in–phase signal level) would result.

The problem was alleviated by isolating the shield on the receiver board from earth and using non–conductive nylon anchoring bolts. Anomalous phase excursions were no longer observed even with vigorous mechanical agitation applied to the equipment rack.

2.7 Pilot 10 Channel Transmitting System

Final design and integration of the 10 channel transmitter subsystem was substantially carried out by an external contractor with extensive consultation with the author. The subsystem integrates 10 power amplification modules, 10 phase–control modules, 10 filter/TR modules, a cooling fan unit, a power supply and a transmitter control interface. The transmitter

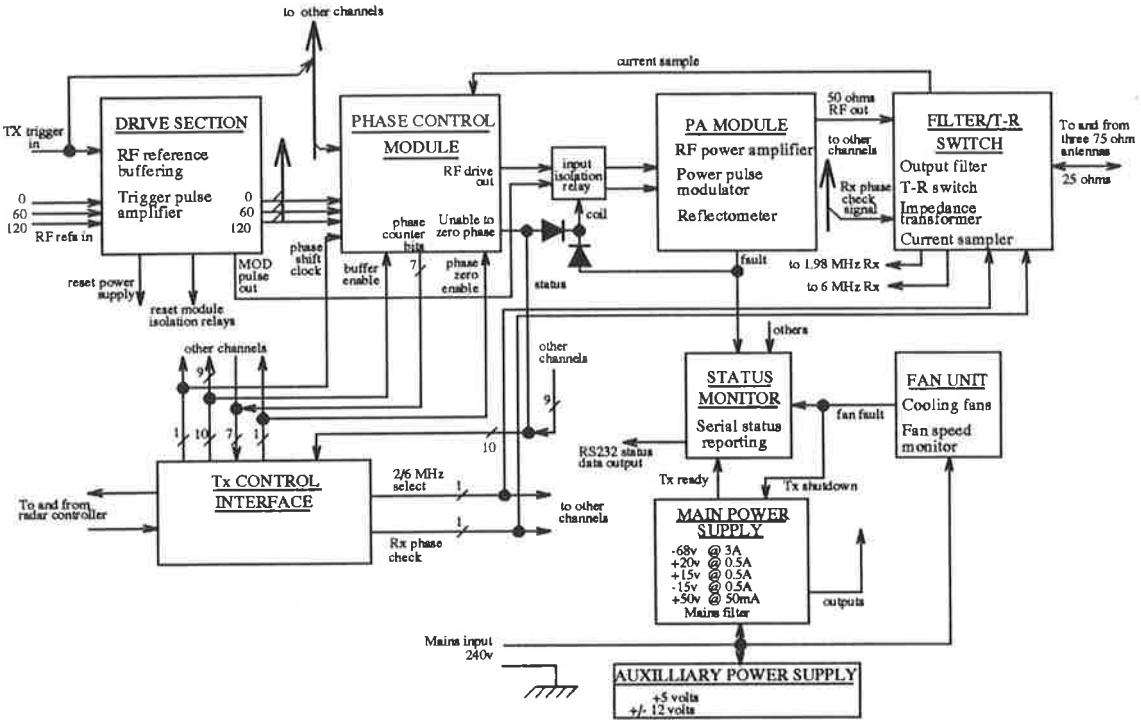

Figure 2.28: A block diagram of the 10 channel transmitting system with interaction to other 10 channel transmitting subsystems indicated.

control interface is resident in only one of the transmitter subsystems as it is responsible for control and information flow to all three racks. A block diagram of the transmitter system showing the relationship between these different modules appears in Figure 2.28. Each 10 channel subsystem is easily portable to other field sites and may be used as a stand–alone transmitting system for any existing antenna array. Usage of the transmitter subsystems in this way may necessitate the construction of some additional hardware (such as antenna tuner units etc.) which, in general, will be dependent on the local antenna array's characteristics.

For the Buckland Park array, implementation of the 30 channel transmitting/10 channel receiving system required the replacement of the original two patch boards with a total of three new patch boards. As was the case with the original patch board design, two new patch boards (fitted with BNC instead of Belling–Lee connectors) are connected directly to the antenna array. It is on these two patch boards that the antenna configuration for transmission is selected, and hence they are named the transmission patch boards. The transmission patch boards are also used to measure the impedances of the antennae.

Groups of antennae may be connected to receivers in one of two different ways. If it is desired that each receiver be connected to the same antennae as the corresponding PA modules, then the receivers are simply attached to the rear of the appropriate filter/TR

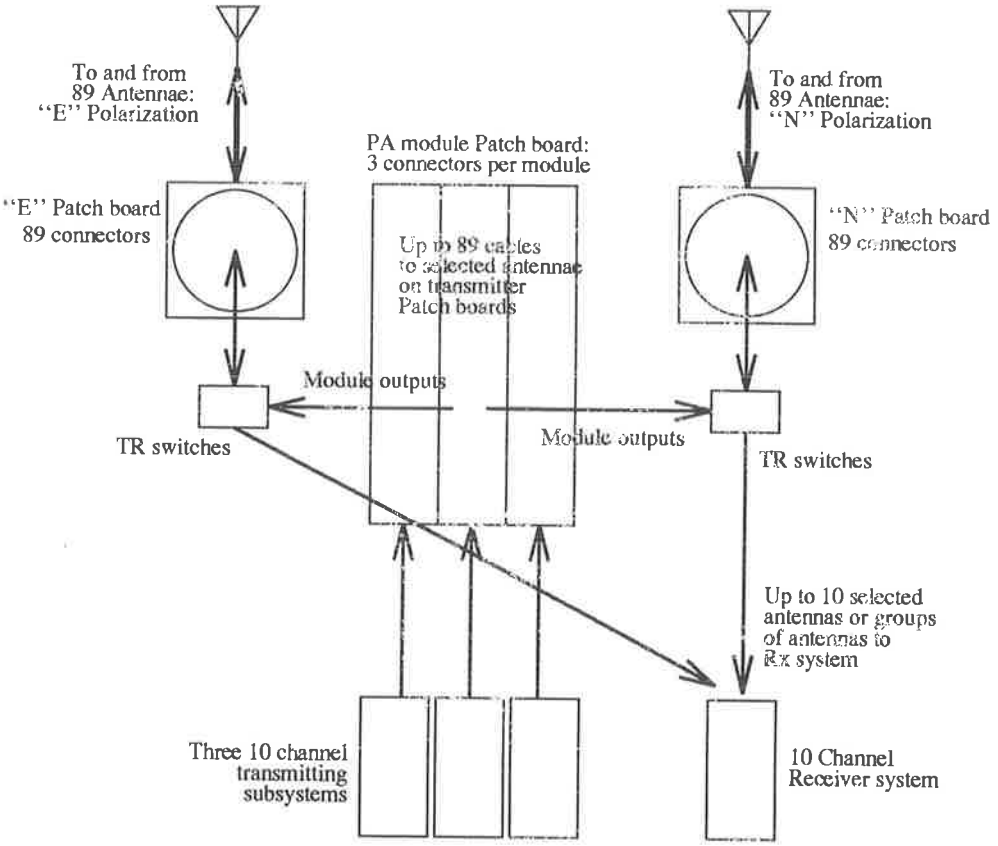

Figure 2.29: A block diagram of the 30 channel transmitting system/10 channel receiving system patch board arrangement.

boards. In this configuration, no extra TR switches are needed. If, however, it is necessary to connect the receivers to groups of antennae other than those used for transmission, then additional TR switches, mounted in separate boxes, are inserted between the PA module and the transmitter patch boards. Note that one isolating TR switch must be inserted for each antenna to be used for reception. The receivers are then connected to the isolated outputs of the TR switches in the desired configuration.

The third patch board is used to connect the 30 PA module outputs to the selected antennae on the transmission patch boards. The module outputs are soldered directly onto the rear of this central patch board, (see Figure 2.29), each module output being connected to three BNC sockets. Thus a total of 90 connectors are available on the front of the PA module patch board to be connected to a total of 89 antennae (of one polarization) on the transmission patch board. The unused PA module output is loaded by a 75 Ω dummy load to present the correct impedance to the PA module's filter.

In Figure 2.30 appears a photograph of one of the 10 channel transmitter subsystems and the 8 channel receiver system installed at the Buckland Park field site. The transmitter

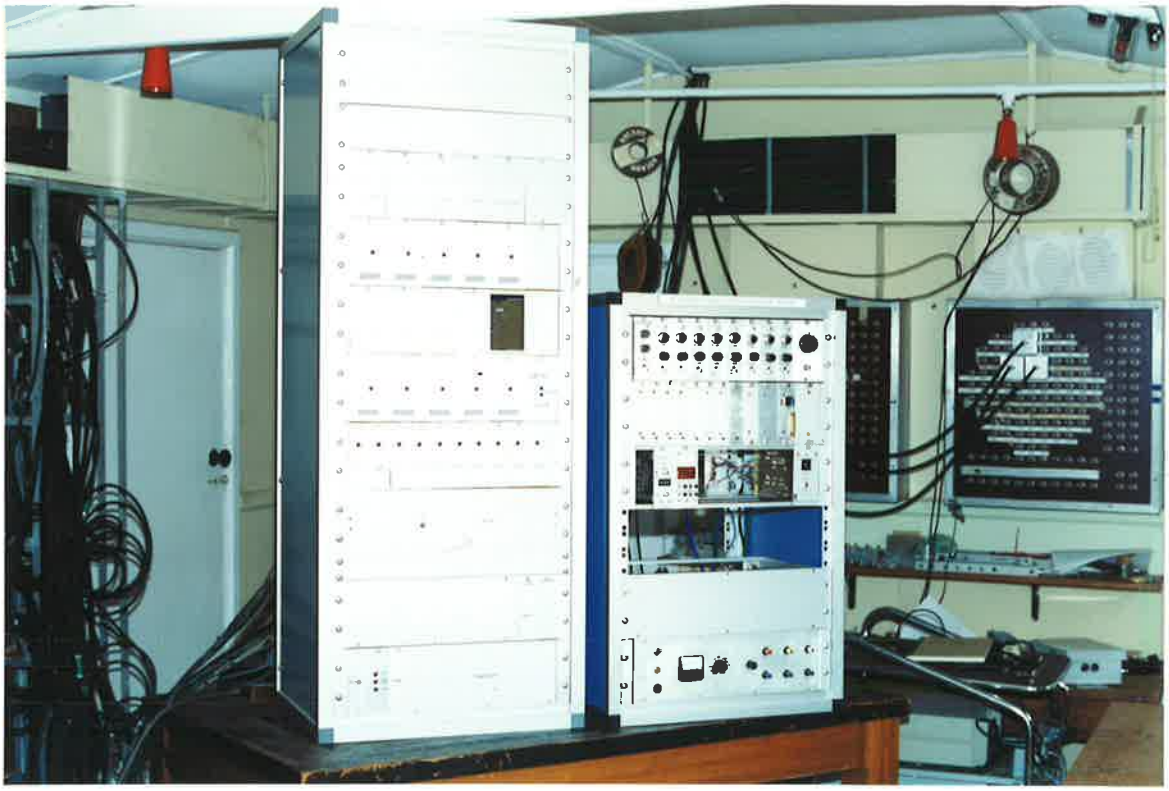

Figure 2.30: A photograph of the 10 channel transmitter and 8 channel receiver system installed at Buckland Park. The transmitter system is to the left of the receiver rack. See text for details.

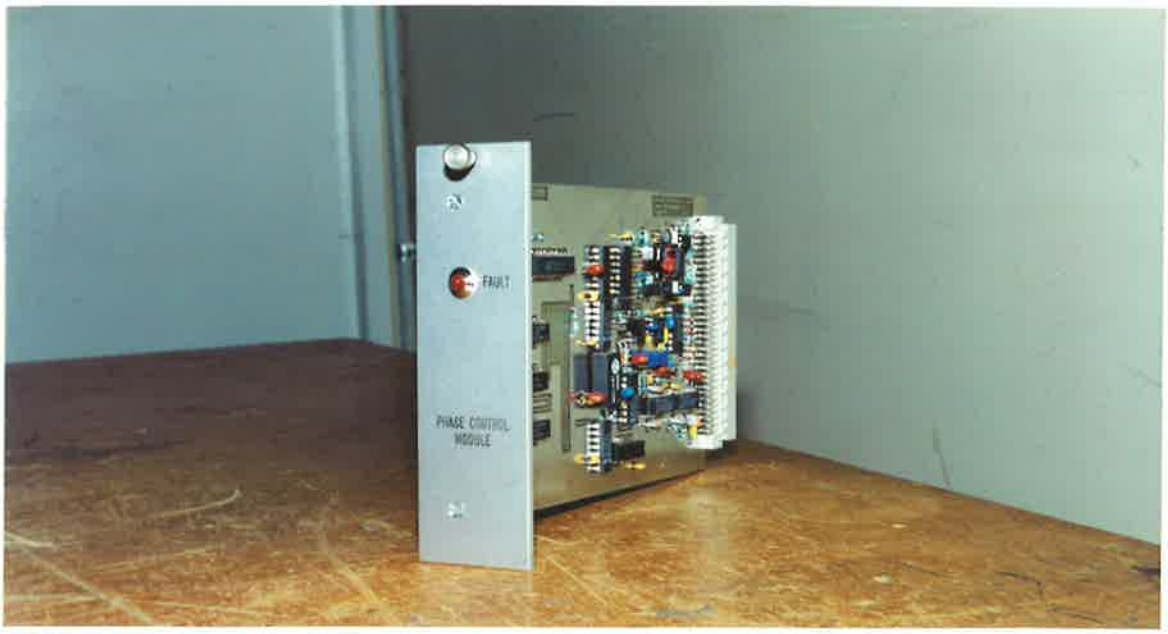

Figure 2.31: A photograph of one of the phase control modules used in the 10 channel transmitter system. See text for details.

is the taller of the two equipment racks and sits to the left of the receiver system. The components of the transmitter, from the bottom of the rack upwards, are;

- 1^{st} chassis: transmitter power supply,
- 2^{nd} chassis: transmitter control interface,
- 3^{rd} chassis: cooling fan unit,
- 4^{th} chassis: phase control modules 1 to 10,
- 5^{th} chassis: power amplification modules 6 to 10, and trigger pulse amplifier,
- 6^{th} chassis: TR switch/filter boards 6 to 10[3],
- 7^{th} chassis: power amplification modules 1 to 5 and
- 8^{th} chassis: TR switch/filter boards 1 to 5.

The 8 channel receiver system on the right of the transmitter rack is composed, again from the bottom of the rack upwards, of;

- 1^{st} chassis: receiver power supply,
- 2^{nd} chassis: frequency synthesis and phase test signal units,
- 3^{rd} chassis: rack mounted CRO (presently vacant),
- 4^{th} chassis: from left to right: range marker card, crystal clock and automatic gain control card,
- 5^{th} chassis: signal processor boards 1 to 8, memory buffers and DMA card,
- 6^{th} chassis: ground pulse blanking card and receivers 1 to 8.

In the background of Figure 2.30, to the right of the 8 channel receiver system, one of the original antenna patch boards is visible. At the time that the photograph was taken, a 3 channel spaced antenna radar experiment was underway (in an adjacent room). The three three impedance–matching boxes used to combine the groups of four antennae used in the spaced antenna experiment are visible on the front of the patch board. These boards will shortly be replaced with more modern versions in a new laboratory.

[3] At the time the photograph was taken TR/filter board 10 was missing

In Figure 2.31, a close–up photograph of one of the phase control modules is shown. Approximately equidistant from the front panel of the module and the 96–way connector on the rear of the card, and about two–thirds of the way down from the top of the card lies the 3–bit–programmable electronic phase–delay chip. The "fault light" on the front of the PCM becomes illuminated only when an adequate phase–zero state can not be reached during the phase–zero cycle.

2.8 Summary

In this chapter, the design and partial construction of a true MF Doppler radar has been described. Much attention was focussed on the problems associated with upgrading a 25 year–old array used only for reception to a modern, beam–steerable transmit/receive Doppler radar. These considerations divided naturally into two types; those associated with damage to, and ageing of the array, and those associated with the increased power levels inherent with transmission.

As an aid to antenna configuration selection and PA module distribution, an aperture–modeling computer program was developed. Parameters considered by the program included varying cable attenuation, antenna height above ground, radiated phase errors due to incorrect cable lengths or reactive impedance errors, phase–grouping the radiation of groups of elements to simulate antennae driven by single PA modules and progressive phase delays across the array to simulate beam steering. Different portions of the Buckland Park array were modeled, at both 1.98 MHz and 5.94 MHz, and it was demonstrated that groupings of three antennae was the optimum solution for the design parameters pertaining. Imperfect arrays were also modeled using the computer program, and it was concluded that a surprisingly large departure from an "ideal" array is required before significant aberrations are observed in the modeled power radiation pattern.

Design criteria relating to the new hardware required for transmission were discussed, and the results of construction and testing of various hardware elements reported. The three major pieces of hardware designed and built as part of this work were; the PA module filter, the phase control module and the new antenna balun. In particular, 30 antenna baluns were assembled in plastic boxes and mounted on the antenna poles at the Buckland Park field site. Experiments utilizing these 30 antennae and one of the new 10 channel transmitter subsystems are discussed in Chapter 4.

The problems associated with upgrading and refurbishing the old 5 channel Buckland Park MF receiver system were discussed in Section 2.6. Three extra receiver and signal processor channels were added, and the computer interface upgraded to allow connection to an IBM–PC. The relative gains of the in–phase and quadrature channel amplifiers in the signal–processors were equalized, reducing the error incurred by any phase–critical measurements to be made. In addition, a computer–controlled phase check facility was added to the equipment, allowing minimization of the error caused by different phase propagation delays between receivers. The use of this facility is discussed in Chapter 3. Several earth loops were discovered in the receivers which may, in the past, have caused some anomalous measurements to have been made. These were eradicated by careful earthing of the receiver boards, and elimination of multiple earth paths to the equipment chassis.

Chapter 3

RADAR INTERFEROMETRY

3.1 Introduction

Some of the first direction–finding studies of radio reflections from the atmosphere, and in particular, the ionosphere were conducted by Eckersley and Farmer in 1940. In their experiment, *Eckersley & Farmer* [1945] employed four vertically oriented loop antennae at the corners of a square and compared the phase differences of the voltages sampled at each of the diagonally opposed antennae. The experiment was intended to measure the tilt angles of the F and sporadic E layers, and to a lesser extent, the normal E layer. In later years other researchers [*Bramley & Ross*, 1951; *Bramley*, 1953] conducted similar experiments which included longer term observations of ionospheric tilts. *Baulch & Butcher* [1978] also utilized the phase differences between spaced antennae to measure the apparent angle of arrival of a signal reflected obliquely from the day–time E layer. Other researchers, also motivated by an interest in the motion of inhomogeneities in the E region, used other related, but distinct techniques, such as the amplitude–drift experiment (see, e.g., *Meeklah et al.* [1972]), and phase–path measurements (see, e.g., *Vincent* [1972]).

The first researcher to employ a frequency–domain analysis with the signals received at spaced antennae was *Pfister* [1971]. In his work, Pfister related the slope of the phase of the cross–spectrum to the azimuth and zenith angles of the apparent scattering point. *Whitehead & Monro* [1975] recognized the advantages of working in the frequency domain to provide enhanced angular resolution for relatively small HF/MF radars, and appear to be the first researchers to state that echoes from differing angles of arrival may be differentiated by their unique Doppler shifts. Others to subsequently employ Doppler radar interferometry

in studies of the upper atmosphere include

- *Jones* [1981], who employed a raster scanning MF/HF radar to study disturbances in the E–region,
- *Whitehead et al.* [1983], who considered the relative merits of the Doppler beam forming experiment with those of the spaced antenna drift experiment,
- *Adams et al.* [1985], who promoted the idea of phase consistency along orthogonal rows of antennae as a means of scatterer identification in the imaging Doppler interferometer (IDI) experiment,
- *Meek & Manson* [1987], who compared D–region winds obtained by a spaced antenna experiment with those obtained by Doppler–sorted radar interferometry,
- *Franke et al.* [1990], who considered the significance of smoothed and unsmoothed (sample) cross–spectra, and their relation to the so–called "true" and "apparent" wind velocities derived by the spaced antenna method,
- *Kudeki & Woodman* [1990a], who used post–statistics beam–steering techniques and Doppler radar interferometry with the Jicamarca VHF radar to determine the three–dimensional wind field and scatterer aspect sensitivity in the lower mesosphere and
- *Brosnahan & Adams* [1993], who presented some of the first results from an IDI system taken during the AIDA[1] campaign in 1989.

Doppler radar interferometry has also been employed to study the scatterers and winds in the troposphere and stratosphere with VHF radars by researchers such as *Röttger & Ierkic* [1985], *Liu et al.* [1990], *Palmer et al.* [1991] and *VanBaelen et al.* [1991b].

From these efforts over the last four decades, four distinct experiments utilizing coherent scatter radars to measure winds and other atmospheric parameters over various height regions have emerged. These are:

- the spaced antenna Full Correlation Analysis (FCA),
- the spaced antenna Radar Interferometer (RI),
- the multiple Doppler Beam forming Radar (DBR) and

[1] Arecibo Initiative in Dynamics of the Atmosphere

- the Imaging Doppler Interferometer (IDI).

In this work each technique is either utilized or at least discussed, and so a brief outline of each is now warranted.

3.2 The Spaced Antenna Full Correlation Analysis

The spaced antenna full correlation analysis was first described by *Briggs et al.* [1950]. In the present analysis, the time series of the backscattered or reflected signals from the atmosphere recorded at three spaced antennae are compared at various relative time shifts, or lags. The time shift of maximum correlation corresponds to the velocity of the diffraction pattern across the ground and, if the structures responsible for the scattering do not change in time, then this velocity can be identified as twice the mean wind [*Pawsey*, 1935; *Mitra*, 1949; *Felgate*, 1970]. In the more realistic situation of turbulent motions being advected through the radar's field of view, the velocity derived from the cross–correlation maxima is termed the "apparent" velocity, and can be shown to be larger than the background wind velocity, or "true" velocity. The method of full correlation analysis attempts to remove this bias to larger velocities caused by random motions in the moving pattern, and also accounts for errors associated with pattern elongation and scale. For a complete review of the full correlation analysis, and a discussion of some of the experimental difficulties involved, see *Briggs* [1984].

3.3 The Spaced Antenna Radar Interferometer

Although the original usage of the term "interferometer" referred to the physical addition of signals of differing amplitude and phase from spatially displaced sources to form a single signal of some measurable intensity, the modern–day radar interferometric technique bears only a mathematical resemblance to this notion. Despite this, the term "interferometer" will be taken to refer to any system in which phase and amplitude from multiple signals are combined to yield a measurement of phase difference between signals, an apparent direction of arrival, or a signal amplitude distribution with angle. In such a direction finding system, one of two approaches may be taken. In the first instance the time series at each receiver may be analysed using cross–correlation techniques to find an average direction of arrival. If

the coherent voltage sampled by receiver k, at location (x, y), is written as

$$E_k(x, y, t) = A_k(x, y, t)e^{i\phi_k(x,y,t)} , \tag{3.1}$$

then the spatial cross–correlation function for receivers k and l, separated by the vector (ξ, η), can be written

$$\rho_{kl}(\xi, \eta, \tau) = \frac{\sum_{t=1}^{N} [E_k(x, y, t)E_l^*(x + \xi, y + \eta, t + \tau)]}{\sqrt{\sum_{t=1}^{N} |E_k(x, y, t)|^2 \sum_{t=1}^{N} |E_l(x + \xi, y + \eta, t + \tau)|^2}} , \tag{3.2}$$

and the numerator of Equation 3.2 may be re–written as

$$\rho_{kl}(\xi, \eta, \tau) = \sum_{t=1}^{N} A_k A_l e^{i(\phi_k - \phi_l)} . \tag{3.3}$$

Thus, the argument of Equation 3.3 calculated at zero time lag represents the average phase difference of the received signal between the two antennae k and l over the time period in question. Utilizing simple geometrical arguments, similar to those applied in diffraction theory, we can show that the average phase difference between the two antennae $(\Delta\phi)$ is related to the off-zenith angle of arrival of the signal by

$$\Delta\phi = \frac{2\pi d}{\lambda} \sin\theta , \tag{3.4}$$

where d is the separation between the two antennae, and θ is defined as the off–zenith angle. In order to completely define the direction of arrival in three dimensions, a minimum of three antennae are required. The three antennae pairs yield three phase difference measurements from which the two angles describing the angle of arrival may be obtained. These angles may be expressed in terms of an azimuth and off–zenith pair or, more easily, as two direction cosines. For a given angle of arrival, the phase differences between the three receivers are, of course, dependent upon the geometrical arrangement of the three antennae. We may express this relationship as a matrix equation

$$\begin{pmatrix} \psi_{12}(0) \\ \psi_{23}(0) \\ \psi_{31}(0) \end{pmatrix} = \frac{2\pi d}{\lambda} \begin{pmatrix} \xi_{12} & \eta_{12} \\ \xi_{23} & \eta_{23} \\ \xi_{31} & \eta_{31} \end{pmatrix} \begin{pmatrix} l_o \\ m_o \end{pmatrix} , \tag{3.5}$$

where $\psi_{kl}(0)$ are the average phase differences between each antenna pair, l_o and m_o are direction cosines defined relative to the x– and y–axis respectively, and the ξ_{kl} and η_{kl} are the separations between antennae k and l in the x and y directions. This matrix equation may be extended to cover the use of more than three antennae, and is easily inverted in order to find the angle of arrival direction cosines from the receiver phase differences.

Inherent in Equation 3.4 is the possibility of phase ambiguities occurring between antenna pairs as the phase difference between two antennae is defined only to modulo 2π. Thus, depending on the antenna spacing to wavelength ratio of the array in use, phase ambiguities may result. In general, when the antennae are spaced further apart than one half–wavelength, arrival angles at larger off-zenith angles are mapped back towards the zenith.

In Subsection 3.6.1 we examine some of the antenna patterns used in the interferometric studies, and the phase ambiguities expected.

The second technique available for use with the radar interferometer is that of Doppler sorting. In this technique each frequency component of the received signal is associated with a unique angle of arrival. In order to Doppler sort the signal, the time series of the coherent voltage samples at each of the three antennae are firstly Fourier transformed to yield the three complex auto–spectra $f_k(\nu)$. Cross–spectra for each of the three antenna pairs are then formed using

$$W_{kl}(\nu) = f_k^*(\nu) f_l(\nu) \; . \tag{3.6}$$

We then define the phase for each frequency "bin" of the cross–spectrum by taking the argument of the cross–spectrum and relate this phase difference to an angle of arrival for that frequency shift. This phase difference is exactly analogous to that formed from the cross-correlation function at zero lag, except that is defined for each Doppler shift. The cross-correlation phase at zero time lag can be thought of as the weighted average of all of the cross–spectral phases over the entire frequency range considered. The cross–correlation derived phase differences will hitherto be referred to as the "mean angle of arrival", while the cross–spectral phase differences will be referred to as the "Doppler sorted" angle of arrival.

3.4 The Doppler Multiple Beam Forming Radar

Doppler beam forming radars utilize either cumbersome sets of cable delays or electronic phase shifting to produce some number of independent beam pointing directions. In its simplest form, a single Doppler beam directed towards some off–zenith angle may be formed by joining rows of antennae together and introducing the appropriate length coaxial cable between these rows. The signals produced by the cable delays are then summed together (taking some care that impedances are matched) to form a single signal. Multiple beams may be formed by again connecting rows of antennae together and splitting the signal produced

by each row into (at least) two. These two signals may then be used in separate delay configurations to yield two independently directed radar beams. Note that the beam direction must always be perpendicular to the antenna rows which were originally formed. Electronic beam forming (as discussed in Chapter 2) is perhaps more elegant, and allows radar beam pointing directions at arbitrary angles, provided that individual antennae (or at least small groups of antennae) are independently phased.

Multiple simultaneous off–zenith directed radar beams allow the measurement of various atmospheric dynamics parameters. Of principle interest among these is the measurement of wind velocity. A Doppler radar with a beam pointing in the direction (θ, ϕ), will measure a radial velocity at range R, of

$$V_R(R,\theta,\phi) = u(R,\theta,\phi)\sin\theta\sin\phi + v(R,\theta,\phi)\sin\theta\cos\phi + w(R,\theta,\phi)\cos\theta \ , \tag{3.7}$$

where u, v and w are the zonal, meridional and vertical components of the mean wind at location (R,θ,ϕ), and R, θ and ϕ are coordinates in the standard three–dimensional polar coordinate system [*Reid*, 1987]. Given a multiple beam Doppler radar, possessing two beams lying in a plane at angles $+\theta$ and $-\theta$ to the zenith respectively, (see Figure 3.1) the horizontal and vertical wind vectors may be found from the two measured radial Doppler velocities V_1 and V_2, provided only that that the wind field is invariant between the two radar pulse volumes. Then

$$\begin{aligned} V_H &= \frac{1}{2\sin\theta}(V_1 - V_2) \text{ and} \\ V_V &= \frac{1}{2\cos\theta}(V_1 + V_2) \ , \end{aligned} \tag{3.8}$$

where V_H is the component of the horizontal wind projected into the plane containing the two Doppler beams, and V_V is the vertical velocity.

Due to the finite beam–width of practical radars, allowance must be made for the effect that the aspect sensitivity of the atmospheric scatterers has on the effective radar beam pointing direction [*Lindner*, 1975a; *Lindner*, 1975b; *Röttger*, 1981]. Since the power back–scattered from the atmosphere falls rapidly as a function of off–zenith angle, the effective beam pointing direction is forced back towards the zenith. If this effect is neglected, DBR measurements of atmospheric winds will be biased towards smaller values.

Another useful parameter obtainable from the dual coplanar radar experiment is the measurement of momentum flux. Gravity waves encountering critical levels in the mesosphere break and deposit both energy and momentum in the surrounding atmosphere. Such deposition results in statistically correlated fluctuating components of the vertical and horizontal

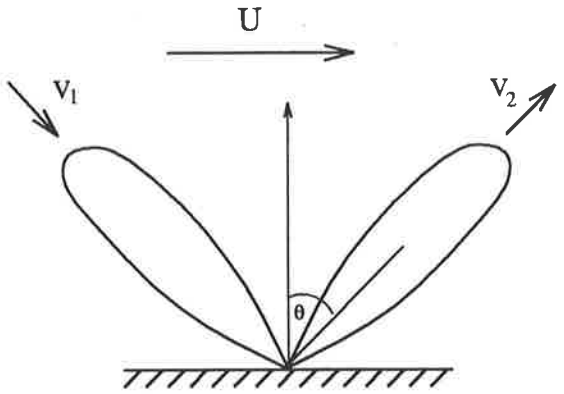

Figure 3.1: A dual coplanar Doppler beam radar configuration showing the line of sight components of the mean wind, V_1 and V_2.

wind velocity. These terms, such as $\rho\overline{u'w'}$ and $\rho\overline{v'w'}$, are measurable with dual, coplanar Doppler radars (see, e.g., *Vincent & Reid* [1983]).

3.5 The Imaging Doppler Interferometer

The imaging Doppler interferometer (IDI) employs multiple antennae spaced evenly in two orthogonal directions [*Adams et al.*, 1985; *Adams et al.*, 1986; *Brosnahan & Adams*, 1993]. In the case of the MAPSTAR[2] radar deployed in Arecibo during the AIDA campaign, a total of 10 receivers were connected to two orthogonal arrays comprised each of three evenly–spaced crossed half–wave dipoles. Circularly polarized radiation was used in the experiment which allowed interfering linearly polarized signals from nearby radio stations to be removed [*Adams et al.*, 1986]. The underlying premise of the IDI is that there exist, on occasion, well defined discrete scattering locations in the atmosphere, each having its own unique Doppler velocity. Such discrete scattering locations are associated with unique positions in the sky and should, therefore, give rise to backscattered signals emanating from that point. These backscattered signals would then have the property that measurements of the signal's phase along a line on the ground will reveal a linear relationship with distance. In other words,

$$\phi(\xi) = m\xi + \phi_o \ , \tag{3.9}$$

where m is a measure of the phase change with distance. Given two orthogonal rows of antennae, such consistent phase differences between the antennae are readily related by Equation 3.5 to a uniquely specified location in the sky. It is proposed by Adams et al that the motion of these discrete scattering locations is a true representation of the background

[2] Middle Atmosphere Periodic Structure Associated Radiance

wind velocity at that point, and that a least squares fitting of their Doppler velocities is a reliable estimate of the mean wind.

3.6 Angle Of Arrival Measurements

Time domain angle of arrival (AOA) measurements using the radar interferometer configuration allow the average direction of signal return from a volume scattering region to be determined. A minimum of three spaced antennae are required to fully determine the AOA, and these must be spaced such that the maximum distance between antennae is less than one-half of the wavelength of the radiation being used. If this condition is not satisfied, then any scattered signal arriving from larger off-zenith angles will be mapped back into the zenith region. The Buckland Park antenna array used in these studies has a base antenna spacing of about $\frac{3}{5}\lambda$, and therefore does not satisfy the condition for unambiguous AOA determination. For this reason, some effort was expended on determining the region of sky from which scatter could be expected for various antenna configurations.

3.6.1 Calculation of angle of arrival domain

A simple calculation from Equation 3.4 suggests that the maximum off-zenith angle obtainable with the Buckland Park antenna array is 56°. Radiation emanating from the sky at this angle from the zenith produces a phase difference between two antennae separated by $\frac{3}{5}\lambda$ (where $\lambda = 151.5$ m for the radar currently in use) of π rad. If the radiation emanates from a still larger off-zenith angle then the phase difference produced is then larger than π rad. This phase difference, of course, is ambiguous, as it is indistinguishable from a phase difference of opposite sign, and slightly less than π rad.

Extending the model to the three dimensional case yields slightly different results. In Figure 3.2 three antennae selected from the main array are depicted forming a right triangle of minimum size. Also shown are two separate sets of wavefronts approaching the sub–array from the West and North–West. For the purposes of this argument we shall assume that the wave fronts are arriving from an off–zenith angle of 90°. If the antenna spacing d, corresponds to three fifths of the wavelength of the incoming wavefronts, then quite clearly the wavefronts approaching from the West will produce a phase difference between antennae 1 and 2 (and also antennae 1 and 3) of more than π rad. However, the radiation approaching from the North–West is detected by the antennae 1 and 2 (or 3 and 2) with a projected

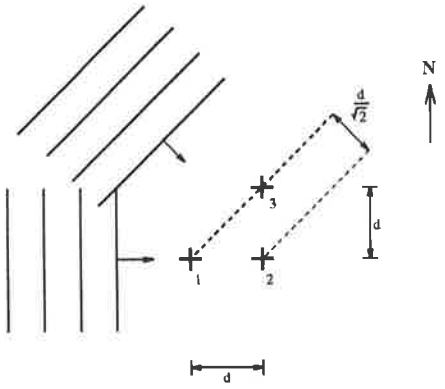

Figure 3.2: Angle of arrival information is not always ambiguous for an antenna array with basic spacing larger than one–half wavelength. The wavefronts approaching from the West result in a phase difference between antennae 1 and 2 of more than π radians, whereas the wavefronts from the North–West result in a phase difference between antennae 1 and 2 of less than π radians.

baseline of only $\frac{d}{\sqrt{2}}$ and thus produces a phase difference of

$$\begin{aligned} \Delta\phi &= 2\pi\frac{\frac{d}{\sqrt{2}}}{\lambda} \\ &= 2\pi\frac{3}{5\sqrt{2}} \\ &\simeq 0.85\pi \text{ rad.} \end{aligned}$$

This is an unambiguous phase difference as it is less than π rad. Thus, antennae selected from an array with a basic antenna separation of $\frac{3}{5}\lambda$ can, under certain conditions, detect incoming radiation to off–zenith angles of 90°. Similar arguments may be used to show that the maximum off–zenith angle that is detectable for scatter from the North–East and South–West is only 36° – far less than the one–dimensional model for which 56° was calculated.

A full picture of the AOA domain of the array depicted in Figure 3.2 may be revealed by calculating the angle of arrival resulting from three random phase differences between the three antenna pairs. If this calculation is performed many times from many different random phase differences the complete AOA domain will eventually be found. Figure 3.3 depicts the AOA domain resulting from the antenna configuration shown in Figure 3.2. This configuration is similar to one utilized in a study which is described in Section 3.7.

One area of recent interest in this field has been the attempt to remove these 2π phase ambiguities by means of the circular redundancy condition. Measuring the phase differences between three pairs of antennae yields three equations in two unknowns. Thus, the problem is over–determined and must be solved by some form of fitting technique. The additional

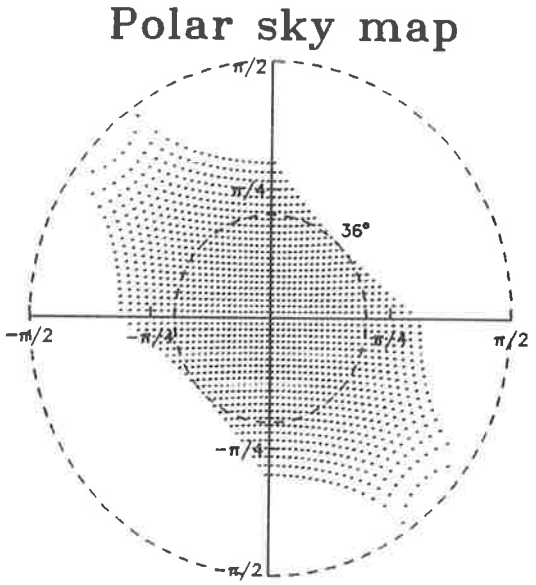

Figure 3.3: The angle of arrival domain for the antenna configuration displayed in Figure 3.2. The information is displayed in polar form with the off-zenith angle increasing from the centre of the plot outwards. Thus, lines of constant azimuth are radii and lines of constant off-zenith angle are circles. Note that the shaded region extends out to the "horizon" to the North–West and South–East, but only to 36° in the orthogonal directions.

information may also be used, in certain circumstances, to decode any possible phase ambiguity. In the case where no phase ambiguity exists, the sum of the three measured average phase differences should be (ideally) zero.

Meek & Manson [1987] have invoked this condition to yield a figure of merit they call the "normalized phase discrepancy," or NPD. They define

$$NPD = \frac{|\sum_{i,j\ i\neq j} \psi_{ij}(0)|}{\sum_{i,j\ i\neq j} |\psi_{ij}(0)|}\ , \tag{3.10}$$

where the $\psi_{ij}(0)$ are the three average phase differences between the three receivers derived from the phase of the cross–correlation function at zero lag. This condition is equally applicable to individual cross–spectral phases from single frequency "bins", and was in fact used for this purpose by Meek and Manson. A NPD of 0.3, they say, represents a 70% confidence limit that the incoming radiation is in the form of a plane wave.

For the purposes of phase ambiguity detection, it is more convenient if the signed denominator of Equation 3.10 is used. It is quite clear that if a phase ambiguity has occurred in one of the three phase differences then the numerator of Equation 3.10 will have a value of $\pm 2\pi$, and an attempt may be made at "unwrapping" the phase. It turns out, however, that this is not always possible. There are two reasons for this difficulty. First, the phase

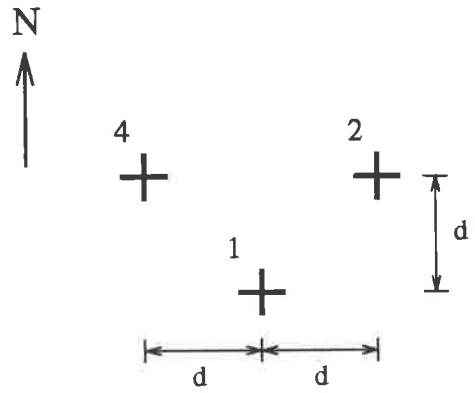

Figure 3.4: The antenna configuration used for consideration of phase difference ambiguities. This configuration, along with that depicted in Figure 3.2 is used in the angle of arrival study discussed in Section 3.7.

ambiguity may not have occurred between only one antenna pair, and second, even if only one phase ambiguity has occurred, it is not possible to determine which phase difference is responsible.

To illustrate this point, consider the antenna configuration displayed in Figure 3.4. The antennae depicted are selected from the Buckland Park array and have a fractional wavelength spacing of $\frac{3}{5}$. Let the measured average phase differences between the three antenna pairs be ψ_{ij}, and suppose that these are produced by plane wave radiation incident upon the array from a variety of angles. For radiation incident from the South at an off–zenith angle of 90°, it is clear that a $+2\pi$ phase ambiguity will occur in ψ_{12}, no phase ambiguity will occur in ψ_{24} and a -2π phase ambiguity will occur in ψ_{41}. At this point we introduce a more compact notation and label the phase ambiguities inherent in the three phase difference measurements with the 3 element vector, δ_{ij}. In this case $\delta_{ij} = (+2\pi, 0, -2\pi)$. Thus, the total phase difference between the three antenna pairs may be written

$$\Delta\phi_{ij} = \psi_{ij} + \delta_{ij} \ . \tag{3.11}$$

From simple geometry, we know that

$$\sum_{i,j \ i\neq j} \Delta\phi_{ij} = 0 \ . \tag{3.12}$$

In other words, if the complete phase relationship between the three antennae is known, then for incoming plane–wave radiation, the circular sum of the phase differences between antenna pairs must equal zero. For the example given above,

$$\sum_{i,j \ i\neq j} \delta_{ij} = 0 \tag{3.13}$$

also. Therefore the measured phase differences between the antenna pairs must sum to zero, and the normalized phase discrepancy condition will be satisfied, despite the existence of two phase ambiguities. In fact, there are seven distinct combinations of phase ambiguities for which the sum of δ_{ij} is zero, and these correspond to seven distinct regions of the sky. Scattered radiation incident from these regions (one of which surrounds the zenith) will not be rejected on the basis of the NPD criterion.

In addition to the seven regions for which the sum of the three δ_{ij} is zero, there exist eight more regions for which their sum is $\pm 2\pi$. (Four regions yield phase difference ambiguity sums of $+2\pi$, and four yield -2π.) Although the NPD criterion will not be satisfied for scatter emanating from these eight regions of sky, it is still not possible to determine which region of the four possible is responsible. Figure 3.5 displays the 15 separate regions of sky which give rise to distinct phase ambiguities. Different antenna configurations, of course, give rise to different numbers and regions of phase difference ambiguity.

The salient feature of scatter from the D and E–regions of the atmosphere allowing the use of such antenna configurations is its inclination to aspect sensitivity. Power backscattered from these altitudes decreases rapidly with off-zenith angle [*Lindner*, 1975b; *Hocking*, 1979; *Röttger*, 1981; *Reid*, 1987; *Meek*, 1992], and is parameterized as

$$P(\theta) \propto e^{-\left(\frac{\sin^2\theta}{\sin^2\theta_S}\right)} , \tag{3.14}$$

where θ_S is a function of altitude and season ranging between values of 2° and 14°. Thus, even in the worst–case scenario of $\theta_s = 14°$, the power returned from off–zenith angles larger than 20° will be at least 10 dB less than that returned from the zenith, provided that there is no systematic tilt to the scattering layer. Therefore it would seem unlikely that any atmospheric returns would cause the measured angle of arrival to deviate from the zenith by more than a few degrees. It turns out, however, that not only atmospheric returns are present in the signals recorded at Buckland Park, with both sea scatter and RF interference (especially at night) detectable.

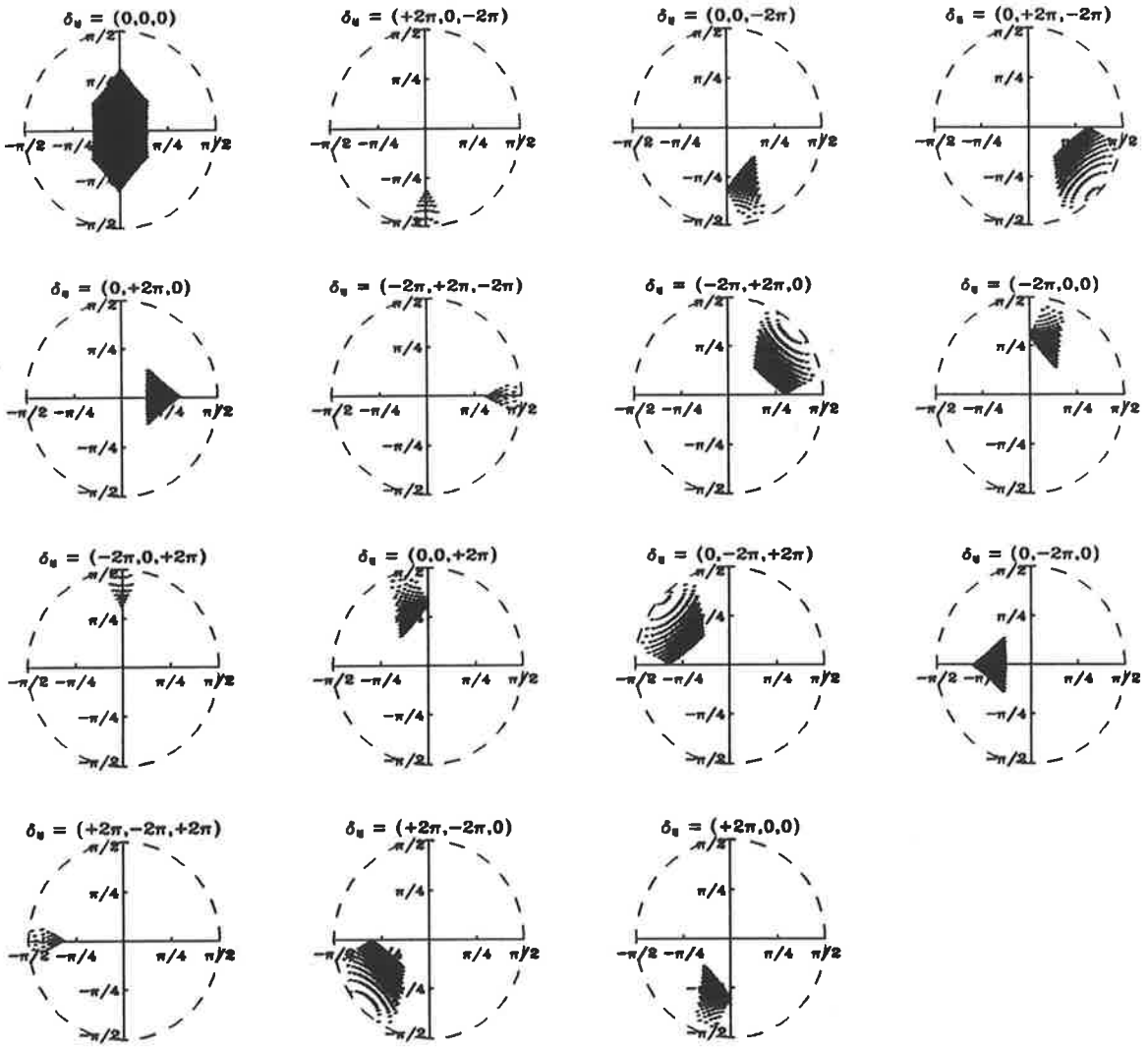

Figure 3.5: The 15 regions giving rise to distinct combinations of phase difference ambiguities for the antenna configuration shown in Figure 3.4. Superimposed, these regions form a complete coverage of the sky.

3.7 Angle Of Arrival Experiment

Upon completion of the refurbishment of the 8 channel data acquisition system in 1992 a series of experiments were conducted on a campaign basis at the Buckland Park field–site. The data presented here comprise the first continuous campaign which began in mid–afternoon on the 16^{th} of September, 1992 and continued for a period of 33 hr. Due to teething problems with the equipment, circularly polarized "O" mode radiation was transmitted during both daytime and night–time periods. For this reason night–time data was excluded from this study as extraneous interfering signals dominated the atmospheric returns. The existing 25 kW 10 channel solid–state transmitter system (used for spaced antenna wind measurement experiments) connected to the broad beam small transmitting array was slaved to the new 8 channel receiving system (see Figure 2.1). Each of the 8 receivers was connected to a single dipole selected from the 89 available in the "N" polarized array. (see Figure 3.6.) Thus, linearly polarized radiation was received with a subsequent power loss of 3 dB. The system PRF was set at 80 Hz (during the day) and 32 coherent integrations were performed per data point, resulting in an overall sampling frequency of 2.5 Hz. Coherent time series of 256 points were collected at each of 20 range gates yielding a total time span of 102.4 s. The intermediate frequency (IF) gain of the receivers was dynamically adjusted by the computer between data acquisitions such that the receiver gain was optimized for the 74 km range gate. Although all of these parameters were fully adjustable, the above values were selected in order to provide compatibility with previous work performed with the same, (but not upgraded) receiving system. It must be emphasized that single dipoles possessing extremely broad beam patterns were used for reception in this experiment. This, in general, has not been a common configuration used with the Buckland Park array where, at least for spaced antenna experiments, each receiver is usually connected to four dipoles. These facts must be borne in mind when interpreting the data presented in this chapter.

Of particular interest during this first campaign was the high quality of the data recorded. Shown in Figure 3.7 are time series for receivers 1, 2 and 4 taken during mid–afternoon on the 16^{th} September, 1992. The range gate selected in this case was 78 km. In Figure 3.8 the three cross–correlation functions between the same three receivers are displayed out to ± 20 lags. Note especially the smooth, well–behaved nature of the cross–correlation amplitudes which exhibit well–defined peaks. Note also that the cross–correlation phases are extremely well–behaved and show little variation near zero time lag.

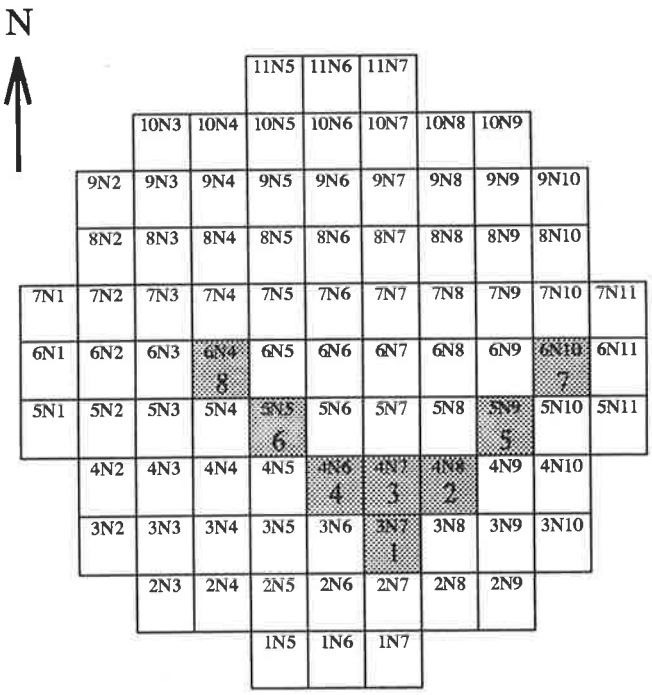

Figure 3.6: The antenna configuration used for the bp920916 data set. The antennae labeled 1 to 8 are connected to the respective receivers 1 to 8.

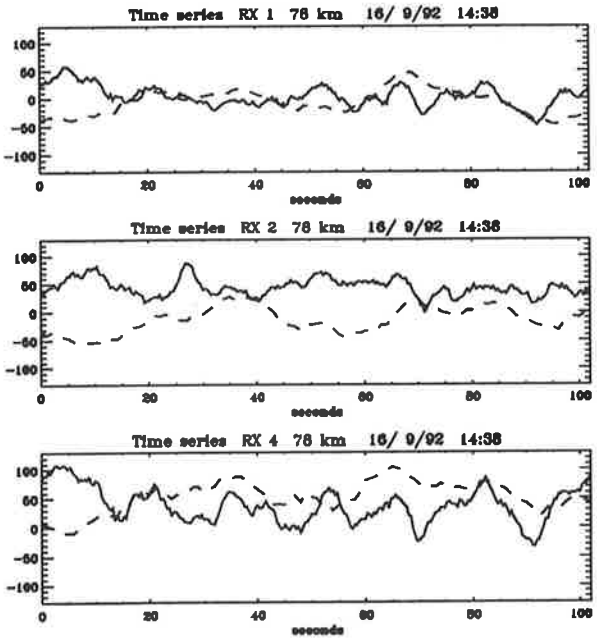

Figure 3.7: A typical time series for three of the 8 receivers used for angle of arrival calculations. The solid line represents the in–phase component of the signal, while the dashed line represents the quadrature component. The abscissa scaling for the three time series is measured in raw digitizer steps ranging between -128 and +128.

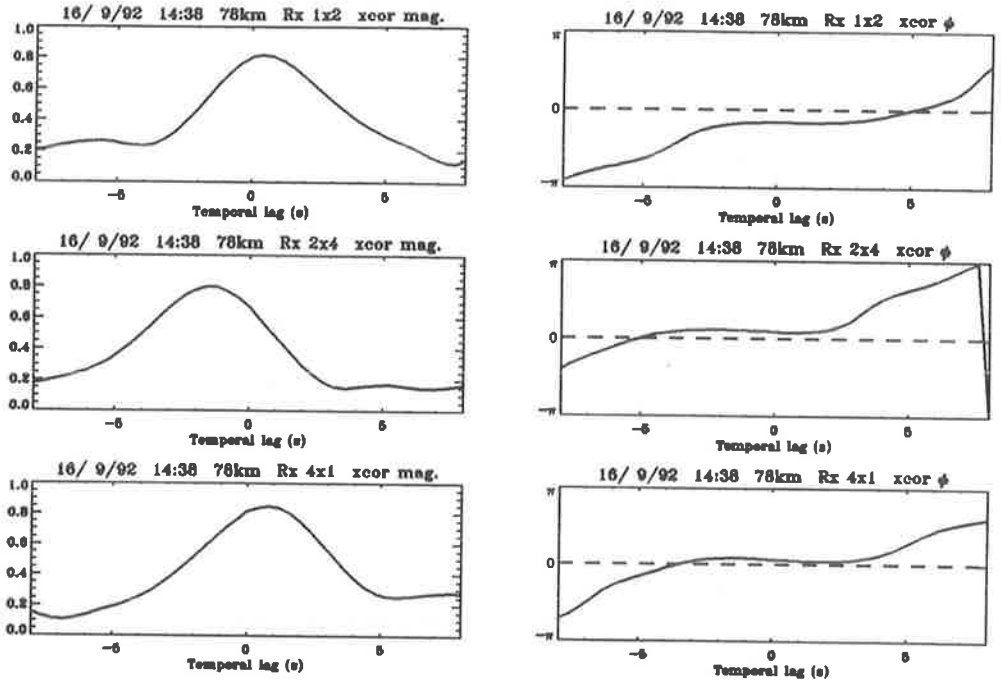

Figure 3.8: Cross–correlation functions calculated from the three time series shown in Figure 3.7.

To calculate a mean angle of arrival from such a data record, the phase of each cross–correlation function at zero time lag is used in Equation 3.5. For the data appearing in Figure 3.8, the relevant phases are

$$\begin{pmatrix} \psi_{12}(0) \\ \psi_{24}(0) \\ \psi_{41}(0) \end{pmatrix} = \begin{pmatrix} -0.507 \\ 0.297 \\ 0.193 \end{pmatrix}, \tag{3.15}$$

and their sum (the numerator of the NPD figure of merit) is -0.017. This phase sum has a magnitude which is clearly far less than π indicating that the scatter is probably incident from the zenith. Inverting Equation 3.5 with the appropriate coordinates for antennae 1,2 and 4 yields the two direction cosines for the mean angle of arrival. These are

$$\begin{pmatrix} \ell_0 \\ m_0 \end{pmatrix} = \begin{pmatrix} 0.108 \\ 0.093 \end{pmatrix}, \tag{3.16}$$

where ℓ_0 is the direction cosine relative to the x–axis, and m_0 is defined relative to the y–axis. If the correct transformation of coordinates is applied, the azimuth angle, ϕ and off–zenith angle, θ of the incident radiation may be defined. These coordinate transformations are

$$\begin{aligned} \phi &= \arctan \frac{m_0}{\ell_0} \text{ and} \\ \theta &= \arcsin \sqrt{\ell_0^2 + m_0^2}, \end{aligned} \tag{3.17}$$

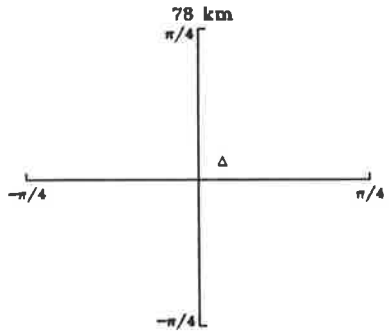

Figure 3.9: The mean angle of arrival of the signal depicted in Figures 3.7 and 3.8. Note that North is defined in the positive–y direction, and East in the positive–x direction. The azimuth and off–zenith angles of the signal (depicted by the symbol "Δ") are 40.7° and 8.2° respectively. Note that the off–zenith scale extends to only $\frac{\pi}{4}$ radians in this figure.

where ϕ is defined anti–clockwise relative to East, and θ is defined relative to the zenith. For the particular direction cosines listed above, we find that $(\phi, \theta) = (40.7°, 8.2°)$. In other words, the scatter emanates from 8° off–zenith in an approximately North–Eastwardly direction. A convenient form of display for such angle of arrival information is the polar sky map introduced in Subsection 3.6.1. Plotted in this way, the angle of arrival calculated above appears in Figure 3.9.

If the entire daytime data set is analysed in this way, each mean angle of arrival may be overlayed on such a diagram, and the distribution of points examined. Since the characteristics of the scatter from different altitudes are different, it is helpful to display these polar sky maps for individual range gates. Figure 3.10 displays all of the angle of arrivals (as calculated from receivers 1, 2 and 4) for the daytime data from the bp920916 data campaign in this manner. Note that no data have been rejected on the basis of low signal–to–noise ratio, and so spurious returns, not associated with atmospheric scatter, are visible in the lowest five or six range gates. A total of 464 data points, representing more than 16 hours of data appear on each polar sky map.

Two features of the data are worth commenting upon.

First, it is quite apparent that the data displays a systematic bias away from the zenith towards the East with a magnitude of about 8°. Since over such a length of time (> 16 hr) it is unlikely that a stratified atmosphere could maintain a systematic tilt of 8°, (especially over such a height range) we conclude that this bias is an instrumental effect. Possible contributions to this systematic error include

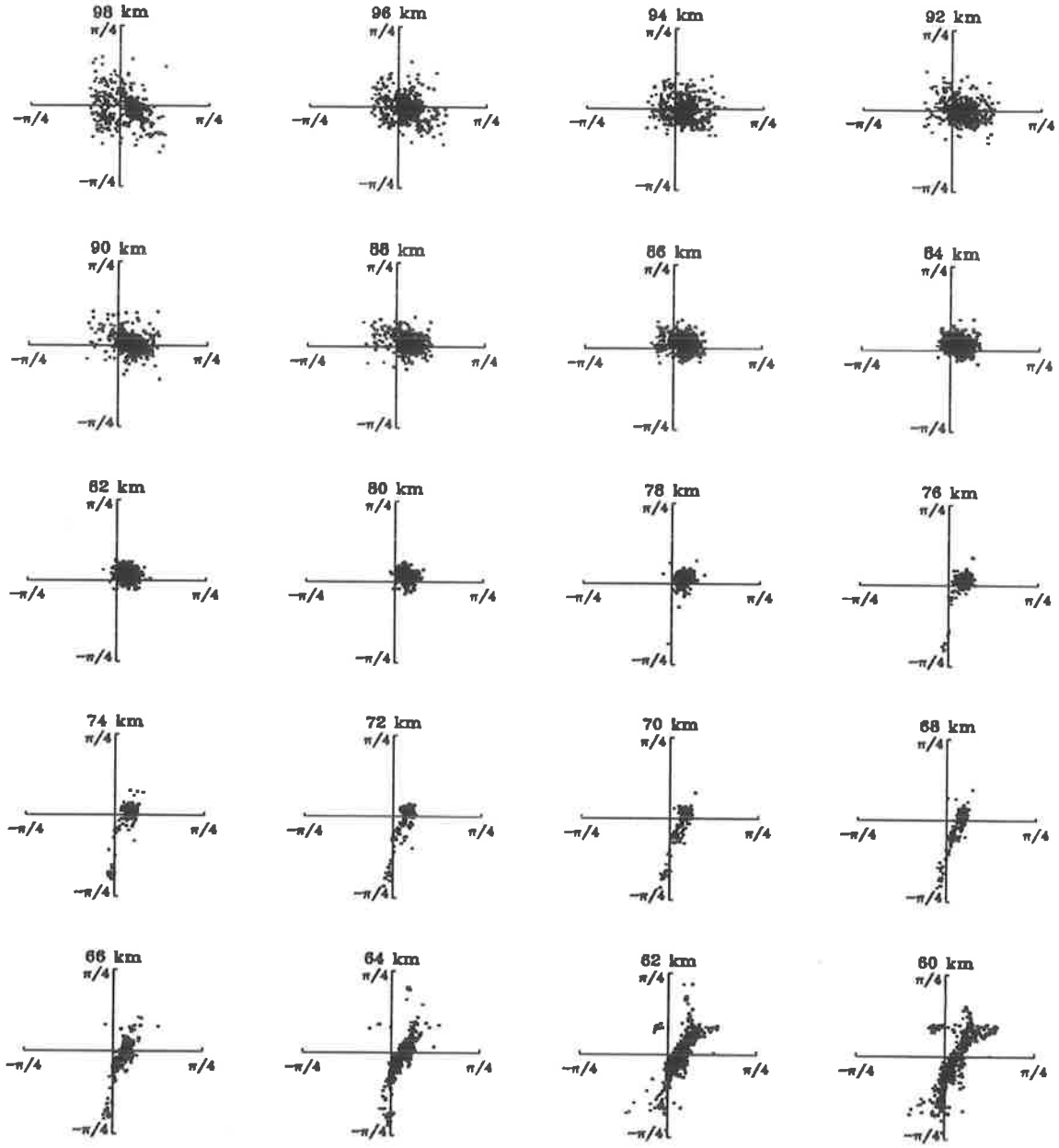

Figure 3.10: The mean angle of arrival of the bp920916 data set as calculated from receivers 1, 2 and 4 for daytime returns only. A systematic off–set from the zenith is apparent, as is a tendency to more aspect sensitive scatter with decreasing range gate. No data heve been rejected on the basis of low signal–to–noise ratio, and so many spurious returns are visible below about 72 km. Examination of the power spectra calculated for this data reveal that broadcast interference, sea scatter and relatively stable interfering RF signals are possible causes of these spurious measurements (see Figure 3.37). Note that the off–zenith scale extends to only $\frac{\pi}{4}$ radians in this figure.

Table 3.1: An example of the absolute and relative phase measurements of the 8 receivers from the bp920916 data set. Also shown are the amplitudes (in digitizer steps: ±128) of the test signal. These particular measurements were taken with an IF gain setting of zero (a minimum). The relative phases are differences relative to the phase of receiver one.

Receiver	In–phase	Quadrature	Amplitude	ϕ (°)	Relative ϕ (°)
1	62	26	68	23	0
2	102	31	107	17	-5.5
3	64	69	95	47	24.3
4	67	52	85	38	15.5
5	64	35	74	29	6.2
6	40	7	41	10	-12.7
7	88	7	89	5	-17.8
8	65	24	70	20	-2.4

- differences in the phase propagation delays through receivers,
- differences in coaxial cable electric lengths connecting the central laboratory with the antennae and
- variations in antenna impedance reactances causing a non-representative phase to be measured at the receiver end of the coaxial cable.

As the upgraded 8 channel data acquisition system was intended for use in interferometric studies, a zero beat frequency phase test signal facility was included in the design of the new equipment (see Section 2.6). At the beginning of each data acquisition, the phase delay through each receiver was measured. From these measurements, relative phase corrections could be determined and applied retrospectively to the data. Typical absolute and relative phase measurements from the bp920916 data set appear in Table 3.1. From the table it is apparent that a phase spread of 20° exists between receivers 2 and 4. This error may be removed by multiplying each point in the coherent time series by the appropriate complex correction factor for that particular receiver. (The factor is simply $e^{-i\phi_j}$, where ϕ_j is the phase difference measured between receiver j and receiver one.) It is of some interest to consider the variation of these phase measurements with time over the length of the bp920916 data set.

Figure 3.11 shows the phase propagation delay through receiver one as a function of time. Two aspects of the receiver's behaviour are noteworthy. The first is the apparent bimodal nature of the phase delay. This is caused by the change in IF gain setting from record

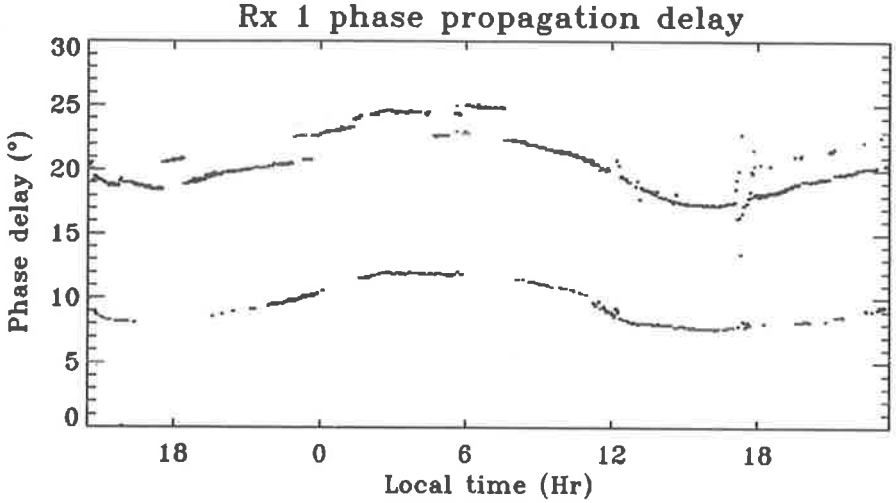

Figure 3.11: The phase propagation delay through receiver one during the bp920916 campaign. The lower trace varying between 8° and 12° is due to an IF gain setting of one, while the trace immediately above this varying between 17° and 23° is due to an IF gain setting of two. Note the temperature dependence of the phase propagation delay which exhibits a diurnal oscillation with a peak–to–peak amplitude of about 5°.

to record. As the strength of the backscattered echos increase or decrease, the computer automatically adjusts the receivers' IF gain such that during the next record, the signal strength will be within acceptable limits. At times this procedure causes the IF gain setting to oscillate between two values from record to record. At other times the IF gain setting is stable. Thus Figure 3.11 demonstrates that the receiver phase propagation delay is dependent upon the IF gain setting with adjacent gain steps producing phase changes of up to 10° in receiver one. The second aspect of note is the diurnal oscillation evident in the phase propagation delay for receiver one. This oscillation is caused by temperature variations in the main laboratory (which was not air–conditioned) with peaks in the phase propagation delay occurring during colder periods, and troughs occurring during the warmer periods. Interestingly, receivers one and seven are the only two to respond to temperature variations in this way as the other six receivers track the temperature in the opposite manner. In other words, assuming that the ambient temperature in the main laboratory can be modeled by a sinusoidal function, the phase propagation delays through receivers one and seven vary inversely to the ambient temperature, while the phase propagation delays through the remaining six receivers vary in proportion to the ambient temperature.

Angle of arrival information is ultimately derived from the phase differences between receiver pairs connected to spaced antennae on the ground. Any static difference in receiver

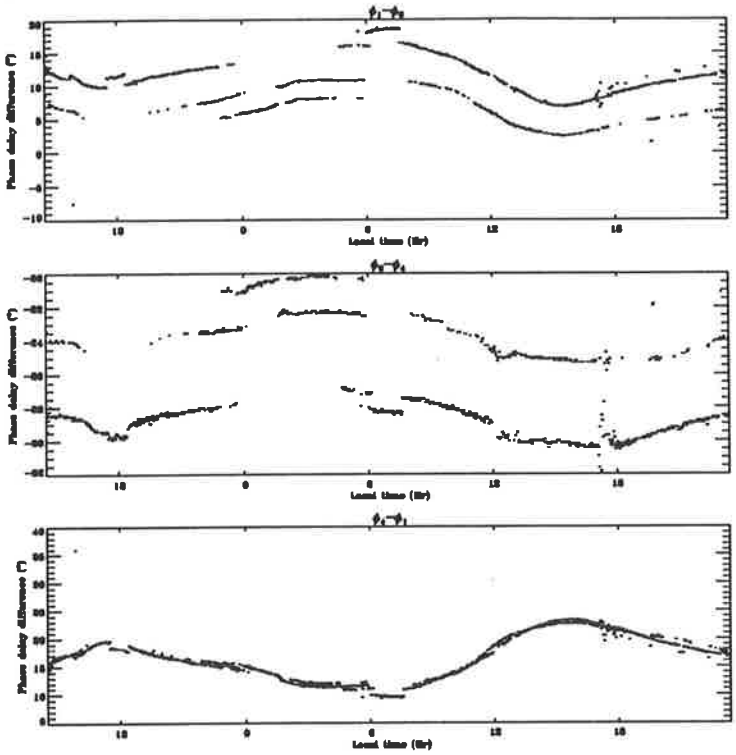

Figure 3.12: Differences in the phase propagation delays between receivers one, two and four one during the bp920916 campaign.

phase propagation will result in a systematic bias in the measured angle of arrival of incident radiation throughout the data set. Such a systematic bias may be easily removed by examining the distribution of receiver phase differences calculated from the entire data set and subtracting the offset of the distribution peak from the phase of each receiver (see Figure 3.15). This approach is pursued later in this chapter. It is clear, however, that if the phase propagation delay difference between two receivers is not static, then additional quasi–random errors will result. In order to establish the existence of this variation, we now examine the phase propagation delay differences between receiver pairs (1,2), (2,4) and (4,1). These appear as time series in Figure 3.12. Quite clearly the phase delay propagation differences between receivers are not constant, and if not removed represent a significant source of error in the analysis.

The data obtained from the bp920916 campaign were corrected by the appropriate phase factor (measured from the phase test signal applied every two minutes), and new daytime angle of arrival results were calculated. These appear in Figure 3.13. Although difficult to quantify from these figures, the mean off–zenith angle of scatter has been reduced with the use of the receiver phase test signal corrections. It is, however, quite clearly not reduced

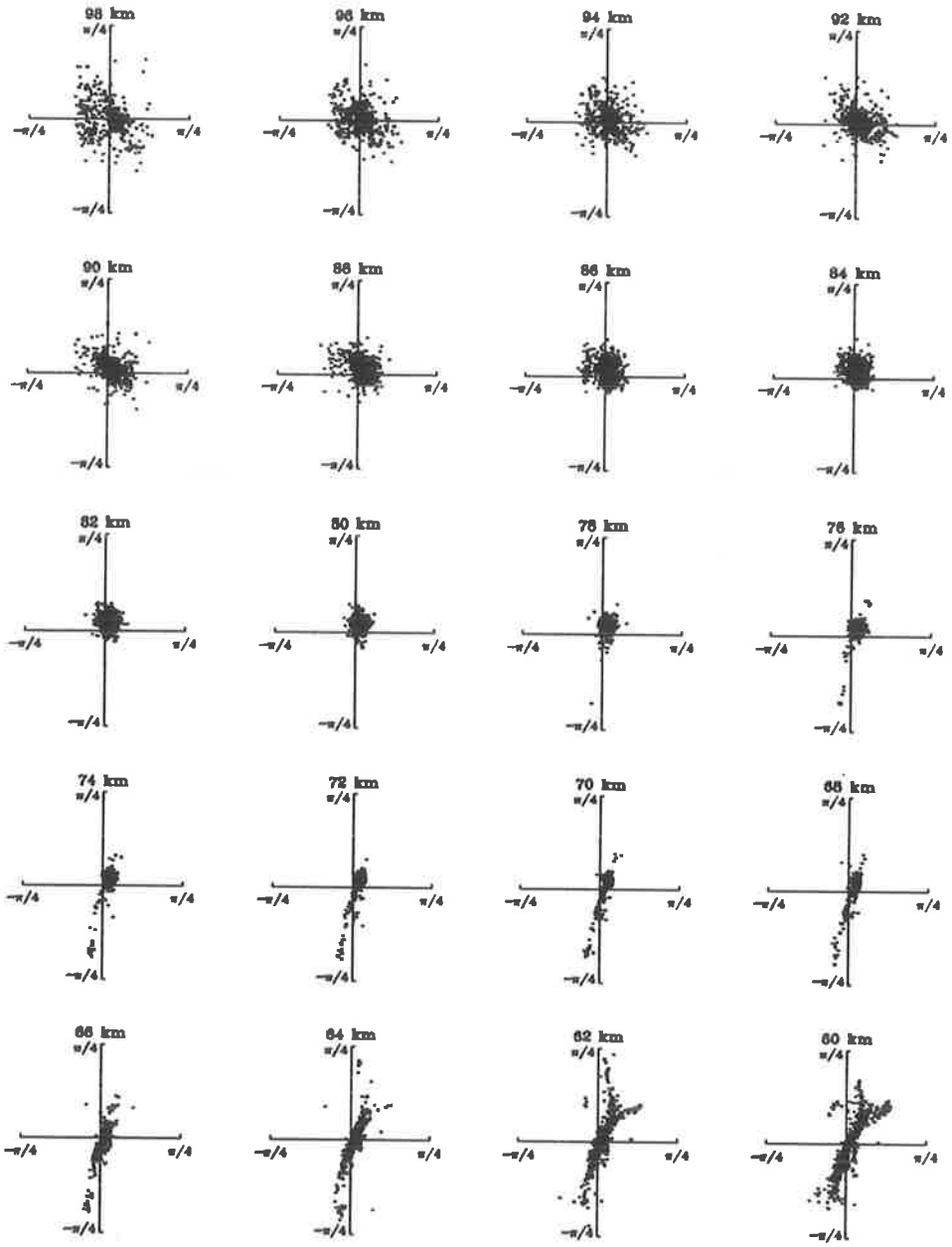

Figure 3.13: The mean angle of arrival of the bp920916 data set as calculated from receivers 1, 2 and 4 for daytime returns only. The receiver phase delay propagation differences are corrected for by means of the receiver phase correction test signal modifier obtained for each data record. As with Figure 3.10, no data have been rejected on the basis of low signal–to–noise ratio nor by any other criteria.

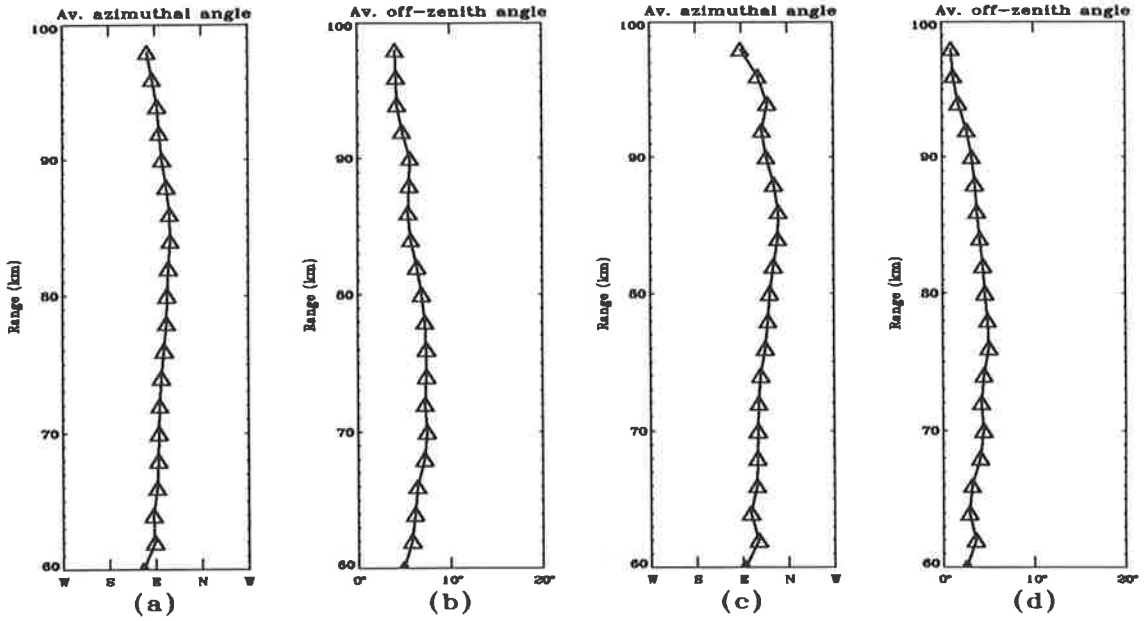

Figure 3.14: The mean angle of arrival of the bp920916 data set as calculated from receivers 1, 2 and 4 for daytime returns only. The mean azimuth and off–zenith angles for the uncorrected data appear in (a) and (b), while the receiver phase test signal corrected data appears in (c) and (d).

to zero. At this stage it is helpful to display the two sets of data as a profile of mean azimuth and off–zenith angle. Some care must be exercised when finding the mean of these sets of angle of arrivals as the (azimuth, off–zenith) coordinate system is non–linear. The angle of arrival information must be transformed back into the direction cosine coordinate system where, provided care is taken with circular statistics, a mean may be found. The mean direction cosines are then transformed back to the (azimuth, off–zenith) coordinate system and plotted in height profile form. The height profile of mean angle of arrival for the uncorrected data appears in Figures 3.14a and 3.14b, while the phase test corrected data appears in Figures 3.14c and 3.14d. Quite clearly, other sources of phase uncertainty contribute to this systematic off–zenith bias. Aside from transmitting a test signal from a known position in the far–field of the receiving array, the only possible method of removing this systematic phase error is to assume that the direction of incoming radiation, on average, is from the zenith. Scrutiny of Figures 3.10 and 3.13 reveals that the scatter does indeed tend to cluster about a direction in the sky. It seems reasonable to assume that over such a large length of time this cluster of points represents the zenith. At this point, some consideration must be given to the bi–static nature of the Buckland Park radar as configured for this experiment. Since the transmitting array was located some 770 m distant from the

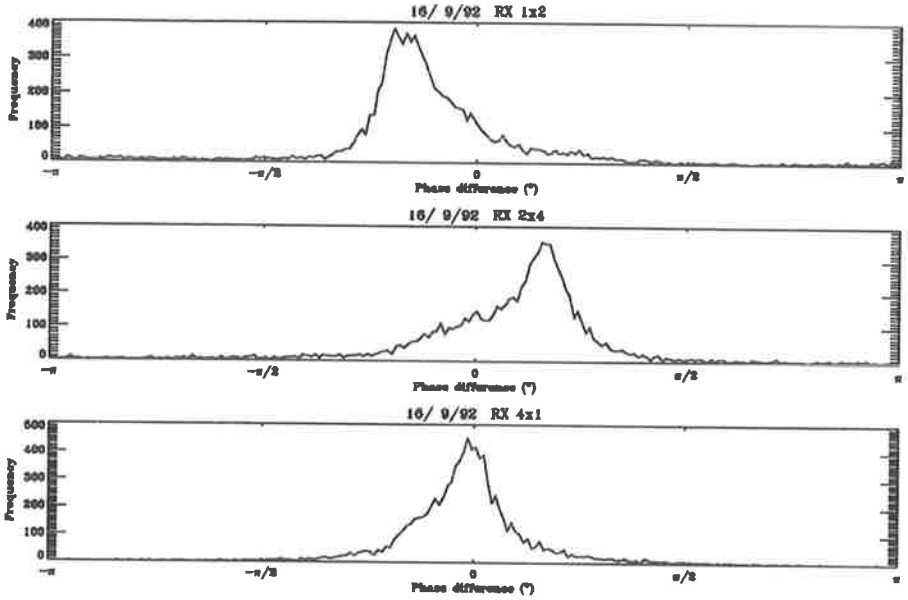

Figure 3.15: Histograms of cross–correlation phase at zero lag for the bp920916 data set. Data from all range gates are included in this figure, and has been corrected for variations in phase propagation delay. The histogram bin–size is 0.03 radians, or about 1.7°, yielding a total of 210 phase bins. Only daytime data is included. Note the asymmetry evident especially in the distribution for receiver pair (2,4).

receiving antennae selected, the backscattered signals sampled by the receiving system will not, on the average, have emanated from precisely the zenith. A brief consideration of the geometry of the experiment reveals, however, that the errors involved are negligibly small. The magnitude of the error in off–zenith angle ranges from 0.23° at 98 km, to 0.37° at 60 km, and is clearly insignificant when considered against the difficulties in making reliable interferometric measurements at MF.

If the raw cross–correlation phases at zero lag are examined it becomes clear that they, as well as the points in azimuth–off–zenith space, cluster about a certain value. By forming the histograms of the zero lag phases and selecting the most appropriate phase, all instrumental effects upon the measured phase differences may be removed. It remains to be determined, however, which phase is most appropriate. In Figure 3.15 the distributions of phase differences between the three receiver pairs are displayed. Clearly some asymmetry is evident, particularly in the distribution for receiver pair (2,4). Upon closer inspection it becomes evident that the main contribution to this asymmetry comes from the lowest few range gates, possibly from those ranges where incoherent noise begins to dominate the atmospheric returns. It seems logical, then, to exclude data from those ranges for which we expect appreciable non-zenith returns to occur. In addition to this exclusion, we may

conclude from further examination of Figure 3.13 that returns from the highest five or six range gates are more likely to come from larger off–zenith angles. This is due in part to the lower aspect sensitivity of the RF scatterers at higher altitudes, and in part to total reflections from "glints" in the E–layer (see Section 3.8). Thus, in order to best quantify the instrumental component of the receiver phase differences, we select those ranges for which the clustering of angle of arrival points is greatest. These ranges are those between, and including, 76 km and 86 km.

Once the distributions of the phase differences between the three receivers have been formed, some peak selection process must be carried out. Three methods are immediately apparent. These are:

- selection of the most probable phase difference (largest peak selection),
- calculation of the first moment of the distribution and
- fitting of some function to the data with the peak of the fitted function yielding the best phase difference estimate.

Given that the variations in the phase differences from their mean are randomly distributed, we expect that their functional form will be Gaussian in nature. Therefore, if the third option above is deemed appropriate, three fitted Gaussian functions will provide the three estimates of the instrumental bias.

In Figure 3.16 the three phase difference distributions obtained from range gates 76 km to 86 km are displayed with the three estimates of the instrumental phase zero marked. Note firstly that much of the asymmetry evident in Figure 3.15 has been eliminated. It is also quite apparent that the functional form of the phase difference distribution conforms remarkably well with that of the Gaussian distribution. In fact, the Gaussian fitted distribution appears to yield a very good estimate of the instrumental phase bias while, by comparison, both the most probable and first moment approach suffer from some inaccuracy. In the case of the first moment of the distribution, it appears to be weighted towards smaller absolute values of phase difference than an "eyeball" estimate would indicate was correct. This effect can be traced to the presence of noise in the distribution. Any noise will occur with equal likelihood at all phase difference values. Thus, if we separate the distribution into noise and noise–free components, the first moment of the noise distribution (by definition) will be zero, while that of the noise–free distribution will be the finite value which we require. By finding the

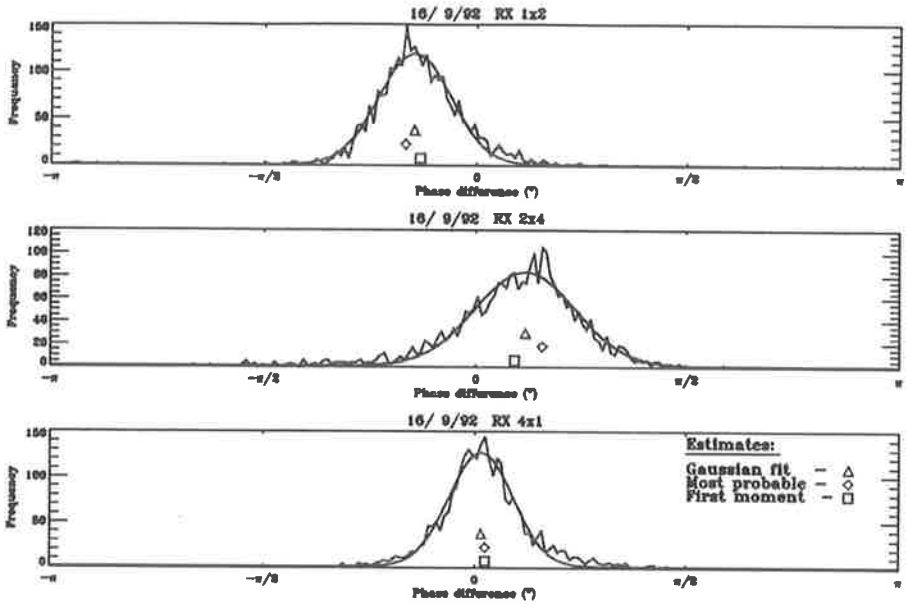

Figure 3.16: Fitted histograms of cross–correlation phase at zero lag for the bp920916 data set. Daytime data from range gates 76 km to 86 km only is included in this figure. The histogram bin–size is 0.03 radians, or about 1.7°, yielding a total of 210 phase bins. Only daytime data is included. Each histogram is fitted with a Gaussian function whose peak value is indicated relative to the ordinate axis by a $\triangle$. Also indicated on each distribution is the most–probable phase value, ($\diamond$) and the first moment of the distribution, ($\square$).

first moment of the complete distribution we are effectively finding the average of these two separately calculated moments. This value is clearly weighted away from the "correct" value towards zero.

The most probable peak estimator also seems unworkable when applied to experimental data. Inspection of the phase difference distribution for receivers 1 and 2 in Figure 3.16 shows that the peak of the distribution is susceptible to local "spikes". Thus, although the general trend of the distribution may have a centroid as indicated by the fitted Gaussian function, a neighbouring spike may in fact have a larger frequency of occurrence. This, if selected, would lead to an erroneous estimate of the instrumental phase bias.

Using the peaks of the Gaussian–fitted phase difference distributions, we find that the values of the three receiver pair's phase bias are (-24.6°, 21.0°, 2.6°). Table 3.2 sets out the phase differences measured by the three methods discussed above. We note that whatever the magnitude of the phase errors between the receiver pairs, the sum of the three error estimates should ideally be zero. It can be seen in Table 3.2 that the Gaussian fitting technique yields a sum of phase corrections which is the closest to zero of the three techniques.

We now apply the Gaussian fitted estimates of the instrumental phase difference bias

Table 3.2: The receiver phase difference biases as measured by Gaussian fitting, most probable peak selection and the first moment of the phase distribution.

Estimator	Rx 1x2	Rx 2x4	Rx 4x1
Gaussian fitting	-24.6°	21.0°	2.6°
Most probable peak	-30.1°	28.4°	4.3°
First moment	-24.0°	16.5°	4.3°

to the measurements of phase propagation delay corrected mean angle of arrival. This is done by simply subtracting the estimated phase bias from each of the three cross–correlation phases at zero lag for each angle of arrival measurement. Figures 3.17 and 3.18 display the corrected angle of arrivals for each range and in average profile form.

Note now that the scatter appears to be centred on the zenith, with average off–zenith angles of less than 1° being recorded at range gates 76, 78 and 80 km. Above and below these range gates, however, mean off–zenith angles of up to 5° are still observed. This observation would appear to be inconsistent with the expected behaviour of the scatterers at these altitudes. Since no data has yet been rejected on the basis of low signal–to–noise ratio, it seems likely that, at least in the lower range gates, this comparatively large mean off–zenith angle is due to poor signal levels. To investigate this possibility, the data were reprocessed with a signal–to–noise ratio rejection threshold set at -6 dB. Subsequent adjustment of this threshold to 0 dB yielded little improvement in data quality, and so the calculations produced by this second analysis are not presented here. In Figure 3.19 those records in the bp920916 data set which exhibit signal–to–noise ratios of less than -6 dB are displayed. Note that the ordinate axis is scaled in hours of local time, with a large discontinuity at nightfall at 18:14 (marked by an asterisk on the ordinate axis in Figure 3.19). This corresponds to the beginning of the large increase in rejections at range gates between 68 km and 76 km. Thus, some of these rejections occur in the late afternoon of the 16^{th} of September, while others occur in the early morning on the 17^{th}.

In Figure 3.20 the mean angle of arrivals of each record after low signal–to–noise ratio rejection are displayed. Note that no data are rejected from range gates above 76 km, and so no differences will be observed between Figures 3.17 and 3.20 in the upper range gates. It is clear, however, that a number of spurious returns have been eliminated in the lower 9 range gates. As can be seen in Figure 3.21b and 3.21d, the average off–zenith angle is unchanged by the signal–to–noise ratio rejection criterion above 76 km. Cursory examination of these two

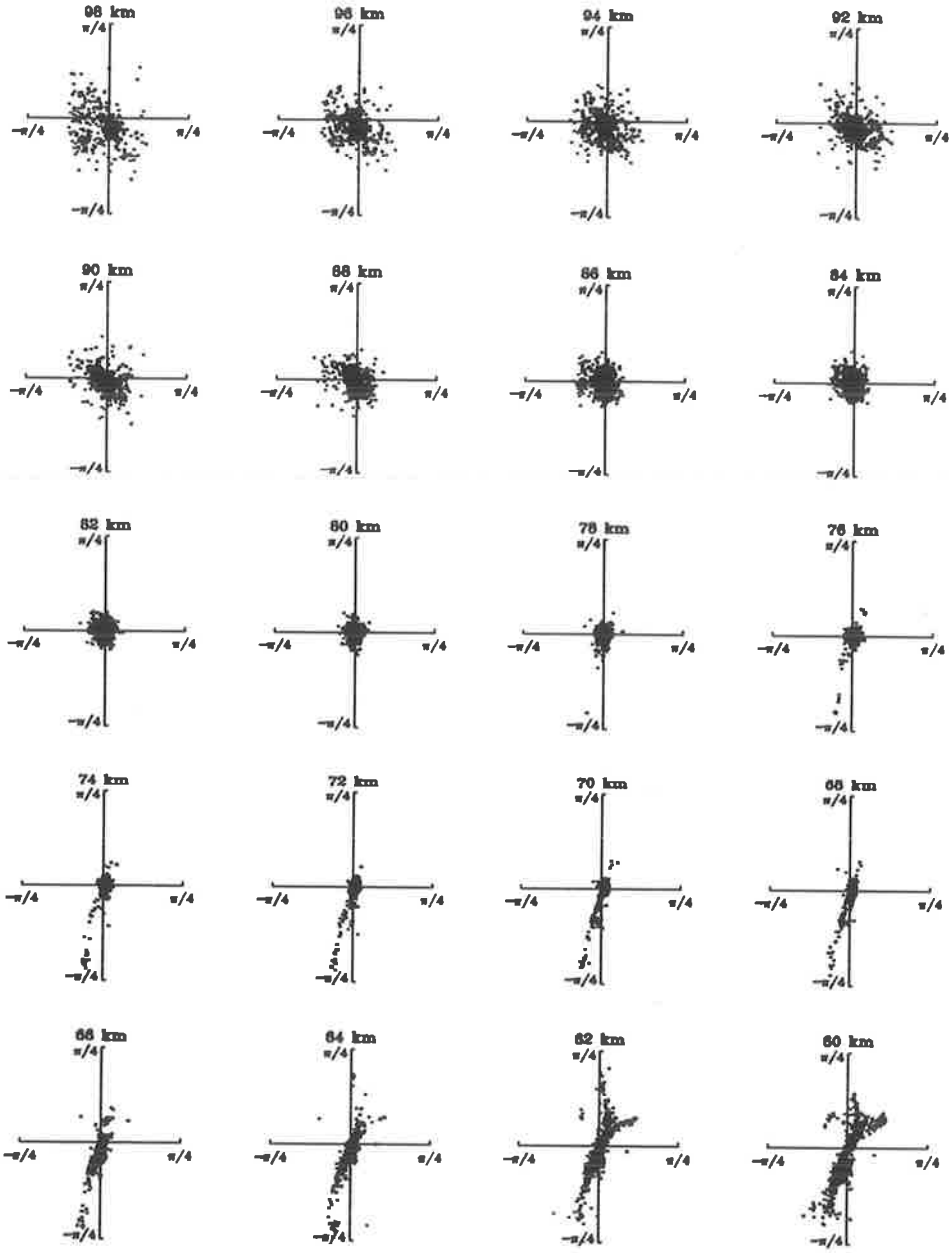

Figure 3.17: Mean angle of arrivals for the bp920916 data set as calculated from receivers 1, 2 and 4 for daytime returns only. The channel phase delay propagation differences are corrected for by means of fitted Gaussian functions to histograms of the phase propagation delay corrected receiver phase differences. Again, no data have been rejected on the basis of low signal–to–noise ratio.

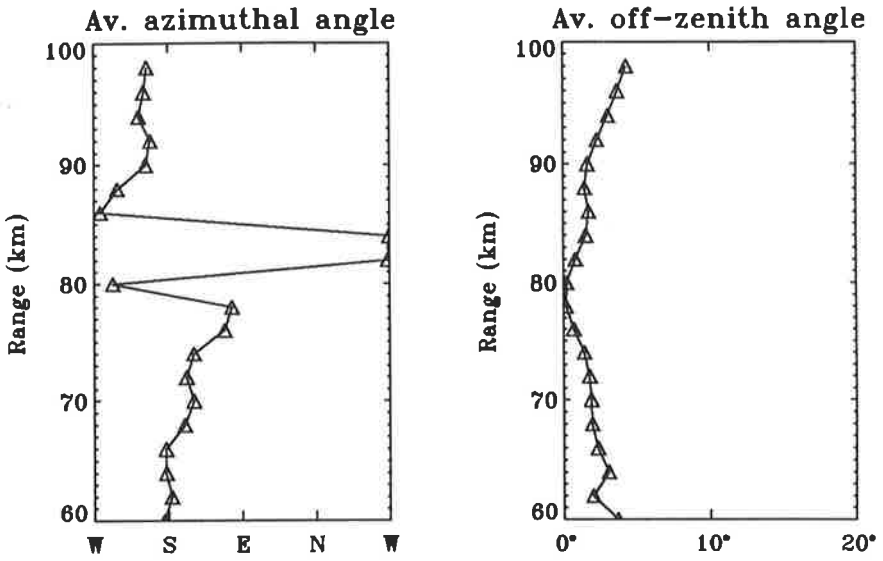

Figure 3.18: Profiles of the mean angle of arrival of the bp920916 data set as calculated from receivers 1, 2 and 4 for daytime returns only. Data has been corrected for instrumental bias by means of Gaussian fitted receiver phase difference histograms after the receiver phase propagation errors have been corrected for. Note that the apparent large jump in azimuth angle between range gates 80 km and 82 km is, in fact, merely a small change in azimuth from slightly South of West at 80 km, to slightly North of West at 82 km. No data have been rejected on the basis of low signal–to–noise ratio.

figures reveals a somewhat surprising feature. The average off–zenith angle for the signal–to–noise ratio filtered data at 60 km is, in fact, 3° larger than for the unfiltered data. In contrast to this behaviour, the off–zenith angle is an average of 0.4° smaller for the filtered data for the range gates between 64 km and 74 km. Thus we conclude that there may exist some strong and coherent source of interference in the lowest two range gates which dominates the atmospheric returns and is not removed by signal–to–noise ratio filtering. One candidate for such interference is sea scatter. Ocean waves have the unique property that each spatial scale of the wave moves with its own characteristic velocity, given to first order by

$$v = \sqrt{\frac{g}{k}}\,, \tag{3.18}$$

where g is the acceleration due to gravity and k is the spatial wavenumber of the ocean wave in question. Due to the Bragg scatter condition, those ocean wave spatial scales equal in size to one–half of the radar wavelength will dominate the returned signal. Thus, for the Buckland Park radar, we set

$$k = \frac{2\pi}{75.8} \tag{3.19}$$

in Equation 3.18 to find $v = 10.87$ ms^{-1}. Examination of the spectra displayed in Figure 3.37

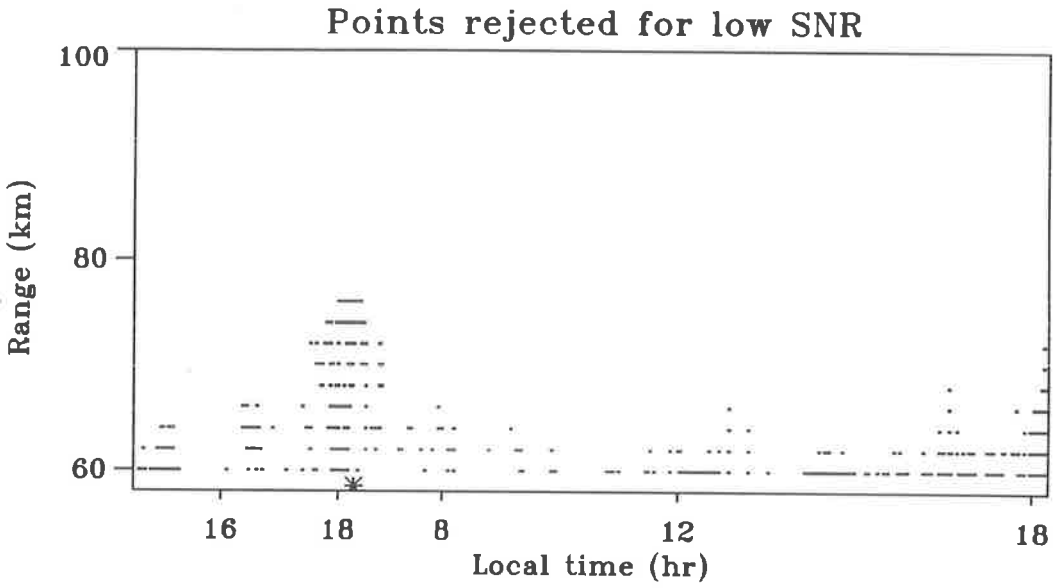

Figure 3.19: Low signal–to–noise ratio data rejection occurrences for the bp920916 data set. The signal–to–noise ratio rejection threshold has been set to -6 dB. Note that the ordinate axis is broken by a 12 hr discontinuity marked by an asterisk at 18:14 local time.

show a persistent sea scatter spectral peak at at positive Doppler shift of 0.147 Hz, or 11.1 ms^{-1}. Since the spectral resolution of the radar in the configuration used for this campaign is ± 0.005 Hz, the error in the sea scatter velocity estimate is ± 0.4 ms^{-1}. Thus the ocean wave velocity calculated from Equation 3.18 falls in this spectral "bin", and we conclude that these data are affected by sea scatter returns. This is not surprising given the extremely broad radiation pattern of the single half–wave dipoles used for reception in this experiment. Figure 3.22 shows an example of a single power spectrum recorded at a range of 66 km by receiver one near the start of the bp920916 campaign. The sea scatter peak is quite clearly visible at a Doppler shift of about +0.15 Hz. Note that unlike Figure 3.37 the power spectrum has not been displayed in logarithmic units, and so this example represents an extremely strong sea scatter signal.

Data affected by sea scatter are relatively easily corrected with the use of filtering techniques in the frequency domain. Since the sea scatter signal is restricted almost exclusively to a single Doppler "bin" it can be removed by one of several techniques. Spectra may simply be "notched" by setting the spectral amplitude of the frequency affected to zero. Alternatively, an average of the spectral amplitudes in the neighbouring frequency bins may be used to replace the sea–scatter contaminated frequency. This technique has the advantage that it may be applied to all range gates with minimal adverse effect on those range gates which

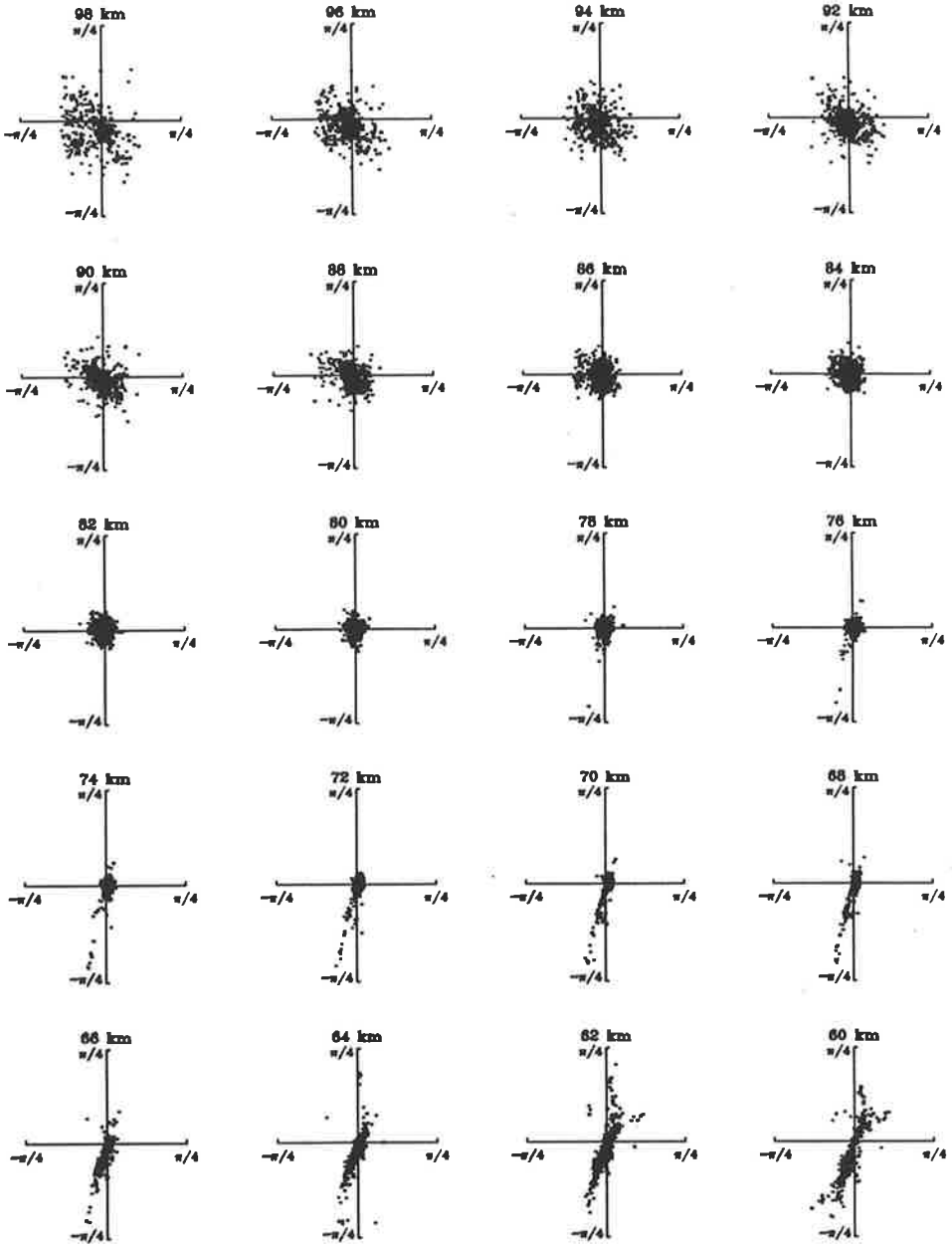

Figure 3.20: Mean angle of arrivals for the bp920916 data set as calculated from receivers 1, 2 and 4 for daytime returns only. The channel phase delay propagation differences are corrected for by means of fitted Gaussian functions to histograms of the receiver phase differences after phase propagation correction, and after records exhibiting signal-to-noise ratios of less than -6 dB have been rejected.

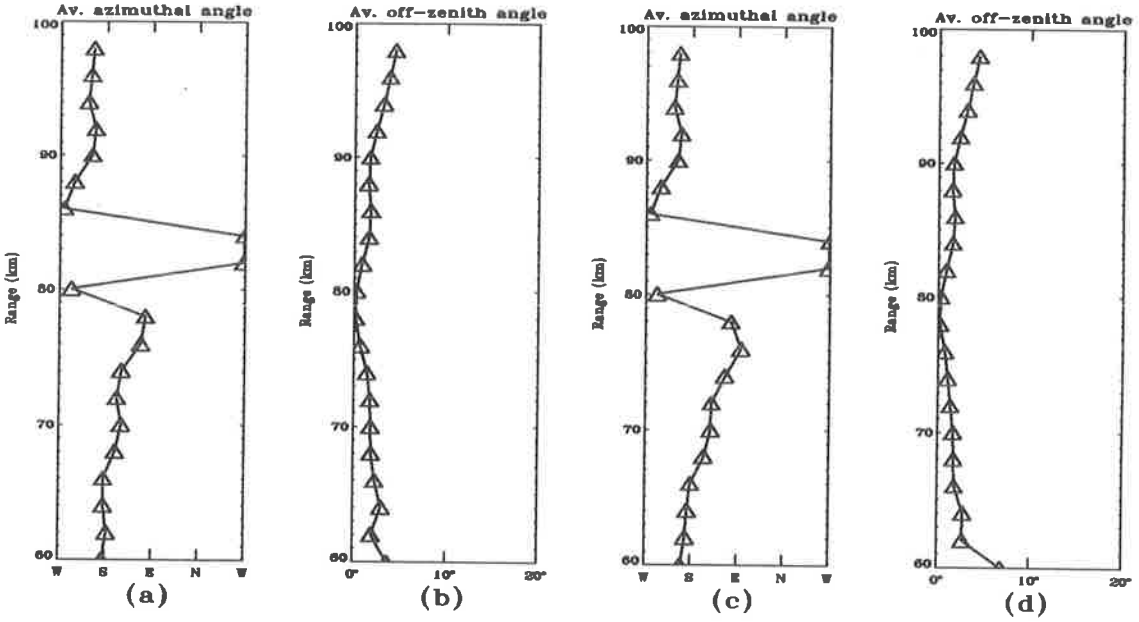

Figure 3.21: Profiles of average angle of arrival for no signal–to–noise ratio rejection; (a) and (b), and for a signal–to–noise ratio rejection threshold of -6 dB; (c) and (d). No rejections occur above the 76 km range gate.

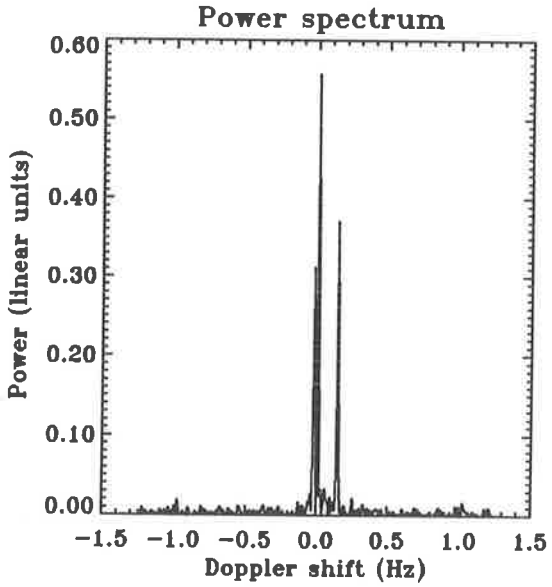

Figure 3.22: A typical sea scatter signal recorded at a range of 66 km by receiver one. This particular record was taken in mid–afternoon near the start of the bp920916 campaign. Note that the spectrum is scaled in linear units and thus displays a strong sea scatter signal at 0.15 Hz. The atmospheric returns are visible near zero Doppler shift.

are free from the sea scatter contamination. For this reason the data were reanalysed using the local spectral averaging technique to remove the sea–scatter signal and new mean angle of arrival results found.

In Figure 3.23 sea–scatter filtered mean angle of arrivals are displayed in the usual form. It is clear that a large number of spurious returns have been removed from the lower eight range gates when this figure is compared to Figure 3.20. Note that the -6 dB signal–to–noise ratio rejection threshold has also been applied to the sea–scatter filtered data. It appears that majority of these sea scatter returns are located on these polar sky map diagrams in the South–Western quadrant at off–zenith angles of up to 40°. Recalling that these calculated angle of arrivals represent mean arrival directions weighted by signal power, it is not surprising that sea scatter contamination would tend to weight the measurement of angle of arrival away from the zenith towards the source of the sea scatter signal. In the case of the Buckland Park field site, the only ocean existing at ranges of 60 km to 70 km lies towards the South to South–West. The persistence of scattering points at large off–zenith angles in the lower range gates of Figure 3.23 in areas where sea–scatter filtering has removed most spurious signals seems to indicate that some sea scatter signals are "leaking" into adjacent spectral bins. This is possible since the sea scatter signal is not located in the centre of the 0.147 Hz Doppler frequency bin and may, in fact, vary its Doppler shift as the ocean waves are superimposed upon a mean sea surface current. Some evidence of this spectral leakage is visible in the power spectra, but further efforts to reduce the contaminating effect of sea scatter are not pursued at this point.

It is of some interest to compare the profiles of mean azimuth and off–zenith angle of arrival for sea scatter filtered data and data for which sea scatter has not been removed. In Figure 3.24 these profiles are displayed showing the marked reduction in mean off–zenith angle in the lower five range gates for the sea–scatter filtered data. Quite clearly the sea–scatter signal has a contaminating effect in the lowest five range gates. In order to more closely examine the effect that sea–scatter filtering has upon the mean off–zenith angle profile, Figure 3.25 displays the difference between the two profiles in Figure 3.24b and d. Note that positive values in Figure 3.25 indicate that the sea–scatter filtered off–zenith angles are closer to the zenith than the non–filtered data, and that negative values indicate the converse. This diagram indicates that sea scatter contamination begins to influence the angle of arrival measurement from 72 km in range downwards, with the effect becoming progressively more severe with decreasing altitude. Small deviations of less than 0.1° are

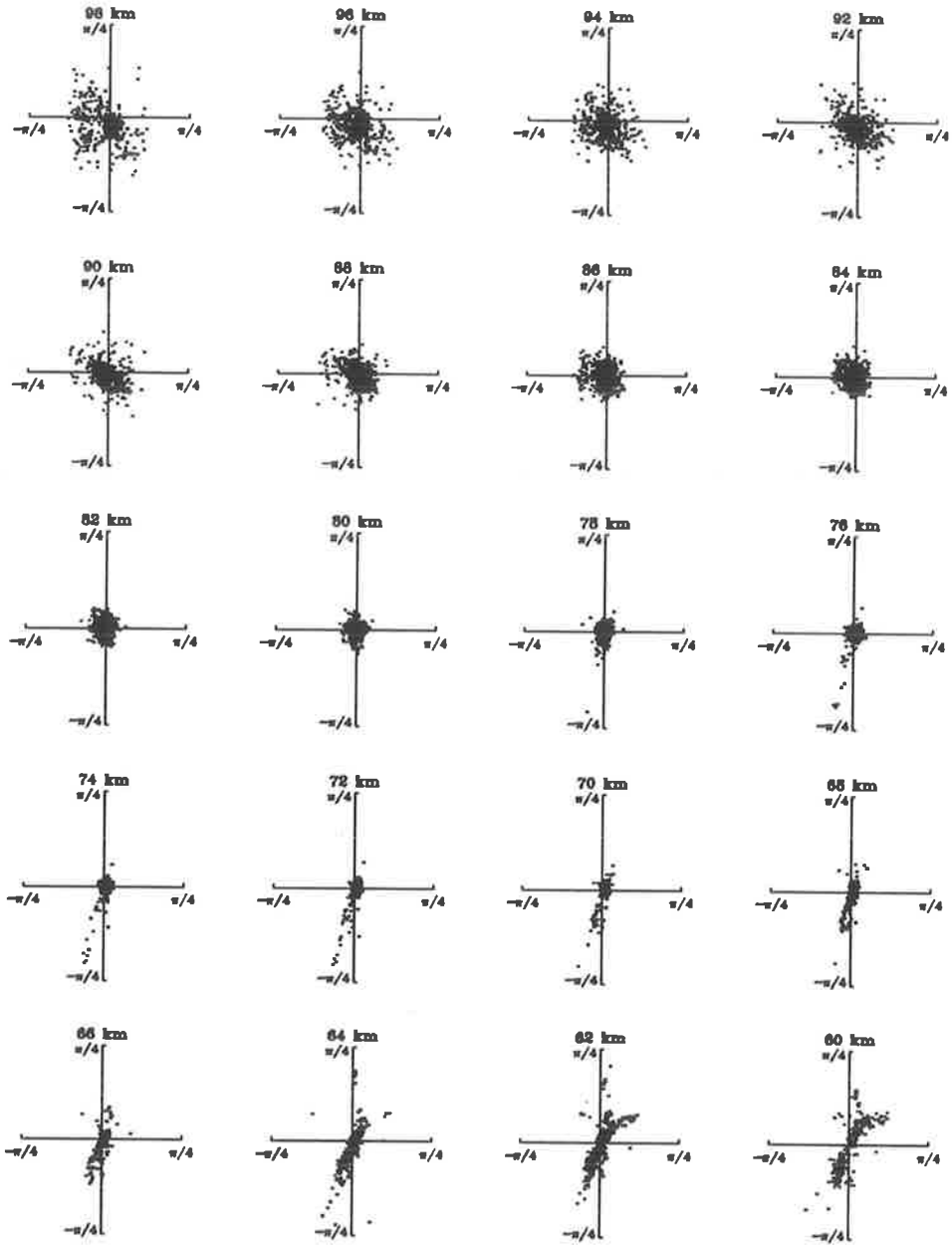

Figure 3.23: Mean angle of arrivals for the bp920916 data set as calculated from receivers 1, 2 and 4 for daytime returns only. Sea scatter signals have been removed by filtering in the frequency domain. The channel phase delay propagation differences are corrected for by means of fitted Gaussian functions to histograms of the receiver phase differences after records exhibiting signal–to–noise ratios of less than -6 dB have been rejected.

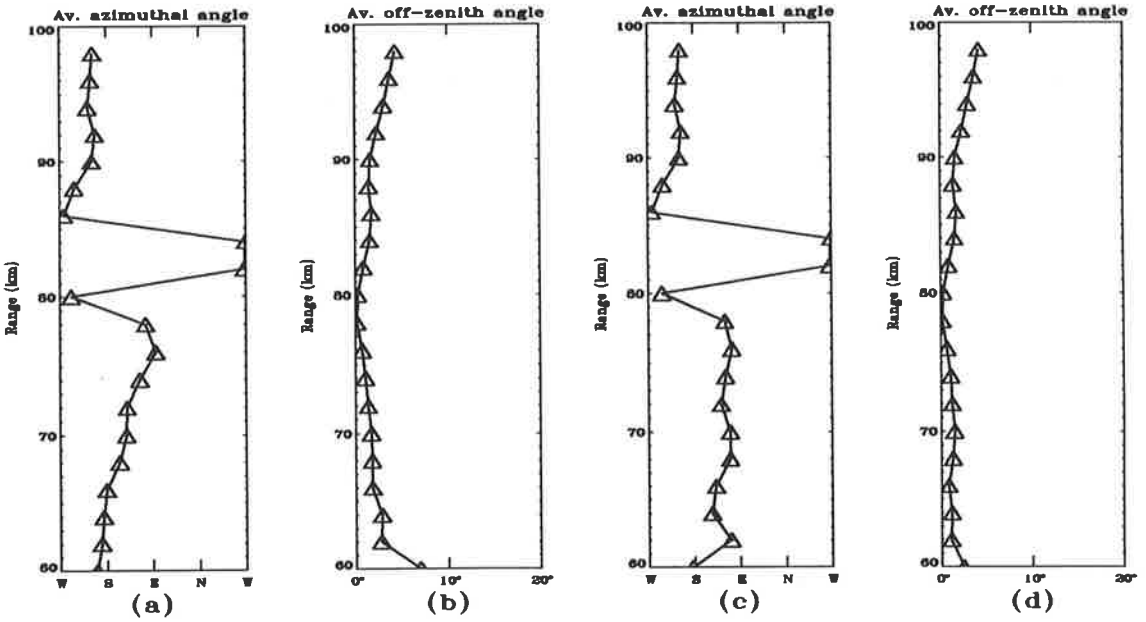

Figure 3.24: Profiles of average angle of arrival for data with no sea scatter filtering; (a) and (b), and for data subjected to frequency domain sea–scatter removal; (c) and (d). For both data sets the -6 dB signal–to–noise ratio rejection criterion has been applied.

also evident in the highest two range gates, but these can be considered as small statistical fluctuations.

Re–examination of Figure 3.23 reveals that, although the mean off–zenith angle of arrival in the lowest four range gates is small, individual points stray from the zenith by as much as 25°. It so happens that these points are fairly evenly distributed on a line extending either side of the zenith and, on average, are centred on the zenith. This tendency for the angle of arrival points to be clustered about a line extending from the South–South–West to the North–North–East is somewhat suggestive of an instrumental effect. Since receivers one and two are connected to antennae lying near this line, it would not be surprising to find that the distribution of average phase differences for this receiver pair did not conform to a Gaussian shape. Figure 3.26 clearly shows that this is the case and may be contrasted with the functional forms displayed by the receiver phase difference distributions depicted in Figure 3.16. Although all of these phases are calculated from records with signal–to–noise ratios in excess of -6 dB, it is difficult to accept that this effect is not due to some form of interference. Note, however, that the phase difference distribution displayed by receiver pair (4,1) in Figure 3.26 has a readily recognizable form not unlike that found at mid–range altitudes.

Considerable effort has been concentrated on ascertaining the cause of this odd clustering

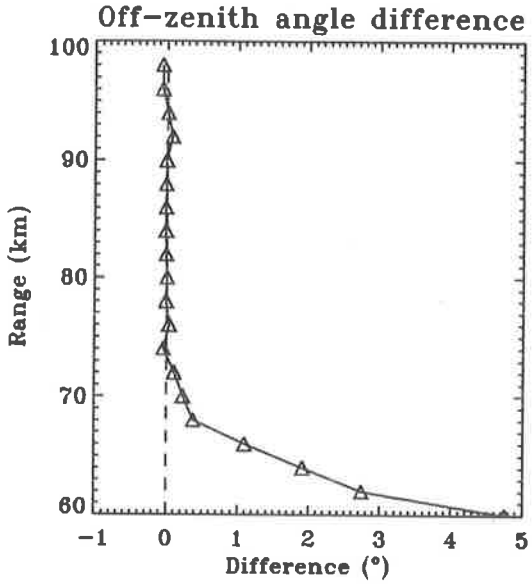

Figure 3.25: Profile of difference between average off–zenith angle calculated from data without sea–scatter filtering and with sea–scatter filtering. Positive values indicate that the sea–scatter filtered measurements lie nearer the zenith, while negative values indicate the converse. Note that sea scatter contamination becomes worse with decreasing altitude.

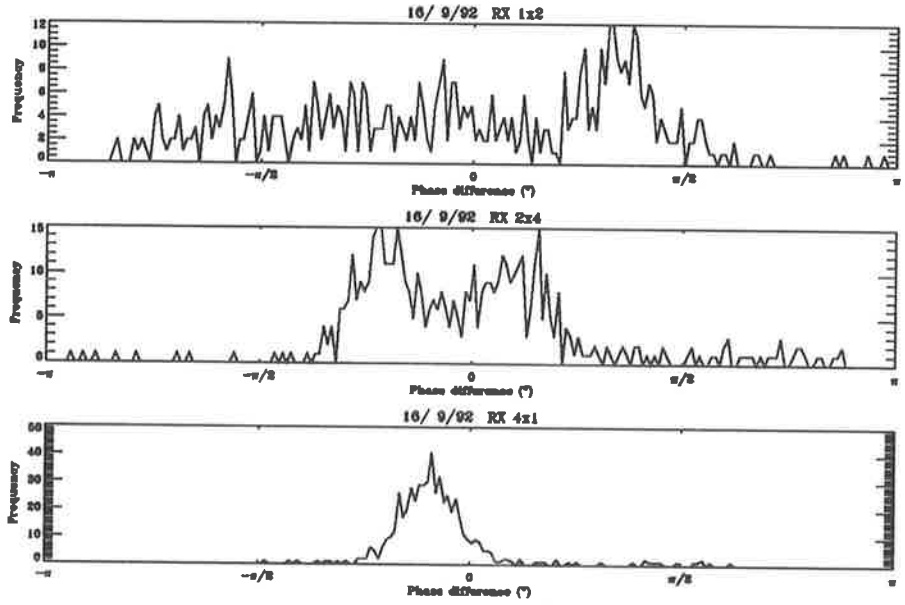

Figure 3.26: Phase difference distributions for the three receiver pairs calculated from the lowest two range gates (60 km and 62 km). Note the absence of any functional form in the distribution for the receiver pair (1, 2) which gives rise to the skewness in the angle of arrival polar sky maps for these altitudes.

of angle of arrival points about the South–South–West to the North–North–East line at low altitude. Although providing greater understanding of other features of the analysis, these efforts have yielded no further progress in elimination of these (presumably anomalous) points. It is interesting to note that not only do these points satisfy the minimum signal–to–noise ratio criterion, but they also satisfy any reasonable normalized phase discrepancy test. Rejecting data on a NPD level of 0.3 and above seems only to "thin out" the angle of arrival points with little preference for position in the sky.

Before moving on to discuss the deviation of the mean angle of arrival measurements from the zenith at higher altitudes, we pause briefly to consider one consequence of a frequently applied analysis technique. The technique in question is that of subtracting the mean of the sampled time series of receiver voltages before calculating correlation functions or spectra. The assumption used in most analysis of atmospheric returns is that the in–phase and quadrature components of the sampled time series are normally distributed with zero mean. There are, however, three situations in which the mean of the time series may be non–zero. These are

- hardware related offsets caused by poorly adjusted signal processors,
- specular atmospheric returns from stable stratified layers and
- non–fading returns from ground clutter.

Clearly evident in the data from the bp920916 campaign is a progressively larger mean offset of the sampled time series with decreasing range gate. Since large amplitude specular atmospheric returns are not observed at altitudes below about 66 km with MF radars, and because hardware induced mean offsets are identical in amplitude at all range gates, it seems clear that this mean offset is due to ground clutter. In fact, if the mean angle of arrival is calculated for this data without removing the mean of the time series, then the consistency of the result at 60 km is remarkable. Figure 3.27 depicts the apparent angle of arrival of the mean offset of the sampled time series. Note that 464 points representing 15 hr of data (spanning a total of 33 hr) are tightly clustered about an azimuth[3] of 30° and an off–zenith angle of 30°. Assuming that this return emanates from an off–zenith angle of nearly 90°, then it is possible to remove the angle of arrival ambiguity to find that the true angle of arrival is probably from -19.6° in azimuth. While it is not possible to uniquely determine the

[3]The azimuth angle here is defined in an anti–clockwise sense with Eastward corresponding to 0°.

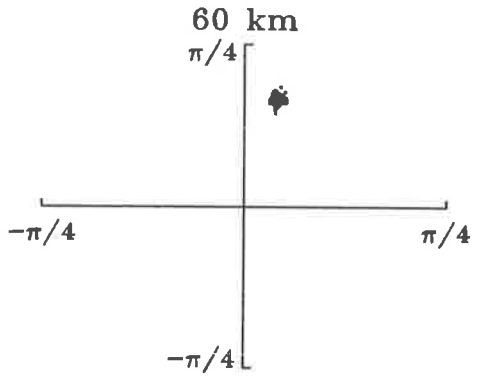

Figure 3.27: The angle of arrival of the ground clutter signal at 60 km. These are calculated from sampled time series whose mean has not been removed. Note that the tight cluster of arrivals to the North–North–East contains 464 data points. These, when remapped to remove angle of arrival ambiguity, appear to emanate from an azimuth of -19.6°.

feature responsible for this strong ground clutter echo, it is clear that there exist a number of candidates in the area identified by the interferometric analysis. These include two local peaks in the Mount Lofty Range, an electrical transmission line nearly aligned with the radar line–of–sight, a ridge line at right angles to the radar line–of–sight and a water supply dam. Any one, or any combination of these could be responsible for the ground clutter echo. It is interesting to note that if future plans to analyse back–scattered signals from lower range gates are pursued, ground clutter from Mount Lofty, the highest peak in the range, may represent a challenge.

We now consider the tendency for the average angle of arrival from higher range gates to come from larger off–zenith angles. Alhtough the mean off–zenith angle is about 2° at 90 km in range, it uniformly increases to about 5° at 98 km. It again seems unlikely that an average tilt of this magnitude could be sustained in the atmosphere over this length of time. Examination of Figure 3.23 reveals a large number of points at large off–zenith angles in the Western half–plane in the upper three range gates. Since we expect total reflection echos, or "glints", to be observed occasionally at these altitudes, it is not surprising to find larger off–zenith angles of arrival in these records. There exists an increased possibility that at these altitudes multiple interfering scattering points may occur, yielding mean angle of arrival measurements not associated with atmospheric motion. It seems likely that some, if not all, of these spurious returns will not satisfy the normalized phase discrepancy condition (NPD), as the radiation returned from such multiple reflection points could hardly be described as a "plane wave." Thus we now invoke the NPD criterion to further filter the angle of arrival measurements in an attempt to remove E–region total reflection effects.

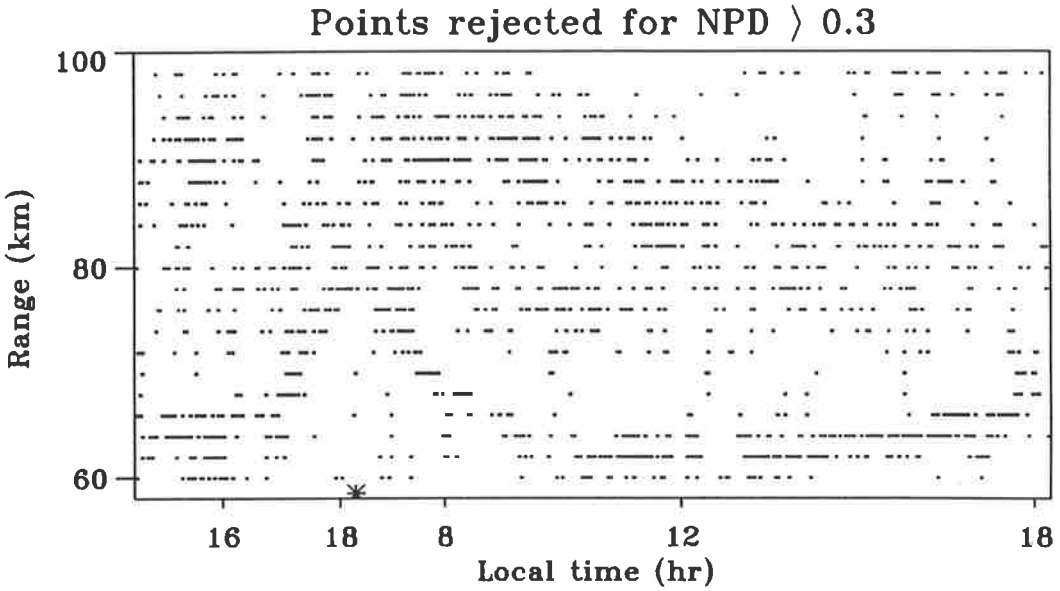

Figure 3.28: Poor normalized phase discrepancy data rejection occurrences for the bp920916 data set. The NPD rejection threshold has been set to 0.3. Note that the ordinate axis is broken by a 12 hr discontinuity marked by an asterisk at 18:14 local time.

In Figure 3.28 those data with signal–to–noise ratios in excess of -6 dB but not satisfying a NPD rejection threshold of 0.3 are displayed. The data have also been subjected to the frequency–domain filtering of sea scatter signal as discussed above. Note that there does not seem to be any preferential height or region for NPD rejection. There is, perhaps, a reduced likelihood of rejection around the 70 km range gate, corresponding to a region in which slowly fading stable echos are often observed. It appears that the occurrences of NPD rejection are also "patchy" in nature. In fact these rejections occur near those points that have already been rejected on the basis of low signal–to–noise ratio. It may be that the NPD rejection criterion is a useful counterpart to the low signal–to–noise ratio rejection criterion, removing those spurious points with appreciable signal strength, but little information. For the most part it is apparent that the NPD rejections occur in groups extended in range. This may indicate that the atmosphere is more disturbed during those periods than during other, "quiet" periods. As has already been stated, however, the use of the NPD rejection criterion does not seem to preferentially reject points lying far from the zenith and, in particular, it does not eliminate those points lying in the Western half plane at larger off–zenith angles.

A more detailed investigation of these points lying at large off–zenith angles in the upper few range gates shows that, in many cases, several anomalous points occur in succession. Calculation of the power spectra associated with these particular records demonstrates that

they are often composed of a single dominant frequency. It seems possible that these sequences of anomalous returns may be caused by a single reflection point, or "glint" moving either with the background wind or, more probably, tracking the phase speed of a gravity wave. Tracking these targets is the object of the following section.

3.8 Discrete Target Tracking

An interesting method of enhancing various persistent spectral features in atmospheric backscatter data was first implemented by *Röttger* [1980*a*] using the SOUSY[4] VHF radar in 1977. The technique involves forming the power spectrum of the time series of each record, and displaying these in spectra–intensity form. Thus, the frequency axis of the spectra is displayed on the abscissa, and the temporal axis is displayed as the ordinate. The power at each spectral frequency is represented by varying colours or intensities, with the more intense returns displayed with the brightest colour. In Figure 3.29 the power spectra for receiver one at a range gate of 98 km are presented for the entire bp920916 data campaign.

Note the tendency for the stronger returns to move from positive to negative Doppler shift with increasing time. This is a common feature between power spectra recorded from the highest range gates, and is easily explained in terms of geometrical arguments. If we consider a long–lived scattering centre being advected over a radar by some mean wind, it is quite apparent that as the scatterer comes into the radar's field of view that it will possess a positive Doppler shift since the scatterer must be moving toward the radar. As the scatterer moves overhead, or as the scatterer's line–of–sight velocity crosses through zero, the Doppler shift associated with the scatterer will also pass through zero. Finally, the scatterer moves away from the radar producing a negative Doppler shift. Therefore this feature is entirely consistent with enhanced regions of scatter moving through the radar's field of view. Note that at lower range gates, clearly defined scattering regions are not evident in the power spectra, which is indicative of a volume scattering situation. Possible mechanisms for these E–region echoes include scatter from "blobs" of enhanced electron density, ripples in the E–layer advected with the mean wind, and "glints" from gravity wave phase fronts.

Given that these echoes emanate from localized, well–defined discrete targets, we would expect that, at least in some instances, they could be tracked by means outlined in the previous section. Since the angle of arrival information calculated from the time series forms

[4]Sounding System

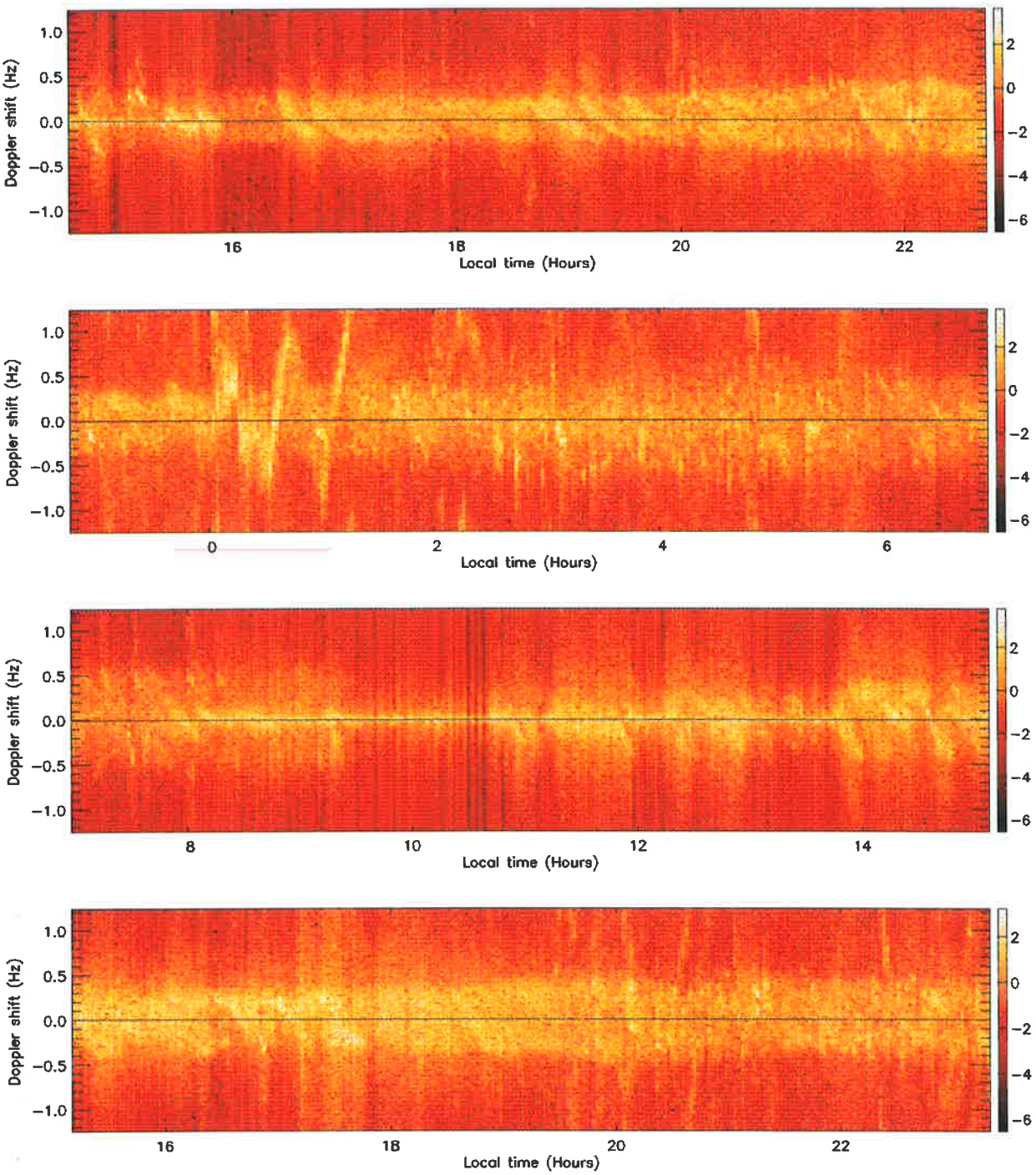

Figure 3.29: A running time–series of spectra–intensity plots for receiver one at a range gate of 98 km for the complete bp920916 campaign. Note the tendency for the more powerful returns to change from positive to negative frequencies in time. Night–time data should be ignored as the incorrect circular polarization was transmitted. (Hence disregard wild Doppler variations especially around 24 hr local time.) The power–intensity scale is indicated by the scale bar to the right of the plot in units of dB. The time scale is marked in local hours starting from 14:32 on 16/9/92 and ending at 23:25 on 17/9/92.

only a mean direction, competing signals may, at times, cause the calculated target track to deviate from that expected. We can, however, perform the study on a case–by–case basis.

The first instance of discrete target motion discernible in the bp920916 spectral records occurs at 15:26 local time on the 16^{th} of September, 1992. Figure 3.30 depicts a total of seven power spectra in the same format as Figure 3.29. A total of 14 min of data is shown. Over this period the peak of the power spectrum can clearly be seen moving from a positive Doppler shift of about 0.1 Hz, through zero Doppler shift, and on into negative Doppler shifts of about -0.05 Hz. This corresponds to line–of–sight velocities of about 7.5 ms^{-1} to -3.7 ms^{-1} respectively. It is also evident from the figure that the rate at which the Doppler shift is changing is decreasing: the Doppler shift falls rapidly from +0.1 Hz towards zero Hz, but then less rapidly to more negative Doppler shifts. Given that a discrete target was responsible for this echo, we would expect that its position in the sky would change rapidly at first, but then "slow down" and converge to some point. Examination of the angle of arrival information for these seven data records shows that this behaviour does indeed occur. Figure 3.31a displays the seven points on a polar sky map with the first of these marked with the symbol "▫", and subsequent points linked with a line, while Figure 3.31b displays the radial velocity associated with each of the angle of arrival points. The averaged spaced antenna estimate of the mean wind over these 14 min was aligned with the direction of motion of the discrete scatterer and had a magnitude of 55 ms^{-1}.

The second case of discrete target identification occurred at 19:08 on 16/9/92. This is an especially interesting case due to certain features in the power spectra. Inspection of the nine power spectra displayed in Figure 3.32 again reveals a general trend from positive to negative Doppler frequencies, but also indicates that there exist, at times, multiple reflection points at discrete Doppler frequencies. *Vincent* [1972] attempted to explain the corresponding features in his phase–path measurements in terms of distortions in the totally–reflective E–layer. In Figure 3.34 we see a symmetrical ripple in the E–layer being advected over the radar producing three "glints". These three reflection points will each have a distinct Doppler shift associated with it, with the two off–vertical reflections' Doppler shifts being equal but opposite in sign. This, of course, only occurs when the ripple is directly overhead. While the ripple is centred at some off–zenith angle, only one reflection point will be visible, and this will possess a finite, non–zero Doppler shift. As with all discrete targets, this Doppler shift will be positive to begin with, and negative as the ripple recedes from the radar. Figure 3.32 shows this behaviour remarkably well, with three reflections of distinct Doppler shift visible

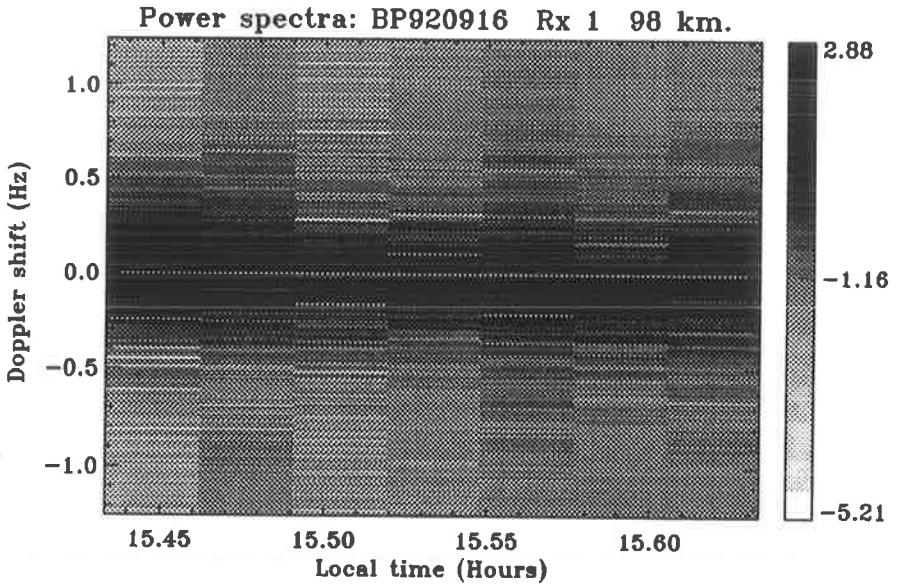

Figure 3.30: The seven power spectra for discrete target tracking case 1. Note the rapid decrease in Doppler shift through the first few spectra and the subsequent stabilization in frequency.

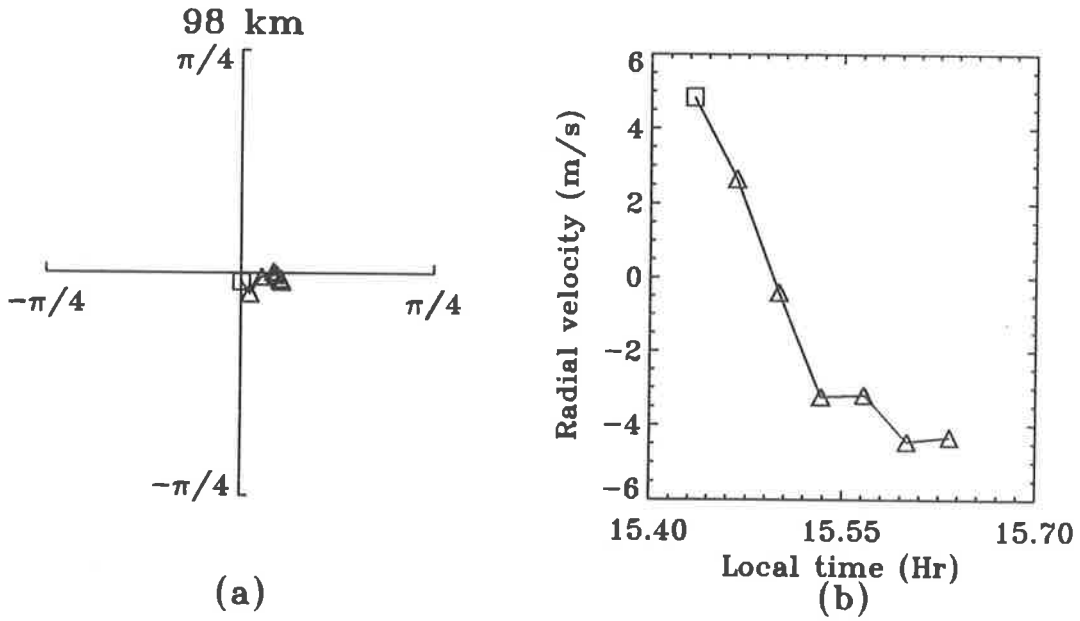

Figure 3.31: (a) The angle of arrival information for the seven power spectra displayed in Figure 3.30. (b) The average radial velocity associated with each of the seven angle of arrival points in (a). The first point in time is labeled with the symbol "□", while the remainder are labeled with triangles. Note the decrease in the spacing between points with increasing time.

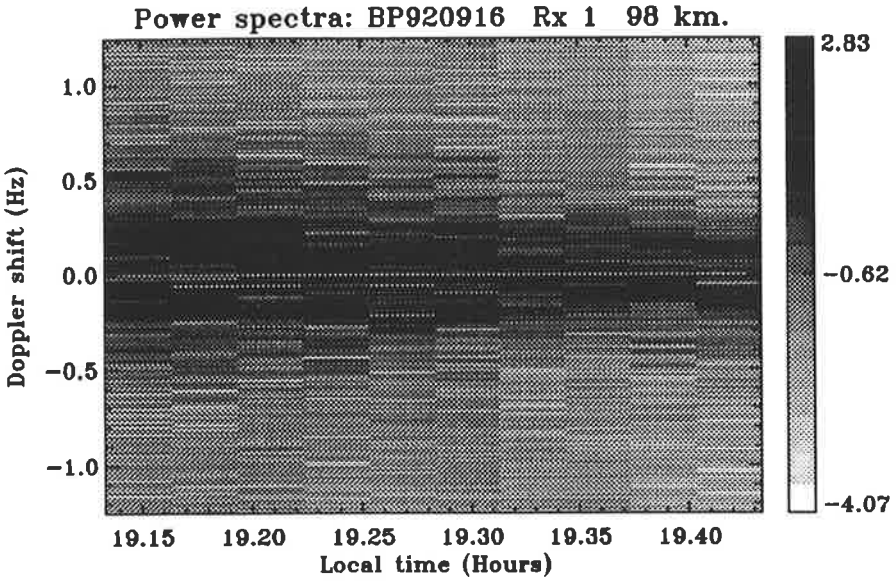

Figure 3.32: The ten power spectra for discrete target tracking case 2. Note the even decrease in Doppler shift through the ten spectra, and the triple reflection point evident at the mid–point of the record.

near the centre of the record. The true physical situation is more complicated than this, of course, and it is difficult to visualize a process by which reflections from significant off–zenith angles might result. Possible mechanisms include

- traveling disturbances in iso–ionic contours tilted at right angles to the radar's line of sight,
- highly localized wave packets resulting in reflections from "edge effects" and
- small moving regions of enhanced ionization with low aspect sensitivity.

The angle of arrival information for these ten spectra is displayed in Figure 3.33a. Note that in this case, the reflection points are reasonably evenly spaced in the sky. This correlates well with the constant peak spectral power slope evident in Figure 3.32. Again, the averaged spaced antenna estimate of the mean wind over these 20 min was aligned with the direction of motion of the discrete scatterer, and had a magnitude of 21 ms^{-1}.

The third case of discrete target motion discernible in the bp920916 spectral records occurs at 16:24 local time on the 16^{th} of September, 1992. Figure 3.35 depicts a total of eight power spectra in the same format as Figure 3.29. A total of 16 min of data is shown. In this case the peak of the power spectrum moves from a positive Doppler shift of about 0.28 Hz in a fairly linear way to a negative Doppler shift of about -0.15 Hz. This

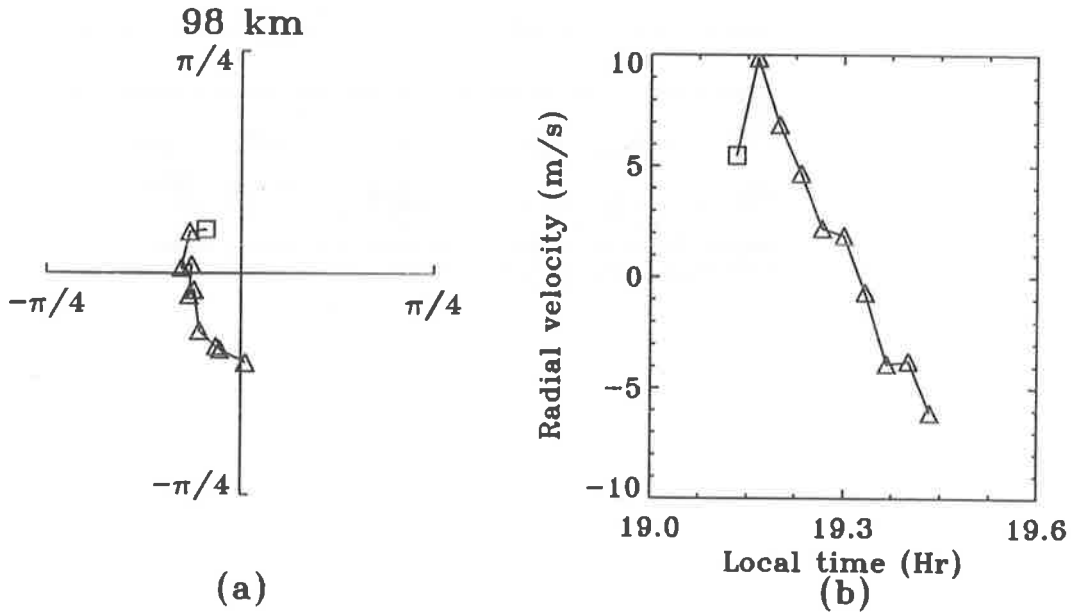

Figure 3.33: (a) The angle of arrival information for the ten power spectra displayed in Figure 3.32. (b) The average radial velocity associated with each of the ten angle of arrival points in (a). The first point in time is labeled with the symbol "□", while the remainder are labeled with triangles. Note the even spacing between points with increasing time.

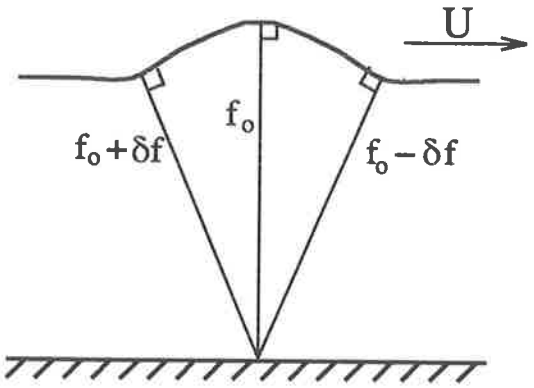

Figure 3.34: A model of the three reflections from an E–layer ripple advected through the radar's field of view. (After *Vincent* [1972].)

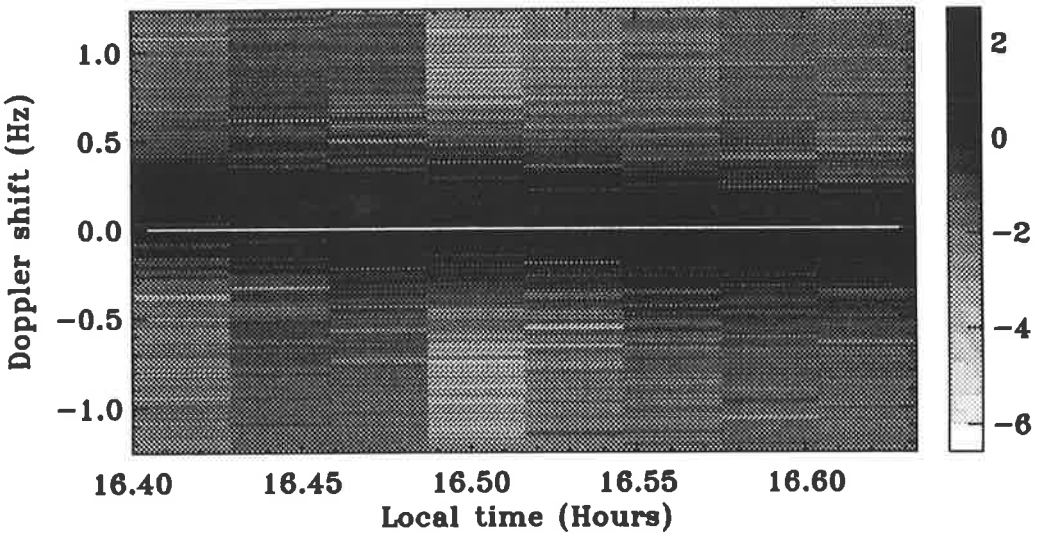

Figure 3.35: The eight power spectra for discrete target tracking case 3. Note the fairly linear motion of the power spectra peaks from about +0.28 Hz to -0.15 Hz.

corresponds to line–of–sight velocities of about 21 ms^{-1} to -11 ms^{-1} respectively. In this case, any trackable discrete target should move with approximately even spacing across the sky, and Figure 3.36a supports this expectation. In this case, however, the averaged spaced antenna estimate of the mean wind over these 16 min was not aligned with the direction of motion of the discrete scatterer, and had a magnitude of 30 ms^{-1}. The spectra–intensity time series method of display also allows us to discern temporally coherent features in the data which are not normally visible. Examination of a single power spectrum often is not sufficient to reliably find pertinent signals. An example of such a signal is the sea–scatter peak which, in data taken from the Buckland Park radar system, has been hitherto difficult to display. In Figure 3.37 running power spectra taken at a range gate of 66 km are displayed for the bp920916 campaign. Many features in the data are readily discernible, probably the most prominent of which is the strong sea–scatter component. This spectral line has a Doppler frequency of approximately +0.15 Hz which corresponds to an ocean wave speed of 11.4 ms^{-1}.

Also visible in Figure 3.37 are several weak, time–coherent signals which appear to vary in frequency in an orderly manner. One instance, for example, occurs at about 1630 in the top panel of Figure 3.37 where a signal at about -1.2 Hz can be seen moving towards zero Hz. Over a number of records the signal approaches within about 0.5 Hz of zero, and then returns once more to larger negative Doppler shifts. At first sight, this signal might appear to be

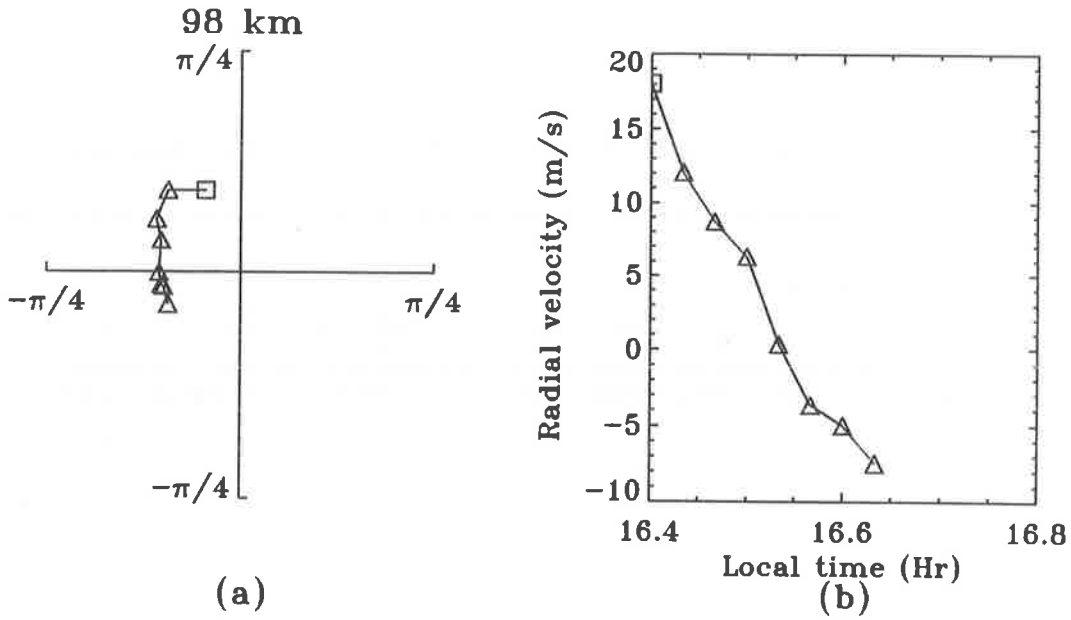

Figure 3.36: (a) The angle of arrival information for the eight power spectra displayed in Figure 3.35. (b) The average radial velocity associated with each of the eight angle of arrival points in (a). The first point in time is labeled with the symbol "□", while the remainder are labeled with triangles.

caused by total reflection from a "hard target", such as an aircraft or ship, but it is difficult to reconcile either possibility with the velocity that such a target would posses. (The Doppler shift of the target approaches -100 ms^{-1} at the beginning of its track.) Attempts at direction finding the target using cross–spectral techniques do not yield consistent or realistic results. It appears that the signal is most likely a crystal stabilized transmission whose frequency lies within about 30 kHz of the Buckland Park radar's base frequency of 1.98 MHz. Such a signal may then be aliased back into the receiver power spectrum provided it was within the bandwidth of the radar receiving system. Slow movement in frequency of the signal may represent a temperature associated drift in either the external transmission's base frequency, or in the Buckland Park receiving system.

3.9 Summary

We have seen that direction finding studies may be performed upon signals scattered from the atmosphere by calculating cross–correlation functions from samples of the coherent signal time series. The angle of arrival determination is, in general, not unique, with ambiguity occurring as a result of the antenna spacing being larger than $\frac{\lambda}{2}$. The ambiguity in angle of arrival is not constant with azimuth, with the antenna spacing projected upon the azimuth

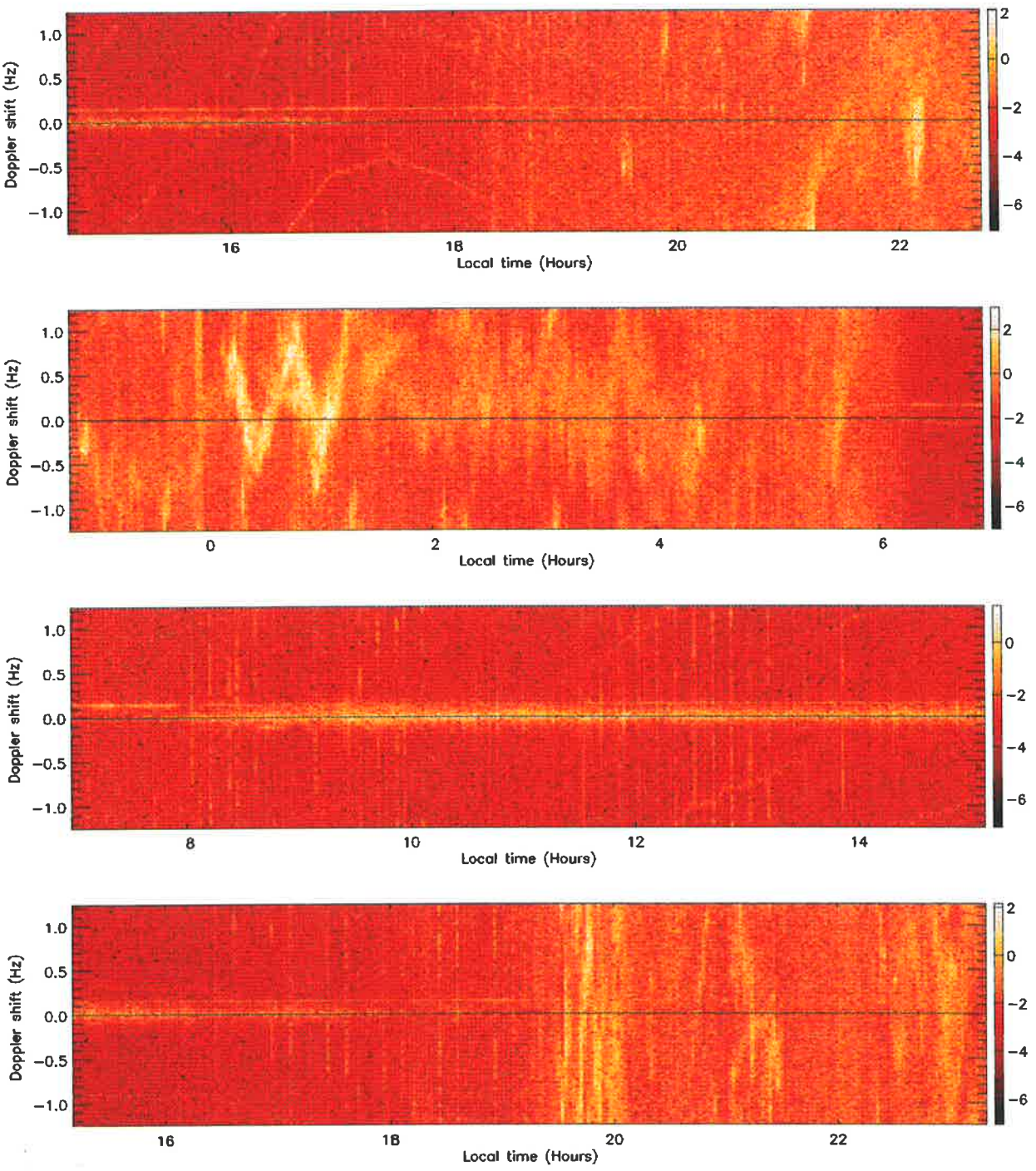

Figure 3.37: Power spectra for campaign bp920916 taken at a range gate of 66 km. The sea scatter peak is clear for most of the record at a Doppler shift of +0.15 Hz. A large amount of noise is visible during the night due to the incorrect polarization mode used. See text for a discussion of some of the other interesting features.

of arrival being the determining factor. The NTD criterion developed by *Meek & Manson* [1987] neither ensures that signals come from the zenith region, nor allows us to determine from whence the signals emanate. Further, eliminating signals from larger off–zenith angles does not eliminate the possibility of ambiguous returns. In general, only the rapid fall–off in backscattered power with off–zenith angle displayed by atmospheric scatterers allows angle of arrival studies to be performed with non–ideal antenna arrays with any confidence.

An experiment was performed with the Buckland Park antenna array and the refurbished 8 channel data acquisition system to characterize the distribution of backscattered power from the D– and E–regions. The quality of data obtained was excellent, surpassing all previous measurements. It was found that the attempt to eliminate the phase propagation delays through the receiver/signal processor channels was only partially successful due to the contribution to the phase error from the antennae reactances and cable electrical lengths. The complete channel error may only be eliminated by transmitting a test signal in the far field of the array, (difficult at these frequencies) or by assuming that on average the atmospheric returns emanate from the zenith. The random phase error distribution appears to be Gaussian in shape and and we have satisfactorily corrected for this bias by subtracting the phase of the Gaussian–fitted distribution peak from the measurement of each receiver phase difference. The receiver phase check facility has shown, however, that significant variations in receiver phase propagation delay occur due to both ambient temperature changes and also IF gain changes. A diurnal variation in phase propagation delay is evident in all receivers. Most significantly, the variations in receiver phase propagation delay are not consistent between receivers.

The known aspect sensitive nature of the atmospheric scatterers and its dependence on altitude is echoed in the spread of the angle of arrival measurements at each range gate and the mean off–zenith angle measured. Returns from the highest range gates at times emanate from off–zenith angles as large as 5° as total reflections from E–layer "glints" may dominate the signal. Returns from the lowest range gates are dominated by broadcast interference and sea scatter although a clustering of echoes centred on the zenith is still evident. Meaningful azimuthal profile information is obtainable from the analysis provided that the instrumental phase bias is adequately removed.

Discrete targets produced by disturbances in the E–layer may be seen in the running time series of power spectra and tracked using the angle of arrival analysis. The movement of these targets in time is consistent with the information derived from their Doppler shifts.

Triple reflection phenomena have been observed with characteristics consistent with a simple model considered by *Vincent* [1972]. Detection of these discrete targets is not difficult as they are a relatively common occurrence in the daytime E–layer. In contrast, discrete scatterers do not appear to exist in the D–region, where volume scatter appears to dominate.

Time series of spectral–intensity have been found to be a useful tool to aid in the detection of weak time–coherent signals. Sea scatter peaks are easily seen using this technique and appear to possess Doppler shifts consistent with the predicted motion of ocean waves of the appropriate scale for the Bragg scatter condition.

Chapter 4

TRANSMISSION USING THE MAIN BUCKLAND PARK ARRAY

4.1 Introduction

In April of 1993, upgrading of 30 of the Buckland Park main receiving array's 89 "E" dipoles was completed while, simultaneously, final interfacing between the interim 8 channel receiving system and one of the new, electronically phase–controlled 10 channel transmitter subsystem had been achieved. On the 30^{th} of April, the first data collection campaign with this system was initiated with the transmitter beam phased to point vertically. (At this point the computer software was not in place to allow the transmitter beam to be phased to point in arbitrary off–vertical directions.) In Figure 4.1, the 30 refurbished antennae used in the campaign and the manner in which they were joined together to form groups of three is displayed. This formation of antennae has a one–way power polar diagram with a half–power half–width of about 7.5° (see Figure 4.2) and side lobe suppression of at least 18 dB. The impedances of the 30 refurbished antennae were checked to ensure that all were in good working order before transmission commenced. All 30 antennae appeared quite acceptable with impedance magnitudes ranging from 48 Ω to 90 Ω, while the impedance phase angles were remarkably small, ranging from -9° to +15° (see Table 4.1).

After some effort it was found that the phase control module threshold levels were adjustable such that all 10 PA modules were transmitting in phase and were recognized as

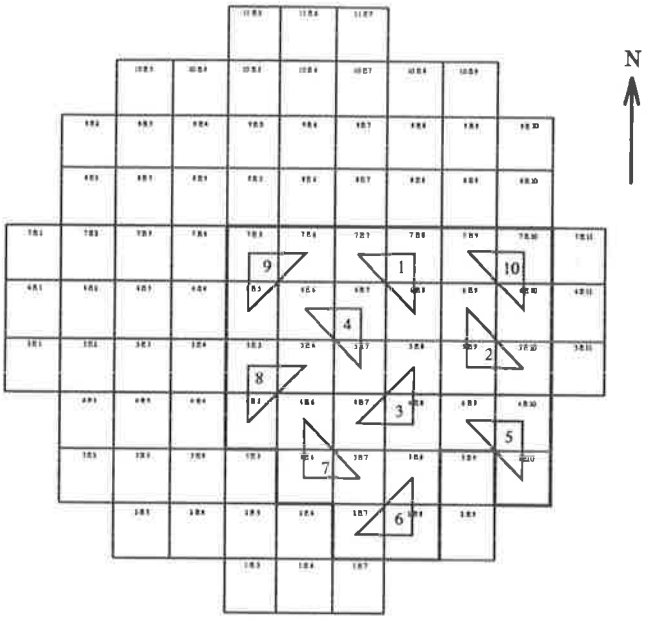

Figure 4.1: The 30 refurbished antennae used in the first transmission using the main receiving antenna array at Buckland Park. Each of the 10 solid–state PA modules is connected to three antennae. The groups of antennae used are joined together by triangles, while the number in the centre of each triangle indicates which PA module drives that group. The eight receivers are connected to groups one to eight respectively. Note that the "E" polarization is used for both transmission and reception and that the facility to transmit circularly polarized radiation is not yet implemented.

being out of phase when stepped off phase by only one step (about 8.6°). The PA modules' phases were checked at the beginning of each two minute record, and any which failed this test were individually turned off for that record. After the threshold levels were established satisfactorily, the phase control modules were rarely unable to find the optimum phase–zero when required, although two of the 10 channels were somewhat more unstable than the remaining 8. The cause of this comparative instability was not clearly apparent, but possible contributors included enhanced noise on individual antennae, variations in antenna impedance and "cross–talk" between adjacent phase control modules and/or PA filters in the transmitter rack. An investigation into these possibilities continues.

The transmitter was triggered at a PRF of 80 Hz during the day which, with 32 coherent integrations performed per final data point, yielded an overall sampling frequency of 2.5 Hz. In all, data from 20 range gates were collected from nominal altitudes of 60 km to 98 km. Due to a hardware problem in the range marker card, these nominal altitudes corresponded to actual altitudes from 58 km to 96 km respectively. All diagrams and references to altitude in this chapter, unless specifically excluded, refer to the hardware range gate selected. Thus

Table 4.1: The impedances of the 30 refurbished antennae measured at 1.98 MHz on the 30^{th} of April, 1993. Although the magnitudes of the of the impedance measurement vary by up to 50% from the ideal of 75 Ω, the majority of phase angles are remarkably small.

Antenna	$\|Z\|$ (Ω)	$\angle Z$ (°)	Antenna	$\|Z\|$ (Ω)	$\angle Z$ (°)
2E7	64	+4	5E8	58	+2
2E8	82	+4	5E9	80	+11
3E6	56	+4	5E10	77	-8
3E7	67	+6	6E5	54	+1
3E8	74	+4	6E6	54	0
3E10	65	+7	6E7	77	0
4E5	62	+10	6E8	57	+2
4E6	70	+6	6E9	58	+6
4E7	81	+12	6E10	66	+8
4E8	60	0	7E5	53	0
4E9	63	+5	7E6	48	0
4E10	64	+2	7E7	54	+9
5E5	82	+6	7E8	70	+15
5E6	50	+3	7E9	83	+5
5E7	78	+5	7E10	90	+3

the reader must subtract 2 km from the nominal range referred to to find the actual range.

The 8 channel receiving system was connected to 24 of the same 30 antennae used for transmission. Isolating TR switches ensured that the receivers were protected during the transmission of a pulse. In this particular configuration each receiver was connected to three antennae, these being the same three dipoles connected to the corresponding PA module (see Figure 4.1).

The bp930430 campaign extended over a period of two weeks with the equipment in this configuration. A selection of this data is presented in Section 4.2 to demonstrate the high quality of the observations obtained with this new equipment.

During the validation of the new transmitting/receiving system at Buckland Park, software modifications were made to the radar acquisition program enabling the transmitter beam pointing direction to be altered from the vertical. The first test of this beam–steering facility was the bp930514 campaign, in which the transmitter beam was directed 10° off–zenith towards the East and West on alternate data acquisitions. A second experiment was then performed, in which the transmitter beam was directed to the zenith and then 10° off–vertical towards the East, West, North and South in succession. These data were taken during the bp930523 campaign. Results from these two experiments are presented in

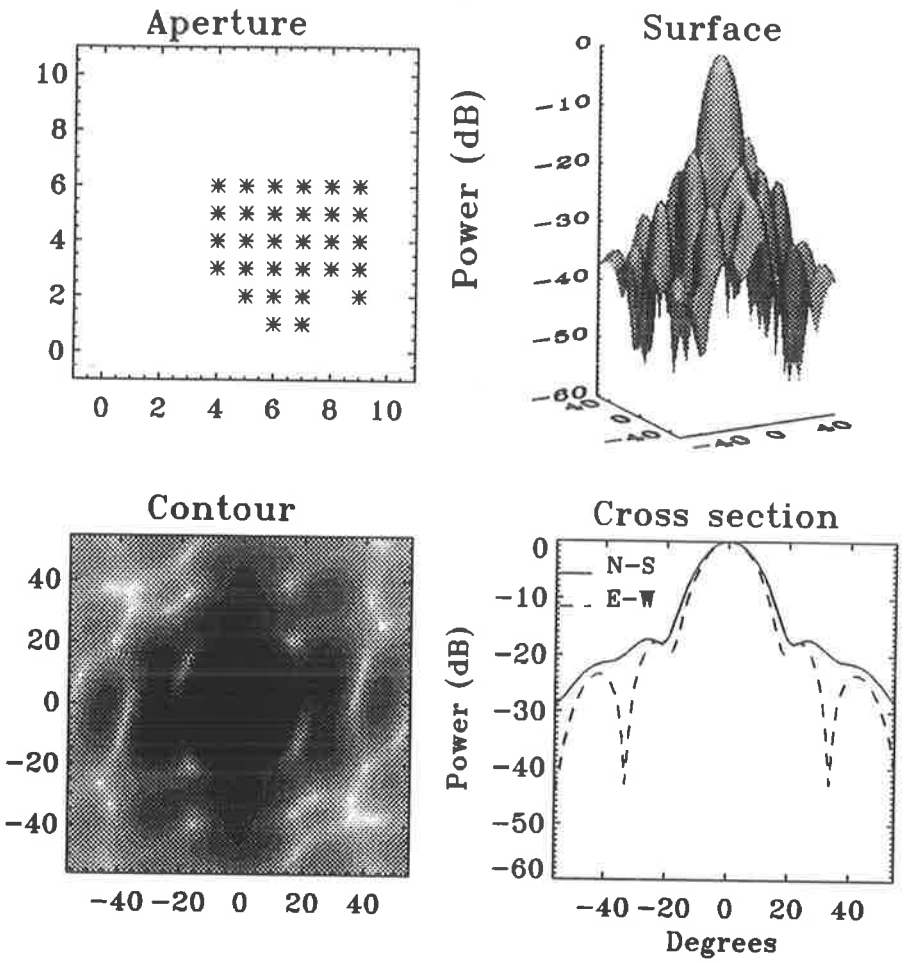

Figure 4.2: The power polar diagram of the 30 antennae array used for the inaugural transmission on the main array. The one–way half–power half–width of the main lobe is around 7.5° while the main side lobes are suppressed by at least 18 dB.

Sections 4.3, and 4.4.

4.2 Transmission Using A Vertically–Directed Beam

The bp930430 campaign commenced at 13:37 on the 30^{th} of April, 1993. Observation of the IF output of the receivers with a CRO revealed an extremely strong return from the E–layer, with a readily discernible E_3 echo also usually present. For the first documented time in the Buckland Park MF radar's history, an E_5 echo was also visible. These casual observations seem to indicate that a large amount of power per solid angle was being radiated by the 10 channel transmitter in combination with the 30 antenna transmitting array.

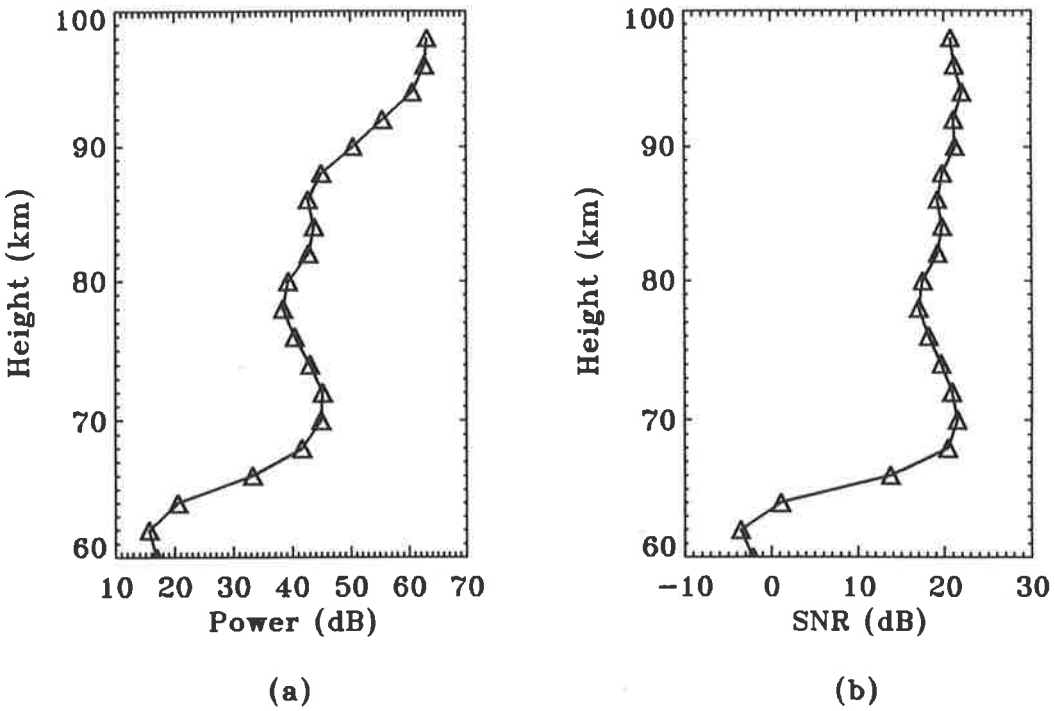

Figure 4.3: Average profile of (a) backscattered power and (b) signal–to–noise ratio for the first hour of the bp930430 data set. Note the enhancement in returned power between 70 km and 74 km. These profiles were calculated from data collected by receiver one.

4.2.1 Power profiles

Average power and signal–to–noise ratio profiles calculated from receiver one over the first hour of this data set appear in Figures 4.3a and b. Of interest in the power profile displayed in Figure 4.3a is the clear enhancement in echo power between apparent altitudes of 70 km and 74 km. This "layer" appears to be associated with very stable long–lived echoes and is common throughout the day–time data set. This enhancement interrupts an otherwise linear (in logarithmic units) fall off of power with decreasing altitude.

The average signal–to–noise ratio profile shown in Figure 4.3b reveals an almost constant ratio of 20 dB from 98 km down to 68 km whereupon the ratio drops rapidly below zero dB. Bearing in mind the 2 km discrepancy between apparent and correct range, this corresponds to an excellent signal–to–noise ratio down to 66 km.

4.2.2 Time domain interferometry

Time domain interferometric angle of arrival information was calculated for this data set and appears in Figure 4.4. The receiver phases were corrected using the receiver phase test

signal and residual channel phase errors were subsequently removed by the phase histogram normalization technique described in Section 3.7. In this case, the residual phase offsets for the three receiver pairs were calculated as -26.7°, 11.6° and 20.6°. The salient features of this angle of arrival information are the remarkable lack of spread of the points from the zenith for apparent altitudes down to 64 km, and the relatively small number of points accepted below this height. Also of some interest is the small number of points in the "halo" around the zenith in the highest range gates. This would seem to indicate that the likelihood of occurrence of discrete E–layer "glints" in this data set is somewhat less than that observed with the bp920916 data set analysed in Chapter 3. The average profiles for these data appear in Figure 4.5 and highlight the adherence of the majority of the angle of arrival points to the zenith.

Although some of this reduction in spread from the zenith may be explained in terms of smaller reception and especially transmission beam patterns, it would seem that many spurious returns have also been eliminated due to the marked increase in transmitter power–aperture product.

4.2.3 Spaced antenna wind analysis

Although no ideal antenna spacings for the spaced antenna experiment were available in the configuration selected for the bp930430 campaign, antenna groups 2, 3 and 5 were selected as the most nearly equilateral (see Figure 4.1). This triangle had side lengths of 117 m, 155 m and 192 m and interior angles of 70°, 60° and 49°. The data from these three antennae were analysed using the standard spaced antenna technique [*Briggs*, 1984]. Figure 4.6 displays the results in the form of hourly–average profiles of zonal and meridional winds. In each case the horizontal scale extends from -100 to +100 ms^{-1}, and the vertical scale extends from 60 km to 100 km. The most concerning feature of the data is the significant reduction in wind acceptances below about 86 km at night. The majority of these rejections appear to be due to poor signal–to–noise ratios, and appear to occur more frequently than is observed with the routinely–operated spaced antenna system at the same site. This routinely–operated spaced antenna system differs from the current experiment in that circularly–polarized radiation is transmitted, although only linearly polarized radiation is currently used on reception. Although the night–time loss of the D–region and the subsequent reduction in amplitude of the backscattered signal is partially responsible for these poor signal–to–noise ratios, it is possible that the use of linearly polarized radiation on transmission and reception is also a

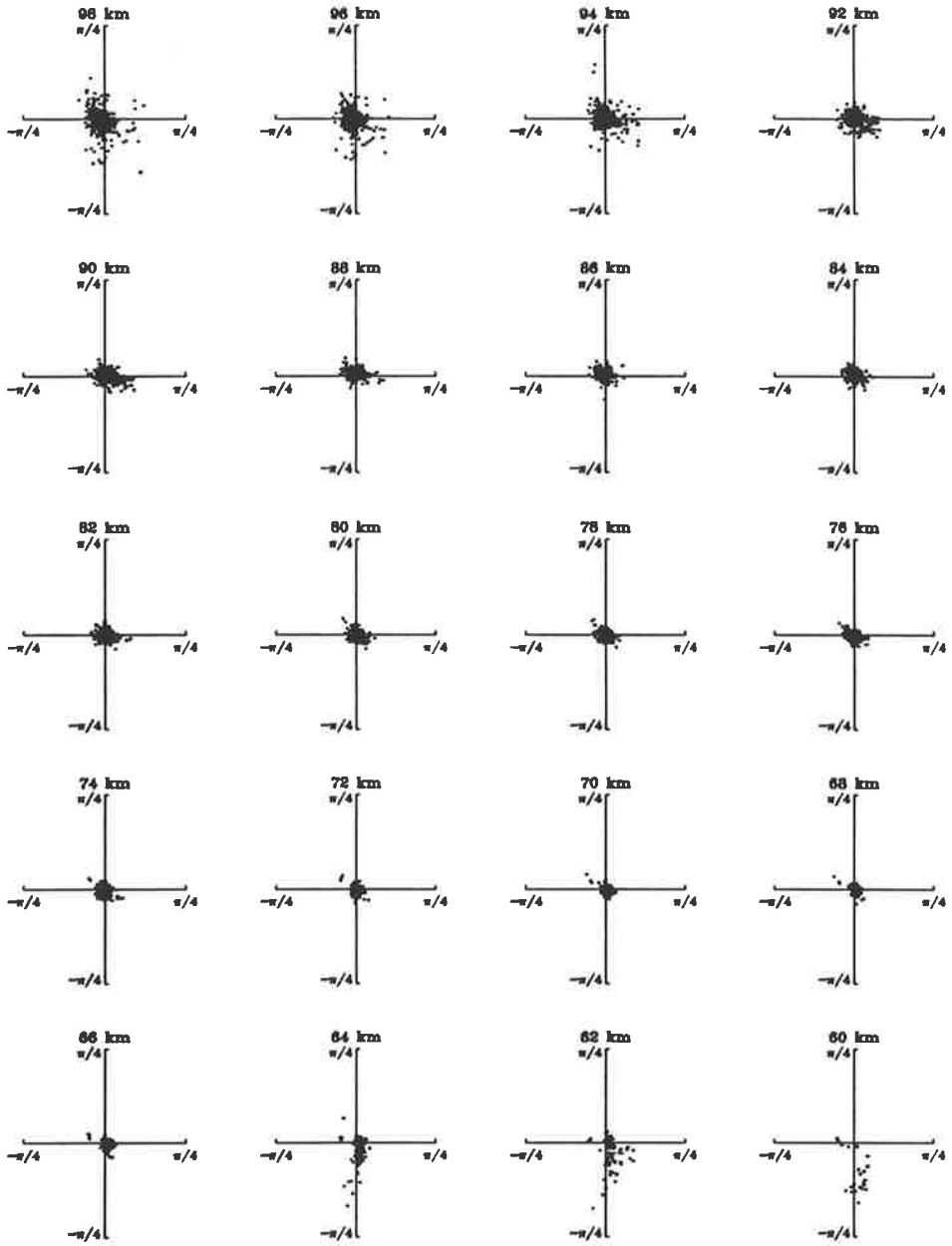

Figure 4.4: The mean angle of arrival of the data set bp930430 as calculated from receivers 3, 4 and 8 for day–time returns only. The receiver phase delay propagation differences are corrected for by means of the receiver phase correction test signal and residual channel errors removed by histogram normalization. Data with signal–to–noise ratios of -6 dB or less have been excluded.

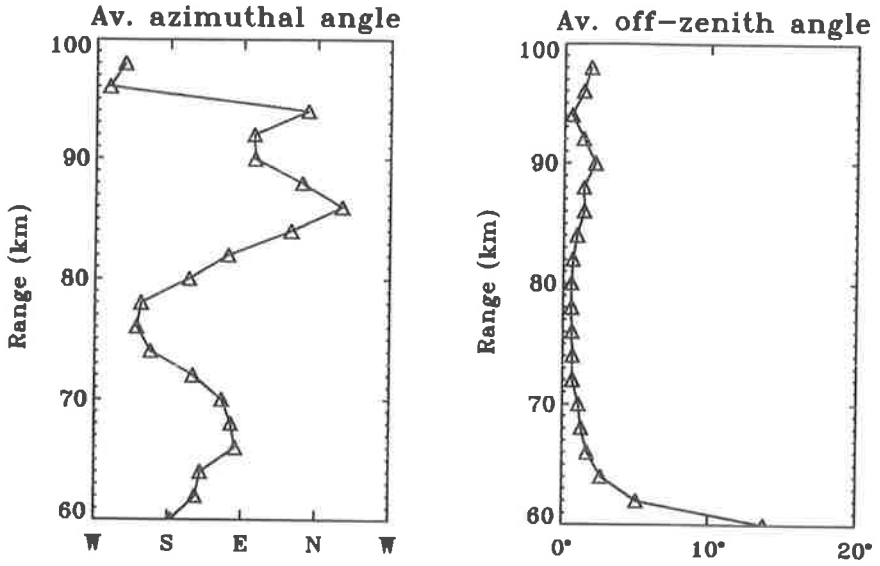

Figure 4.5: Average profile of mean angle of arrival information for the bp930430 data set as depicted in Figure 4.4.

factor. Realization that the ionosphere is a birefringent medium leads to the consideration of the effect of Faraday rotation of the polarization vector. The total rotation of the plane of polarization of the transmitted wave is given by

$$\Phi \propto \frac{1}{\omega^2} \int N B \, ds \ , \tag{4.1}$$

where w is the angular frequency of the transmitted radiation, N is the local number density of electrons in the medium, B is the magnetic field strength, and ds is an infinitesimal element of the traversed path, S. Clearly, if Φ is an odd multiple of $\frac{\pi}{2}$, then the radiation incident at the ground will be polarized at right angles to the dipoles' alignment, and the received signal strength, which is proportional to $\cos\Phi$, will be zero. Thus, as the electron number density varies between day and night, changing the rotation angle of the polarization vector, different strengths of backscattered signal will be received by the antennae aligned North–South. Independent numerical simulations, however, (*Elford* – private communication) have shown that at a frequency of 1.98 MHz, multiple rotations of the polarization vector occur above 60 km in altitude in both the day–time and night–time ionosphere. Clearly, then, we would expect the received signal strength on the ground to vary between a maximum and a minimum from one range to the next as the polarization vector rotated through multiples of $\frac{\pi}{2}$. Also, as the local electron density increases with altitude, we expect the rate of Faraday rotation to increase with range. In other words, we expect the lowest rate of

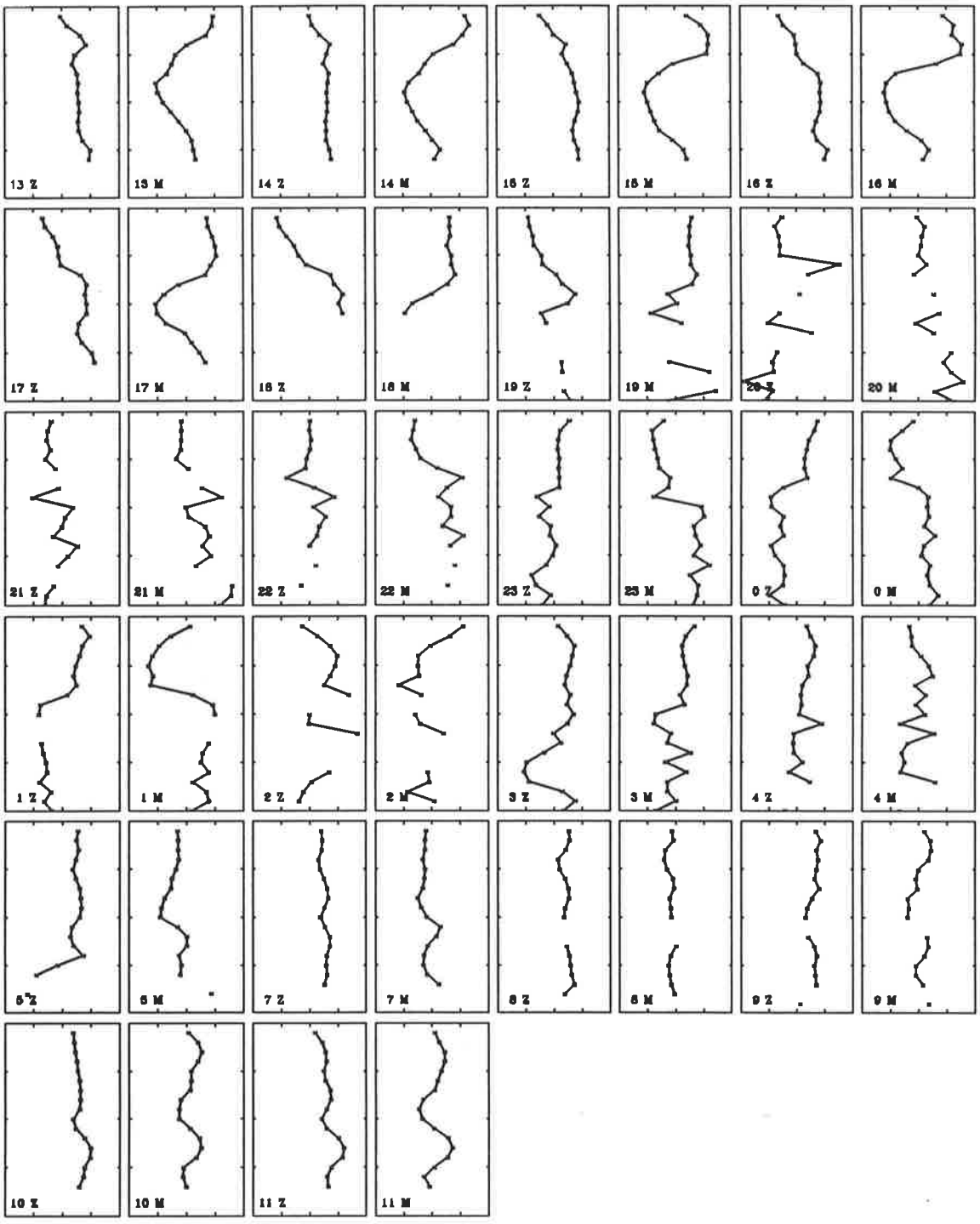

Figure 4.6: Spaced antenna–derived hourly mean wind profiles of zonal (Z), and meridional (M) winds. The number in each panel indicates the starting time of that average in local time (hr). Zonal and meridional profiles for each hour are displayed over a total of 22 hr. The first profile was recorded at 1300 on 30/4/93, while the last was recorded at 1100 on 31/4/93. In all cases the horizontal scale extends from -100 ms^{-1} to 100 ms^{-1}, and the vertical scale extends from 60 km to 100 km. Note the lack of data in the lower range gates at night.

rotation (perhaps none) in the lower range gates, with the polarization vector rotated more rapidly as the range of interest is situated higher in the ionosphere. This hypothetical signal strength behaviour is clearly inconsistent with that exhibited by this particular data set, as the received signal power is fairly constant above 86 km. We therefore discount Faraday rotation as the main cause of the apparently diminished signal strengths during the night as compared to the routinely–operated spaced antenna radar system. It must be noted, however, that the use of linearly–polarized radiation for both transmission and reception is not an optimal configuration for a spaced antenna experiment, since ionospheric propagation factors such as Faraday rotation and the resultant signal loss and magneto–ionic fading may result in poor data quality or, in extreme cases, erroneous results.

The low night–time data rate issue is set aside for now, and our attention is turned to other dynamical features of the data.

Although the presence of tidal motion is obvious, the hourly profiles do show good agreement with the expected prevailing winds at this latitude and time of year. The existence of a large Southward meridional jet at 80 km and an Eastward zonal flow peaking at about 75 km and decreasing with altitude is typical of the transition from Summer to Winter flow regimes during April and May. On the other hand the Summer flow for this latitude is largely Eastward above 84 km and Westward below, with little meridional flow during those months [*COSPAR*, 1990].

In Figure 4.7a and b the one–day average wind profiles for the 30^{th} April and the 1^{st} May respectively, beginning and ending in mid–afternoon in both cases, are depicted for both the zonal and meridional components. These four panels indicate the variability in the daily–averaged wind due to fluctuating tidal components and also the unstable nature of the wind profile during this transition period. Other effects which may be biasing the average wind profile include the relative sparseness of the data at night. From about 80 km in range downwards approximately only 10% of the data over a 24 hr period occurs at night. Clearly the average in these cases will be markedly biased towards the day–time wind which, in many instances, will not be representative of the daily average due to tidal contamination.

4.2.4 Post–set beam steering

The post–set beam steering experiment, (PBS) was first presented in the literature by *Röttger & Ierkic* [1985]. In the PBS experiment, the coherent voltage time series sampled from each antenna group is stored in its entirety for later analysis. A pointing angle is then selected

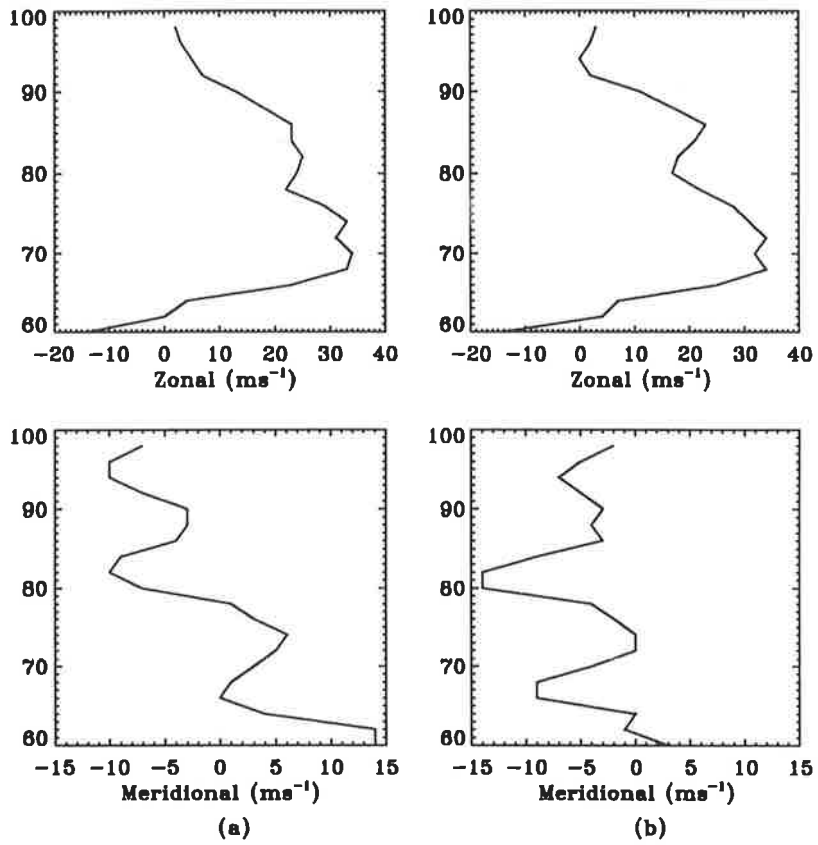

Figure 4.7: Spaced antenna–derived daily mean wind profiles of zonal and meridional wind components for data beginning on (a) 30^{th} April, and (b) 1^{st} May, 1993. The vertical scale in each instance is the radar range gate measured in km.

for the desired beam direction and each time series is multiplied by the appropriate complex constant $e^{j\phi_k}$, where ϕ_k is the additional phase lag required for receiver k. The phase lag for each receiver in matrix form is given by

$$\underline{\phi} = \begin{pmatrix} \xi_1 & \eta_1 \\ \xi_2 & \eta_2 \\ \vdots & \vdots \\ \xi_n & \eta_n \end{pmatrix} \begin{pmatrix} \sin\theta_E \\ \sin\theta_N \end{pmatrix} , \tag{4.2}$$

where the ξ_k and η_k are the x– and y–coordinates of the antenna groups respectively, and the θ_E and θ_N are the off–zenith angles in the Eastward and Northward directions respectively. These modified time series are then summed together and normalized to form a single time series. This mathematical process of selectively retarding the phase of each receiver is exactly equivalent to inserting cable delays of the appropriate length connecting each receiver and antenna. Forming such Doppler radar beams by physical cable delays is now known as pre–set beam steering. The advantage of PBS, however, is that the delay lengths are infinitely

adjustable, and the beam may be steered in any direction.

In an interesting modification to the PBS technique, *Kudeki & Woodman* [1990a] have shown that, due to the linearity of the auto– and cross–correlation function equations, the complex multiplier used to modify each time series may be applied instead to the auto– and cross–correlation coefficients of each unmodified time series, which are then summed to yield the auto– or cross–correlation of the tilted beam. They have called this technique the post–statistics steering technique (PSS), and have used it to examine velocities and aspect sensitivities of scatterers in the lower mesosphere at VHF [*Kudeki et al.*, 1990b]. The only use of PSS at MF was reported by *Sürücü et al.* [1992], who used the technique to steer a 10–element array in two orthogonal directions in order to estimate the 3–dimensional wind. *Sürücü et al.* [1992] found good agreement between the winds measured using the PSS technique and spaced antenna–derived true winds.

The PSS technique is mathematically equivalent to the PBS technique, and is essentially a useful method of reducing the data storage needs for a radar controller by including some form of data pre–processing. For the purposes of the following section, only the PBS technique was used as the data storage available was not a significant limitation.

Following the technique described in Section 3.7, the receiver phase propagation delays were eliminated by means of the receiver phase test signal which was recorded prior to each data acquisition. Residual channel errors were then minimized by fitting Gaussian functions to histograms of each of the cross correlation phases at zero lag obtained from each receiver pair. The positions of the peaks of these Gaussian functions were then used as estimators of the residual channel phase error.

The phase corrected time series were then used to form beams in a total of 441 directions in a raster–scan pattern centred on the zenith and spanning between $\pm 15°$ in both the East–West and North–South planes. Thus, it was anticipated that the mathematically–formed reception beam would scan through the vertically–directed transmission beam out to at least two transmission beam one–way half–widths in all directions from the zenith. The reformed time series may then be used to calculate various radar parameters such as returned power, frequency spectra and Doppler velocities.

Figure 4.8 displays both the returned power and Doppler shift as a function of the beam pointing direction of the receiving array at a range of 80 km. In Figure 4.8a the returned power is displayed in three dimensional surface form where the vertical axis represents the power in dB units, and the x– and y–axes range between $\pm 15°$. The surface is viewed from

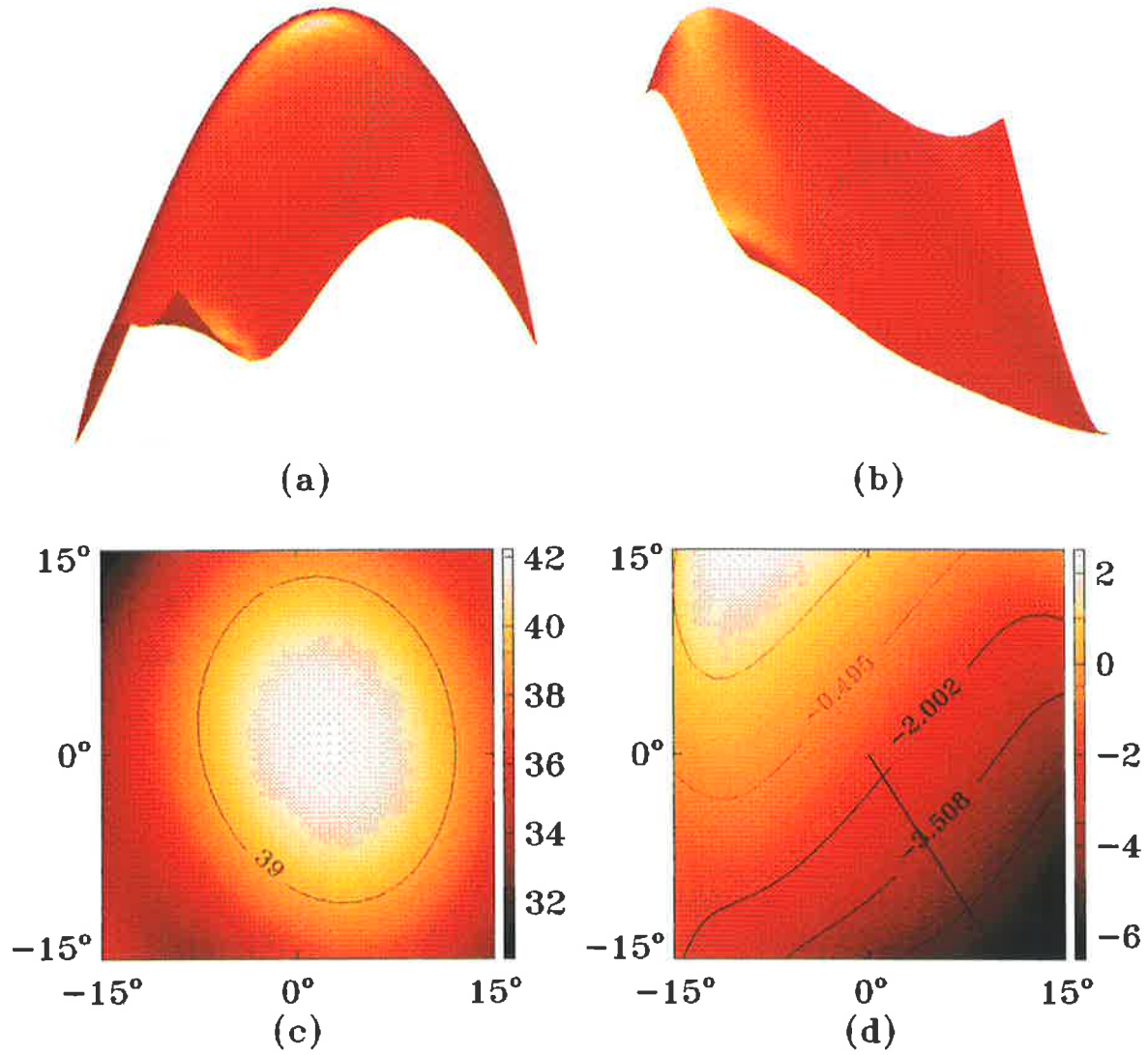

Figure 4.8: Returned power as a function of beam pointing direction at a range of 80 km displayed as (a) a three–dimensional surface, and (c) as a power–angle–intensity plot. The sole contour drawn in (c) represents the half–power level. The Doppler velocity as a function of beam pointing direction appears similarly in panels (b) and (d). In all instances the x– and y–axes range from -15° to +15°. Note that the transmitted beam was phased to point vertically. See text for more detail.

an azimuth of about 45°, thus presenting an isometric perspective. In Figure 4.8c the same surface as viewed from above is displayed in image–contour form, where the sole contour plotted represents the 3 dB level of the two–way beam. As can be seen, the contour is somewhat elliptical with semi–major and semi–minor axes of about 11° and 9° respectively. As will be described shortly, the mean wind as determined by the spaced antenna analysis at this height and time coincides in direction with this elongation of the beam pattern. Although an interesting possibility exists that this elongation may be systematically related to the wind direction, no such study has been performed as part of this work. The point is made, however, that many other records when analysed using the PBS technique show no elongation in the returned power surface. We conclude, then, that the changing aspect sensitivity of the scatters is responsible for the changing asymmetry in the beam's power surface. We do not claim that the direction of elongation is necessarily in the direction of the mean wind.

More careful inspection of Figure 4.8c reveals that the centre or peak of the beam power pattern does not coincide with the zenith. In fact, the direction of peak returned power as found using the PBS technique is conceptually analogous with the mean angle of arrival calculated using time–domain interferometry as described in Chapter 3[1]. As was found with the interferometric studies where the direction of the mean scatter varies with time about the zenith, the direction of strongest return found with PBS also moves about the zenith.

In Figures 4.8b and d the Doppler shift measured as a function of the receive beam direction is displayed in the same manner as Figures 4.8a and c. Note that the calculated radial velocity varies smoothly with angle from a maximum of about 2 ms^{-1} to the North–West, to about -6 ms^{-1} to the South–East. Also indicated on Figure 4.8d is the direction of the mean wind as calculated by the spaced antenna technique. In this case the wind was to the South–East with a magnitude of 48 ms^{-1}. Note that the measured radial Doppler velocity at 15° off–zenith is significantly lower than would be expected for a horizontal wind of 48 ms^{-1}. This under–estimation is due to leakage of signal from the zenith into the main radar lobe which is centred on 15° off–zenith and has a half–power half–width of 7.5°. If the effect of the aspect sensitivity of the scatterers is included then it is clear that the power–weighted beam direction is much closer to the zenith than would otherwise be expected. For this reason a comparison is made between spaced antenna wind direction and the directions of maximum and minimum Doppler velocities only. Casual examination of several data sets

[1] Provided that the beam power pattern is not too asymmetrical.

reveals that the two are certainly well correlated, and a more rigorous pursuit of wind velocity measurement using interferometric techniques is discussed in Section 4.4.

4.3 Transmission Using Two Off–Vertical Beams

Off–vertical beam directions of 10° East and 10° West were selected for the bp930514 data campaign. The data acquisition software was modified to allow antenna coordinates and beam pointing directions to be entered. The program was easily changed such that any number and combination of beam directions could be specified, with alternating East/West beams selected for the first experiment. The impedances of the 30 antennae selected for transmission and reception were again checked to ensure that no breakages had occurred and the antennae were configured as detailed in Section 4.2. Two days of data were collected with the range gates, PRF and all other radar parameters set exactly as set out in Section 4.2. Unfortunately, on retrieval of the data set, only the first 24 hr were recovered due to faulty magnetic media, and it is these data which are presented here.

4.3.1 Time domain interferometry

The bp930514 data set was first analysed by finding the time–domain mean angle of arrival of each 102.4 s long record. Samples from antennae 3, 4 and 8 were phase corrected firstly with the phase propagation delay test signal, and then with the measurement of the residual channel error from the bp930430 data set. Clearly this removal of the residual channel error estimated from a data set recorded some two weeks earlier may have been a source of error, but since no vertical beam was in use during the bp930514 campaign, no other means of error correction was available. The residual channel errors for receivers 3, 4 and 8 for the bp930430 data set were (-26.7°, 11.6°, 20.6°), and the application of these three phase corrections to the bp930514 data set did achieve a significant improvement in the data quality. Figure 4.9 displays the mean angle of arrival measurements from the bp930514 data set. A number of features of the data are worth commenting upon.

The most striking characteristic of the data appears to be the systematic deviation of the azimuth of the off–zenith scatter away from the East–West baseline. Given that the transmitter beam direction lay within the East–West plane, it is difficult to conceive a mechanism by which the mean angle of arrival of scatter could emanate from a direction not coinciding with the x–axis. Systematic tilts of atmospheric layers at all range gates over

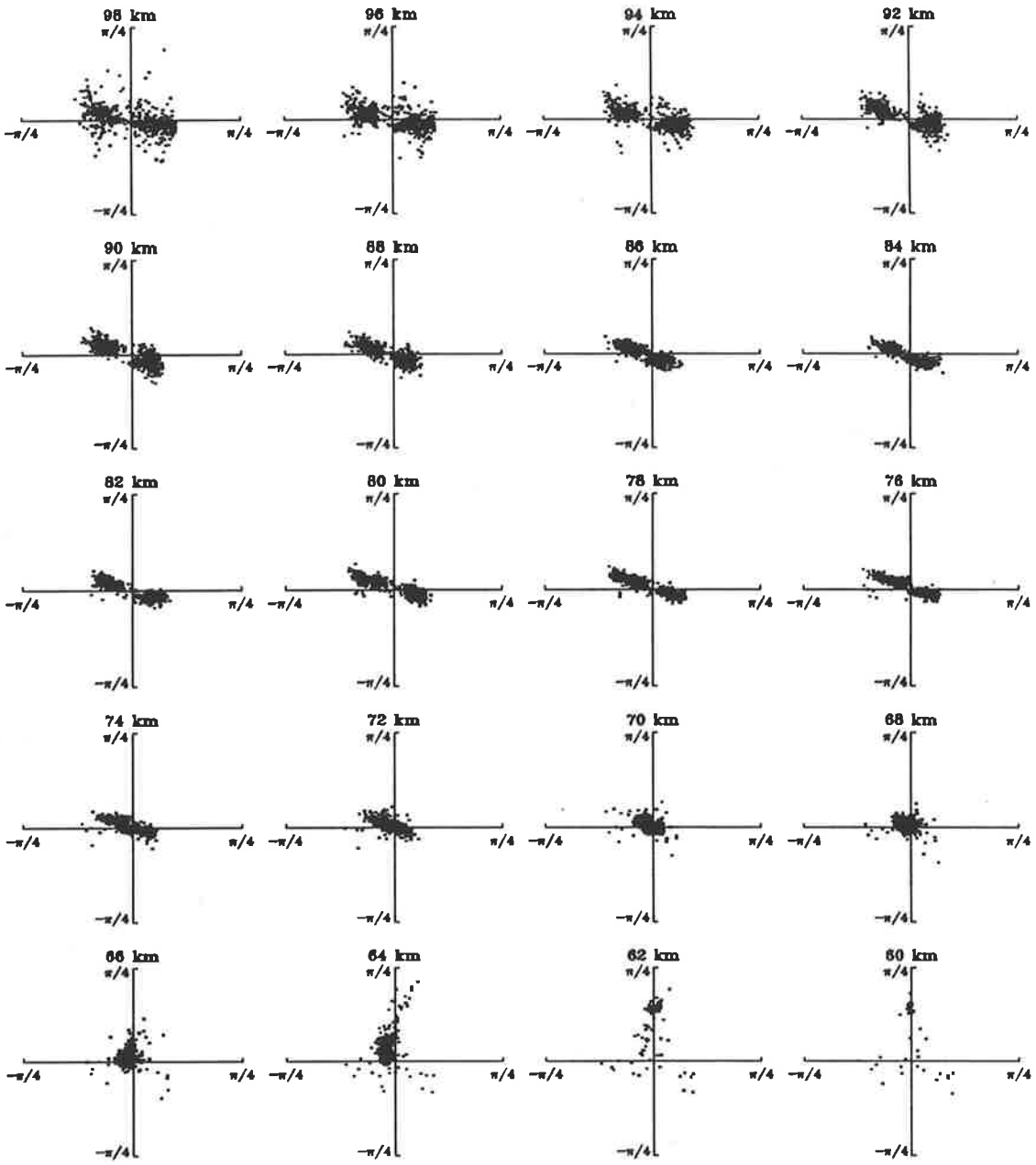

Figure 4.9: The mean angle of arrival of the data set bp930514 as calculated from receivers 3, 4 and 8 for day–time returns only. The receiver phase delay propagation differences are corrected for by means of the receiver phase correction test signal and residual channel errors removed by histogram normalization as calculated from the bp930430 data set. During this data set the transmitted signal was steered on alternate records 10° off–zenith towards the East and West. Data with signal–to–noise ratios of -6 dB or less have been excluded.

24 hr in duration would appear physically impossible. It would seem, at first, that the only conclusion possible is that the transmitter beam direction did not lie in the East–West plane, and so considerable effort was expended in attempting to locate the source of the suspected error. The transmitting array power polar diagram was calculated and examined for skewed side–lobes which might have been the cause of the skewed returns, but none were located. Next, the phase control modules' phase steps were extracted from the campaign log files and compared with the theoretical phase steps required to produce the correct beam pointing direction. Again, no discrepancy was discovered. At this stage attention was focussed on the receiving array, and it was finally noted that the three antennae used to calculate the time–domain angle of arrival information were configured as an isosceles triangle with the longest side aligned with a bearing some 10° North of West. As has been shown with the spaced antenna wind analysis, wind vectors and spatial correlation ellipses tend to line up along the longest side of the antenna triangle used [*Golley & Rossiter*, 1970; *Meek*, 1990]. It is believed that, as occurs in the spaced antenna analysis, the calculation of the time–domain mean angle of arrival by means of cross–correlation phases at zero lag is biased by the use of non–equilateral triangles with significantly different side lengths.

In order to verify this suspicion, a second antenna group with more equal triangle–side lengths was used in the mean angle of arrival analysis. Antenna group (2, 3, 5) was selected with side lengths of 155 m, 177 m and 193 m. This compared with side lengths of 152 m, 152 m and 215 m for antennae (3, 4, 8). Unfortunately, the longest side of antenna group (2, 3, 5) was aligned in a similar direction to the longest side of antenna group (3, 4, 8), the directions being 8° North of West for the latter, and 18° North of West for the former. Examination of Figure 4.10 shows that, despite this non–ideal configuration, the mean angle of arrival results calculated from antennae (2, 3, 5) are not biased to the extent that the results from the (3, 4, 8) antenna group were.

As a more rigorous test of this problem, all 8 receivers were used in a post–set beam steering experiment. The aim of the experiment was to demonstrate that, when free of antenna configuration biases, the received power as a function of zenith angle was centred on the East–West baseline. The phases of the 8 receivers were again corrected with the use of the phase correction information derived from the bp930430 data set. Since the transmitter beam direction was steered on alternate records, data from the first and second acquisitions are presented in Figure 4.11a–d. The data in Figure 4.11a and b are from the first data acquisition at a range of 92 km, while those shown in Figure 4.11c and d are from the

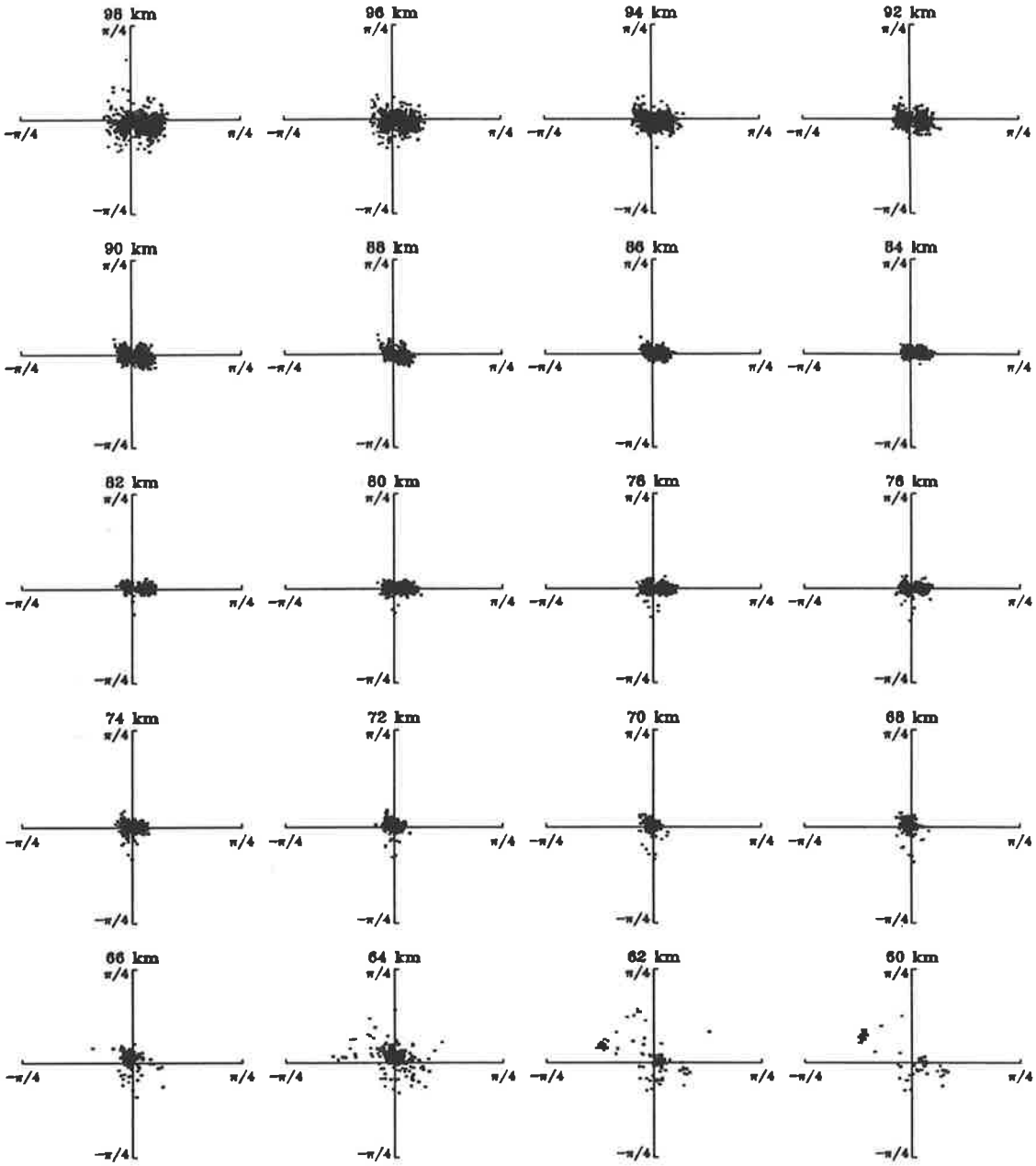

Figure 4.10: The mean angle of arrival of the data set bp930514 as calculated from receivers 2, 3 and 5 for day–time returns only. The receiver phase delay propagation differences are corrected for by means of the receiver phase correction test signal and residual channel errors removed by histogram normalization as calculated from the bp930430 data set. During this data set the transmitted signal was steered on alternate records 10° off–zenith towards the East and West. Data with signal–to–noise ratios of -6 dB or less have been excluded.

second acquisition at the same apparent range. The two panels on the left are power–angle–intensity representations of the returned power as a function of beam pointing angle, and are of most interest here. Those panels on the right of Figure 4.11 are Doppler–angle–intensity representations of the radial Doppler velocity as a function of beam pointing angle. Note that, unlike Figure 4.8, the direction of the mean wind has not been superimposed upon the Doppler velocity contours. In fact, it was not possible to calculate the spaced antenna winds for this data set since at no stage was a vertically–directed beam used. It is for this reason that wind derivation and analysis is reserved for a later data set in which five transmitter beams were available; one vertical and four off–vertical. This and other examples using the PBS technique clearly demonstrate that, on average, the majority of the returned power from transmitter beams directed at off–zenith angles does emanate from the expected azimuth and has a zenith angle which lies between the transmitter beam zenith angle and the zenith. It was therefore concluded that the deviation of the mean angle of arrival results in Figure 4.9 from the East–West baseline was an artifact of the antenna geometry used for reception, and not a consequence of the transmitted beams' pointing angle. Clearly, this raises interesting questions relating to the antenna configurations used for both time– and frequency–domain interferometry and the possible biases thereby induced. It is apparent that some care may need to be taken when selecting these antenna configurations in order to avoid these biases, although at this stage it is only suspected that an equilateral triangle configuration may minimize the problem.

As a final check to ensure that the transmitted beam pattern was not simply a "dual lobe" arrangement pointing simultaneously to the East and West, the angle of arrival measurements from alternate records were separated into even (West) and odd (East) groups. These two groups were examined to ensure that the angle of arrival measurement lay only in the Eastern half–plane for the Eastwardly directed transmitter beam records, and in the Western half–plane for the other records. This was indeed the case, as is shown in Figure 4.12 which presents data from every second range. Also indicated in Figures 4.12a and b is the 3 dB threshold of the transmitter beam. Note that the scattering points often lie beyond this threshold. This is not particularly surprising, as the aspect sensitivity of the scatter may "drag" the scattering points closer to the zenith than the 3 dB edge of the beam.

Another interesting feature of the data is the tendency for the off–zenith angle of the returned signal to decrease with range. In the uppermost range gates the data appear for the most part to cluster about the expected 10° off–zenith angle. As we move our attention

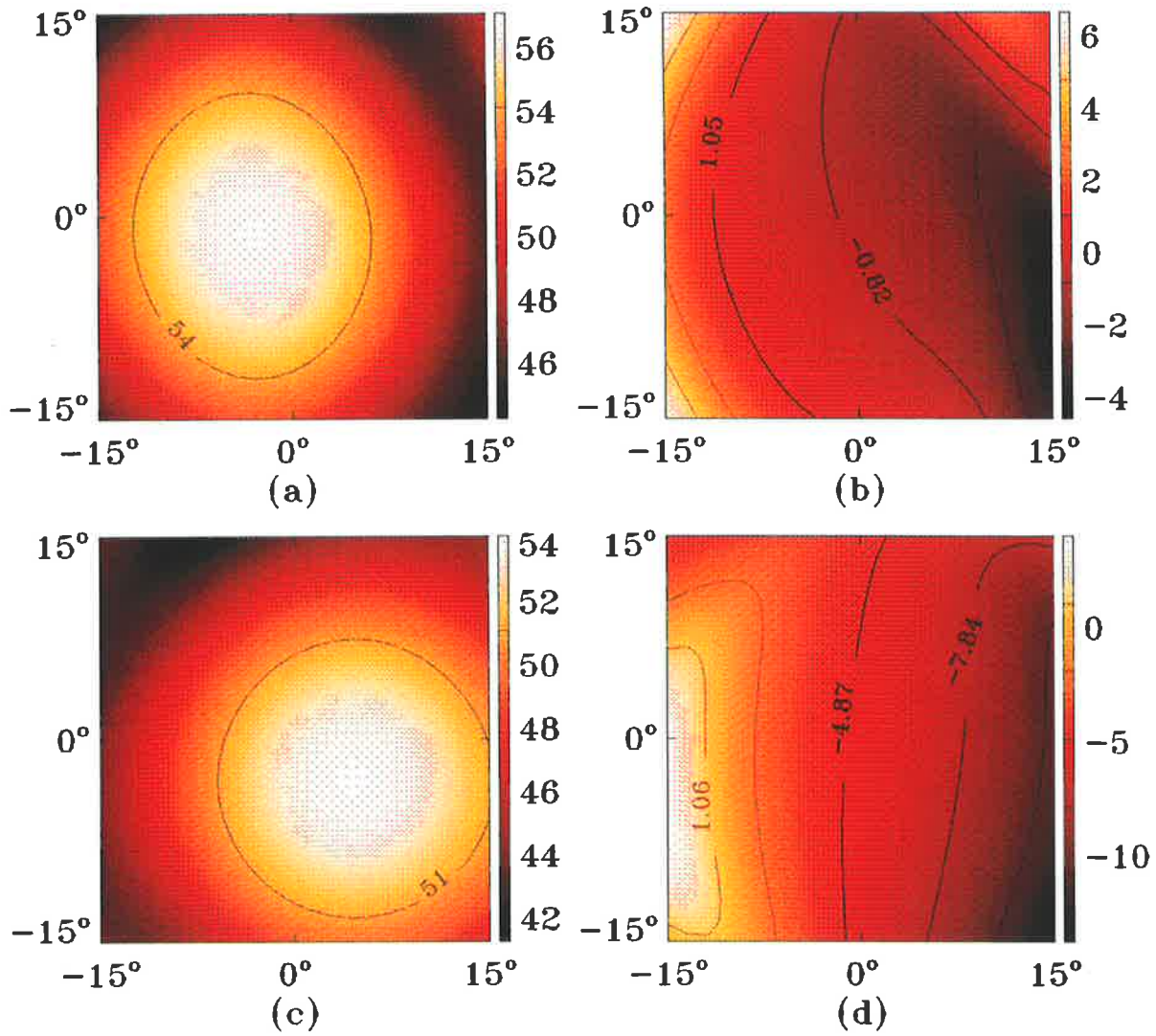

Figure 4.11: Angle–intensity plots of returned power and Doppler velocity as a function of beam pointing direction at a range of 92 km for the first two data acquisitions of the bp930514 data set. Acquisition one (Westwardly–directed transmitter beam) is displayed in panels (a) returned power, and (b) Doppler velocity, while acquisition two (Eastwardly–directed transmitter beam) is displayed similarly in panels (c) and (d). For both beam directions the off–zenith angle on transmission was 10°.

to lower altitudes, however, we notice that at first the scattering locations appear to "smear out" back towards the zenith, then seem to cluster about ever decreasing off-zenith angles until, in the lower range gates, the scatter returns predominantly to the zenith. This is a clear indication of the increasing aspect sensitivity of the atmospheric scatterers with decreasing altitude and demonstrates the the manner in which off-vertical Doppler radar beams are biased to apparent pointing angles much closer to the zenith than their nominal pointing angle would indicate, and is qualitatively consistent with other researchers' measurements of this parameter [*Lindner*, 1975b; *Hocking*, 1979; *Röttger*, 1981; *Reid*, 1988; *Reid*, 1990]. In the following subsection, we attempt to quantitatively determine the aspect sensitivity of the scatterers using the θ_S parameter.

4.3.2 Aspect sensitivity

In Chapter 3, the θ_S parameter was introduced in Equation 3.14 as

$$P(\theta) \propto e^{-\left(\frac{\sin^2\theta}{\sin^2\theta_S}\right)} . \tag{4.3}$$

If the power–polar diagram of the antenna aperture is modeled as Gaussian in form, then the power returned at angle θ to the zenith relative to that returned from the zenith is given by

$$P(\theta) = \exp\left\{-\left(\frac{\sin^2\theta}{\sin^2\theta_S}\right)\right\} \times \exp\left\{-\frac{(\sin\theta - \sin\theta_A)^2}{\sin^2\theta_B}\right\} , \tag{4.4}$$

where θ_A is the apparent beam–pointing direction and θ_B is the half–power half–width of the transmitter beam. As demonstrated by *Whitehead et al.* [1983], the effective beam direction, when aspect sensitivity effects are included, is equal to the angle at which the peak power is returned. Thus, Equation 4.4 is differentiated to yield

$$\frac{\partial P(\theta)}{\partial\theta} = -2\cos\theta\left\{\frac{\sin\theta}{\sin^2\theta_S} + \frac{\sin\theta - \sin\theta_A}{\sin^2\theta_B}\right\} P(\theta) . \tag{4.5}$$

Clearly, this may be zero if

- $\cos\theta = 0$, whereupon $P(\theta)$ is a minimum,
- $P(\theta) = 0$, whereupon $P(\theta)$ is a minimum or
- $\frac{\sin\theta}{\sin^2\theta_S} + \frac{\sin\theta\sin\theta_A}{\sin^2\theta_B} = 0$ whereupon $P(\theta)$ is a maximum.

The maximum value of $P(\theta)$ occurs at some angle which we denote θ_E. Thus

$$\sin\theta_E = \frac{\sin\theta_A \sin^2\theta_S}{\sin^2\theta_S + \sin^2\theta_B} . \tag{4.6}$$

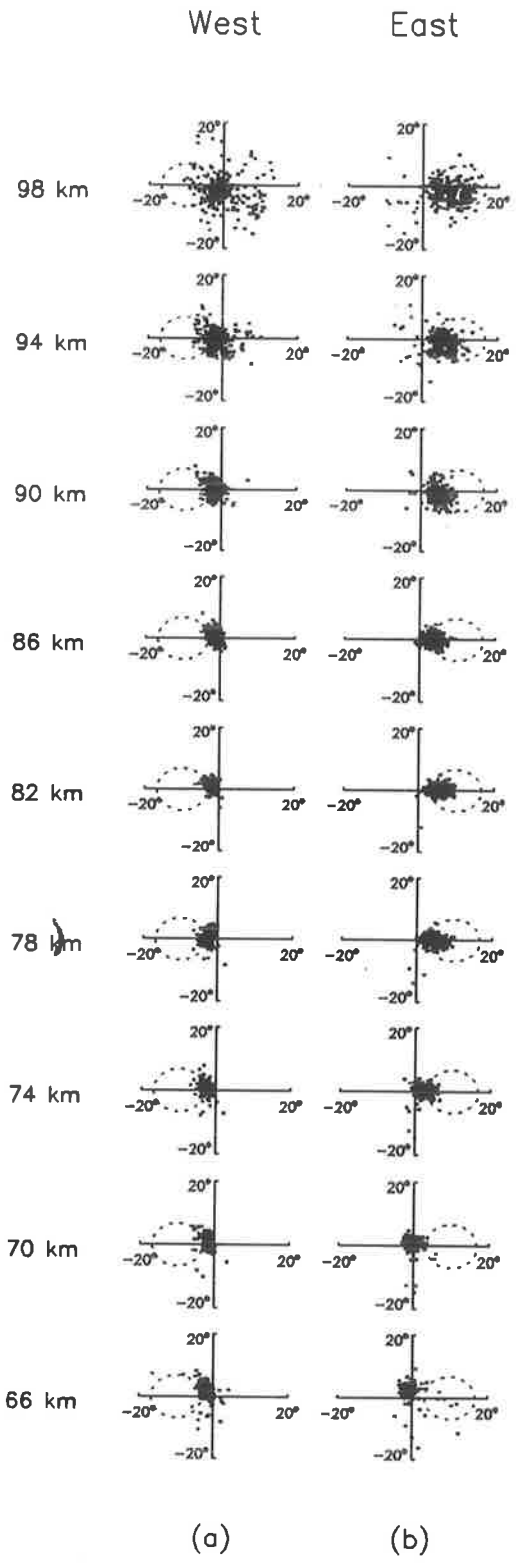

Figure 4.12: Angle of arrivals for 9 range gates calculated from receivers (2, 3, 5) and separated into (a) West and (b) East transmitter beam directions. Note that the mean off–zenith angle of scatter decreases with decreasing range. Note also that the maximum off–zenith angle labeled on each of the axes is ±20°. The dotted circles on each panel represent the 3 dB level of the transmitted beam.

We may rearrange Equation 4.6 to find θ_S so,

$$\sin^2\theta_S = \frac{\sin^2\theta_B}{\frac{\sin\theta_A}{\sin\theta_E} - 1} \,. \tag{4.7}$$

Therefore, knowing the apparent radar beam–pointing direction (θ_A), and the radar beam–width when the array is phased to point in the direction θ_A, and measuring the angular position of the peak of the backscattered signal power (θ_E), the aspect sensitivity of the scatterers θ_S, may be determined.

The radar beam width θ_B, was found by modeling the 30 antenna array phased to point 10° off–zenith towards the West. The aperture modeling program, "xsect" was used and the one–way half–power half–width of the tilted beam in the East–West plane was found to be 6.76°. θ_A was set in the current experiment at ±10°. In order to determine θ_E, the surfaces of returned power as a function of beam angle derived by using the post–set beam steering technique were examined. The position of the maximum was noted, and an East–West cross section was taken through this position. Since the angular separation between individual beam–pointing directions calculated using the PBS technique was only 1.5°, it was necessary to interpolate between angular steps to find the best estimate of the power maximum. Thus, a second–order polynomial was fitted to the points in the immediate vicinity of the maximum, and the position of the maximum of the fitted function was taken as the effective beam–pointing direction θ_E.

The analysis was performed on the first two data records obtained during the bp930514 campaign and the results appear in Figure 4.13a and b. In Figure 4.13a the profile of the aspect sensitivity parameter θ_S, is calculated from the first data record of the bp930514 data set. During this record, the transmitting array was phased to point Westwards at an off–zenith angle of 10°. As can be seen, the average value of θ_S as determined by the analysis appears to be about 6°, with a tendency for the θ_S values to increase in magnitude with altitude. Consideration of Equation 3.14 reveals that larger values of θ_S denote less aspect sensitive scatter, while small values of θ_S denote highly specular scatter. In contrast to this general behaviour, a large enhancement in the θ_S magnitude can be seen at an altitude of 82 km. Whether this enhancement is real, or simply some artifact of the analysis technique is uncertain. Clearly assumptions regarding the functional form of the scatterers' backscattered power as a function of angle may, at times, be incorrect. Alternatively, these layers of more isotropic scatter may indeed be real, and it is noted that *Fritts & Vincent* [1987] found a similar enhancement in θ_S at an altitude of 76 km, also at medium frequencies.

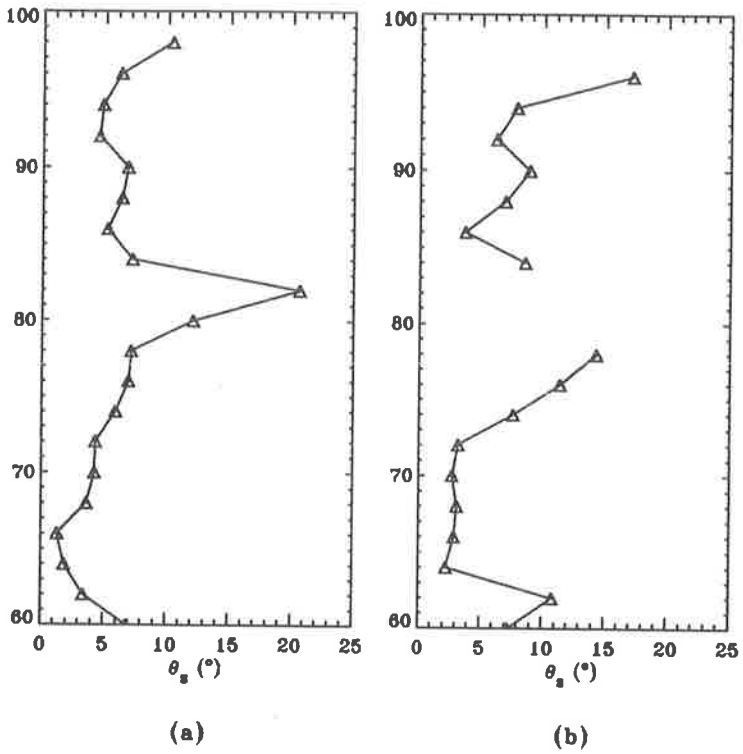

Figure 4.13: Profiles of the aspect sensitivity parameter θ_S derived from data steered using the PBS technique. In panel (a), the first 102.4 s data record from the bp930514 data set was used in the θ_S calculation, while in (b) the profile was calculated using data from the second 102.4 s record. Note that the transmitter beam was directed at 10° to the zenith along a Westward and then Eastward bearing during the first and second data acquisitions respectively.

In Figure 4.13b the θ_S values calculated using the data from the second acquisition are displayed. During this second acquisition, the transmitter beam was directed at 10° to the zenith on an Eastwardly bearing. Missing data points at altitudes of 80 km and 82 km are due to unphysically large values of θ_S obtained from data which caused the analysis to become extremely unstable. Again, there is some tendency for the θ_S values to increase with altitude, and again there is evidence for an enhancement in θ_S magnitude at about 78 km. The average value of θ_S obtained from Figure 4.13b is approximately 7°.

These unaveraged estimates of aspect sensitivity in the mesosphere clearly demonstrate the validity of the measurement technique. Even in its least refined form, this method shows promise for the routine measurement of mesospheric aspect sensitivities in the future.

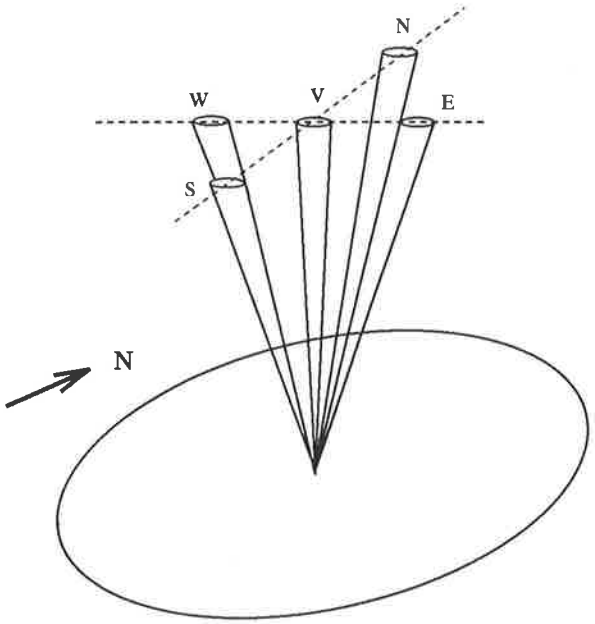

Figure 4.14: The transmitter beam geometry for the bp930523 data set. The five beams are directed towards the zenith and at 10° from the zenith in the Westward, Eastward, Southward and Northward directions.

4.4 Transmission Using Five Beam Directions

With minimal modification, the acquisition software was configured such that the transmitter beam was steered to a total of five separate directions. The directions, in order of acquisition, were vertical, West, East, South and North, with each of the non–vertical beams having off–zenith angles of 10°(see Figure 4.14). Since each individual data record required two minutes to acquire, the five beam direction cycle was completed in a total of 10 minutes. In this experiment, spaced antenna winds were calculated using the information from the vertically–directed beam, and were therefore available every 10 minutes. The remaining radar parameters were left unchanged from the bp930514 campaign, as was the antenna configuration. The experiment commenced on the 23^{rd} of May, 1993 and will be referred to as the bp930523 campaign, or data set.

4.4.1 Time domain interferometry

The first analysis undertaken with the bp930523 data set was the standard time–domain interferometry technique described in Chapter 3. In this case, however, residual channel phase errors were removed by subtraction of the position of the phase difference histogram peak calculated from the vertically–directed beam data only. In this way, the uncertainties involved with using two–week old phase corrections were avoided.

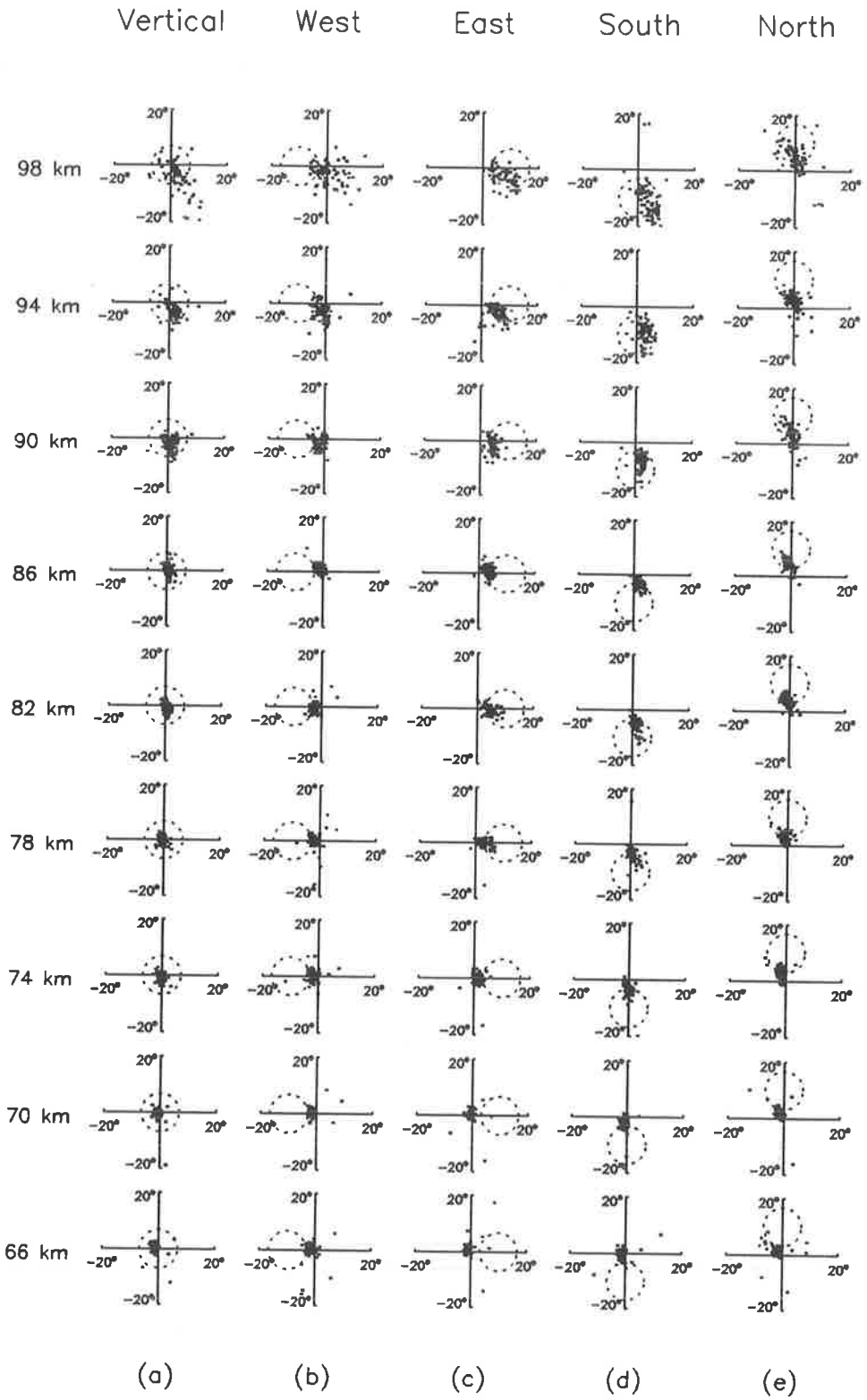

Figure 4.15: Angle of arrivals for the bp930523 data set calculated from receivers (2, 3, 5) and separated into (a) Vertical, (b) West, (c) East, (d) South and (e) North 10° off–zenith directions. Only 9 representative range gates have been displayed. Note that the axes in this figure are scaled between ±20°. Also indicated on each panel is the 3 dB threshold of the steered transmitter beam.

In Figure 4.15 the time–domain mean angle of arrival information is displayed for nominal ranges from 66 km to 98 km. The angle of arrival information is further separated into five groups, each representing one of the five beam directions implemented in this experiment. In Figure 4.15a the vertically–directed beam returns are shown from which we note the usual reduction of scatter from the zenith with decreasing range. In Figures 4.15b–e the mean angle of arrivals for transmitter beams directed at 10° to the zenith in the West, East, South and North directions respectively are displayed. We note that in each case the mean off–zenith position of the scatter moves closer to the zenith with decreasing altitude, again indicating the presence of increasing scatterer aspect sensitivity. As in Figures 4.9 and 4.10 some systematic bias of the scatter away from the cardinal directions is apparent, as is a tendency for the scatter to be displaced to the East in Figures 4.15b and c. This Eastward shift may be due to a residual phase error, but inspection of the data at ranges below 74 km seems to indicate that the shift is slightly reversed, and towards the West. For this reason no attempt was made to eliminate any residual phase error, the resultant shift being considered too small to cause concern at present.

Inspection of Figures 4.15a–e clearly shows that the mean position of the backscattered power is qualitatively consistent with the transmitter beam direction and the known angular reflectivity characteristics of the atmospheric scatterers as a function of altitude. It was concluded that the beam steering software, as configured for the five beam directions, was functioning as expected and that the transmitter beam was being successfully directed towards the required azimuth and zenith angle.

With the inclusion of the vertically–directed beam in the bp930523 data set, it was possible to compute spaced antenna winds for every fifth record. The experiment was designed primarily to validate the beam steering function of the new Doppler radar, but had also as its aim a comparison of spaced antenna and time–domain interferometric–derived winds. In the next subsection, spaced antenna winds are presented, while in the following subsection, time–domain interferometric winds are calculated and compared with the space antenna–derived winds.

4.4.2 Spaced antenna wind analysis

The standard spaced antenna wind analysis was applied to those records in the bp930523 data set for which a vertically–directed transmitter beam was in use. Antennae (2, 3, 5) were selected for the analysis in order to minimize antenna configuration biases in the results.

Antennae (3, 4, 8) were also used in a separate spaced antenna wind analysis and provided a check to ensure that the measured wind vector did not depend markedly on the particular antenna triangle selected. Few spaced antenna wind velocities were successfully calculated below about 66 km, and so little emphasis should be placed upon the wind measurements made in this altitude region. It should also be emphasised that, since wind measurements were available at best every 10 min, the statistical significance of any average wind vector, such as an hourly average, must necessarily be lower than if only a vertical beam had been in use. With these points in mind we examine Figure 4.16 which depicts the two average wind profiles for the antenna groups (2, 3, 5), represented by the symbol "□", and group (3, 4, 8) represented by the symbol "△", for (a) zonal, and (b) meridional wind components. Each average profile is calculated from a total of 23 hr of data.

As can be seen from Figure 4.16, the agreement between the two spaced antenna groups is good, with all points of the second profile overlapped by the standard deviations of the points of the first. Indeed, below 94 km the agreement is often exact, with some deviation between 80 km and 84 km. Below 68 km in this data set, little reliability is attached to any accepted wind measurement, and so variations between the two spaced antenna groups are neither surprising, nor significant.

4.4.3 Time–domain interferometric wind estimation

Associated with each angle of arrival in Figure 4.15 is an estimate of line–of–sight Doppler velocity. If we assume that the mean angle of arrival represents the power weighted mean position of the backscattered signal over the radar's beam width, then the Doppler velocity associated with the average return must represent the power–weighted line–of–sight velocity of the illuminated region. If three or more non–colinear points are available at any particular range gate, then the 3–dimensional wind velocity vector, (u,v,w) may be estimated if the mean wind field is assumed to be linear. In theory, if enough independent angle of arrival points are available, more complicated wind fields may be measured, but this is clearly impractical when using time–domain interferometry, as the time resolution of each wind field estimate would be far too low. Since only one angle of arrival measurement can be extracted for each 104.2 s time series, at least three data records must be analysed to find the linear mean wind field. In practice, five data acquisitions were used to determine each wind field as this was the number of acquisitions making up a complete cycle of steered beam directions on transmission.

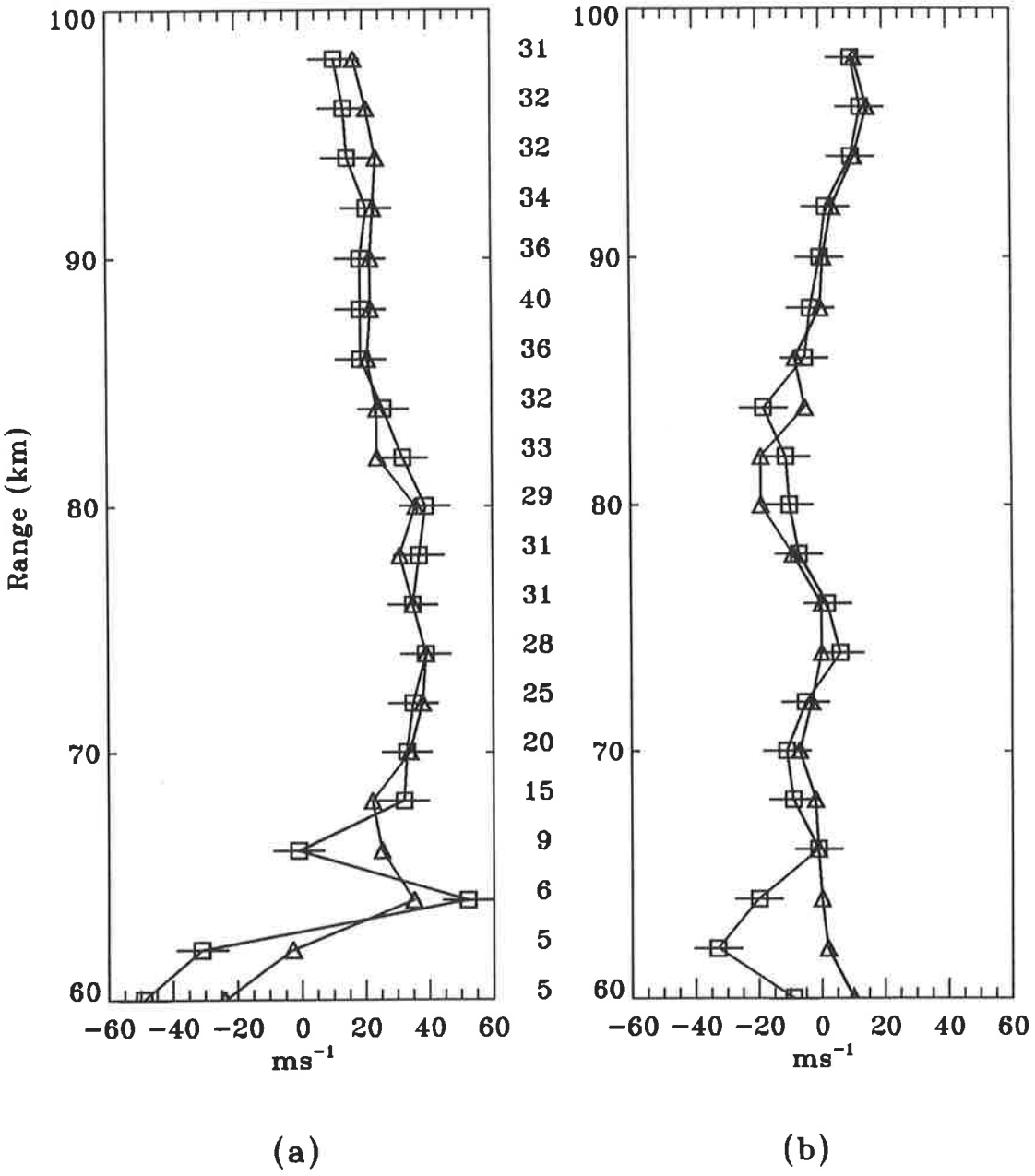

Figure 4.16: Spaced antenna wind profile for the bp930523 data set calculated from antenna groups (2, 3, 5), represented by the symbol "□", and (3, 4, 8) represented by the symbol "△", for (a) zonal, and (b) meridional wind components. The horizontal error bars are the average differences between the simultaneous measurements of the wind as estimated from the two different antenna groups. The integers appearing between the two profiles indicate the number of accepted data points at each height used to calculate the average profile and are also only applicable to antennae (2, 3, 5). The profiles are calculated from a total of 23 hr of data.

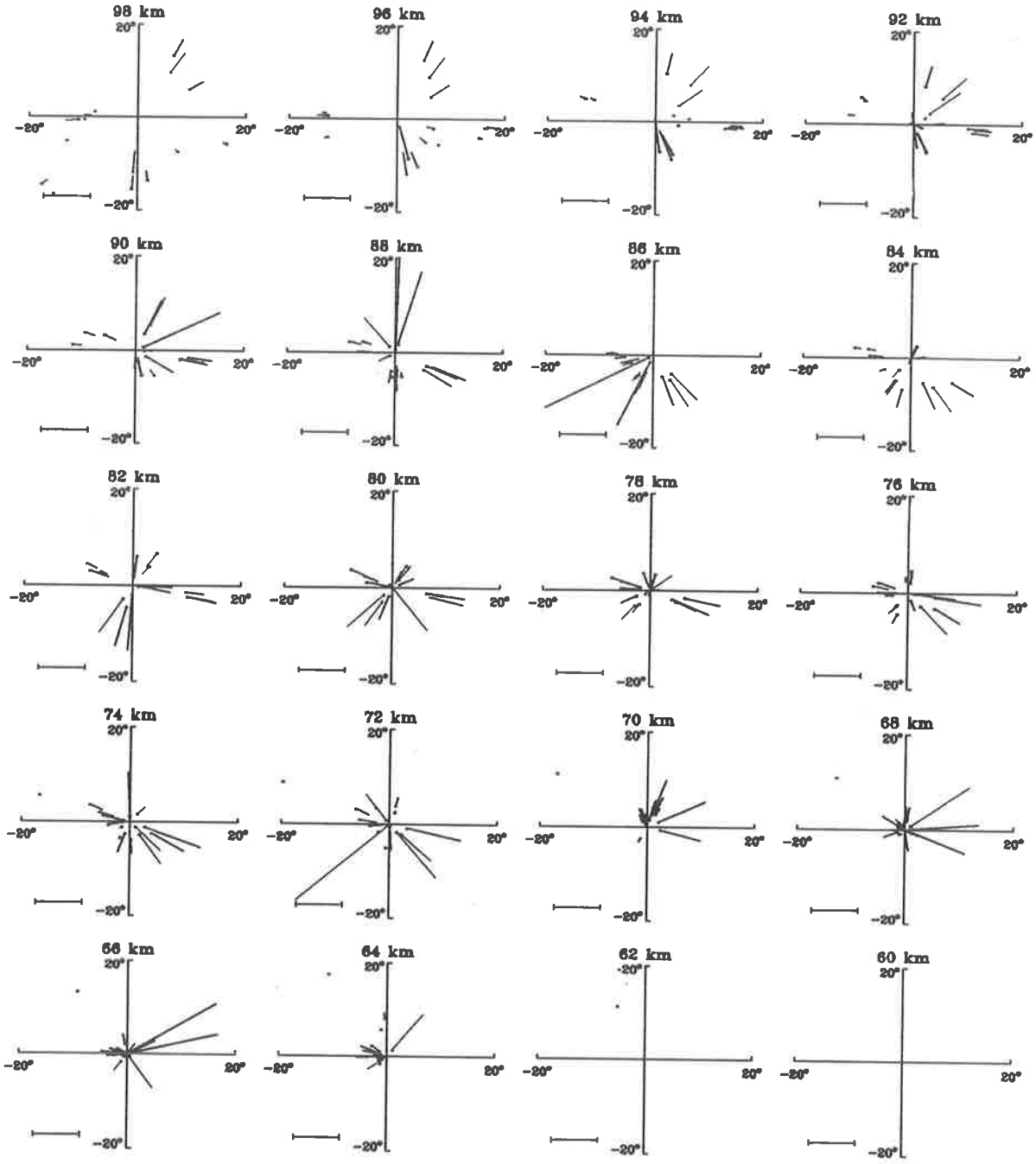

Figure 4.17: Angle of arrivals for the bp930523 data set with associated Doppler velocities indicated by lines extending from the angle of arrival point. The data have not been range corrected (see text). The velocities indicated are actually inferred horizontal velocities calculated with the assumption of no vertical velocity. A horizontal wind speed of 100 ms^{-1} is indicated by the horizontal bar located in the lower left–hand corner of each sky map. Note the axis scaling which extends to $\pm 20°$ in each case.

In Figure 4.17 the angle of arrival information for one–half hour of data from the bp930523 data set are displayed with the associated Doppler velocity for each point indicated by a line extending from the angle of arrival point in the direction of the radial velocity. The length of the line in each case is an estimate of the horizontal wind vector that would have given rise to the particular radial Doppler velocity in the absence of any vertical motion. A horizontal velocity estimate of 100 ms^{-1} is indicated by the bar in the lower left–hand corner of each sky map. It should be noted that before these velocities can be used to estimate a mean linear wind field, they must be range–corrected to ensure that each velocity is used for the appropriate height. For example, a mean angle of arrival appearing at an off–zenith angle of 10° in the 90 km range gate is actually associated with atmospheric motion at an altitude of approximately 88 km. In Figure 4.18b, the range–corrected distribution of returns with altitude are shown. Note that each uncorrected range can have a maximum of 323 returns, the maximum number being achieved only if none of the records were rejected on the basis of poor signal–to–noise ratio. Inspection of Figure 4.18a shows that many of the records in the lower range gates have been excluded. In the highest range gate, only about one–third of the angle of arrival points remain once range correction is carried out. Excellent numbers of returns are available at corrected ranges from 64 km to 96 km.

With the angle of arrival points range–corrected, the Doppler velocities associated with these points are fitted using the least–squared fitting procedure reported by *Adams et al.* [1986] and used by other researchers such as *Meek & Manson* [1987] (although both of these studies utilized the least–squared fitting technique on Doppler sorted interferometric data). A brief outline of this three–dimensional fitting technique follows.

Suppose that the mean wind field at some height h, is linear throughout the field of view of the radar, and is described by

$$\underline{V} = u\underline{i} + v\underline{j} + w\underline{k} \, . \tag{4.8}$$

Let the radar measure a radial velocity V_R, at some position with x, y and z direction cosines l, m and n. V_R is simply the projection of the mean wind vector onto the radar's (unit) line–of–sight vector $\underline{L}$,

$$\underline{L} = l\underline{i} + m\underline{j} + n\underline{k} \tag{4.9}$$

with n determined from l and m by

$$n = \sqrt{1 - l^2 - m^2} \, , \tag{4.10}$$

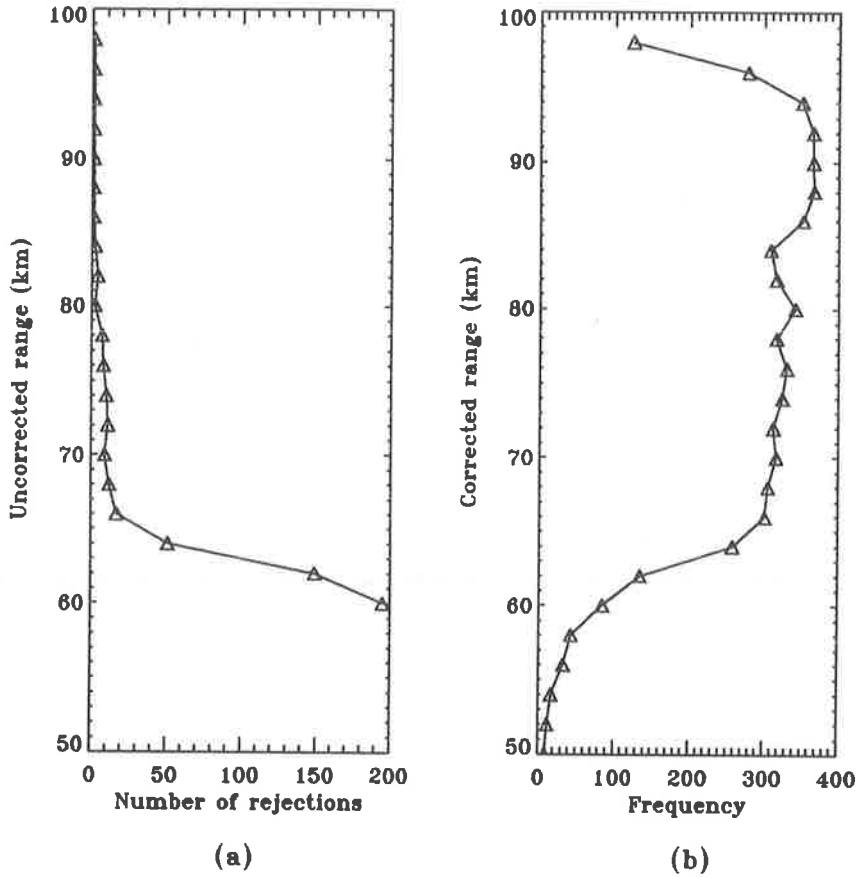

Figure 4.18: (a) The distribution in range of the number of records excluded on the basis of low signal–to–noise ratio for the bp930523 data set. (b) The distribution in height of the number of range–corrected angle–of–arrival points. Note that 323 data points at each uncorrected range were available.

and so

$$\begin{aligned} V_R &= \underline{L} \cdot \underline{V} \\ &= lu + mv + \sqrt{1 - l^2 - m^2}w \ . \end{aligned} \tag{4.11}$$

We must choose our fitted u, v and w to minimize the mean squared error,

$$\epsilon = \frac{1}{N} \sum_i \left\{ V_{R_i} - l_i u - m_i v - \sqrt{1 - l_i^2 - m_i^2} w \right\}^2 \ , \tag{4.12}$$

where N is the total number of points fitted. In order to minimize ϵ, the partial derivatives with respect to u, v and w of Equation 4.12 must be found and examined for turning points. Performing the differentiations and setting the derivatives to zero yields

$$\frac{\partial \epsilon}{\partial u} = 0 \ , \ \textit{iff}$$

$$\begin{aligned}
\sum_i l_i V_{R_i} &= u\sum_i l_i^2 + v\sum_i m_i l_i + w\sum_i l_i n_i \ , \\
\frac{\partial \epsilon}{\partial v} &= 0 \ , \ \textit{iff} \\
\sum_i m_i V_{R_i} &= u\sum_i l_i m_i + v\sum_i m_i^2 + w\sum_i m_i n_i \ \text{and} \\
\frac{\partial \epsilon}{\partial w} &= 0 \ , \ \textit{iff} \\
\sum_i n_i V_{R_i} &= u\sum_i l_i n_i + v\sum_i m_i n_i + w\sum_i n_i^2 \ , \qquad (4.13)
\end{aligned}$$

where n_i is as defined in Equation 4.10. We can rewrite Equation 4.13 in matrix form as

$$\begin{pmatrix} \sum_i l_i^2 & \sum_i l_i m_i & \sum_i l_i n_i \\ \sum_i l_i m_i & \sum_i m_i^2 & \sum_i m_i n_i \\ \sum_i l_i n_i & \sum_i m_i n_i & \sum_i n_i^2 \end{pmatrix} \begin{pmatrix} u \\ v \\ w \end{pmatrix} = \begin{pmatrix} \sum_i V_{R_i} l_i \\ \sum_i V_{R_i} m_i \\ \sum_i V_{R_i} n_i \end{pmatrix} , \qquad (4.14)$$

and solve for u, v and w by using standard single–value decomposition computational techniques.

In Figure 4.19a–c the wind profile calculated using the time–domain interferometric technique appled over the 10 minutes of data required for the complete cycle of 5 transmitter beam directions is compared with the spaced antenna–derived wind. Figure 4.19a depicts the magnitude of the wind, while Figure 4.19b depicts the direction of the wind as a bearing. Finally, in Figure 4.19c the vertical velocity measured by TDI, and the approximate vertical velocity measured by the spaced antenna analysis are displayed together. In all three panels, the TDI wind estimate is marked by the symbol "$\triangle$", while in panels a and b the spaced antenna true wind is marked by the symbol "$\diamond$", and the apparent wind by the symbol "$\square$". In Figure 4.19c the spaced antenna vertical velocity estimate is marked by the symbol "$\diamond$".

Following Figure 4.19 are Figures 4.20 and 4.21. The three figures represent comparisons between the TDI velocities and spaced antenna true wind velocities which we qualitatively describe as "good", "average" and "poor" respectively.

Examination of about 7 hr of data in this form yielded the following qualitative assessment of the frequency of the three types of agreement; good agreement 40%, average agreement 33% and poor agreement 27%. A possible source of error in all of the profiles examined is a result of the temporal non–stationarity of the atmosphere. Since the spaced antenna analysis can only be performed on data recorded during transmission using a vertically–directed beam, the spaced antenna winds are only available for 2 out of 10 min. The winds calculated from the TDI analysis, on the other hand, are estimated using the full 10 min of data. Clearly, if the wind field varies over a period of 10 min, then the TDI and spaced

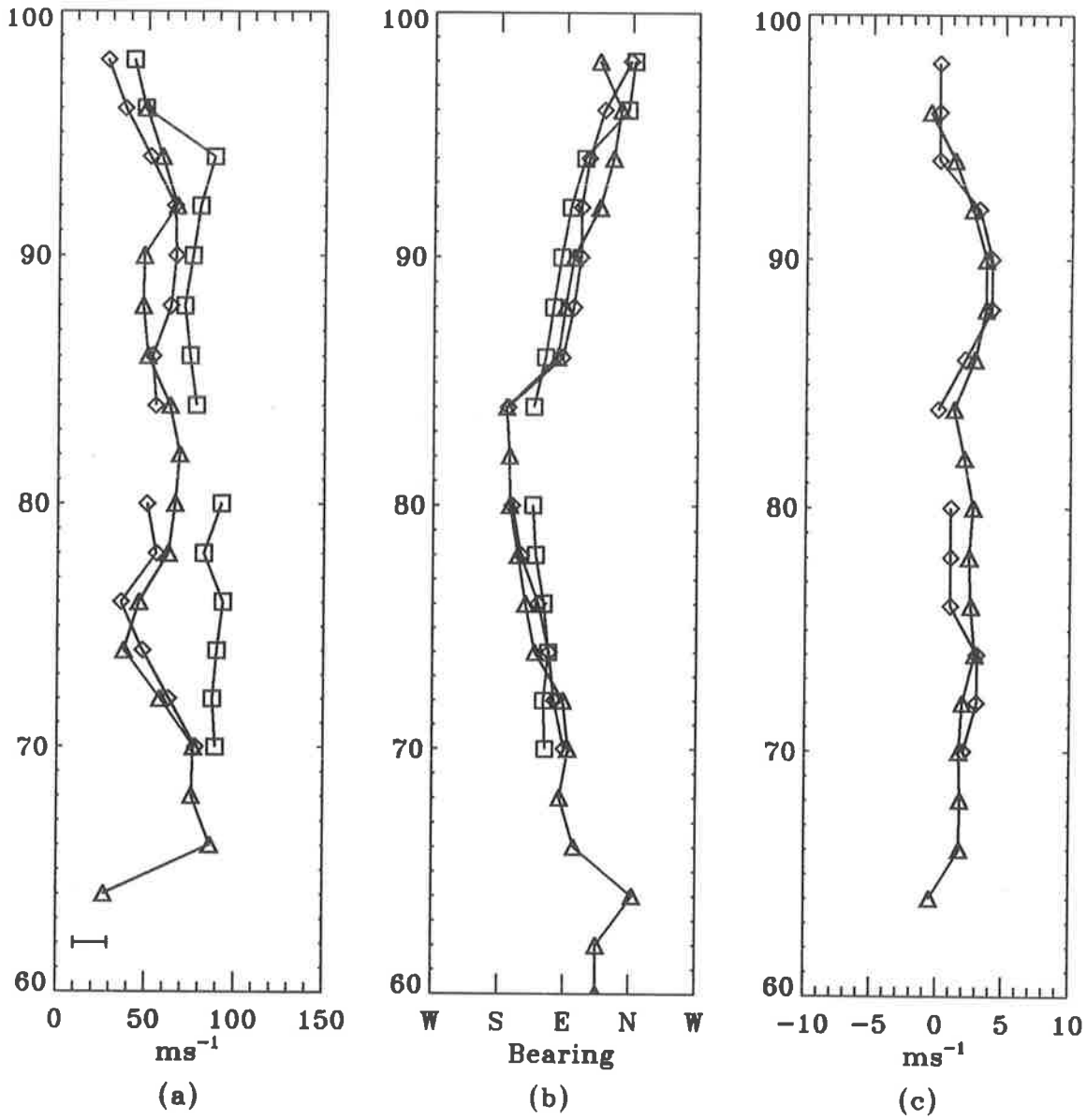

Figure 4.19: (a) 10 min profiles of wind magnitudes measured by TDI "△", spaced antenna true velocity "◇" and spaced antenna apparent velocity "□". A representative error bar for the spaced antenna true velocity appears in the lower left–hand corner of the panel. (b) As in (a), but for the wind direction. (c) As in (a), but for vertical velocities. Note that the spaced antenna measurement of vertical velocity is an estimate only. These profiles represent "good" agreement between the spaced antenna true wind, and the TDI–derived wind.

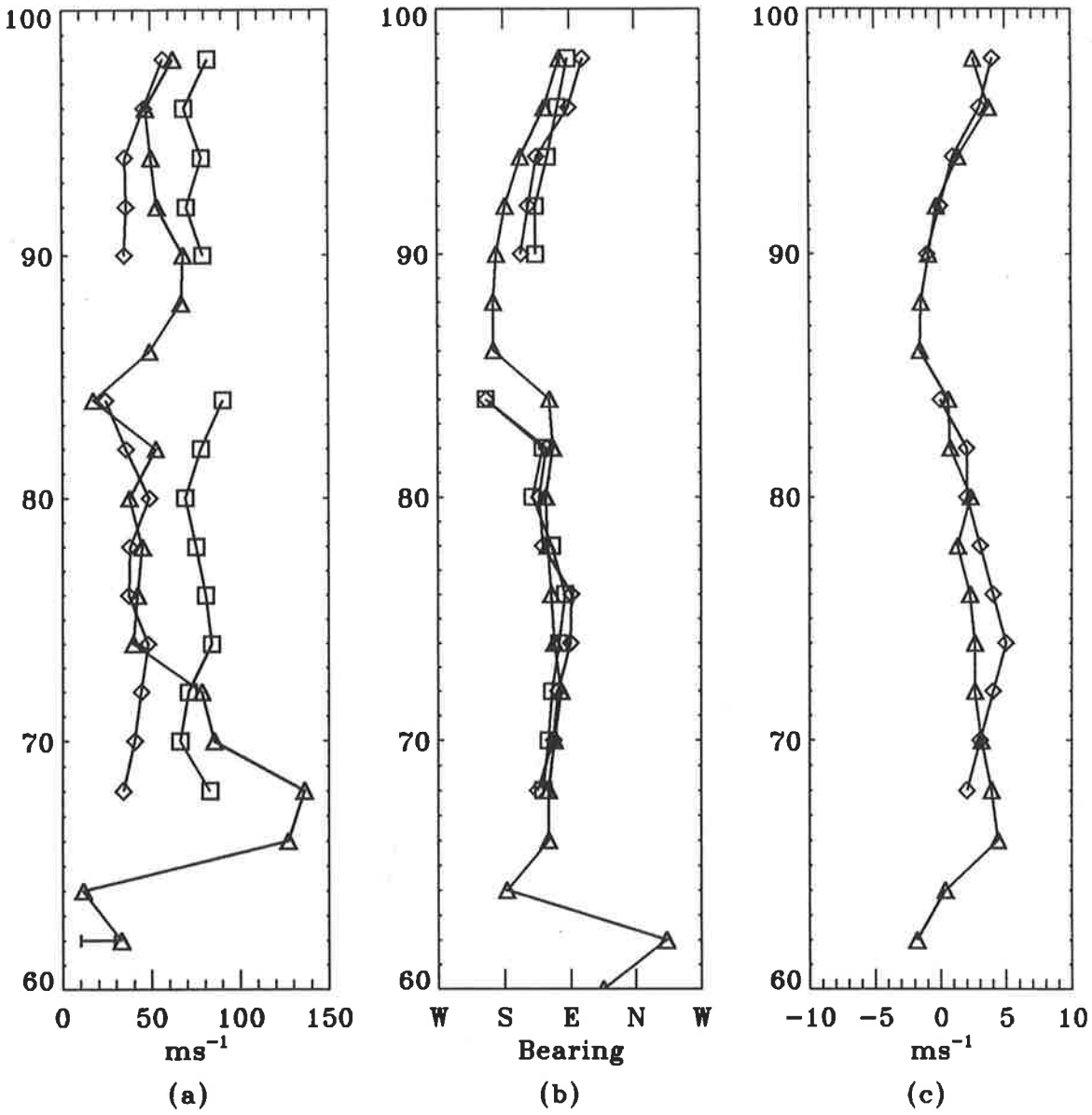

Figure 4.20: As for Figure 4.19, but for data displaying only "average" agreement between the TDI wind estimate and the spaced antenna true velocities.

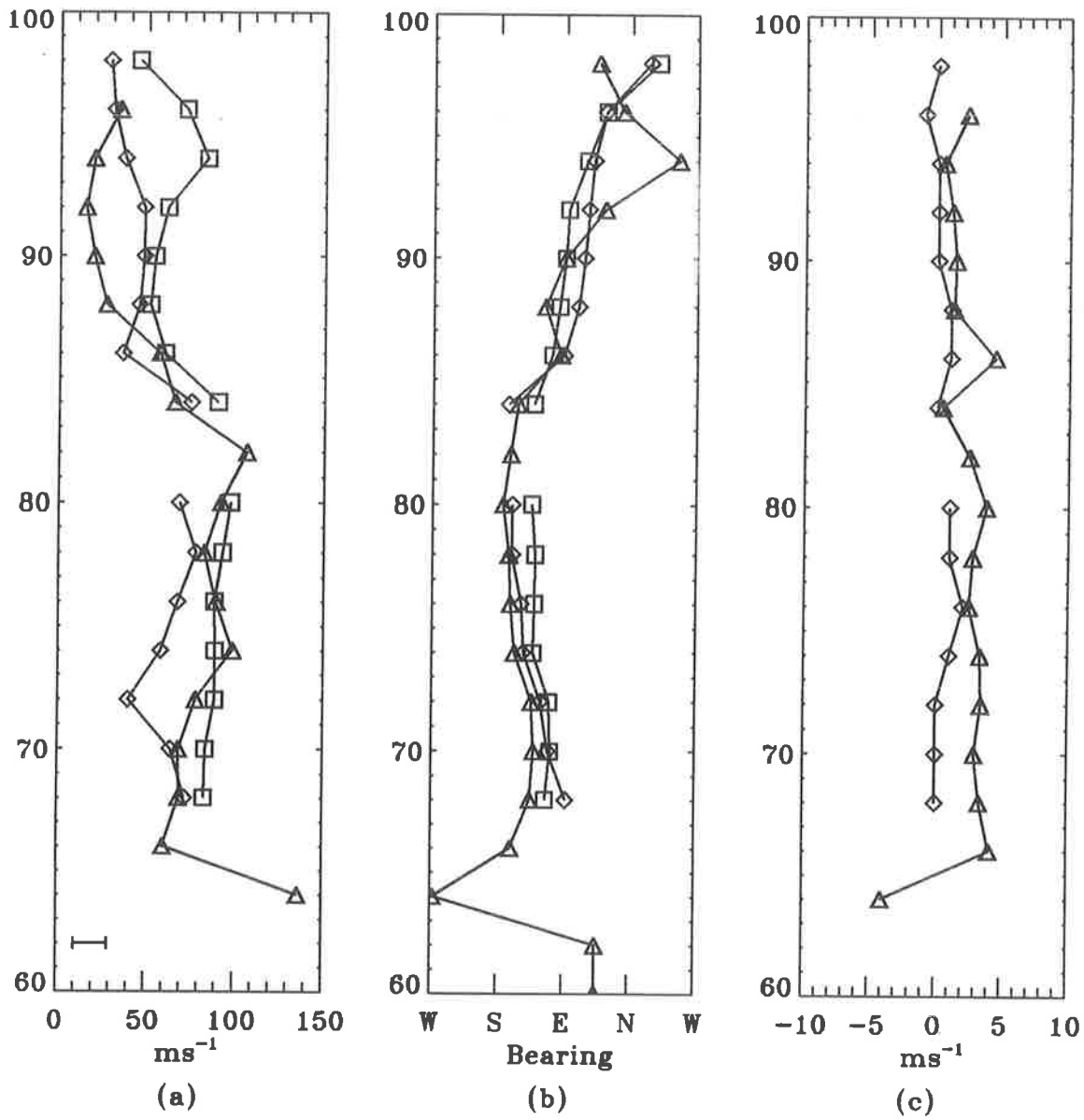

Figure 4.21: As for Figure 4.20, but for data displaying only "poor" agreement between the TDI wind estimate and the spaced antenna true velocities.

antenna wind estimates must diverge, as the TDI estimate is displaced in time (on average) by about 4 min.

Two other similar sources of error are also possible. The first again involves the temporal non–stationarity of the atmospheric wind field. Given that the (linear) wind field varies during the 10 min data acquisition, it is unclear what wind the TDI analysis will record. If the wind changes rapidly enough for the spaced antenna record to be affected, then additional uncertainty must be present. The second additional source of error involves the linearity of the wind field. The TDI analysis explicitly assumes a linear wind field, and must therefore be in error if a non–linear wind field is present. It is less clear, however, the manner in which the spaced antenna analysis estimates a single velocity vector from an inhomogeneous wind field, as no explicit assumption of linearity is made. It is neither a simple task, nor one within the scope of this thesis to examine the effect of non–linear wind fields on either the spaced antenna or TDI wind estimate, and the reader is directed to studies performed by *Kudeki et al.* [1993] for more information.

A final source of error involves the number of range corrected points available in each range gate for fitting. A minimum of three non–colinear points are required in order to uniquely determine Equation 4.14. If the three points all lie near the zenith, however, the resultant uncertainty in the estimate of the horizontal wind field will be large. Consequently, the data were recast as one–half hourly profiles thus encompassing a total of 15 data acquisitions. That is, a total of three complete cycles of the five transmitter beam directions. Instead of simply averaging the three profiles obtained from the one–half hour of data, all of the angle of arrival points available were collated and used in the least–squared fitting algorithm to determine a single wind vector for the data set. The three profiles obtained from the spaced antenna analysis, on the other hand, were simply averaged in the normal way. Figures 4.22 to 4.24 display the first 3 half–hourly profiles of the bp930523 data set. The symbols used are as described for Figures 4.19 to Figure 4.21.

Clearly, these half–hourly profiles are much better behaved than the shorter 10 min profiles, and the agreement between the spaced antenna true wind and the TDI–derived wind is now quite evident. Although the agreement between the spaced antenna–estimated vertical velocity and that obtained by the TDI technique can only be described as poor, the profiles do exhibit excellent agreement on some occasions. Such poor agreement is hardly surprising, given the difficulting involved with measuring such small vertical velocities which are easily contaminated by large horizontal wind components. We expect the spaced antenna

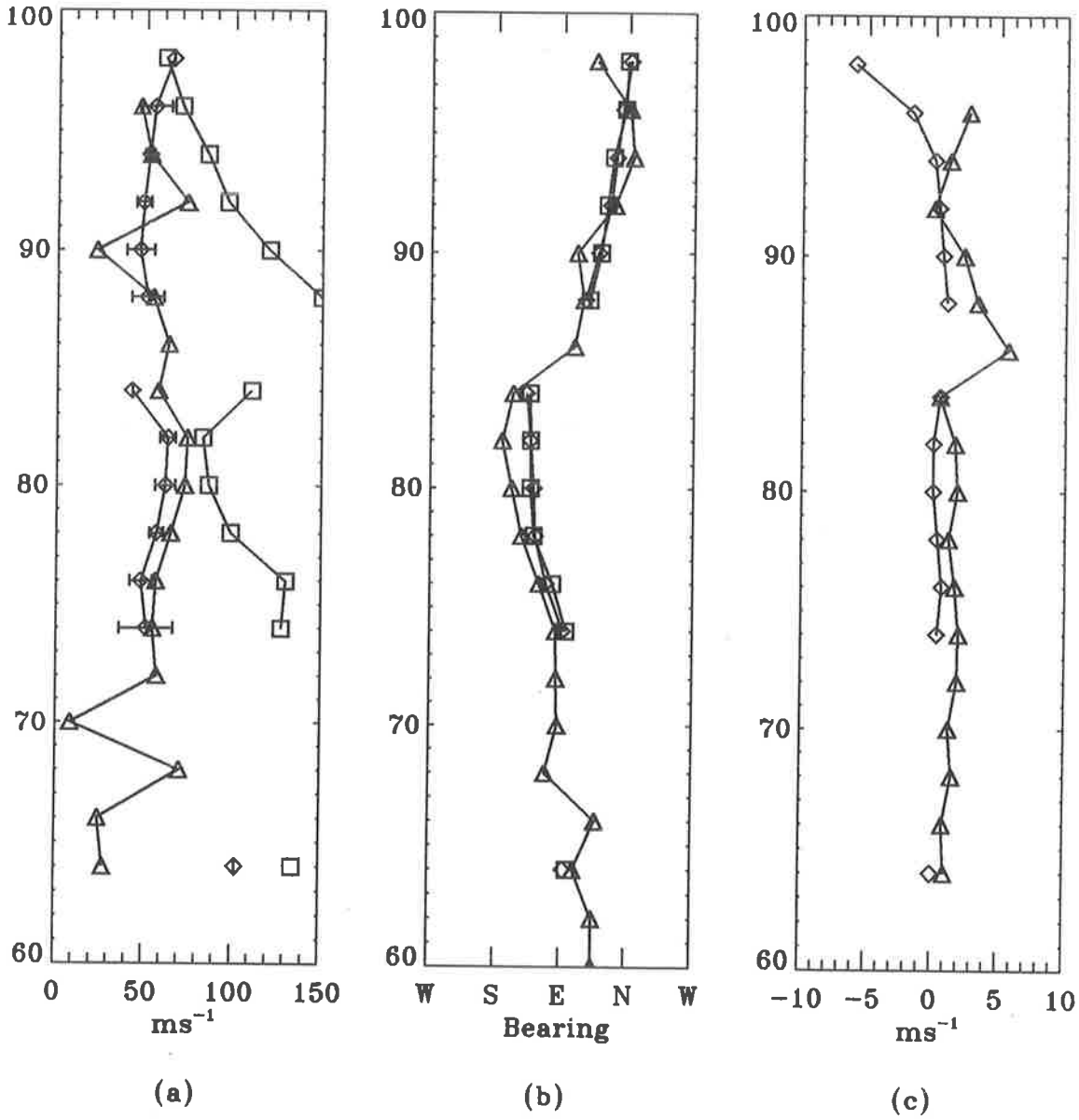

Figure 4.22: (a) 30 min profiles of wind magnitudes measured by TDI "△", spaced antenna true velocity "◇" and spaced antenna apparent velocity "□". (b) As in (a), but for the wind direction. (c) As in (a), but for vertical velocities. Note that the spaced antenna measurement of vertical velocity is an estimate only. Where possible, error bars derived from the standard deviation of the three wind estimates have been indicated for the spaced antenna true velocity only. These profiles were measured from the 1^{st} half–hour of the bp930523 data set.

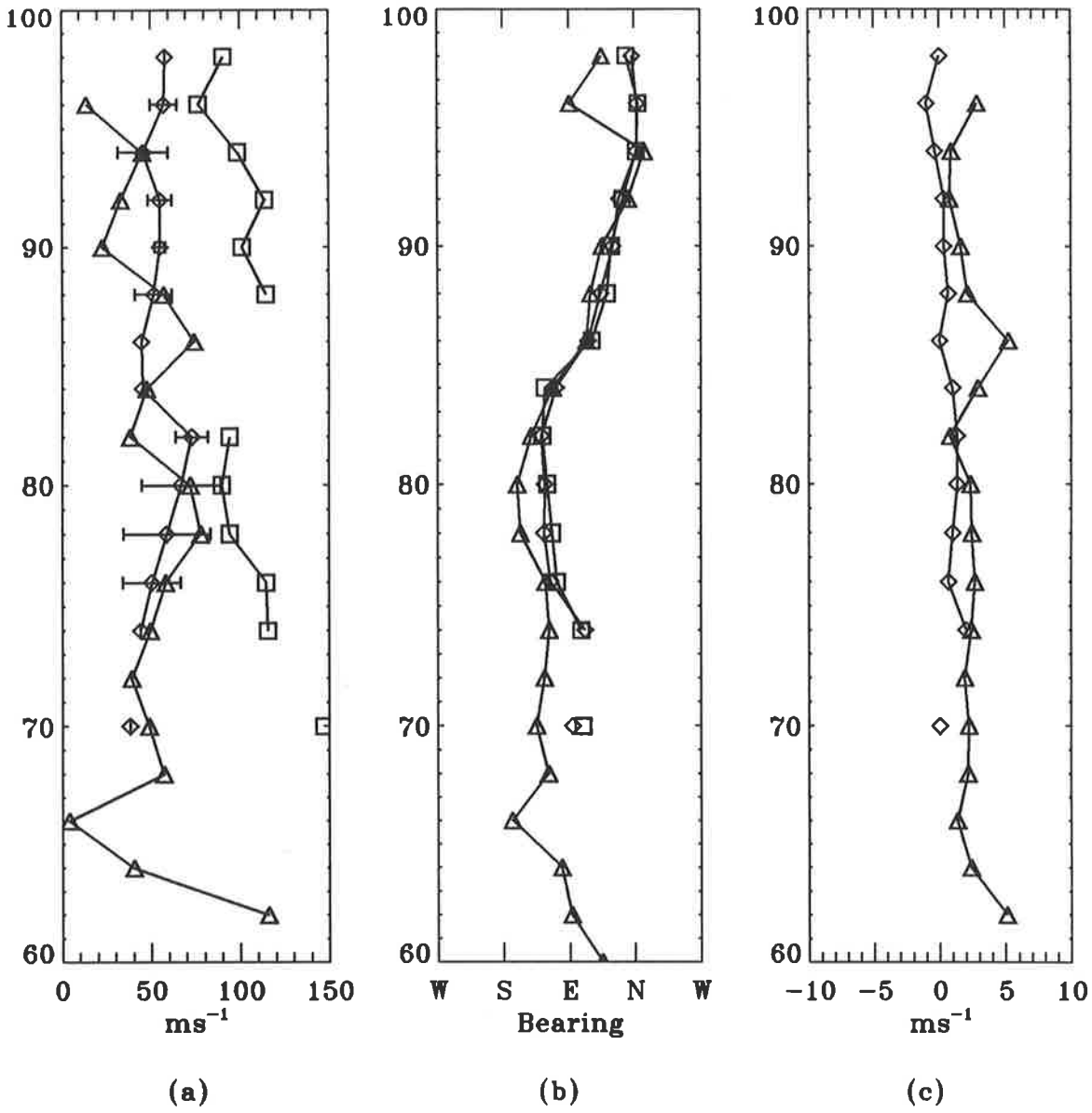

Figure 4.23: As for Figure 4.19, but for data taken during the 2^{nd} half–hour of the bp930523 data set.

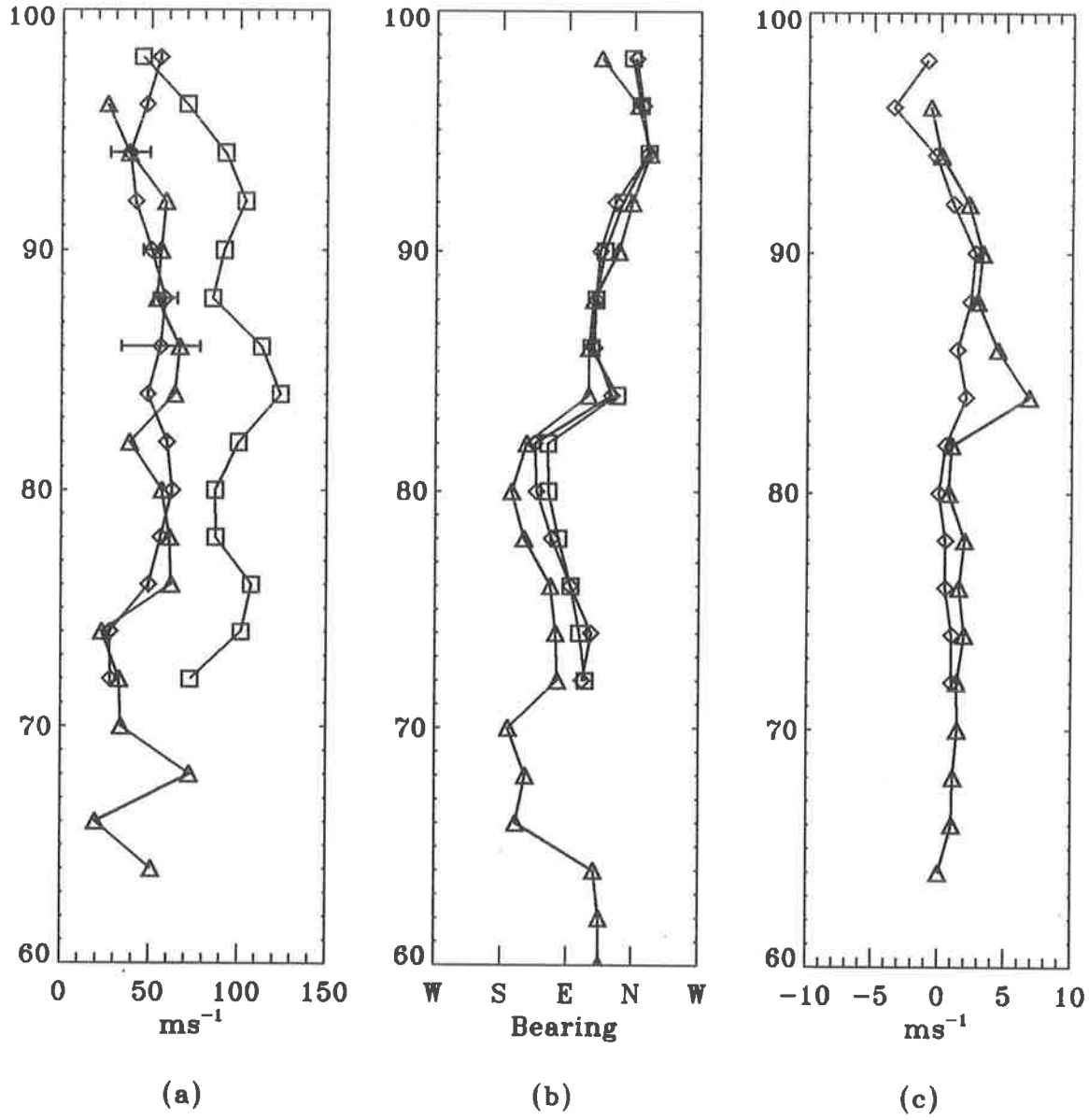

Figure 4.24: As for Figure 4.20, but for data taken during the 3^{rd} half–hour of the bp930523 data set.

estimate of vertical velocity to be in error if there exists any average tilt in the scattering layer. This gives rise to some finite off–zenith angle of arrival of the backscattered power and will allow some component of the horizontal velocity to "leak" into the radial Doppler velocity measured by a radar with a finite beam–width [*Palmer et al.*, 1991]. The TDI measurement of vertical velocity relies upon arguably more strict assumptions than that of the spaced antenna estimate. Thus, the TDI measurement of vertical velocity may be equally responsible for the large discrepancies sometimes observed.

Such measurements of radial Doppler velocity utilizing relatively broad beam–widths on reception and angle of arrival information are conceptually similar to true pre– and post–set beam steering experiments with multiple narrow–beam Doppler radars. In fact, the use of angle of arrival information arguably yields a better estimate of the mean position of the returned power than the use of narrower steered Doppler beams. For example, even with the use of the entire Buckland Park receiving array, the one–way half–power beam–width at 1.98 MHz is still 4.5°. If the returned power as a function of angle from the centre of the beam is not symmetrical, then the effective beam pointing angle will be incorrect. Due to the aspect sensitivity of atmospheric sattering layers, this is clearly the case in the mesosphere, [*Lindner*, 1975b; *Hocking*, 1979; *Röttger*, 1981; *Reid*, 1987; *Meek*, 1992], and corrections to the beam pointing angle must be applied. At best these corrections are valid on the average, as the day–to–day variability of mesospheric aspect sensitivity has been documented by *Czechowsky et al.* [1988] and *Lesicar* [1993]. The use of angle of arrival information obviates the need for these corrections, as the mean angular position of the returned power, and hence the effective beam pointing direction is known.

Although time–domain angle of arrival information has been utilized in the past, these measurements appear to represent the first use of the angle of arrival information to obtain the 3–dimensional wind field. *Meek & Manson* [1990] used TDI to find the directions and Doppler velocities of meteor trails at MF at Saskatoon, while others have used the TDI angle of arrival information to determine vertical velocities from uncorrected radial velocities at both MF, [*Brown*, 1992] and VHF, [*Larsen & Röttger*, 1991].

4.5 Summary

A total of 30 of the Buckland Park receiving array's 89 "E" dipoles were upgraded to allow transmission using the main array for the first time. The first of three transmitter sub–systems was installed and interfaced with the interim 8 channel receiving system. The first experiment conducted saw ten 2.5 kW power amplification modules phased together to produce a vertically–directed transmitter beam with a one–way half–power half–width of 7.5°. Power and signal to–noise ratio profiles were measured showing satisfactory day–time returns from 64 km to 98 km in altitude. Signal–to–noise ratios of about 20 dB were typical for all but the lowest four range gates. Time–domain interferometry was used to locate the power–weighted mean angle of arrival of the backscattered radiation. These angle of arrival data were consistent with those measured in Chapter 3, except for the reduction in spread from the zenith. This adherence to the zenith was ascribed to a combination of effects; first, the smaller two–way beam–width produced by the experimental configuration and second, the increase in power–aperture product and the resultant reduction in spurious returns at larger off–zenith angles. A spaced antenna wind analysis was also performed on the data and one–hour profiles were obtained which clearly showed the presence of the diurnal tide. The one–day average profiles for the 30^{th} of April and the 1^{st} of May, 1993 illustrated the presence of the Eastward zonal jet below the mesopause expected for this time of year. A large reduction in the data acceptance rate at night was noted and ascribed to the use of linearly polarized radiation. Post–set beam steering using the 8 receivers available was performed with the synthesised receiver beam steered to a total of 441 directions about the zenith. Both returned power and radial Doppler velocity were measured at each of the beam directions. The radial Doppler velocities were shown to be consistent with the spaced antenna–derived true wind estimate.

The radar's data acquisition software was modified to allow the independent phasing of the transmitter power amplification modules. The first transmitter beam steering experiment was conducted using two beams directed at 10° off–zenith on alternate data acquisitions towards the West and East. Time–domain interferometry was used to show that the direction of arrival of the mean power of the backscattered radiation came from the expected off–zenith direction on each data acquisition. A hitherto unseen effect, in which the time–domain angle of arrival information appeared to be biased towards the longest baseline of the antenna triangle used was found, and was shown to be dependent upon the antenna configuration

selected. Again, PBS was conducted, this time to confirm that the transmitter beam was directed in the East–West plane and that antenna configuration biases were responsible for the skewness observed with some antenna groups. In addition, an experiment was conducted which allowed the measurement of the mesospheric aspect sensitivity profile from the PBS information.

The data acquisition software was again modified in order to produce 5 beam directions on transmission. In addition to the four 10° off–zenith beams, a vertically–directed beam was included so that a standard spaced antenna analysis could be performed. Time–domain angle of arrival information was calculated to ensure that the expected beam directions were produced during the appropriate data acquisitions. The spaced antenna analysis was performed on two independent groups of spaced antennae and daily mean profiles examined to ensure that no significant differences existed. Radial Doppler velocities associated with each range–corrected angle of arrival point were used to estimate a linear wind field for each range gate in which three or more points existed. Profiles were obtained every 10 min and were compared to the spaced antenna–derived winds. Although the tendency for the interferometric–derived wind to agree with the spaced antenna–derived true wind was clear, significant differences between the two were often observed, with "good" agreement only seen in some 40% of the records. The data were then reanalysed in 30 min blocks and compared with 30 min averages of spaced antenna true and apparent wind profiles, whereupon the agreement was found to be excellent. Most significantly, the TDI–derived wind was found to be clearly at variance with the spaced antenna–derived apparent wind. Vertical velocities measured by the two techniques were found to agree well only during some periods.

Chapter 5

ON DOPPLER INTERFEROMETRY

5.1 Introduction

Despite many years of speculation and study, the precise mechanism, or mechanisms responsible for the backscatter observed at medium frequencies is, as yet, unclear. It is possible, however, to categorize the backscatter in terms of its aspect sensitivity. Generally, below about 80 km, quasi–specular backscatter is observed. Above 80 km, the backscatter becomes more isotropic, although strong specular returns are still occasionally observed.

Most radar techniques used for measuring various atmospheric parameters in the mesosphere assume a volume scatter model. That is, they assume that the backscattered signals recorded by the radar are distributed across the sky with varying phase and amplitude [*Ratcliffe*, 1956]. Examples of such "volume scatter" techniques include the spaced antenna technique and the multiple beam Doppler radar. Alternatively, techniques such as the Imaging Doppler Interferometer (see e.g., *Adams et al.* [1985]; *Adams et al.* [1986]; *Brosnahan & Adams* [1993]) generally assume discrete scatter, supposedly guaranteed in the experiment by phase differences between antennae indicating plane–wave down–coming radiation.

Other researchers [*Franke et al.*, 1990; *Sürücü et al.*, 1992] have employed a technique similar to the IDI technique in which phase differences are not checked for consistency with the plane–wave hypothesis. We will refer to this new experiment as the "Doppler radar interferometer" henceforth, and note that the technique is distinct from both the spatial radar interferometer [*Farley et al.*, 1981; *Palmer et al.*, 1991; *VanBaelen & Richmond*, 1991a;

VanBaelen et al., 1991b; *Larsen et al.*, 1992], and the Doppler–sorted radar interferometer experiment [*Meek & Manson*, 1987].

In this chapter we examine some aspects of the IDI technique from the point of view of time–domain correlation theory and their consequences for the frequency–domain measurement of wind velocities.

5.2 Theory

The "IDI" technique makes use of the unsmoothed cross–spectra calculated between the backscattered voltages measured at several spaced antennae. The following theory is valid for smoothed or averaged cross–spectra, but experimental results appear to indicate that it makes predictions which may be applied successfully to techniques utilizing unsmoothed cross–spectra. Because the "IDI" technique is patented, We refer to such techniques as "IDI–like" analyses.

In the IDI–like analysis, the down–coming phase front detected at the spaced antennae is checked for linearity. This is done by examining the unsmoothed cross–spectral phases for each sequential antenna pair at each available Doppler frequency. If the phases detected by both orthogonal arms of the interferometer at some particular Doppler frequency are sufficiently linear, then it is assumed that the signal originates from a single discrete scattering point and the analysis assigns a position and unique Doppler shift to that scatterer. From an ensemble of such scatterers, a linear wind field is fitted which minimizes the total squared error in the line–of–sight component of the fitted wind vector for all scattering points. However, *Briggs* [1993] has shown that phase consistency in the cross–spectra between equally spaced antennae situated in rows does not necessarily imply a single scattering point. We follow, for the moment, the analysis and notation of *Briggs* [1993].

Correlation analysis begins by assuming that the returned signals from any given range constitute a diffraction pattern on the ground whose lines of equal signal strength, or contours, are satisfactorily described by a spatial correlation function $\rho(\xi, \eta)$, with an elliptical argument, viz

$$\rho(\xi, \eta) = \rho(A\xi^2 + B\eta^2 + 2H\xi\eta) \,, \tag{5.1}$$

where ρ is an arbitrary smooth and differentiable function which takes values of unity for zero argument, and falls monotonically to zero as the argument increases in magnitude. Also, ξ and η are spatial separations in the x and y directions, and the coefficients A, B and H are

constants defining the ellipse. We note that the ellipse need not be aligned with the cardinal axis unless the coefficient H is zero.

Equation 5.1, of course, describes a motionless diffraction pattern on the ground. In practice we find that both random change due to turbulence and a mean motion due to the background wind are present. We first deal with random change by introducing a spatio–temporal correlation function,

$$\rho(\xi, \eta, \tau) = \rho(A\xi^2 + B\eta^2 + 2H\xi\eta + K\tau^2) \ , \tag{5.2}$$

where τ is the time–lag in the correlation function and K describes the degree of random change in the pattern. Clearly we recover Equation 5.1 by setting $K = 0$ in Equation 5.2, which corresponds to the situation for which there is no random change in the pattern.

The mean wind (u, v), is introduced by allowing the diffraction pattern on the ground to move with velocity $\underline{V} = (V_x, V_y)$ equal to twice that of the mean wind. In other words, $(V_x, V_y) = (2u, 2v)$. We make the Galilean transformations

$$\begin{aligned} \xi' &= \xi - V_x\tau \text{ and} \\ \eta' &= \eta - V_y\tau \ , \end{aligned} \tag{5.3}$$

such that the pattern appears motionless to an observer at the origin of the "primed" reference frame. The full form of the spatio–temporal correlation function is then

$$\rho(\xi, \eta, \tau) = \rho\left[A(\xi - V_x\tau)^2 + B(\eta - V_y\tau)^2 + 2H(\xi - V_x\tau)(\eta - V_y\tau) + K\tau^2)\right] \ . \tag{5.4}$$

As the IDI technique often makes use of evenly spaced antennae in two orthogonal directions, we take those directions, without loss of generality, to correspond to the x– and y–axis and find the observed cross–correlation function between antennae separated by ξ_o along the x–axis to be

$$\rho(\xi_o, 0, \tau) = \rho\left[(AV_x^2 + BV_y^2 + 2HV_xV_y + K)\tau^2 - 2\xi_o(AV_x + HV_y)\tau + A\xi_o^2\right] \ . \tag{5.5}$$

For those antennae separated by η_o along the y–axis we have

$$\rho(0, \eta_o, \tau) = \rho\left[(AV_x^2 + BV_y^2 + 2HV_xV_y + K)\tau^2 - 2\eta_o(BV_y + HV_x)\tau + B\eta_o^2\right] \ . \tag{5.6}$$

Equations 5.5 and 5.6 will have maxima at respective time shifts τ_x' and τ_y' given by

$$\tau_x' = \frac{\xi_o(AV_x + HV_y)}{AV_x^2 + BV_y^2 + 2HV_xV_y + K} \text{ and} \tag{5.7}$$

$$\tau_y' = \frac{\eta_o(BV_y + HV_x)}{AV_x^2 + BV_y^2 + 2HV_xV_y + K} \ . \tag{5.8}$$

The cross–spectra used by the IDI technique are the Fourier transforms of Equations 5.7 and 5.8, the phases of the cross–spectra being given by the shift theorem as

$$\phi_\xi(f) = \frac{2\pi f(AV_x + HV_y)}{AV_x^2 + BV_y^2 + 2HV_xV_y + K}\,\xi_o \text{ and} \tag{5.9}$$

$$\phi_\eta(f) = \frac{2\pi f(BV_y + HV_x)}{AV_x^2 + BV_y^2 + 2HV_xV_y + K}\,\eta_o\,. \tag{5.10}$$

Clearly, for any given correlation ellipse of the diffraction pattern on the ground, all coefficients in Equations 5.9 and 5.10 will be constants. Thus, the cross–spectral phases recorded at different evenly–spaced antennae for some Doppler frequency f, must themselves lie on a straight line. The IDI technique, of course, will interpret this return as implying a down–coming plane wave of radiation emanating from a discrete scattering point. As this phenomenon is a consequence of a volume–scattering mechanism, it is clear that such an interpretation is unjustified, and we follow the terminology of [*Briggs*, 1993] by calling these scattering points "effective scattering points".

Given the cross–spectral phase at some frequency f, and the antenna separation in the interferometer in the x and y directions, we can define the angle of arrival for the effective scattering points in terms of the x– and y–direction cosines l and m. For plane–wave radiation of wavelength λ, incident at angle θ to the baseline connecting two antennae separated in the x direction by ξ_o, the phase difference measured between the two antennae is given by $2\pi\xi_o l/\lambda$, where $l = \cos\theta$. With this in mind, and rearranging Equations 5.9 and 5.10, we find

$$l(f) = \frac{\lambda(AV_x + HV_y)f}{AV_x^2 + BV_y^2 + 2HV_xV_y + K} \text{ and} \tag{5.11}$$

$$m(f) = \frac{\lambda(BV_y + HV_x)f}{AV_x^2 + BV_y^2 + 2HV_xV_y + K}\,. \tag{5.12}$$

The azimuth(s) upon which the scatterers lie is given by the ratio of their direction cosines,

$$\frac{l(f)}{m(f)} = \frac{AV_x + HV_y}{BV_y + HV_x}\,, \tag{5.13}$$

and as it is independent of the Doppler frequency of interest, all scattering points must possess the same azimuth. This azimuth will henceforth be called the "predicted scatter azimuth", as it is the azimuth upon which the IDI effective scattering points lie as predicted by the spaced antenna full correlation analysis. We note that the degree of turbulence present, parameterized by K, does not affect the predicted scatter azimuth, but that the diffraction pattern anisotropy, given by the ratio of A to B and the magnitude of H, does.

Finally, we consider the zenith angles of the effective scattering points. The angle made with the zenith θ, obeys the relation $\sin^2\theta = l^2 + m^2$. Substituting Equations 5.11 and 5.12 into this expression yields

$$\sin^2\theta = \frac{\lambda\left[(AV_x + HV_y)^2 + (BV_y + HV_x)^2\right] f}{(AV_x^2 + BV_y^2 + 2HV_xV_y + K)^2} . \tag{5.14}$$

As one would expect, as the Doppler frequency increases, so too does the off–zenith angle. In addition, the effect of turbulence, or random change in the diffraction pattern, is to move the effective scattering point closer to the zenith. This can be seen by considering the result of increasing the magnitude of the turbulence parameter in the denominator of Equation 5.14. Clearly, as K increases, so too must the size of the denominator, and hence the ratio on the right hand side of Equation 5.14 must decrease. Since the sine function monotonically increases in magnitude for angles between zero and $\frac{\pi}{2}$, if the argument of the sine function is decreased, the angle made with the zenith must also decrease. Hence as the intensity of turbulence is increased, the effective scattering points must move back towards the zenith.

We now depart from the analysis of *Briggs* [1993] and examine the effect that this movement of the effective scattering point has on the measurement of the mean wind field.

Consider a Doppler radar with a beam directed at angle θ to the zenith. If the radar measures a radial Doppler velocity of V_R in this beam, then the inferred horizontal wind in the absence of vertical motion is

$$\begin{aligned} V_H &= \frac{V_R}{\sin\theta} \\ &= \frac{\lambda\Delta f}{2\sin\theta} . \end{aligned} \tag{5.15}$$

In the case of the IDI technique, each scattering point's radial velocity may be thought of as analogous to the Doppler radar's measurement of radial velocity except that, in the former's case, many inferred horizontal winds are averaged, or fitted to find the mean linear wind field. We have shown that, in the presence of turbulence, the off–zenith angle of the IDI effective scattering point is reduced. This effective off–zenith angle θ, was defined in Equation 5.14, and may be used in Equation 5.15 to find the mean linear horizontal wind field measured by the IDI analysis. Performing this substitution yields

$$V_H = \frac{AV_x^2 + BV_y^2 + 2HV_xV_y + K}{2\sqrt{(A^2 + H^2)V_x^2 + (B^2 + H^2)V_y^2 + 2(A + B)HV_xV_y}} . \tag{5.16}$$

Note that V_x and V_y are pattern velocities, and hence a factor of two is included in the denominator of Equation 5.16 to retrieve the horizontal wind velocity, V_H.

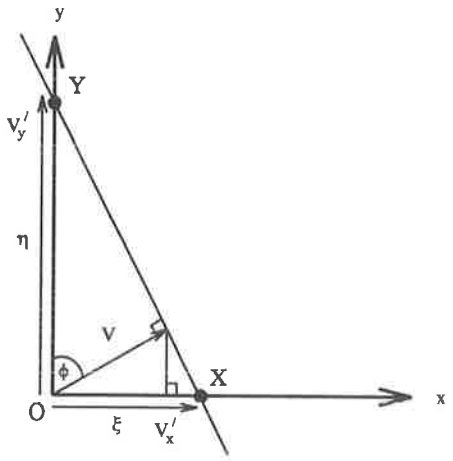

Figure 5.1: The geometrical construction used to find the apparent velocity from the trace velocities, V_x' and V_y'.

In order to derive the apparent velocity in terms of the spaced antenna parameters, we consider the diagram in Figure 5.1. If τ_x' and τ_y' are the lags at which the cross–correlation functions between sensors OX and OY maximize respectively, then the trace velocities V_x' and V_y' are given by

$$V_x' = \frac{\xi}{\tau_x'} \tag{5.17}$$

$$V_y' = \frac{\eta}{\tau_y'} , \tag{5.18}$$

where ξ is the distance between sensors O and X, and η is the distance separating sensors O and Y. It is important to note that V_x' and V_y' are not components of the total velocity, V. In fact, after some geometrical construction, we find

$$V = \frac{V_x' V_y'}{\sqrt{V_x'^2 + V_y'^2}} . \tag{5.19}$$

The maxima of the cross–correlation functions, τ_x' and τ_y' have been found by differentiation of the correlation functions. Recalling Equations 5.7 and 5.7, we have

$$\tau_x' = \frac{\xi(AV_x + HV_y)}{AV_x^2 + BV_y^2 + 2HV_xV_y + K}$$

$$\tau_y' = \frac{\eta(BV_y + HV_x)}{AV_x^2 + BV_y^2 + 2HV_xV_y + K} .$$

These equations, when substituted into Equation 5.19, yield an expression for the horizontal velocity

$$V = \frac{AV_x^2 + BV_y^2 + 2HV_xV_y + K}{\sqrt{(A^2 + H^2)V_x^2 + (B^2 + H^2)V_y^2 + 2(A + B)HV_xV_y}} \tag{5.20}$$

which, when compared with Equation 5.16, differs only by a factor of two. This factor of two is, not surprisingly, simply due to the conversion between pattern and wind velocity. Equation 5.20 was derived in terms of pattern velocity, and so must have a factor of two included if it is to describe wind velocity. This factor of two is a result of the well–known "point–source effect" [*Pawsey*, 1935; *Mitra*, 1949; *Felgate*, 1970].

We therefore conclude that the wind velocity derived using an IDI–like technique is the same quantity as the spaced antenna apparent velocity. Consequently, in the presence of random change in the diffraction pattern on the ground, this wind estimate will be in error.

We now investigate these predicted effects using the 8 channel receiver system with the large Adelaide MF antenna array. In particular, we test the hypothesis that the IDI effective scattering points lie along the spaced antenna predicted scatter azimuth, and that the wind estimated using the IDI technique agrees best with the spaced antenna apparent velocity.

5.3 Experiment

The Buckland Park receiving array has a basic square–grid spacing of 91.4 m and was operated during this experiment at its fundamental frequency of 1.98 MHz. Thus, the basic antenna spacing was about $\frac{3}{5}\lambda$, although for antennae situated along a diagonal of the array, it is closer to $\frac{4}{5}\lambda$. Eight antennae were selected from the 89 dipoles aligned in the East–West direction in the Buckland Park array. The locations of these eight antennae are depicted in Figure 5.2. This arrangement provides the two orthogonal rows of antennae required for an IDI–like analysis with row one composed of antennae 1, 2, 5 and 7, and row two composed of antennae 1, 4, 6 and 8. We note that this configuration provides a total of four antennae in each of the interferometer arms from which the linearity of spectral phases may be evaluated. The experimental configuration utilized in this work therefore differed from that used by *Brosnahan & Adams* [1993] during the AIDA'89 campaign in that one additional phase measurement was available from each arm of the interferometer. Further, our configuration differed from that used by *Adams et al.* [1986] in that one less phase measurement was available from each interferometer arm.

In addition to the interferometric analysis, antennae 1, 2 and 4 were used for a standard spaced antenna analysis to calculate both the wind profile above the radar for each 2 min period, and the correlation ellipse parameters of the diffraction pattern on the ground. Although the spacing of the antennae was not ideal for the spaced antenna analysis, a more

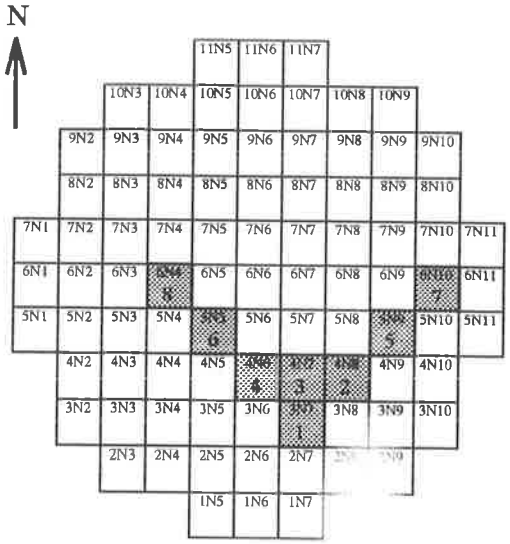

Figure 5.2: The eight antennae selected for these observations. Antennae 1, 2, 4, 5, 6, 7 and 8 were used for the IDI–like analysis, while antenna 3 was used only for other, unrelated studies.

suitable arrangement was not available due to the necessity of configuring the antenna array for the IDI–like experiment. In particular, right angle triangles should be avoided when configuring spaced antenna arrays if unbiased measurements are to be made [*Golley & Rossiter*, 1970].

The radar was operated at a frequency of 1.98 MHz with pulse repetition rate of 80 Hz. Each pulse was modulated by a Gaussian envelope with half–power half–points about 25 μs apart. A total of 32 pulses were coherently averaged to form a final sampling rate of 2.5 Hz. A data record thus consisted of 256 sample points and a final data length of 102.4 s. Only daytime data are considered here, although the results have been shown to be valid at night. These particular parameters were chosen to ensure compatibility with existing and past spaced antenna and interferometric radar systems.

5.3.1 IDI–like analysis

In the IDI–like analysis implemented for this experiment, the seven 256–point time series of voltage samples from the antennae were firstly Fourier transformed to form seven complex auto–spectra. The phases of the auto–spectra were calculated for Doppler frequencies between ± 0.31 Hz. These frequency bounds correspond to limits on the radial velocity of ± 24 ms^{-1}, but delimit the region of the auto–spectra in which most of the spectral power, and hence information is contained, These limits also led to a significant reduction in the

use of computational resources. The differences between the phases of the auto–spectra for adjacent antennae in each arm of the interferometer were then computed at each frequency of interest and corrected for instrumental bias (see Chapter 3). The phases were then "unwrapped" following the procedure of *Adams et al.* [1985] to ensure that any 2π ambiguities were resolved. In this procedure, the phase of the first antenna in one arm of the interferometer is taken as a reference, and the phase difference between it and the next antenna is computed. If the magnitude of the difference is larger than π, then 2π is added to, or subtracted from the phase measured at the second antenna such that the magnitude of the phase difference between the two antennae is reduced. This process continues with the adjusted phase measured at the second antenna taken as the reference, and the magnitude of the phase difference between the second and third antennae tested against 2π. Once all phases have been adjusted in this way, a straight line is fitted using a simple linear regression algorithm.

The adjusted phases were tested for linearity using a "χ^2" parameter. For this experiment, the sum of the squared differences between the measured auto–spectral phases (in radians) and the fitted phases was computed, and compared to a threshold value of unity. If the "goodness of fit" for either arm of the interferometer exceeds unity, the information at that particular Doppler frequency is discarded. *Adams et al.* [1986] rejected frequencies exhibiting unsuitable phase variation between antennae by comparing the root–mean–square of the fitted auto–spectral phases from both orthogonal rows of the interferometer to a threshold level of 30°. Comparison between the two methods showed little difference in the number and type of auto–spectral phase ensembles rejected. In fact, in most cases there appeared to be a large observable difference between data retained with a χ^2 parameter less than unity, and those data which were rejected. In addition, data which were discarded were rarely rejected with χ^2 values close to, but exceeding unity.

An example of the corrected and adjusted phases of the auto–spectra for the two interferometer arms at a Doppler frequency of -0.195 Hz and at an altitude of 98 km is shown in Figure 5.3.

In order to impart some sense of the number of accepted frequency bins in a typical set of D–region auto–spectra, the phase measurements for the two interferometer arms at a total 48 frequencies centred on zero Hertz are displayed in Figure 5.4. The data were recorded in mid–afternoon and come from the 82 km range gate. In each case, the abscissa are scaled from $-\pi$ to $+\pi$, while the ordinate axis are scaled as in Figure 5.3. At the bottom

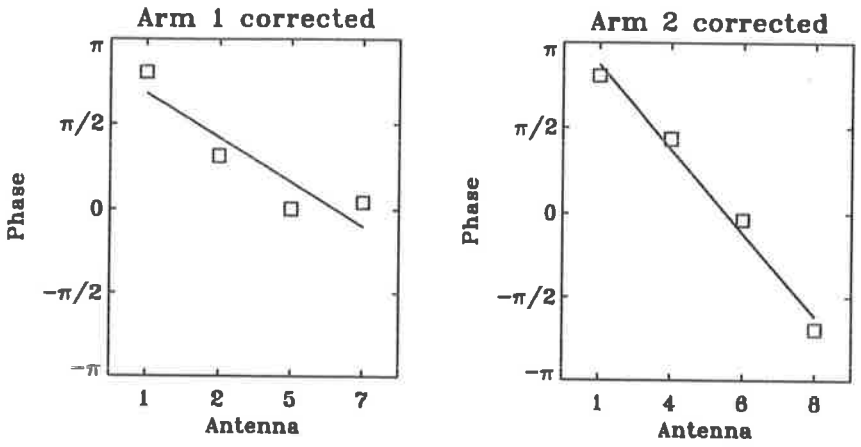

Figure 5.3: An example of the phases of the four auto-spectra in each arm of the IDI interferometer at a Doppler frequency of -0.195 Hz. The solid lines are the lines of best fit which in this instance have χ^2 fit parameters of 0.7 and 0.2. Data are rejected if the χ^2 parameter for either arm exceeds unity.

of each panel, the χ^2 parameter for the line of best fit is also indicated. The data are arranged such that the two sets of phase measurements from the two interferometer arms appear in pairs starting at the lowest Doppler frequency displayed (-0.234 Hz) in the top left–hand corner of the diagram, and progressing in row–major format, from left to right, to the highest Doppler frequency displayed (+0.225 Hz) in the bottom right–hand corner. In this particular case, some 25 of the 48 Doppler frequencies examined were rejected, while the remaining 23 were retained. Also, of the 25 frequencies rejected, only in 5 cases were the fits to the phase measurements made by both interferometer arms poor. The remaining 20 cases were rejected due to poor fits to only one or the other of the interferometer arms. Of these 20 cases, 16 were rejected due to poor fits to the auto–spectral phases measured from arm 1, while only 4 were rejected due to the fits to the phases measured by the second interferometer arm.

It is of some interest to examine the dependence of the frequency of rejection with altitude, and how this varies over a period of several hours. In Figure 5.5, profiles of the percentage of Doppler frequencies accepted over the period of 1 hr are displayed. The four profiles were recorded sequentially in time, with the first sampled from 14:32 to 15:30 LT, and the last sampled from 17:32 to 18:30 LT. The average percentage acceptance for all ranges over the first 3 hr is approximately 20%, with this value falling significantly for the last profile. This is not surprising, however, as the last profile was recorded during twilight at which time the strength of the backscattered signals from the D–region rapidly decreases as the free electron

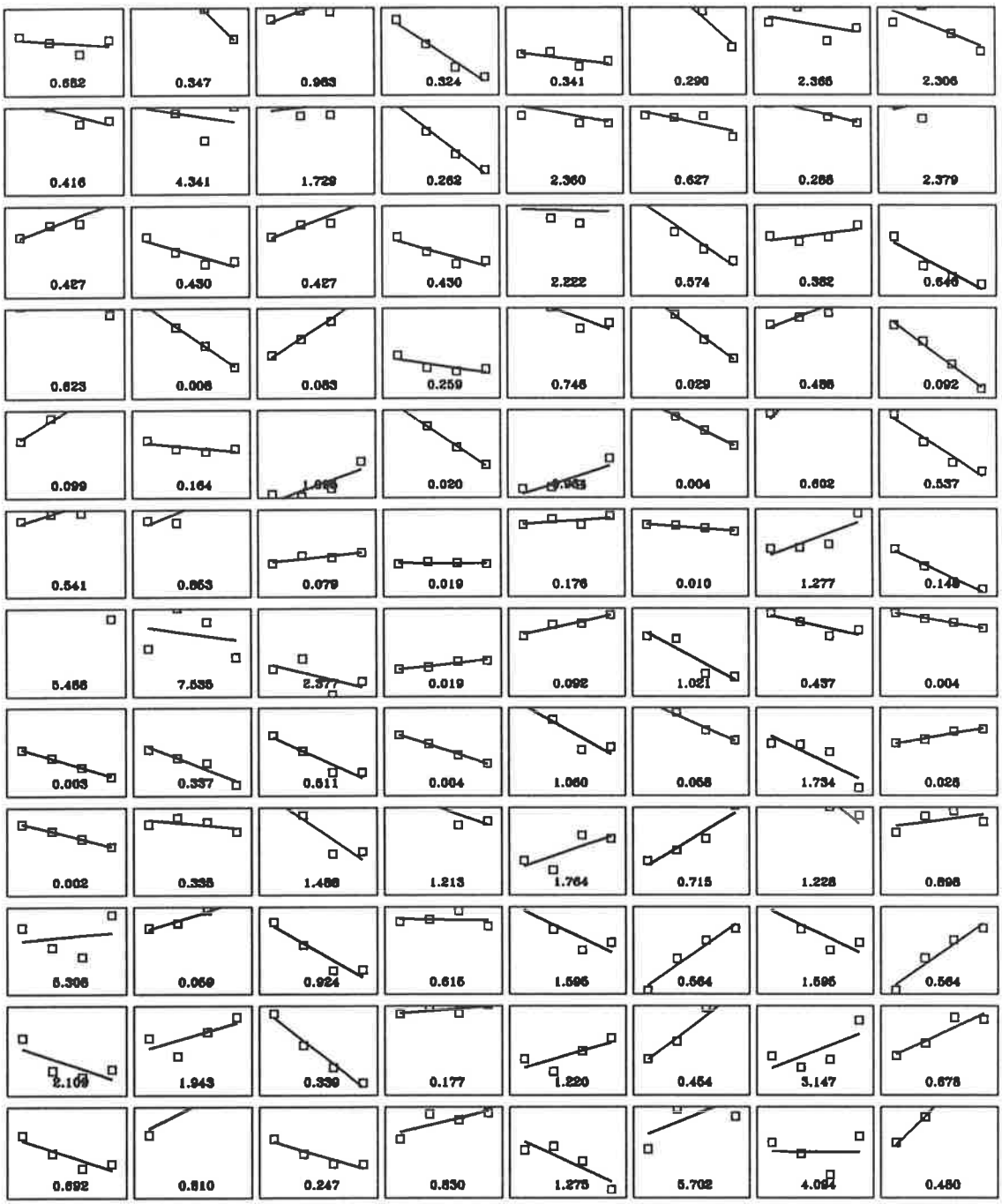

Figure 5.4: An example of the phases of the four auto–spectra in each arm of the IDI interferometer at Doppler frequencies from -0.234 Hz to +0.225 Hz. These data were recorded at an altitude of 82 km. Also indicated on each panel is the line of best fit and the χ^2 of the fit. The abscissa and ordinate axis are as detailed in Figure 5.3. See text for more detail.

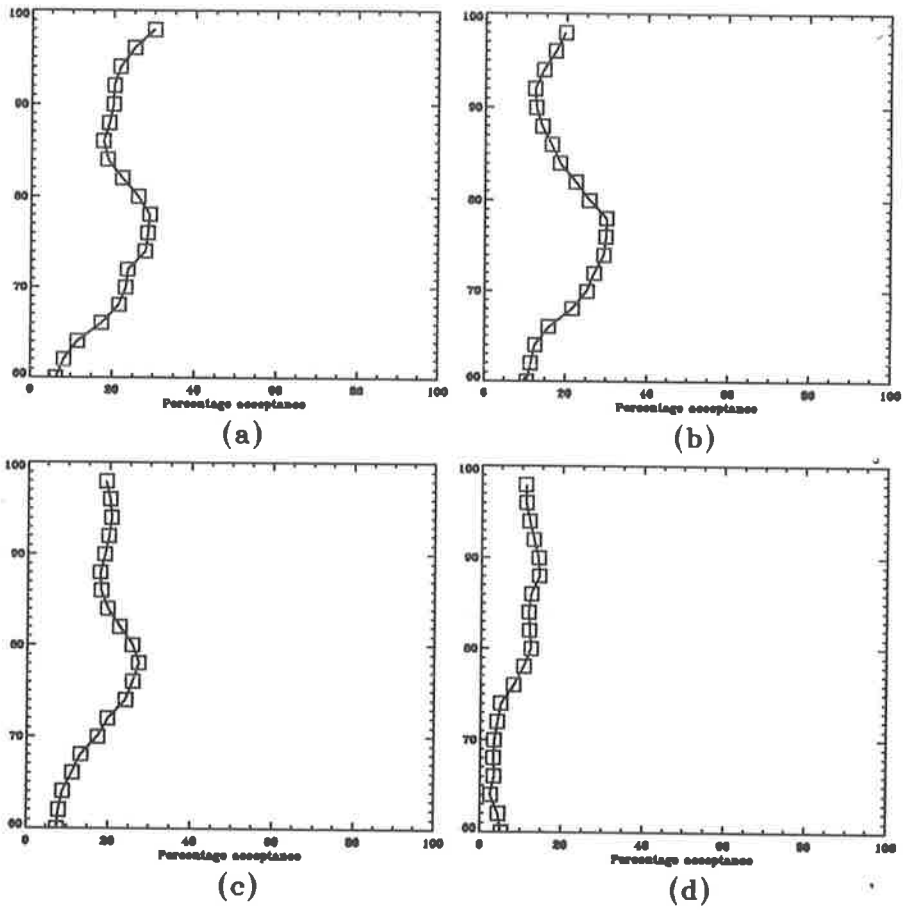

Figure 5.5: Four height profiles of the percentage of points at all Doppler frequencies which were accepted by the IDI analysis as being sufficiently linear. Each profile represents one hour of data, starting at (a) 14:32, (b) 15:32, (c) 16:32 and (d) 17:32.

concentration drops. There appears to be an enhancement in the number of acceptances at about 78 km where a broad peak occurs. This is a common feature in all of the profiles (except perhaps the final profile in Figure 5.5d) and appears to coincide with a commonly–occurring, stable, stratified and slow–fading region of the atmosphere. It is interesting to note that the region of enhanced acceptance for the IDI–like technique corresponds to the region in which the spaced antenna analysis rejects many records for "slow fading", often corresponding to more specular reflection. Situations such as these may represent an area in which interferometric techniques have some advantage over correlation techniques.

For those Doppler shifts where the phases of the auto–spectra for both arms of the interferometer were sufficiently linear, an angle of arrival was computed from the two phase

slopes. To find the angle of arrival (l_o, m_o), the matrix equation

$$\begin{pmatrix} \psi_1(f) \\ \psi_2(f) \\ \psi_{12}(f) \end{pmatrix} = \frac{2\pi d}{\lambda} \begin{pmatrix} \xi_1 & \eta_1 \\ \xi_2 & \eta_2 \\ \xi_{12} & \eta_{12} \end{pmatrix} \begin{pmatrix} l_o \\ m_o \end{pmatrix} \tag{5.21}$$

was inverted, where $\psi_1(f)$ and $\psi_2(f)$ are the phase slopes at Doppler shift f for interferometer arms 1 and 2 respectively, $\psi_{12}(f)$ is an inferred phase slope between the arms 1 and 2 derived from the circular redundancy condition, the ξ_i and η_i are the antenna spacings for arm i in the x and y directions respectively, and λ is the radar wavelength. Clearly, using the phase slope as a measure of the average phase difference between antenna pairs implies that the multiple antenna interferometer can be reduced to a simple set of three spaced antennae for the purposes of the angle of arrival calculation. Hence, we are able to use the spacings for antennae 1, 2 and 4, the two measured average phase differences and the one inferred phase difference to find the direction cosines of the effective scattering point, l_o and m_o.

Since these effective scattering points were observed at off–zenith angles of up to 25°, range correction factors of $\cos\theta$, where θ is the measured off–zenith angle, must be applied to the apparent range. The range–corrected data were then placed into the new range gate which most closely matched their corrected altitude. The new range gates were spaced at 2 km intervals, beginning at 60 km and terminating at 98 km in the same manner as the original radar range gates.

In Figure 5.6, the angle of arrival of each accepted effective scattering point are displayed for each corrected altitude. The data were recorded during a single 102.4 s acquisition. The angle of arrival information is displayed in direction cosine form, with the x–direction cosine displayed on the ordinate axis and the y–direction cosine on the abscissa. Both axis are scaled between values of ±1 in all panels. Such diagrams will hitherto be referred to as *l_o–m_o diagrams.* Note that certain features prominent in the average acceptance profiles shown in Figure 5.5 are repeated in the distribution of the number of points displayed in Figure 5.6. Namely, the enhancement of acceptances at around 78 km is clearly visible in the l_o–m_o diagrams. It should also be noted that at the altitudes 86 km, 84 km and 62 km less than three effective scattering points have been accepted, and so no wind vector can be calculated for these heights.

Associated with each effective scattering point is the Doppler frequency at which is was

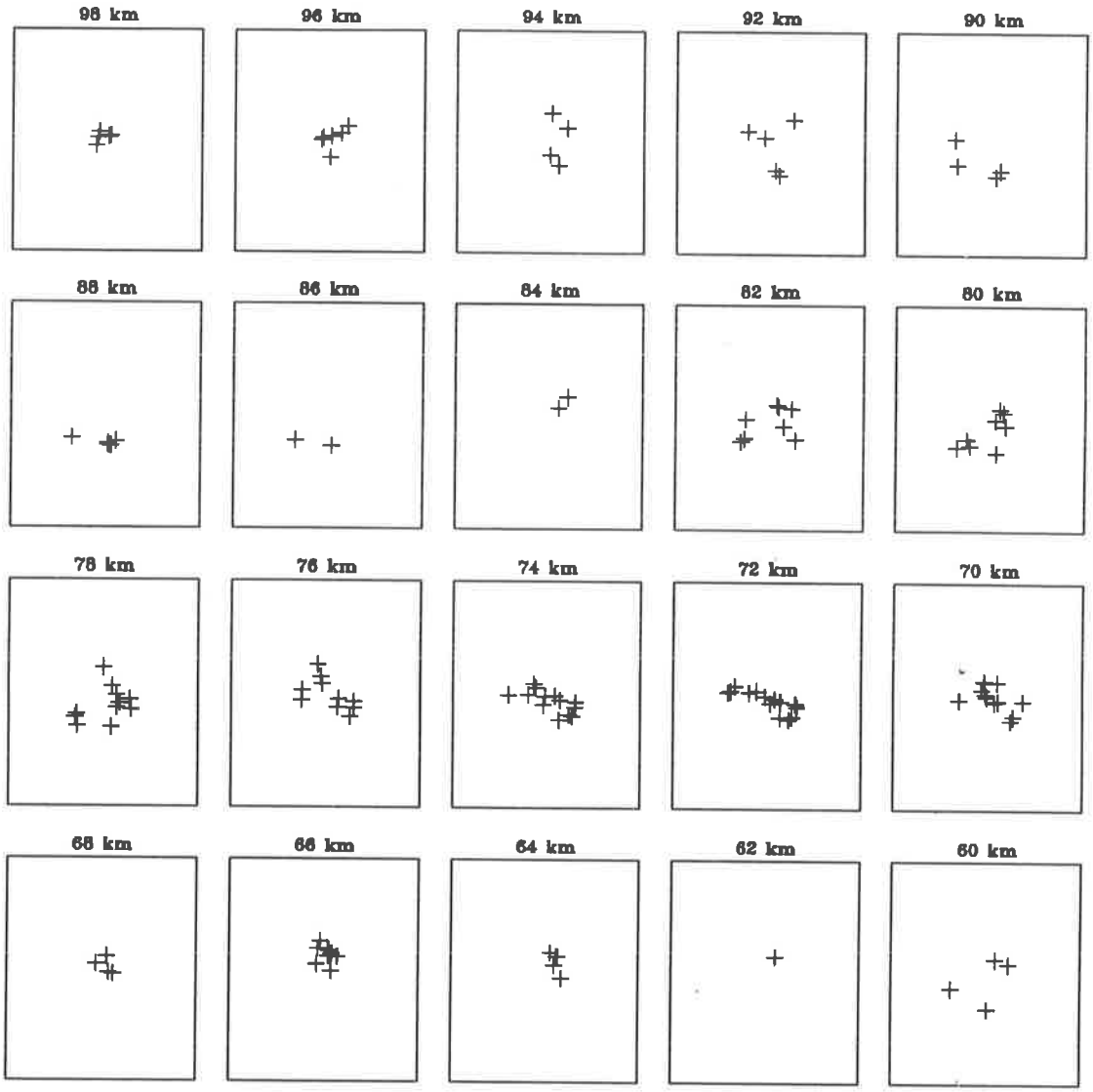

Figure 5.6: l_o–m_o diagrams at each corrected range for one data acquisition. In all cases the x–direction cosine l_o, is displayed on the ordinate axis, while the y–direction cosine is displayed on the abscissa. All axes are scaled between ± 1.

measured, and hence a radial velocity V_R, given by

$$V_R = \frac{-\lambda f}{2} \,. \tag{5.22}$$

For those corrected ranges in which three or more non–colinear effective scattering points were located, a least–squared fit of a three–dimensional linear wind field was applied to the points' radial velocities. The details of this three–dimensional fit to a linear wind field are precisely the same as those documented in Chapter 4, and will not be repeated here. No conditions were imposed on the minimum off–zenith angle of the effective scattering points used in the fit, nor was the vertical velocity initially estimated from points near the zenith

and subsequently removed from the remaining radial velocities to produce a hypothetically uncontaminated horizontal wind field. All points were were used simultaneously in the three–dimensional fit as there appeared to be no advantage resulting from these other methods of wind estimation.

At this point in the analysis, any fitted horizontal wind component with a magnitude in excess of 200 ms^{-1} was rejected as unphysical. These large velocity measurements in general ensued from cases where small numbers of effective scattering points lay in close proximity to the zenith. In these situations a large error in the estimate of the horizontal wind can result, and so these records are excluded. We note that exclusion of large fitted wind velocities is hardly likely to affect the conclusions of this study, and note that *Brosnahan & Adams* [1993] rejected individual scattering points, not the fitted mean wind velocities, whose projected horizontal velocities exceeded 300 ms^{-1}.

In addition to the extraction of wind profiles, the IDI–like analysis determined the spread of effective scattering points at each range gate, and the azimuth along which these points were elongated. To do this, the direction cosines of the points were plotted against each other in an l_o–m_o diagram and a line of best fit was calculated. Since both l_o and m_o could be considered as independent variables, simple linear regression could not be used to find the line of best fit. Simple linear regression attempts to minimize the squared error in the fit to the dependent variable, and so if a large spread of values occur in the dependent variable for a small spread of values in the independent variable, the slope of the line of best fit is severely underestimated. Consequently, the direction of elongation was determined by using a "total regression" technique. Total regression attempts to minimize the squared error in the distance between each data point and the line of best fit at its closest approach to that data point. Thus, both variables involved in the linear fit are considered to be dependent variables. One example of such a fit to a set of data points in the l_o–m_o plane appears in Figure 5.7. In this case, it is clear that the scattering points are elongated along an azimuth lying in the West–North–West to East–South–East direction. Quite often the degree of elongation of the effective scattering points was not so pronounced, although an azimuth of elongation was still assigned to such records. We therefore expect some degree of "random noise" in our estimates of the elongation azimuths, and so the problem of determining the degree of correspondence between the azimuth of effective scattering point elongation and the spaced antenna predicted azimuth of scatter lent itself to a statistical approach.

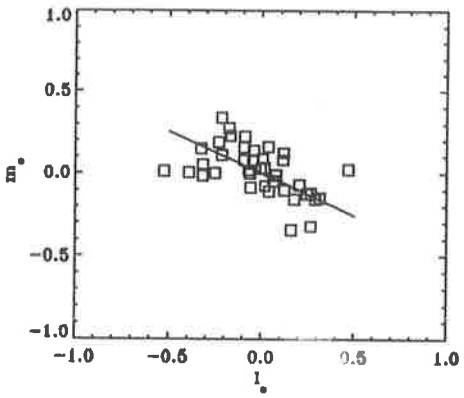

Figure 5.7: An l_o–m_o diagram for a range–correc altitude of 72 km showing the line of best fit to the scattering points. Note that these scattering points are calculated from a single 102.4 s record at one range. These particular data were taken in mid–afternoon on 16/9/92.

5.3.2 Spaced antenna analysis

A standard spaced antenna analysis [*Briggs*, 1984] was performed on antennae 1, 2 and 4 as depicted in Figure 5.2. From this both the true and apparent velocity components were obtained, as well as the full correlation ellipse parameters, a, b, f, g and h. The parameters in this case are written in lower case to identify them as the ratio of their upper–case counterparts to the correlation ellipse parameter C. Thus

$$a = \frac{A}{C}, \tag{5.23}$$

$$b = \frac{B}{C}, \tag{5.24}$$

$$f = \frac{F}{C}, \tag{5.25}$$

$$g = \frac{G}{C}, \tag{5.26}$$

$$h = \frac{H}{C} \text{ and} \tag{5.27}$$

$$k = \frac{K}{C}. \tag{5.28}$$

These "lower–case" ellipse parameters were used as the spaced antenna full correlation analysis does not usually calculate the value of the parameter C, and hence the values of the parameters A, B, F, G, H and K. This, however, does not affect the comparison of the effective scattering point azimuth of elongation with the spaced antenna predicted azimuth

of elongation as Equation 5.13 may be rewritten

$$\frac{l(f)}{m(f)} = \frac{\frac{A}{C}V_x + \frac{H}{C}V_y}{\frac{B}{C}V_y + \frac{H}{C}V_x} \tag{5.29}$$

or, alternatively,

$$\frac{l(f)}{m(f)} = \frac{aV_x + hV_y}{bV_y + hV_x} \,. \tag{5.30}$$

The spaced antenna predicted azimuth of scatter is therefore unchanged, even if the ratio of the ellipse parameters to the parameter C is used.

Using these parameters and Equation 5.30, we can find the theoretically predicted azimuth of the effective scattering points, viz

$$\tan\phi = \frac{aV_x + hV_y}{bV_y + hV_x} \,, \tag{5.31}$$

where ϕ is the azimuth of the scattering location measured in a clockwise sense with Northward defined as 0°.

5.4 Results

5.4.1 IDI–like effective scattering point behaviour

Some three hours of day–time data were processed by the IDI–like algorithm, and effective scattering locations identified. The elongation of the range–corrected points was fitted and an azimuth calculated. In Figure 5.8 appear l_o–m_o diagrams displayed in the same format as Figure 5.6, except that the azimuth of elongation of the effective scattering points has been indicated, as well as the spaced antenna predicted scattering azimuth. Note that only for those altitudes at which spaced antenna winds were calculated was the fitted azimuth of elongation displayed on the l_o–m_o diagrams. Clearly there does not exist a one–to–one correspondence between the predicted and observed azimuth of scatter. After viewing many of such diagrams, however, it would appear that the predicted and observed azimuths are not completely uncorrelated. In fact, taking the azimuths in Figure 5.8 as typical, it is not unreasonable to suggest that there is some degree of correlation between the predicted and observed elongation azimuths, particularly between 70 km and 84 km. Recalling certain results found in Chapter 3, it would be quite surprising if good correlation was found between the interferometric and time–domain technique below about 70 km. Thus, for the moment we ignore discrepancies below 70 km, and concentrate on the remainder of the D–region. Results from the lower E–region may also not correlate well with each other as totally

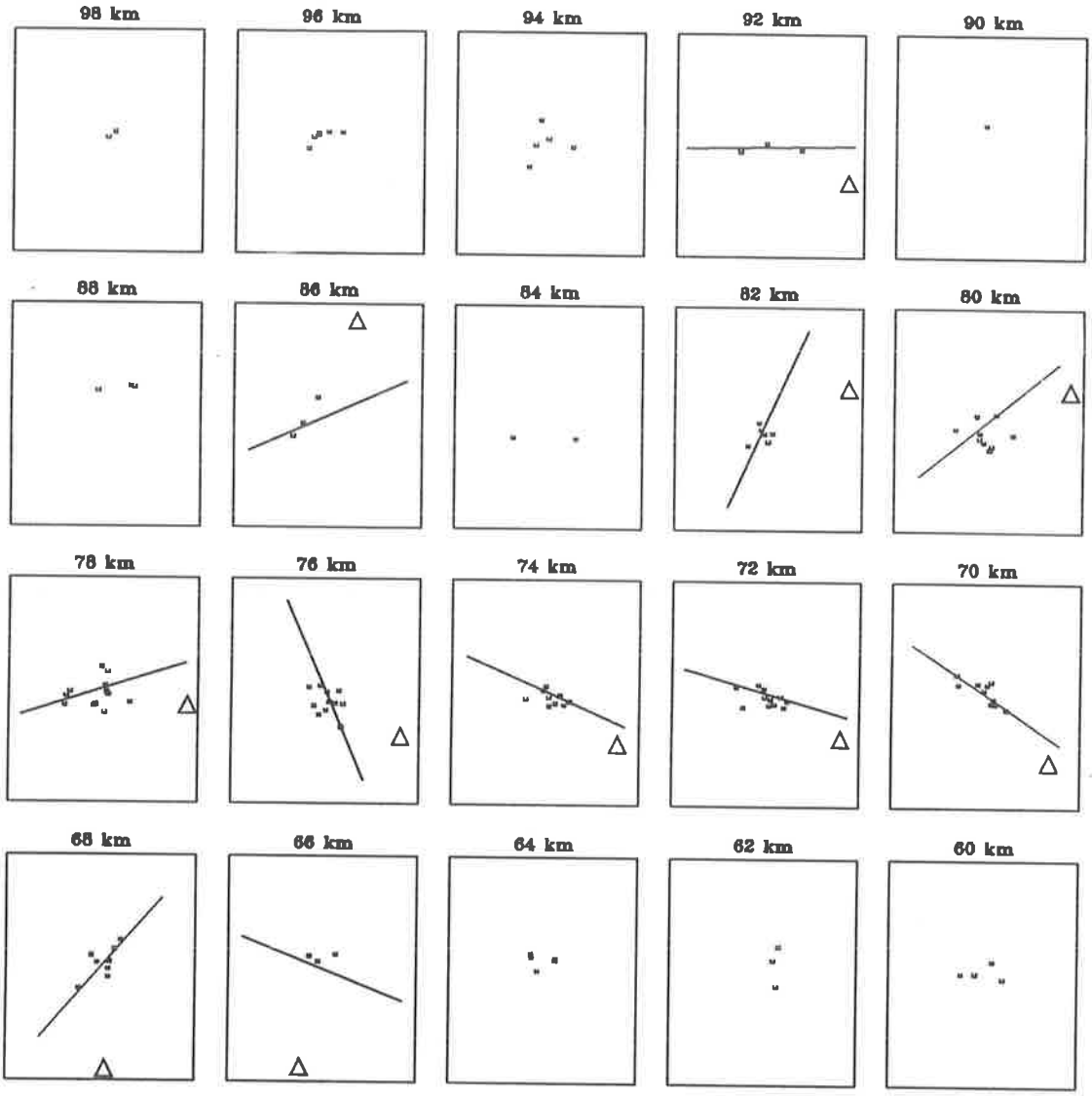

Figure 5.8: l_o–m_o diagrams for all ranges showing the effective scattering point positions, their azimuth of elongation (straight line) and the spaced antenna predicted azimuth of scatter ($\triangle$).

reflective "glints" may violate the assumption of volume scatter. Although this region may satisfy the assumptions inherent in the IDI analysis, we are more concerned with testing the response of the IDI technique in a region where we believe its assumptions are violated. Thus we restrict our attention to ranges between 70 km and 84 km.

Even restricting the study to the upper D–region, we find significant noise superimposed on the observed elongation azimuths. We therefore treat the problem statistically, and propose to examine the distribution of differences between the observed elongation azimuth of the effective scattering points and the spaced antenna predicted azimuth of scatter. These

distributions are presented in histogram form for the first 3 hr of data in the bp920916 data set for the altitudes 70 km to 84 km in Figure 5.9. Clearly, there is some tendency for the distribution of azimuth differences to cluster about some mean value close to or, equal to, zero. To gain more statistical significance in the result, it seems reasonable to amalgamate all of the information from the 8 heights displayed in Figure 5.9. In addition to this, it is useful to consider the distribution of the spaced antenna predicted scatter azimuths only. If these predicted azimuths were clustered tightly around some mean value, then taking the differences between the predicted azimuths and their corresponding observed elongation azimuths would be rather pointless, and the resulting histogram of the azimuth differences would be broader than that of the predicted azimuths alone. Alternatively, if the histogram of the differenced azimuths were narrower than that of the predicted azimuths alone, then this would be a strong indication that the two were closely related.

In Figure 5.10a, data from all eight heights have been combined to form a single histogram of the differences between the spaced antenna predicted scattering azimuth, and the observed azimuth of elongation. In Figure 5.10b appears a histogram of the spaced antenna predicted scattering azimuths; again taken from all eight heights. Note that, although the IDI–derived effective scattering point azimuth of elongation does not coincide precisely with the spaced antenna predicted effective scatter azimuth, it is, on the average, described reasonably well. It is worth emphasizing that defining a direction of elongation of scatter from a small number of effective scattering points is by no means easy, and at times the elongation may be quite small. Since we demand that each set of effective scattering points have a direction of elongation associated with them, it is not surprising that some elongation azimuths may not be statistically significant. We note, however, that such erroneous elongation azimuth determinations will be randomly distributed and, as such, will not influence the average result.

We note also that the histogram in Figure 5.10b is clearly more spread than that in Figure 5.10a. By this we infer that the alignment between the spaced antenna predicted azimuth of scatter and the direction of elongation of the effective scattering points is not simply due to a tight clustering of the predicted azimuths about the average direction of scatter elongation. It appears, then, that these results are strongly indicative of IDI–derived effective scattering points aligning preferentially along the azimuths predicted by the correlation analysis theory. Further, it appears that the volume scatter model of the mesosphere, at least in the middle and upper D–region, best explains the nature of the backscattered

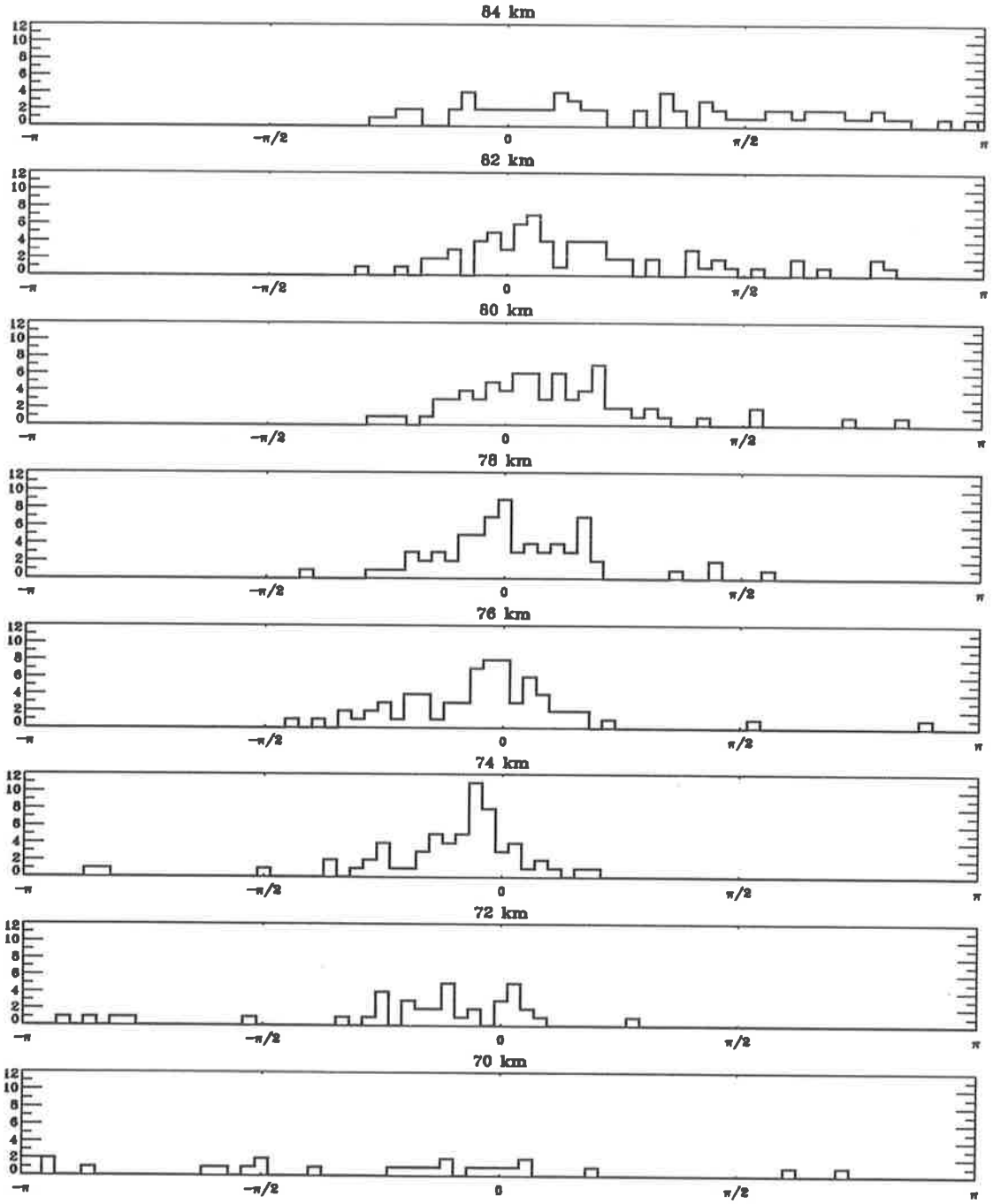

Figure 5.9: Histograms of differences between spaced antenna predicted scatter azimuth and scatter elongation azimuth for the altitudes 70 km to 84 km. A total of 3 hr of data are represented in this figure. The ordinate axes are in each case scaled between $\pm\pi$, while the abscissa all range between 0 and 12 counts.

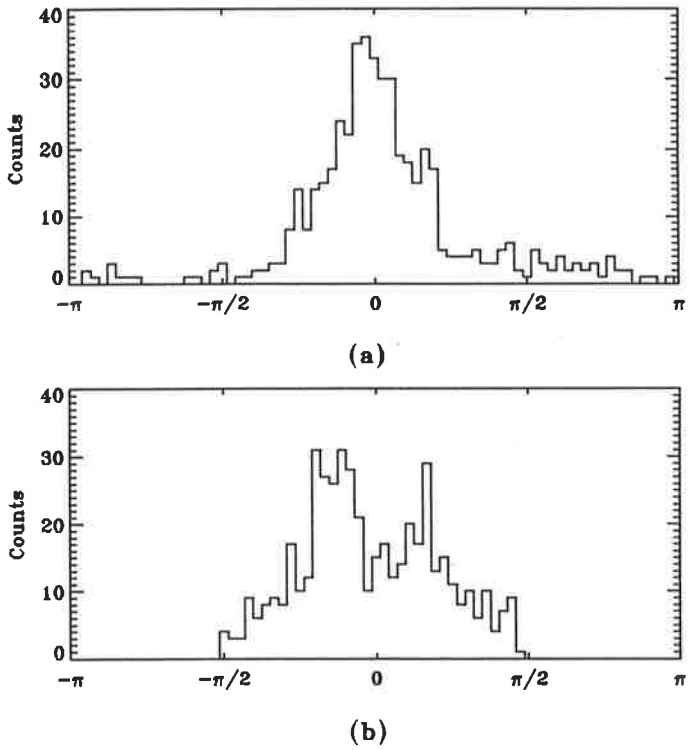

Figure 5.10: (a) A histogram of the differences between the spaced antenna–predicted effective scattering point azimuth and the IDI–derived scatter elongation azimuth. (b) A histogram of the predicted effective scattering azimuths only. Note that the histogram in (a) is more tightly clustered about zero than the histogram in (b), indicating that the alignment of the two azimuths is not coincidental. Data from the height interval 70 km to 84 km collected during the first 3 hr of the bp920916 data set has been included in this figure.

radio signals received at the ground.

5.4.2 Wind profiles

From the ensembles of effective scattering points identified in the last subsection, least squared fits to linear wind fields were calculated wherever three or more effective scattering points were found at the same altitude. The data were analysed as individual records and the winds calculated were then averaged in blocks of one hour. Hourly averages were used as time–series of individual 2 min records exhibited a fair degree of "noise", at least compared to the spaced antenna analysis winds. In Figures 5.11a-f, the wind profiles derived by both the IDI–like technique, and spaced antenna full correlation analysis are shown. Figures 5.11a–b were calculated from data recorded during the first hour of the experiment, while Figures 5.11c–d and Figures 5.11e–f were recorded during the second and third hours of the experiment respectively. Three wind profiles are displayed on each panel and are

identified by three different symbols. The spaced antenna true wind velocity is plotted using the symbol "◇", the spaced antenna apparent velocity is plotted using the symbol "□", and the IDI–like analysis average wind measurements are plotted using the symbol "△". Note that both the magnitudes of the winds and their directions are indicated in Figures 5.11a–f, where the wind speeds are displayed in the top three panels, and the directions in the bottom three. Error bars representing the standard deviation of the spaced antenna true wind speed are overlayed for the spaced antenna true wind velocity only. Of primary interest in the figure is behaviour of the IDI–derived wind in the D–region.

In Figure 5.11a from 70 km to 84 km in altitude, the IDI–derived wind agrees remarkably well with the spaced antenna apparent velocity. As was the case in Subsection 5.4.1 where scattering point azimuths were considered, we discount the variation below 70 km due to the difficulty in reliable interpretation of interferometric results with such low signal levels. The behaviour of the profiles above 84 km in Figure 5.11a also appears anomalous, with the IDI–like wind velocity estimate diverging significantly from both the spaced antenna–derived true and apparent velocities. This divergence appears to be best explained by the presence of discrete scattering centres associated with the E–region affecting the wind measurements made by both techniques. It is possible, however, that the IDI–like technique is more sensitive to the introduction of these discrete scattering centres. It is important to recognise that such discrete scattering centres need not necessarily move with the background wind, since they may well be a manifestation of gravity wave–induced focusing of the backscattered signal, Indeed, studies of enhanced scattering reported in Chapter 3 have indicated exactly this. Evidence to support this hypothesis can be found in the time–variation of the hourly–mean winds as shown in Figures 5.11a, c and e. It can be seen that the IDI–like average wind measurement in these three figures changes from a maximum of about 80 ms^{-1} at altitudes above 96 km in Figure 5.11a, to a minimum of 10 ms^{-1} at 96 km in Figure 5.11e. The IDI–like wind velocity estimate in Figure 5.11e also exhibits a wind shear of 20 $ms^{-1}km^{-1}$ between 94 km and 96 km. Recalling that this represents an average figure recorded over the period of one hour, we conclude that the measurement most probably suffers from some form of contamination. Although it is difficult to argue that the spaced antenna measurements are not affected by these (hypothetical) discrete scattering centres, a case may be made that they appear to exhibit less anomalous behaviour than do the IDI–like wind velocity measurements.

In Figure 5.11c we see the average profile for the second hour of data, and again note

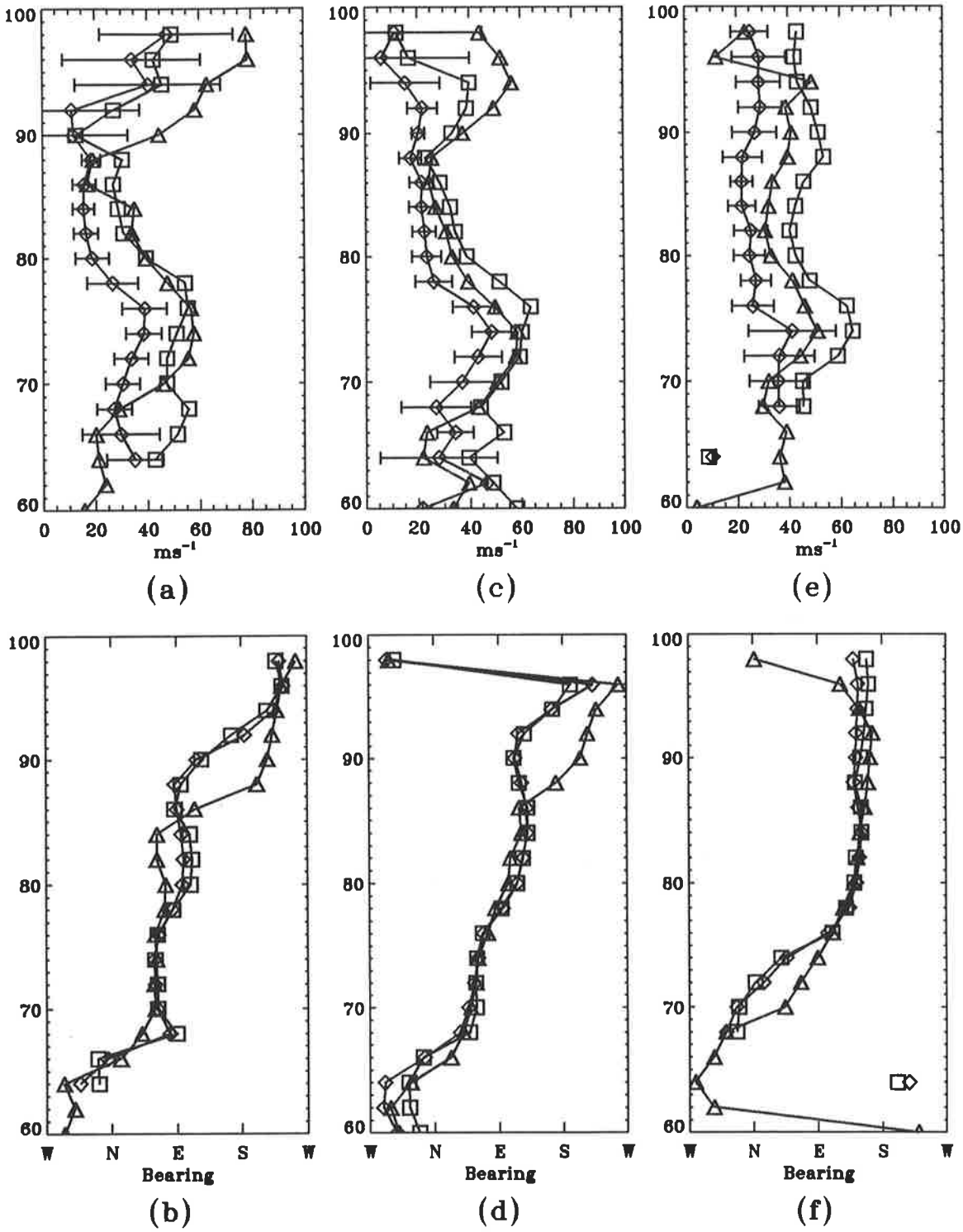

Figure 5.11: One–hour average wind profiles for the spaced antenna true velocity (◇), the spaced antenna apparent velocity (▫), and the IDI wind velocity (△). Panels (a) and (b) represent measurements made during the first hour of the experiment, while panels (c) and (d), and (e) and (f) correspond to the second and third hours of data respectively. The top three panels represent the wind magnitudes for each of the three hours of data analysed, while the bottom three panels represent the wind direction. Error bars are displayed for the spaced antenna true wind speed only.

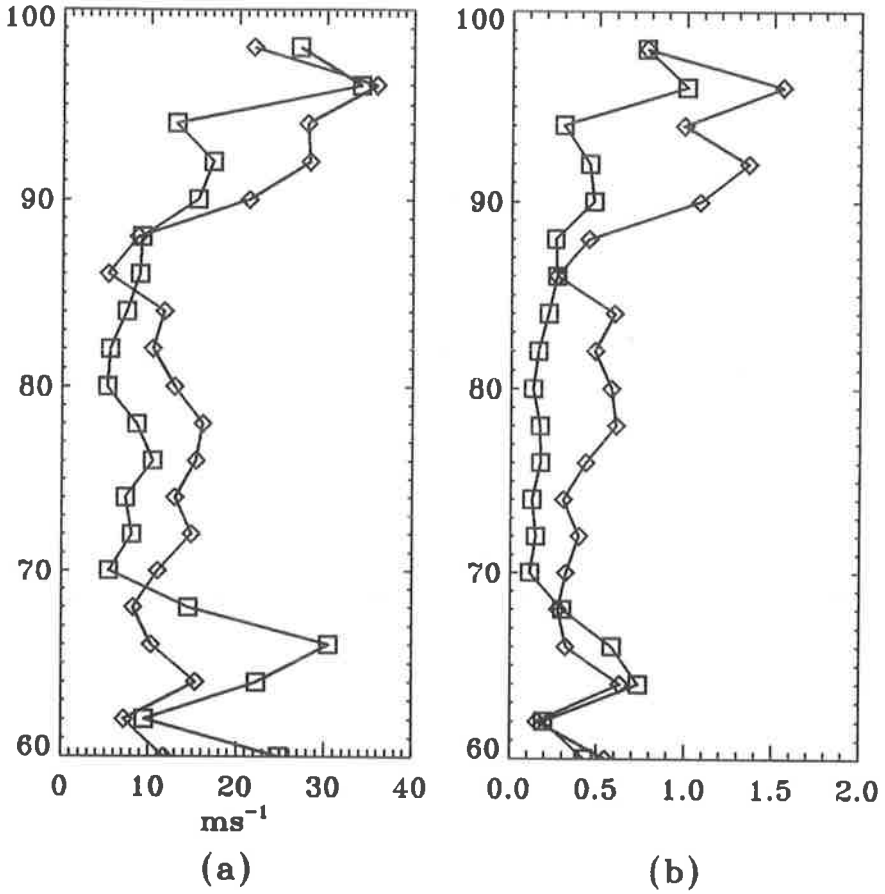

Figure 5.12: Profiles of (a) mean absolute differences and (b) normalized mean absolute differences between both spaced antenna true and spaced antenna apparent wind speed and IDI–like wind speed estimate. The mean absolute differences between the SA true magnitudes and the IDI–like wind magnitude estimates are displayed using the symbol "◇", while the mean absolute differences between the SA apparent magnitudes and the IDI-like wind magnitude estimates are displayed using the symbol "□". Normalization in (b) is carried out by dividing the mean absolute difference at each range by the appropriate mean spaced antenna wind at that range.

that the IDI–derived wind more closely corresponds to the spaced antenna apparent velocity than the true wind. Note that the apparently large change in the direction of all three wind measurements between 96 km and 98 km is, in fact, merely a result of the wind direction changing from slightly South of West to slightly North of West. In Figure 5.11e the correspondence between the IDI–like wind velocity measurement and the spaced antenna apparent velocity is less convincing, but we maintain that there is equally little agreement with the spaced antenna true wind velocity.

In order to quantify the correspondence between the IDI–like wind speed estimate and the spaced antenna apparent wind speed, the mean absolute differences between the two

estimates as a function of altitude were calculated. Also calculated were the mean absolute differences between the IDI–like wind speed estimate and the spaced antenna true wind magnitude. Both of these differences are displayed in Figure 5.12. The mean absolute differences between the SA true magnitudes and the IDI–like wind magnitude estimates are displayed using the symbol "$\diamond$", while the mean absolute differences between the SA apparent magnitudes and the IDI–like wind magnitude estimates are displayed using the symbol "$\square$". Clearly, the mean absolute difference between the spaced antenna apparent wind speed and the IDI–like estimate of the wind speed is substantially less than the mean absolute difference between the spaced antenna true wind speed and that measured by the IDI–like technique, at least in the upper D–region. For altitudes between 70 km and 84 km, the "apparent" mean absolute difference is about 8 ms^{-1}, while over the same range of altitudes the "true" mean absolute difference is closer to 13 ms^{-1}. Note that, even in the case of the spaced antenna apparent wind speed, we do not expect a mean absolute difference of zero, as any randomly–distributed variation in either the spaced antenna apparent velocity or the IDI–like velocity estimate will contribute to the mean absolute difference.

It appears therefore, at least in the true D–region, that the IDI–like wind velocity estimate best agrees with the spaced antenna apparent velocity. Note that this result appears to be in conflict with the work of *Franke et al.* [1990] and also *Sürücü et al.* [1992], who found that velocities derived from the unsmoothed (sample) cross–spectra seem to agree best with the spaced antenna true velocity. However, note also that the results of this study are in agreement with those found by *Meek & Manson* [1987], who also found that the wind velocity calculated using unsmoothed cross–spectra correlated best with the spaced antenna apparent velocity. It is interesting to note that in the two experiments which found agreement between the spaced antenna true velocity and the wind estimated by unsmoothed cross–spectral techniques only three independent antennae were deployed, while, in the case of the experiment conducted by *Meek & Manson* [1987], a total of four independent antenna were deployed. Thus, the additional antenna provided an extra degree of freedom in the estimation of the position of each scattering point identified. Some points relating to this issue are discussed in the following section.

5.5 Discussion

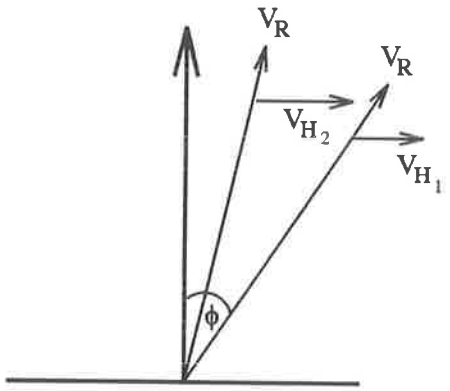

Figure 5.13: Construction showing that a larger horizontal wind vector is inferred if the scattering point is moved toward the zenith but retains the same magnitude of radial Doppler velocity.

It has been shown experimentally that theoretical predictions based on *Briggs* [1993] regarding the performance of Doppler–sorted radar interferometric techniques in the situation of volume scatter are valid, even when unsmoothed, or sample, cross–spectra are used. It is believed that an additional consequence of the volume scatter assumption may explain the over estimation of the true wind velocity by IDI–like techniques. According to Briggs' Equations 15, 16 and 17, the effect of turbulence on the position of the effective scattering point measured by the IDI–like technique is to shift that point closer to the zenith. Thus points with an associated Doppler shift f, appear to emanate from closer to the zenith than would be the case in the absence of turbulence. It is important to note that although the locations of the points have been moved, their Doppler shift remains unchanged. Any horizontal wind inferred from the magnitude of the line–of–sight velocity component in this new direction will be larger (see Figure 5.13).

Thus, the presence of turbulence in a volume scatter situation will cause the IDI–like technique to over–estimate the true wind velocity. It is interesting to note that the difference between the spaced antenna true and apparent velocity is caused by the random changes in the diffraction pattern on the ground. These random changes in the pattern can be directly ascribed to the presence of turbulence in the scattering medium. Thus, the very basis for the difference between the true and apparent velocities in the spaced antenna analysis appears to be responsible for the over–estimation of the IDI–derived wind velocities. It is perhaps not surprising that the over–estimated wind measured by our IDI–like technique compares well with the spaced antenna apparent velocity, and is, in fact, theoretically equivalent.

Serious deviations from the predicted behaviour occur at the higher altitudes recorded

in what appears, at times, to be the lower edge of the E–region at Adelaide. Case studies reported in Chapter 3 have shown that trackable events lasting up to 18 min at 98 km exist in this region of the atmosphere. It appears likely that the IDI–like technique is more susceptible to interference in its measurement of the wind field in the presence of these events. Conversely, the spaced antenna technique appears less affected by the presence of "glints", but it is still believed that the wind measured by the spaced antenna analysis may be somewhat in error. As yet it is unclear to what extent this will be the case. It does seem, however, that the two techniques are not affected in the same way, since at these higher altitudes they report differing wind estimate.

It must be emphasized at this point that the theoretical equivalence of the IDI–derived wind and the spaced antenna apparent velocity rests upon the assumption of functional smoothness of the cross–spectra. Since in IDI–like analyses the cross–spectra are unsmoothed, it is probable that the theoretical assumptions are frequently violated, and it is difficult to predict just what results will ensue.

It has been noted that one of the major differences between those studies using IDI–like analyses which report interferometric wind velocities agreeing best with the spaced antenna apparent velocity, and those which report interferometric wind velocities agreeing best with the spaced antenna true wind velocity is the number of antennae deployed. In those cases where the IDI–like wind velocity agreed best with the spaced antenna apparent velocity, at least one additional antenna was available to provide an extra degree (or degrees) of freedom in the calculation of the angle of arrival of the backscattered signal.

Franke et al. [1990] argued that any Doppler sorting, whether by cross–spectral peak selection or multiple antenna spectral phase consistency criteria, tends to yield a wind estimation close to the spaced antenna apparent velocity because the Doppler sorted spectra approximate arithmetically–smoothed cross–spectra. In the case of spectral peak selection, the phase of the largest local peak in the cross–spectrum is used to identify a scattering point at that Doppler frequency. It was supposed by *Franke et al.* [1990] that such a peak in the unsmoothed cross–spectrum would dominate its neighbourhood in the smoothed cross–spectrum by virtue of its relatively large amplitude. Thus, the phase obtained from such a peak should approximate the phase in that region of the smoothed cross–spectrum. As has been discussed, they found that the smoothed cross–spectrum yielded the spaced antenna apparent wind velocity. In the case of the phase–consistency check, it was argued that since

individual Doppler frequencies in the unsmoothed cross–spectra rarely (if ever) contain information from single scatterers, the strongest scatterer present would tend to dominate the amplitude–weighted average phase at each Doppler frequency. Further, since the strongest returns from scatterers appear nearer the zenith due to the radar beam weighting function, the smoothed cross spectral phases are biased towards zero phase, and an over–estimate of the wind field is obtained.

It is perhaps somewhat artificial to argue that interferometric wind estimates obtained from smoothed cross–spectra yield velocities approximating the spaced antenna apparent wind speed due to biases introduced by the beam brightness weighting function. Although it is clear that the brightness distribution will tend to shift the position of scattering points measured from the smoothed cross–spectrum closer to the zenith, it is not clear that the magnitude of the shift should be such that the over–estimation yields the apparent velocity.

As has been shown in Section 5.2, in the case of functionally smooth cross–spectra, the apparent velocity will be obtained by any IDI–like interferometric technique. Clearly, this theory obviates the need for any ad–hoc arguments based on antenna beam patterns or brightness distribution function biases. The difficulty at present appears to relate to the large extent that the idealized theory discussed in Section 5.2 describes an unsmoothed spectral technique such as the IDI. In addition, it does not seem likely that the arguments presented by *Franke et al.* [1990] regarding phase consistency selection criteria fully explain the situation. It is therefore proposed that there exists some form of spectral averaging inherent in the IDI–like analyses as implemented in this report, and by *Adams et al.* [1986] and *Meek & Manson* [1987]. Whatever the form of this averaging, it appears sufficient to guarantee the functional smoothness of the cross–spectra and the cross–correlation functions required by the theory. Further, the only possible source of this averaging would appear to lie in the use of several spatially separated antennae to sample the backscattered signals on the ground. Each antenna samples (albeit spatially separated) the unsmoothed (or sample) cross–spectrum, and the phase information from all of these cross–spectra is used to obtain an estimate of the *average* phase slope between the antennae. Any unsmooth behaviour in the phases of the cross–spectrum is therefore reduced by this process. *Further, if the phase consistency rejection criterion is applied, any significant departures from functional smoothness are discarded.* Although it seems dubious that a single additional estimate of the cross–spectrum would achieve significant smoothing, four or five estimates must yield a more satisfactory result.

The claim is made, then, that IDI–like analyses, although normally thought of as utilizing unsmoothed cross–spectra, do in fact deal with smoothed spectra to some extent. This claim is contingent on the use of more than three antennae in the experiment, such that extra degrees of freedom are available in the measurement of the scattering points' position from the cross–spectral phases. The claim is also contingent on the signal incident on the spatially separated antennae having some form of statistical similarity. We require that the cross–spectral information in the signal received at all antennae is in some way related to the same (or similar) distribution of backscattered signals from the sky. In other words, we require that there exists some degree of correlation between the received signals. This is clearly the case for experiments conducted in "the real world", provided that the antenna separation is not too large. It is noted that the claim made above is consistent with the results reported by all five experiments (referenced above) utilizing IDI–like analyses.

5.6 Summary

In this chapter, the spaced antenna correlation theory set out by *Briggs* [1993] was introduced, and it was shown that any signals backscattered from a volume scattering medium will produce linear phase variations along equally–spaced rows of antennae, at any spectral frequency. It was also shown that if these linear phase variations are taken as evidence of single, discrete scattering points possessing unique Doppler shifts, then these "effective" scattering points must lie along a single azimuth in the sky. In the presence of turbulence, or random change in the diffraction pattern on the ground, it was shown that the zenith angles of the effective scattering points were reduced. The analysis of *Briggs* [1993] was extended, showing that if a horizontal wind was inferred from the distribution of effective scattering points and their radial Doppler velocities, then a quantity equal to the correlation analysis apparent velocity results. The symmetry between the cause of the IDI–like analysis' measurement of the apparent velocity and the reason for the difference between the apparent and true wind velocities in the correlation analysis was noted.

An experiment was conducted at medium frequency in which the data were analysed by both the spaced antenna FCA, and the IDI–like techniques. It was shown that the IDI–like analysis did indeed yield distributions of effective scattering points which displayed a tendency to elongate along the predicted azimuth of scatter.

Simultaneous wind profiles were calculated between altitudes of 60 km and 98 km using

both techniques, and both the spaced antenna true and apparent velocities were compared to the wind velocity obtained from the IDI–like analysis. Although considerable variation was observed, it was noted that the spaced antenna apparent velocity best described the IDI–like wind velocity. The similarity between the spaced antenna apparent velocity and the IDI–like velocity was observed to be greatest between 70 km and 84 km, while at the higher altitudes the IDI–like analysis wind showed some tendency towards large temporal variation not observed in the spaced antenna winds. It was speculated that these high–altitude deviations from the theory may be caused by the existence of E–region "glints", or other wave phase front–focussed events.

Some points were discussed regarding the nature of smoothed and unsmoothed cross–spectra, and their application to interferometric wind estimation techniques. Ideas proposed by *Franke et al.* [1990] were examined in the light of the results summarized above, and an alternative spectral–smoothing mechanism proposed. It was argued that the use of more than three antennae in the interferometric wind estimation must result in some form of spectral smoothing. It was also demonstrated that those interferometric experiments conducted with more than three antennae had tended to yield the spaced antenna apparent wind velocity. Alternatively, and for reasons as yet unexplained, those experiments utilizing exactly three antennae had tended to yield a wind velocity closer to the spaced antenna true wind velocity.

Chapter 6

SUMMARY AND CONCLUSION

6.1 Summary

The work described in this thesis is primarily concerned with the design, construction and use of a new beam–steerable, transmit/receive, MF Doppler radar. The design process leading to the construction and testing of various pieces of radar hardware is described in Chapter 2. The main focus of the discussion is placed on the problems associated with upgrading a 25 year–old array used only for reception to a modern, transmit/receive Doppler radar. These problems divide naturally into two classes; those associated with damage to, and ageing of the array, and those associated with the increased power levels present with the new transmitters. The emphasis of the design is placed on both experimental flexibility and a low–maintenance, long life–time radar system.

As an aid to antenna configuration selection and PA module distribution, an aperture–modeling computer program was developed. Parameters considered by the program included varying cable attenuation, antenna height above ground, radiated phase errors due to incorrect cable lengths or reactive impedance errors, phase–grouping the radiation of groups of elements to simulate antennae driven by single PA modules and progressive phase delays across the array to simulate beam steering. Different portions of the Buckland Park array are modeled and it is demonstrated that groupings of three antennae is the optimum solution for the design parameters pertaining. Imperfect arrays are also modeled using the computer program, and it is concluded that a surprisingly large departure from an "ideal" array is required before significant aberrations are observed in the modeled power radiation pattern.

The design, testing and construction of several new items of radar hardware is discussed

in section 2.5. These items included a 2.5 kW filter with 3^{rd} harmonic attenuation of 52 dB, a phase–control module with a phase resolution of 8.6°and a new antenna balun capable of withstanding the new transmitter power. Thirty of these new antenna baluns were constructed and mounted in UV–stabilized plastic boxes atop the antenna poles at Buckland Park.

The problems associated with upgrading and refurbishing the old 5 channel Buckland Park MF receiver system are discussed in Section 2.6. Three extra receiver and signal processor channels were added to the 5 channel receiver system, and the computer interface upgraded to allow connection to a personal computer. The relative gains of the in–phase and quadrature channel amplifiers in the signal–processors were equalized, reducing the error incurred by any phase–critical measurements to be made. In addition, a computer–controlled phase check facility was added to the equipment, allowing minimization of the error caused by different phase propagation delays between receivers. Several earth loops were discovered in the receivers which may, in the past, have caused some anomalous measurements to have been made. These were eradicated by careful earthing of the receiver boards, and elimination of multiple earth paths to the equipment chassis.

In Chapter 3, the refurbished 8 channel receiver system is used in conjunction with the existing broad–beamed spaced antenna radar transmitter for interferometric observations. The regions of ambiguity in the angle of arrival calculation are modeled by considering various combinations of phase ambiguity between the three antennae. It is shown that the normalized phase discrepancy check does not guarantee the absence (nor presence) of phase ambiguity. It is argued that the rapid decrease in the cross section for backscatter with zenith angle observed in the mesosphere excludes scatter from large off–zenith angles. Thus, phase ambiguities, at least in the first instance, may be ignored.

Receiver phase check data are examined and a temperature–dependent diurnal variation in receiver phase propagation delay is observed. Both the sense and the magnitude of the variation are seen to be dissimilar for each receiver, resulting in a potential source of error for phase–critical measurements. In addition, phase propagation delays are observed to change by as much as 10° with IF gain changes. Time–domain angle of arrival information was calculated and examined in polar sky–map form. It is shown that the direction of arrival is centred at some distance from the zenith for all ranges. Further, it is shown that inclusion of the receiver phase check information to eradicate receiver propagation delay error does not move the centre of scatter onto the zenith. It is concluded that residual channel errors

due to antenna impedance errors and variations in cable electrical lengths are responsible for the remaining off–zenith angle of scatter. These residual errors are removed by subtracting the offset of the peak of the distribution of the receiver phase differences from each phase difference measurement. The procedure is shown to centre the angle of arrival distribution on the zenith.

Returns from larger off–zenith angles were observed in the highest range gates recorded. These points near the E–layer produce a "halo" about the zenith, and were used to find sequences of moving echoes. These echoes are termed "trackable events", and it is shown that these do not necessarily move in the direction of the background wind. Three such events are presented, although these do not represent the total of such events in the data set. In contrast to the existence of trackable events in the E–region, no such events were found in the D–region. Finally, running time–series of spectral–intensity plots are found to be a useful aid to finding weak, coherent signals in radar data.

In Chapter 4, experiments utilizing the 30 upgraded antennae at Buckland Park and one 10 channel transmitter subsystem are described. It is demonstrated that significant power is radiated during transmission from the large array, and that the TR switches successfully isolated the receivers during the passage of the transmitter pulse. Power and signal–to–noise ratio profiles are measured and show satisfactory day–time returns from 64 km to 98 km in altitude. Signal–to–noise ratios of about 20 dB were typical for all but the lowest four range gates. Angle of arrival calculations performed on the vertical–beam data showed an average off–zenith angle of less than 1° for most range gates. Post–set beam steering experiments showed that the radial velocity as a function of beam–pointing direction was consistent with the background wind vector determined by the space antenna analysis.

Although at first only a vertically–directed beam was used, beam–steering software was later included, allowing transmitter beams to be directed to two and then five directions on successive data acquisitions.

The radar was firstly configured to steer the transmitter beam to off–zenith angles of 10° towards the West and then East. Angle of arrival analysis revealed that the transmitter beam was successfully steered, although an antenna configuration bias appeared to affect the results. It was shown that time–domain scatter preferentially aligned itself with the longest baseline of the antenna triangle. Post–set beam steering calculations show that the bias was not due to the transmitter beam–pointing direction. In addition, it was shown that scatterer aspect sensitivities could be measured using the PBS data. Typical θ_S values of between 2°

and 10° were found for various altitudes within the mesosphere.

The radar was reconfigured to transmit vertically, and then 10° off–zenith towards the West, East, South and finally North on successive data acquisitions. The angle of arrival information from calculated from this data set is used to calculate time–domain interferometric wind profiles, and these are shown to agree well with the spaced antenna–derived true winds. It is argued that the use of angle of arrival information is superior for the purposes of wind velocity determination than is the multiple Doppler beam-forming radar technique. This is due to the need to estimate an effective beam–pointing direction for the off–vertical Doppler radar beam in the case of the DBR which is, at best, a time–averaged correction. With time–domain angle of arrival calculation, changing scatterer aspect sensitivities are accounted for, and effective beam–pointing directions are automatically included in the calculation.

In Chapter 5, the spaced antenna correlation theory is introduced and extended in order to explain the measurement of the apparent wind by Doppler radar interferometric techniques utilizing smoothed cross–spectra. It was also stated that a certain symmetry existed between the cause of the measurement of the apparent wind by IDI–like analyses, and the reason for the difference between the spaced antenna true and apparent wind velocities.

An IDI–like analysis was developed, and it is shown experimentally that the effective scattering points identified by the analysis conform to theoretical predictions made by *Briggs* [1993]. This is shown despite the use of supposedly unsmoothed spectra. The winds derived by the IDI–like analysis are compared to the spaced antenna true and apparent velocities, and it is found that the apparent velocity best describes the IDI–like results. The similarity between the spaced antenna apparent wind and the IDI–like wind estimate appears greatest from 70 km to 84 km. Deviation below 70 km is ascribed to the difficultly in making reliable interferometric phase measurements, while deviations at the highest ranges is ascribed to the existence of E–region "glints" moving with velocities not representative of the mean wind. Finally, it is noted that all Doppler interferometric experiments utilizing more than three antennae tended to yield the spaced antenna apparent velocity, while those utilizing exactly three antennae tended to yield the spaced antenna true velocity. It is speculated that the unsmoothed spectra obtained in the former group of experiments were in some way becoming smoothed, while those in the latter group remained unsmoothed. A mechanism which might explain this "smooth–like" behaviour of unsmoothed spectra is proposed relating to the use of redundant phase information and rejection of unsmooth behaviour. In addition, it is argued that the estimation of an average phase slope along a line of antennae results in some

form of spectral averaging.

6.2 Conclusion

In this thesis, many aspects of radar interferometric techniques have been examined. Much of the work has demonstrated the difficulty involved with this kind of measurement, particularly in the elimination of equipment–induced bias. Short–term time variations in phase propagation delays have been observed, with serious implications for phase–sensitive (interferometric) measurements.

The mean angle of arrival experiment has been shown to yield reliable time–domain interferometric wind velocity measurements when used in conjunction with steered–transmitter beam experiments. In addition, raster–scanning in the post–set or post–statistics beam steering experiment has shown promise as an aspect sensitivity measurement technique.

In contrast to the time–domain interferometric measurement of wind velocity, frequency–domain techniques, such as the IDI technique have been shown both theoretically and experimentally to measure a wind velocity equivalent to the spaced antenna FCA apparent wind velocity. Although the theoretical proof of this was only valid for well–behaved, or smoothed cross–spectra, it was shown that IDI analyses, even though they utilize unsmoothed spectra, appear to obey the theoretical predictions. A possible mechanism by which this might occur was proposed, this being the averaging inherent in a multiple–sensor experiment, and evidence to support this proposal was cited from the results of four IDI–like experiments.

One–third of the new Adelaide MF Doppler radar has been constructed and transmission trials on one linear polarization of the Buckland Park antenna array have shown that usable echoes down to as low as 62 km have been obtained. It is expected that, with an increase in the power–aperture product of an additional factor of 12, echoes below 60 km will be routinely available. The first two beam–steering experiments conducted with the new radar have shown that the transmitter beam is successfully steered and that the effective beam–pointing direction varies with both time and altitude.

6.3 Further Work

Clearly a large amount of technical work remains before the new radar is fully operational. Two transmitter subsystems are yet to be commissioned, as is a new, larger bandwidth 10 channel receiver system. Upgrading of the remaining 59 antennae in the array with the new

high–power baluns contin at the time of writing, as does the design of the new antenna patch boards.

Several enhancements to the current design of the radar have already been mooted. Power upgrades to at least one of the three transmitter subsystems have begun, with a doubling of the power output to 50 kW expected. If such upgrades are performed on the remaining two transmitter subsystems, the new Adelaide MF Doppler radar will achieve peak RMS powers of 150 kW. In addition to this, pulse–coding schemes are being considered which will increase the effective power of the radar by a factor of four. Another area of hardware modification being considered is the addition of a frequency–stepping facility to enable FDI studies to be conducted. This will allow the radar to achieve greater height resolution without requiring extensive widening of the receiver bandwidths.

It is suggested that extensive comparative studies be undertaken to determine the veracity of new measurement techniques presented in this work. In particular, time–domain interferometry appears to offer an alternative wind measurement technique to the spaced antenna full correlation analysis. One possible advantage of the TDI wind measurement technique is that a vertically–directed transmitter beam is not required. Also, the reliability of aspect sensitivity measurements using post–set or post–statistics beam steering on reception with an electronically–steered transmitter beam must be ascertained. More conventional methods, such as aspect sensitivity measurements derived from the spatial auto–correlation function, or those derived from relative power measurements with pre–set multiple Doppler beam arrangements should be compared with those made by the new method.

It is possible that definitive answers to the questions posed by spectral smoothing may be obtained only with the use of numerical modeling. If a particular ensemble of scatterers moving with well–defined mean and fluctuating velocities can be satisfactorily represented by a computer model, then the signals sampled by any number of antennae at arbitrary positions on the ground may be obtained. These may then be analysed by any technique with any degree of spectral smoothing with antennae separated by any distance and the results compared. Since the theoretical background wind is known, techniques susceptible to unexpected aspects of the modeled atmosphere may be identified. In addition, the model atmosphere may be changed to represent pure volume scatter on the one hand, or it may be changed to contain only a few (or one) discrete reflection point.

A promising new area of study with the new radar is that of the sea–surface condition. By remote sensing the sea scatter with the transmitter beam directed at a zenith angle of

90°, and with a suitably high frequency resolution, sea currents may become measurable in the gulf to the South–West of the radar site.

Appendix A

RADIATION PATTERN OF A $\frac{3}{2}$–wave dipole AT 5.94 MHz

We begin with the coordinate system and dipole orientation as depicted in figure 2.5 for which we have equation 2.2. For a $\frac{3}{2}$–wave dipole the appropriate current distribution is

$$I(\zeta) = I_m \cos(\frac{3\pi\zeta}{2\ell}) \tag{A.1}$$

where $\ell = \frac{3\lambda}{4}$. Equation 2.2 can then be written

$$H_\phi = \frac{\jmath I_m k}{4\pi r} e^{-\jmath kr} \sin\theta \int_{-\ell}^{+\ell} \cos\left(\frac{3\pi\zeta}{2\ell}\right) e^{\jmath k\zeta\cos\theta} d\zeta \tag{A.2}$$

This integral can be solved using the identity

$$\cos\phi = \frac{1}{2}\left[e^{\jmath\phi} + e^{-\jmath\phi}\right] \tag{A.3}$$

The integral in equation A.2 is then

$$\begin{aligned}
& \frac{1}{2}\int_{-\ell}^{+\ell} \left(e^{\jmath\frac{3\pi\zeta}{2\ell}} + e^{-\jmath\frac{3\pi\zeta}{2\ell}}\right) e^{\jmath k\zeta\cos\theta} d\zeta \\
= & \frac{1}{2}\int_{-\ell}^{+\ell} \left(e^{\jmath\zeta(\frac{3\pi\zeta}{2\ell} + k\cos\theta)} + e^{\jmath\zeta(\frac{-3\pi\zeta}{2\ell} + k\cos\theta)}\right) d\zeta \\
= & \frac{1}{2}\left[\frac{1}{\jmath\left(\frac{3\pi}{2\ell} + k\cos\theta\right)} e^{\jmath\zeta(\frac{3\pi\zeta}{2\ell} + k\cos\theta)} + \frac{1}{\jmath\left(\frac{-3\pi}{2\ell} + k\cos\theta\right)} e^{\jmath\zeta(\frac{-3\pi\zeta}{2\ell} + k\cos\theta)}\right]_{\zeta=-\ell}^{\zeta=\ell}
\end{aligned}$$

$$= \frac{1}{2}\left\{\left[\frac{1}{\jmath\left(\frac{3\pi}{2\ell}+k\cos\theta\right)}e^{\jmath\left(\frac{3\pi}{2}+k\ell\cos\theta\right)}+\frac{1}{\jmath\left(\frac{-3\pi}{2\ell}+k\cos\theta\right)}e^{\jmath\left(\frac{-3\pi}{2}+k\ell\cos\theta\right)}\right]\right.$$
$$\left.-\left[\frac{1}{\jmath\left(\frac{3\pi}{2\ell}+k\cos\theta\right)}e^{\jmath\left(\frac{-3\pi}{2}-k\ell\cos\theta\right)}+\frac{1}{\jmath\left(\frac{-3\pi}{2\ell}+k\cos\theta\right)}e^{\jmath\left(\frac{3\pi}{2}-k\ell\cos\theta\right)}\right]\right\}$$

To proceed we use the identity

$$e^{\pm\jmath\frac{3\pi}{2}} = \mp\jmath \tag{A.4}$$

and so our integral simplifies to

$$= \frac{1}{2}\left\{\frac{1}{\jmath\left(\frac{3\pi}{2\ell}+k\cos\theta\right)}(-\jmath)e^{\jmath k\ell\cos\theta}+\frac{1}{\jmath\left(\frac{-3\pi}{2\ell}+k\cos\theta\right)}(+\jmath)e^{\jmath k\ell\cos\theta}\right.$$
$$\left.-\frac{1}{\jmath\left(\frac{3\pi}{2\ell}+k\cos\theta\right)}(+\jmath)e^{-\jmath k\ell\cos\theta}-\frac{1}{\jmath\left(\frac{-3\pi}{2\ell}+k\cos\theta\right)}(-\jmath)e^{-\jmath k\ell\cos\theta}\right\}$$
$$= \frac{1}{2}\left\{\left[\frac{-1}{\frac{3\pi}{2\ell}+k\cos\theta}+\frac{1}{\frac{-3\pi}{2\ell}+k\cos\theta}\right]e^{\jmath k\ell\cos\theta}\right.$$
$$\left.+\left[\frac{1}{\frac{-3\pi}{2\ell}+k\cos\theta}-\frac{1}{\frac{3\pi}{2\ell}+k\cos\theta}\right]e^{-\jmath k\ell\cos\theta}\right\}$$
$$= \frac{1}{2}\left[\frac{1}{\frac{-3\pi}{2\ell}+k\cos\theta}-\frac{1}{\frac{3\pi}{2\ell}+k\cos\theta}\right]\left[e^{\jmath k\ell\cos\theta}+e^{-\jmath k\ell\cos\theta}\right]$$
$$= \frac{1}{2}\left[\frac{\frac{3\pi}{2\ell}+k\cos\theta+\frac{3\pi}{2\ell}-k\cos\theta}{-\left(\frac{3\pi}{2\ell}\right)^2+k^2\cos^2\theta}\right]2\cos(k\ell\cos\theta)$$
$$= \frac{\frac{-3\pi}{\ell}}{\left(\frac{3\pi}{2\ell}\right)^2-k^2\cos^2\theta}\cos(k\ell\cos\theta)$$

Now, recall that $2\ell = \frac{3\lambda}{2}$ and $k = \frac{2\pi}{\lambda}$ so that $k\ell = \frac{2\pi}{\lambda}\frac{3\lambda}{4} = \frac{3\pi}{2}$ and $\frac{3\pi}{2\ell} = k$. Our integral then becomes

$$= \frac{-2k}{k^2-k^2\cos^2\theta}\cos\left(\frac{3\pi}{2}\cos\theta\right)$$
$$= \frac{-2}{k\sin^2\theta}\cos\left(\frac{3\pi}{2}\cos\theta\right) \tag{A.5}$$

Substituting A.5 for the integral in equation A.2 we find

$$H_\phi = \frac{-\jmath I_m}{2\pi r}e^{-\jmath kr}\frac{\cos\left(\frac{3\pi}{2}\cos\theta\right)}{\sin\theta} \tag{A.6}$$

The radiation pattern of this $\frac{3}{2}$–wave dipole when the image is included is then

$$K(\theta,\chi) \propto \sin^2(k\Delta h \cos\chi)\frac{\cos^2\left(\frac{3\pi}{2}\cos\theta\right)}{\sin^2\theta} \tag{A.7}$$

which, using equations 2.15 to transform to the (α,β) coordinate system, becomes

$$K(\alpha,\beta) \propto \sin^2\left(\frac{k\Delta h}{\sqrt{1+tan^2\alpha+tan^2\beta}}\right)\cos^2\left(\frac{3\pi\tan\beta}{2\sqrt{1+tan^2\alpha+tan^2\beta}}\right)\frac{1+\tan^2\alpha+\tan^2\beta}{1+\tan^2\alpha} \tag{A.8}$$

Equation A.8 may now be compared to equation 2.16.

Appendix B

A COMPARISON OF DOPPLER AND SPACED ANTENNA TECHNIQUES FOR THE MEASUREMENT OF TURBULENT ENERGY DISSIPATION RATES

This is a reprint of the paper,

Vandepeer, B. G. W. & Hocking, W. H. (1993),'A comparison of Doppler and spaced antenna techniques for the measurement of turbulent energy dissipation rates',*Geophysical Research Letters*, **20**,(1),17–20

GEOPHYSICAL RESEARCH LETTER, VOL. 20, NO. 1, PAGES 17-20, JANUARY 8, 1993

A Comparison of Doppler and Spaced Antenna Techniques for the Measurement of Turbulent Energy Dissipation Rates

B. G. W. Vandepeer and W. K. Hocking[1]

University of Adelaide, Adelaide, South Australia

Abstract. There has been concern in the past that spaced antenna radar measurements of energy dissipation rates in the Mesosphere using broad beam arrays may be contaminated by the effects of atmospheric gravity waves. To investigate this possibility, a 1.98 MHz Doppler radar operated by the University of Adelaide was used in two separate configurations; a narrow vertical beam (4.5° half-power half-width) and three smaller spaced antenna systems with broad beams (20° half-power half-width) were used to simultaneously measure energy dissipation rates in the height region 80 to 100km. The 3 broad beams were also used to determine winds by the spaced antenna method. Although extraction of the energy dissipation rate parameter is a difficult process, temporally and spatially coincident data were obtained enabling some important comparisons to be made. Three years of such data were analysed and the following results noted: (1) the mean energy dissipation rates as measured by the two radars are comparable, (2) the variance of the data as measured by the Doppler radar is larger than that measured by the spaced antenna radar, (3) The spaced antenna radar does not generally over-estimate energy dissipation rates at moderate and large values, but when turbulence is very weak, it may do so. The degree of over-estimation is not as serious as has been inferred in the past. However, there is considerable scatter in the short term ratio of measurements using the two methods, which emphasizes the large degree of spatial variability of turbulence strengths in the middle atmosphere.

Introduction

Turbulent energy dissipation rates in the atmosphere can be determined by measuring the spectral widths associated with radar signals backscattered from the atmosphere [*Hocking*, 1983a; *Hocking*, 1983b; *Frisch & Clifford*, 1974; *Labitt*, 1981; *Bohne*, 1982]. However, other effects apart from turbulence also act to broaden the spectrum, including the effects of mean horizontal motions through the finite beam width, and (for off-vertical beams) wind shear (see e.g., *Hocking* [1983a], *Hocking* [1983b]). These two effects must be carefully removed in order to determine the spectral width due to the turbulence alone.

There are at least two different ways to do this. One is to use measured values of horizontal winds, and the known value of the beam width, to compute the spectral half width due to beam broadening, (f_b say), and then determine the spectral width due to the turbulence through the relation

$$f_{turb}^2 = f_{obs}^2 - f_b^2 \tag{1}$$

where f_{obs} is the observed experimental spectral half-power-half-width. This spectral half-width is readily converted to a root mean square fluctuating scatterer velocity by

$$V_{RMS}^2 = \frac{(\frac{\lambda}{2})^2 f_{turb}^2}{2ln2} \tag{2}$$

where λ is the radar wavelength. The scatterer root mean square velocity then yields an energy dissipation rate from

$$\epsilon = cV_{RMS}^2 \omega_b \tag{3}$$

where ω_b is the Brunt-Väisälä frequency and c is a numerical constant with a value of about 0.4. This has been applied in particular by *Hocking* [1988].

The second procedure is perhaps more elegant. If the spaced antenna method of wind measurement is used (see e.g., *Briggs* [1984], *Hocking et al.* [1989]), then the effects of beam broadening are removed as a matter of course and the rate of natural fading due to fluctuating motion is given by the parameter denoted by *Briggs* [1984] as $T_{\frac{1}{2}}$, the characteristic time. This procedure works even if the radar scatterers are anisotropic, whereas the first procedure requires independent estimates of the effective polar diagram of the scatterers in order to be properly applied. *Briggs* [1980] and *Manson & Meek* [1980, and 1981] described the relation between the fluctuating scatterer velocity and $T_{\frac{1}{2}}$ as

$$V_{RMS} = \frac{\lambda\sqrt{2ln2}}{4\pi T_{\frac{1}{2}}} \tag{4}$$

and several following papers utilized this procedure [*Manson & Meek*, 1980; *Manson et al.*, 1981; *Manson & Meek*, 1987]. However, most applications

[1]Now at: University of Western Ontario, London, Ontario, Canada

of the spaced antenna method utilize receiving antennas with wide radar beams, and this leads to additional problems which mean that the spaced antenna method may over-estimate the energy dissipation rate.

If we consider a gravity wave superimposed on the mean wind, then we note three extra fluctuating non-turbulent effects which might act to broaden the spectrum recorded by a radar on the ground. The first and perhaps most obvious of the three effects is the vertical fluctuating motion due to the wave. Even though the wave may only go through a portion of one cycle during a data record of 102 seconds, a variance in the vertical velocity will occur, which will broaden the spectrum [*Hocking*, 1988; *Hocking et al.*, 1989]. This effect occurs for any vertical or off-vertical radar beam. Secondly, the vertical velocity will vary as a function of position in the radar beam, also leading to an increase in variance since the returned signal is a spatial average over the radar beam width. The third effect is the horizontal fluctuating motion associated with atmospheric gravity waves. Since the radar beam is of finite width, any horizontal velocity vector produces a component of motion towards (or away from) the radar. If the horizontal vector varies as a function of position, then a general broadening of the spectrum is the result. As the angular width of the radar beam increases, so too does the radial contribution of velocity due to horizontal movements. In the case of the spaced antenna beam width of approximately 20°, an arc of length 28 km is encompassed at a height of 80 km. Since gravity waves at this height may have horizontal wavelengths less than this, it is possible that there may be one or more wavelengths of the wave within the beam of the radar. Thus while the atmosphere in one part of the beam may be moving towards the radar, in another part it will be moving away. The combined effect of all these different motions is to broaden the frequency spectrum still more. Narrow beam radars are less likely to be affected by these last two effects. Since the estimate of energy dissipation rate is governed by the width of the Doppler spectrum observed, it can be seen that the wider spectra expected with the spaced antenna analysis may result in an error in the estimate of energy dissipation rate. (It is possible that a gravity wave of correct phase and wavelength will narrow the spectrum observed, but this must be a statistically rare event.) The effect due to the first process described above can be deduced by comparing spectral widths recorded with data of different durations [*Hocking*, 1989b], and is somewhat independent of the radar beam width. The study reported here was designed to test the magnitude of the second and third effects, and thereby infer implications about spaced antenna studies. We wish to emphasize that the complications discussed above mean that there will be considerable scatter in both measurements of the energy dissipation rate. One should therefore not expect extremely high correlation coefficients. For this reason, when making comparisons we are careful to apply statistical theory and determine confidence limits wherever possible. All results should be considered and interpreted with this intrinsic scatter in mind.

Experiment

The radar used was situated approximately 40 km north of Adelaide, South Australia (34° 38' S, 138° 29' E). The narrow beam radar consisted of 89 parallel half wave dipoles with 90 metre spacing, arranged in a square grid with a circular perimeter of 450 metres. Spaced antenna radar measurements were made using a system consisting of 3 sets of 4 parallel half wave dipoles selected from the 89 dipoles and located at the vertices of a triangle of approximate baseline 180 metres. The transmitter used for both Doppler and spaced antenna experiments was located at the same site as the receiving arrays and consisted of four folded dipoles arranged in a square. The transmission frequency was 1.98 MHz and the polar power diagram half-width was about 40°. It is probable that the effective beam width was somewhat less than this due to the effects of the aspect sensitivity of the radio-wave scatterers [*Hocking*, 1987]. The same transmitting array was used for both the spaced antenna and Doppler radars so that only the receiving array configurations were different. The spaced antenna analysis was performed on site and involved taking cross correlations functions of the three antenna signal time series as well as auto correlations of the signals, following *Briggs* [1984]. From these functions it is possible to extract both the wind velocity over the radar, V, and the time scale for random fluctuations in the moving pattern, $T_{\frac{1}{2}}$. This parameter yields the energy dissipation rate as described earlier.

Although the data were not completely contiguous, estimates of energy dissipation rate by the spaced antenna method were obtained every two minutes, each estimate being calculated from a 102.4 s record. These values of energy dissipation rate were then averaged over different time lengths varying between one hour and seven days.

The Doppler analysis was performed at intervals ranging between 90 and 200 min with spaced antenna data taken simultaneously. Each record was again of 102.4 s length, but for the Doppler analysis the entire vertically-directed array of 89 antennas was used. This yielded a much narrower beam width of 4.5° for reception in the Doppler mode. The analysis performed at the radar site consisted of a fast Fourier transform and then Gaussian fitting to the resulting power spectrum. Rigorous rejection criteria were applied to ensure that the spectrum was indeed Gaussian in shape and that sufficient power had been backscattered. The half width of the fit-

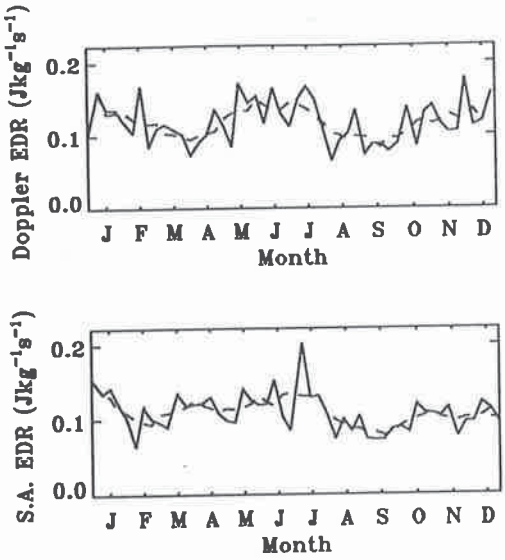

Fig. 1. Time series of weekly averaged energy dissipation rates (solid) for the year 1986 at a height of 86 km. A five point running mean (dotted) is overlayed

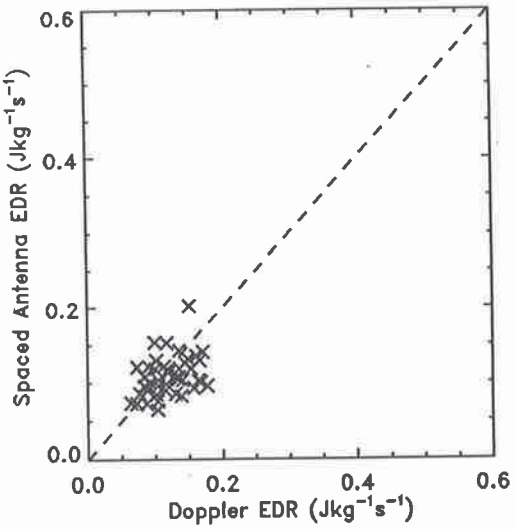

Fig. 2. Scatter plot of weekly averaged energy dissipation rates for the year 1986 at a height of 86 km. The correlation coefficient for these data is 0.39 with a 95 percent confidence interval of 0.11 to 0.62.

ted Gaussian was then recorded. In order for this half width to be used for finding the energy dissipation rate the effects of beam broadening due to background wind had to be removed [*Hocking*, 1983a]. The measurement of wind produced by the spaced antenna analysis was used to do this according to equation 1. Making some assumptions about the atmospheric environment at the height of interest such as the Brunt-Väisälä frequency, we apply equation 3 to yield the Doppler estimate of energy dissipation rate. These values of energy dissipation rate were derived from single 102.4 s data records and were repeated every few hours. These observations of energy dissipation rate were then averaged in similar ways to the spaced antenna estimates.

Results

In Figure 1 the two time series of energy dissipation rates are plotted for the year of 1986. In this case the data have been averaged into 7 day blocks, and a 5 point running mean has been overlayed (dashed line). Similarities between the two data sets are immediately apparent. Firstly the magnitudes of the independent estimates of energy dissipation rate are comparable and agree well with other researchers in the field [*COSPAR*, 1990]. A median value of approximately 0.15 $JKg^{-1}s^{-1}$ is not an unreasonable magnitude of energy dissipation rate for Mesospheric turbulence. Secondly longer term trends in the two data sets match quite well, with maxima occurring in solstices and minima in the equinoxes. The magnitude of the maxima and minima are again comparable between data sets, although the longer term variation in the spaced antenna data is greater than in the Doppler data. A significant difference between the two data sets is the tendency of the short term fluctuations in the Doppler data to be larger than those of the spaced antenna data. This is most easily observed during the Winter and Spring sections of the data from June to September. These short term variance differences become more pronounced as the averaging period is decreased, and are most obvious with the raw data. Our data also suggests a possible double peak effect (apparent in both Doppler and spaced antenna data) during the Winter solstice (Southern Hemisphere) but details of this behaviour will be elaborated upon in a later paper.

A scatter plot comparing the two time series displayed in Figure 1 appears in Figure 2. Each point represents a 7 day average of either a Doppler or spaced antenna estimate of energy dissipation rate. The correlation index in this case is 0.39 with a 95% confidence interval of (0.11, 0.62). The data points are scattered fairly evenly around the 1:1 line and exhibit little tendency to skew on the side of larger spaced antenna measurements. The line of best fit for these data has a slope of 0.34 indicating that the scatter is more horizontally distributed than might be expected. This is a feature observed in many of our data records, and will be discussed shortly.

We now turn to investigations at smaller time scales. In order to do this, the data were not averaged at all; simultaneous individual data points were displayed as scatter plots, each data point derived from a 102 second period. A typical example of these plots appears in Figure 3. This particular data set was recorded in 1987 at an altitude of 88 km. The correlation coefficient in this case is 0.25 which is somewhat lower than the typical correlation

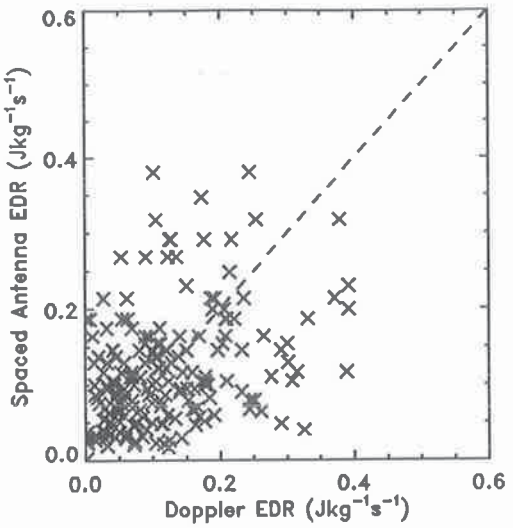

Fig. 3. Scatter plot of unaveraged energy dissipation rates for the year 1987 at a height of 88 km. The correlation coefficient for these data is 0.25 with a 95 percent confidence interval of 0.11 to 0.37.

observed. (Correlations ranged from -0.1 to about 0.7 with approximate errors of ± 0.05) Careful observation of Figure 3 reveals that the data points tend to have a larger degree of scatter in the horizontal direction than in the vertical. That is the Doppler data seems to take on a larger range of values than the spaced antenna data. Closer examination of the ranges of energy dissipation rates recorded by the spaced antenna versus Doppler methods yields ranges of 0.15 $JKg^{-1}s^{-1}$ and 0.20 $JKg^{-1}s^{-1}$ respectively. Horizontal skewness of the data is also indicated by the line of best fit which has a slope of less than one. This trait was exhibited in all scatter plots examined, and is the main result to be reported in this work. In view of the large number of measurements of energy dissipation rates made by the spaced antenna method in the past, this particular feature now deserves some further discussion.

Discussion

We will now discuss the tendency for the mean slope of the scatter to be consistently less than one. That this is so implies that the spaced antenna estimate of energy dissipation rate is larger than the Doppler estimate at smaller values of epsilon. Further, it implies that the Doppler estimate of energy dissipation rate is larger than the spaced antenna estimate at larger values. This tendency of the data at low values of energy dissipation rate to be overestimated by the spaced antenna radar is typical of the expected gravity wave contamination effect. When the turbulence is large in intensity, however, the effects of horizontal gravity wave fluctuations should be relatively minor, and we might expect the spaced antenna method measurements to be similar to those of the narrow beam. However, this is not so - indeed, at higher values of energy dissipation rates, the spaced antenna values are less than those on the narrow beam. One possible explanation lies in the sporadic and "patchy" nature of turbulence in the Mesosphere. When a patch of intense turbulence lies in the narrow beam, it is unlikely that the intense patch covers the whole of the radar volume of the wide beam. There will however be weaker patches of turbulence scattered around the volume. The measured spectral width will be a weighted average of the contributions due to all the patches of turbulence, with higher weighting going to the more intense scatterers. On the wide beam a larger relative contribution from the weaker patches of turbulence, (due to their increased number), will occur. Thus the spectral width recorded on the wide beam will be less than that on the narrow beam. On the other hand, the converse applies when the region observed by the narrow beam contains weak turbulence; there will be more intense patches elsewhere in the wide beam, and the spectral width observed with the wide beam will be larger than on the narrow beam. This description also explains why there is less variability in the energy dissipation rates measured with the wide beam, and hence the tendency for horizontal skewness in the scatter to be exhibited in Figure 2 and especially Figure 3. Thus it would appear that a spaced antenna radar is capable of measuring reliable energy dissipation rates, provided it is realised that these rates are more of a smoothed estimate of the turbulent intensity in the irradiated volume. The localised turbulent intensity at some point in the beam may be slightly higher (or lower) than that measured.

Conclusion

Our comparisons emphasize the tremendous degree of spatial variability in turbulence strengths in the middle atmosphere. We have noted that while there is substantial (geophysical) scatter in our data, the measurements of the energy dissipation rates by the spaced antenna method do not over-estimate the Doppler radar data substantially. Any differences between the two measurements are generally in the nature of increased scatter, not in the form of consistently larger spaced antenna values. Thus measurements of the turbulent energy dissipation rate by the spaced antenna radar are not overly affected by contamination due to the presence of atmospheric gravity waves provided that some caution is exercised. The spaced antenna method is quite useful for obtaining not only winds, but also energy dissipation rates as long as it is realised that the full dynamic range of turbulence intensities may not be observed. More caution may be indicated, however, when using the radar to measure very low levels of energy dissipation rate, as these could well be overes-

timates. The energy dissipation rate as measured by the spaced antenna method can be considered as a weighted spatial average of the turbulence intensity throughout the radar beam width.

References

Bohne, A. R. (1982), 'Radar detection of turbulence in precipitation environments', *Journal of the Atmospheric Sciences* **39**, 1819–1837.

Briggs, B. H. (1980), 'Radar observations of atmospheric winds and turbulence: a comparison of techniques', *Journal of Atmospheric and Terrestrial Physics* **42**, 823–833.

Briggs, B. H. (1984), 'The analysis of spaced sensor records by correlation techniques', *Handbook for the Middle Atmosphere Program* **13**, 166–186. SCOSTEP Secretariat, University of Illinois, Urbana, IL, USA.

COSPAR (1990), *Cospar international reference atmosphere: 1986. Part II: Middle atmosphere models*, Pergamon Press.

Frisch, A. S. & Clifford, S. F. (1974), 'A study of convection capped by a stable layer using Doppler radar and acoustic echo sounders', *Journal of the Atmospheric Sciences* **31**, 1622–1628.

Hocking, W. K. (1983a), 'On the extraction of atmospheric turbulence parameters from radar backscatter Doppler spectra–I. theory', *Journal of Atmospheric and Terrestrial Physics* **45**(2/3), 89–102.

Hocking, W. K. (1983b), 'Mesospheric turbulence intensities measured with a HF radar at 35°S–II', *Journal of Atmospheric and Terrestrial Physics* **45**(2/3), 103–114.

Hocking, W. K. (1987), 'Radar studies of small scale structure in the upper middle atmosphere and lower ionosphere', *Advances in Space Research* **7**, 327–338.

Hocking, W. K. (1988), 'Two years of continuous measurements of turbulence parameters in the upper mesosphere and lower thermosphere with a 2–MHz radar', *Journal of Geophysical Research* **93**, 2475–2491.

Hocking, W. K. (1989b), 'Gravity wave oscillations as a cause of spectral broadening', *Handbook for the Middle Atmosphere Program* **28**, 401–403. SCOSTEP Secretariat, University of Illinois, Urbana, IL, USA.

Hocking, W. K., May, P. & Röttger, J. (1989), 'Interpretation, reliability and accuracies of parameters deduced by the spaced antenna method in middle atmosphere applications', *Pure and Applied Geophysics* **130**(2/3), 571–604.

Labitt, M. (1981), Coordinated radar and aircraft observations of turbulence, Technical Report ATC-108, Lincoln Laboratory, MIT.

Manson, A. H. & Meek, C. E. (1980), 'Gravity waves of short period (5-90 min), in the lower thermosphere at 52° North (Saskatoon, Canada)', *Journal of Atmospheric and Terrestrial Physics* **42**, 103–113.

Manson, A. H. & Meek, C. E. (1987), 'Small-scale features in the middle atmosphere windfield at Saskatoon, Canada (52°N, 107°W): An analysis of MF radar data with rocket comparisons', *Journal of the Atmospheric Sciences* **44**, 3661–3672.

Manson, A. H., Meek, C. E. & Gregory, J. B. (1981), 'Gravity waves of short period (5-90 min), in the lower thermosphere at 52° North (Saskatoon, Canada); 1978/1979', *Journal of Atmospheric and Terrestrial Physics* **43**, 35–44.

B. G. W. Vandepeer, Department of Physics and Mathematical Physics, Universit y of Adelaide, GPO BOX 498, Adelaide 5001, Australia.

W. K. Hocking, Department of Physics, Physics and Astronomy Building, Univers ity of Western Ontario, London Ontario, N6A 3K7, Canada.

(Received April 9, 1992;
accepted May 6, 1992.)

References

Adams, G. W., Brosnahan, J. W., Walden, D. C. & Nerney, S. F. (1986), 'Mesospheric observations using a 2.66 MHz radar as an Imaging Doppler Interferometer: Description and first results', *Journal of Geophysical Research* **91**(A2), 1671–1683.

Adams, G. W., Edwards, D. P. & Brosnahan, J. W. (1985), 'The Imaging Doppler Interferometer: Data analysis', *Radio Science* **20**(6), 1481–1492.

Andrews, D. G., Holton, J. R. & Leovy, C. B. (1987), *Middle atmosphere dynamics*, Academic Press.

Appleton, E. V. (1930), 'On some measurements of the equivalent height of the atmospheric ionised layer', *Proc. Roy. Soc. Lond. A* **A126**, 542–569.

Appleton, E. V. & Barnett, M. A. F. (1925), 'On some direct evidence for downward atmospheric reflection of electric rays', *Proc. Roy. Soc. Lond. A* **A109**, 621–641.

Balsley, B. B. & Ecklund, W. L. (1972), 'A portable coaxial colinear antenna', *IEEE Transactions on Antennas and Propagation* **20**(4), 513–516.

Balsley, B. B. & Gage, K. S. (1980), 'The MST radar technique: Potential for middle atmospheric studies', *Pure and Applied Geophysics* **118**, 452–493.

Balsley, B. B., Ecklund, W. L. & Fritts, D. C. (1983), 'VHF echoes from the high latitude mesosphere and lower thermosphere: Observations and interpretations', *Journal of the Atmospheric Sciences* **40**, 2451–2466.

Balsley, B. B., Ecklund, W. L., Carter, D. A. & Johnston, P. E. (1980), 'The MST radar at Poker Flat, Alaska', *Radio Science* **15**(2), 213–223.

Baulch, R. N. E. & Butcher, E. C. (1978), 'Direction of arrival of radio waves reflected from the E–region', *Journal of Atmospheric and Terrestrial Physics* **40**, 1235–1246.

Bramley, E. N. (1953), 'Direction–finding studies of large–scale ionospheric irregularities', *Proc. Roy. Soc. Lond. A* **220**, 39.

Bramley, E. N. & Ross, W. (1951), 'Measurements of the direction of arrival of short radio waves reflected at the ionosphere', *Proc. Roy. Soc. Lond. A* **207**, 251.

Briggs, B. H. (1951), 'An investigation of certain properties of the ionosphere by means of a rapid frequency–change experiment', *Proc. Roy. Soc. Lond. B* **64B**, 255–274.

Briggs, B. H. (1984), 'The analysis of spaced sensor records by correlation techniques', *Handbook for the Middle Atmosphere Program* **13**, 166–186. SCOSTEP Secretariat, University of Illinois, Urbana, IL, USA.

Briggs, B. H. (1993), On radar interferometric techniques in the situation of volume scatter, *in* '6th MST radar workshop, Taiwan'. Unpublished material.

Briggs, B. H. & Vincent, R. A. (1992), 'Spaced-antenna analysis in the frequency domain', *Radio Science* **27**(2), 117–129.

Briggs, B. H., Elford, W. G., Felgate, D. G., Golley, M. G., Rossiter, D. E. & Smith, J. W. (1969), 'Buckland Park aerial array', *Nature* **223**, 1321–1325.

Briggs, B. H., Phillips, G. J. & Shinn, D. H. (1950), 'The analysis of observations on spaced recievers of the fading of radio signals', *Proc. Phys. Soc. (London)* **B63**, 106.

Brosnahan, J. W. & Adams, G. W. (1993), 'The MAPSTAR Imaging Doppler Interferometer (IDI) radar: Description and first results', *Journal of Atmospheric and Terrestrial Physics* **55**(3), 203–228.

Brown, W. O. J. (1992), MF radar interferometry, PhD thesis, University of Cant.,NZ.

Brownlie, G. D., Dryburgh, L. G. & Whitehead, J. D. (1973), 'Measurement of waves in the ionosphere: A comparison of the ray theory approach and diffraction theory', *Journal of Atmospheric and Terrestrial Physics* **35**, 2147–2162.

COSPAR (1990), *Cospar international reference atmosphere: 1986. Part II: Middle atmosphere models*, Pergamon Press.

Czechowsky, P., Reid, I. M. & Rüster, R. (1988), 'VHF radar measurements of the aspect sensitivity of the summer polar mesospause echoes over Andenes (69° N,16° E), Norway', *Geophysical Research Letters* **15**(11), 1259–1262.

Czechowsky, P., Reid, I. M., Rüster, R. & Schmidt, G. (1989a), 'VHF radar echoes observed in the summer and winter polar mesosphere over Andøya, Norway', *Journal of Geophysical Research* **94**(D4), 5199–5217.

Czechowsky, P., Reid, I. M., Rüster, R. & Schmidt, G. (1989b), 'Correction to "VHF radar echoes observed in the summer and winter polar mesosphere over Andøya, Norway" ', *Journal of Geophysical Research* **94**(D10), 13079.

Eckersley, T. L. & Farmer, F. T. (1945), 'Short period fluctuations in the characteristics of wireless echoes from the ionosphere', *Proc. Roy. Soc. Lond. A* **184**, 196–217.

Farley, D. T., Ierkic, H. M. & Fejer, B. G. (1981), 'Radar Interferometry: A new technique for studying plasma turbulence in the ionosphere', *Journal of Geophysical Research* **86**(A3), 1467–1472.

Felgate, D. G. (1969), Studies of ionospheric drifts using a large ariel array, PhD thesis, University of Adelaide, Adel., Australia.

Felgate, D. G. (1970), 'On the point source effect in the measurement of ionospheric drifts', *Journal of Atmospheric and Terrestrial Physics* **32**, 241.

Flock, W. L. & Balsley, B. B. (1967), 'VHF radar returns from the D–region of the equatorial ionosphere', *Journal of Geophysical Research* **72**(21), 5537–5541.

Folkestad, K., Hagfors, T. & Westerlund, S. (1983), 'EISCAT: An updated description of technical characteristics and operational capabilities', *Radio Science* **18**(6), 867–879.

Franke, P. M., Thorsen, D., Champion, M., Franke, S. J. & Kudeki, E. (1990), 'Comparison of time– and frequency–domain techniques for wind velocity estimation using multiple receiver MF radar data', *Geophysical Research Letters* **17**(12), 2193–2196.

Fritts, D. C. & Vincent, R. A. (1987), 'Mesospheric momentum flux studies at Adelaide, Australia: Observations and a gravity wave–tidal interaction model', *Journal of the Atmospheric Sciences* **44**(3), 605–619.

Fukao, S., Tsuda, T., Kato, S., Wakasugi, K. & Makihira, T. (1985a), 'The MU radar with an active phased array system: 1. Antenna and power amplifiers', *Radio Science*.

Fukao, S., Tsuda, T., Kato, S., Wakasugi, K. & Makihira, T. (1985b), 'The MU radar with an active phased array system: 2. in–house equipment', *Radio Science*.

Gage, K. S. & Balsley, B. B. (1980), 'On the scattering and reflection mechanisms contributing to clear air radar echoes from the troposphere, stratosphere and mesosphere', *Radio Science* **15**, 243–258.

Gardner, F. F. & Pawsey, J. L. (1953), 'Study of the ionospheric D–region using partial reflections', *Journal of Atmospheric and Terrestrial Physics* **3**, 321–344.

Golley, M. & Rossiter, D. (1970), 'Some tests of methods of analysis of ionospheric drift records using an array of 89 aerials', *Journal of Atmospheric and Terrestrial Physics* **32**, 1215.

Gregory, J. B. (1956), 'Ionospheric reflections from heights below the E–region', *Australian Journal of Physics* **9**, 324–342.

Harper, R. M. & Gordon, W. E. (1980), 'A review of radar studies of the middle atmosphere', *Radio Science* **15**(2), 195–211.

Hecht, E. (1987), *Optics*, second edn, Addison-Wesley publishing company.

Hocking, W. K. (1979), 'Angular and temporal characteristics of partial reflections from the D–region of the ionosphere', *Journal of Geophysical Research* **84**, 845–851.

Hocking, W. K., Fakao, S., Yamamoto, M., Tsuda, T. & Kato, S. (1991), 'Viscosity waves and thermal–conduction waves as a cause of "specular" reflectors in radar studies of the atmosphere', *Radio Science* **26**(5), 1281–1303.

Hocking, W. K., May, P. & Röttger, J. (1989), 'Interpretation, reliability and accuracies of parameters deduced by the spaced antenna method in middle atmosphere applications', *Pure and Applied Geophysics* **130**(2/3), 571–604.

Holmes, N. E. (1974), An ultrasonic image forming system for ionospheric studies, PhD thesis, University of Adelaide, Adel., Australia.

Jones, K. L. (1981), 'The interpretation of radar echoes from altitudes near 100 km using a phased antenna array', *Journal of Atmospheric and Terrestrial Physics* **43**, 1015–1026.

Kudeki, E. & Stitt, G. R. (1987), 'Frequency domain interferometry: A high resolution radar technique for studies of atmospheric turbulence', *Geophysical Research Letters* **14**(3), 198–201.

Kudeki, E. & Woodman, R. F. (1990a), 'A post–statistics steering technique for MST radar applications', *Radio Science* **25**(4), 591–594.

Kudeki, E., Rastogi, P. K. & Sürücü, F. (1993), 'Systematic errors in radar wind estimation: Implications for comparative measurements', *Radio Science* **28**(2), 169–179.

Kudeki, E., Sürücü, F. & Woodman, R. F. (1990b), 'Mesospheric wind and aspect sensitivity measurements at jicamarca using radar interferometry and poststatistics beam steering techniques', *Radio Science* **25**(4), 595–612.

Larsen, M. F. & Röttger, J. (1991), 'VHF radar measurements of in–beam incidence angles and associated vertical–beam radial velocity corrections', *Journal of Atmospheric and Oceanic Technology* **8**(4), 477–490.

Larsen, M. F., Palmer, R. D., Fukao, S., Woodman, R. F., Yamamoto, M., Tsuda, T. & Kato, S. (1992), 'An analysis technique for deriving vector winds and in–beam incidence angles from radar interferometer measurements', *Journal of Atmospheric and Oceanic Technology* **9**(1), 3–14.

Lesicar, D. (1993), Study of the structure of partial reflection radar scatterers and their application in atmospheric measurements, PhD thesis, University of Adelaide, Adel., Australia.

Lindner, B. C. (1975a), 'The nature of D–region scattering of vertical incidence radio waves. I-Generalized statistical theory of diversity effects between spaced receiving antennas', *Australian Journal of Physics* **28**, 163–170.

Lindner, B. C. (1975b), 'The nature of D–region scattering of vertical incidence radio waves. II-Experimental observations using spaced antenna reception', *Australian Journal of Physics* **28**, 171–184.

Liu, C. H., Röttger, J., Pan, C. J. & Franke, S. J. (1990), 'A model for spaced antenna observational mode for MST radars', *Radio Science* **25**(4), 551–563.

Marshall, T. G. (1978), Switched power amplification at low and medium frequencies, PhD thesis, University of Adelaide, Adel., Australia.

Meek, C. E. (1980), 'An efficient method for analysing ionospheric drifts data', *Journal of Atmospheric and Terrestrial Physics* **42**, 835–839.

Meek, C. E. (1990), 'Triangle size effect in spaced antenna wind measurements', *Radio Science* **25**(5), 641–648.

Meek, C. E. (1992), Diurnal variation in angle of arrival phase measurements, *in* 'Workshop on multiple receiver radar techniques'. Held at the University of Illinois, Urbana–Champaign, USA.

Meek, C. E. & Manson, A. H. (1987), 'Mesospheric motions observed by simultaneous medium–frequency interferometer and spaced antenna experiments', *Journal of Geophysical Research* **92D**, 5627–5637.

Meek, C. E. & Manson, A. H. (1990), 'MF radar interferometer measurements of meteor trail motions', *Radio Science* **25**(4), 649–655.

Meeklah, J. S., Rees, D. T. & Manson, A. H. (1972), 'Amplitude and phase measurements of medium–frequency radiowaves reflected from the lower ionosphere (60-120 km) - I. E–region', *Journal of Atmospheric and Terrestrial Physics* **34**, 911–925.

Megaw, E. C. S. (1957), 'Fundamental radio scatter propagation theory', *Institute of Elec. Eng. Proc.* **104**(C6), 441–456.

Mines, D. F. (1969), 'A large antenna array for ionospheric research', *Aust. Telecomm. Res.* **3**(1), 28–32.

Mitra, S. N. (1949), 'A radio method of measuring winds in the ionosphere', *Proceedings of the Institute of electical engineers* **96**, 441–446.

Palmer, R. D., Larsen, M. F., Woodman, R. F., Fukao, S., Yamamoto, M., Tsuda, T. & Kato, S. (1991), 'VHF radar interferometry measurements of vertical velocity and the effect of tilted refractivity surfaces on standard Doppler measurements', *Radio Science* **26**(2), 417–427.

Palmer, R. D., Woodman, R. F., Larsen, M. F., Yamamoto, M., Tsuda, T. & Kato, S. (1990), 'Frequency domain interferometry observations of tropo/stratospheric scattering layers using the MU radar: Description and first results', *Geophysical Research Letters* **17**(12), 2189–2192.

Pawsey, J. (1935), 'Further investigations of the amplitude variations of downcoming wireless waves', *Proc. Cambridge Phil. Soc.* **31**, 125.

Pfister, W. (1971), 'The wave–like nature of inhomogeneities in the E–region', *Journal of Atmospheric and Terrestrial Physics* **33**, 999–1025.

Phillips, G. & Spencer, M. (1955), 'The effects of anisometric amplitude patterns in the measurement of ionospheric drifts', *Proc. Phys. Soc. (London)* **B68**, 481.

Ramo, S., Whinnery, J. R. & Van Duzer, T. (1984), *Fields and waves in communication electronics*, Wiley & Sons, New York.

Ratcliffe, J. A. (1956), 'Some aspects of diffraction theory and their application to the ionosphere', *Reports on Progress in Physics* **19**, 188–267.

Reid, I. M. (1984), Radar studies of atmospheric gravity waves, PhD thesis, University of Adelaide, Adel., Australia.

Reid, I. M. (1987), 'Some aspects of Doppler radar measurements of the mean and fluctuating components of the wind field in the upper middle atmosphere', *Journal of Atmospheric and Terrestrial Physics* **49**(5), 467–484.

Reid, I. M. (1988), 'MF Doppler and spaced antenna radar measurements of upper middle atmosphere winds', *Journal of Atmospheric and Terrestrial Physics* **50**(2), 117–134.

Reid, I. M. (1990), 'Radar observations of stratified layers in the mesosphere and lower thermosphere (50–100 km)', *Advances in Space Research* **10**(10), 7–19.

Reid, I. M. & Vincent, R. A. (1987), 'Measurements of mesospheric gravity wave momentum fluxes and mean flow accelerations at Adelaide, Australia.', *Journal of Atmospheric and Terrestrial Physics* **49**(5), 443–460.

Richmond, A. D. (1987), The ionosphere, *in* S. I. Akasofu & Y. Kamide, eds, 'The solar wind and the Earth', chapter 7.

Risbeth, H. & Garriott, O. K. (1969), Introduction to ionospheric physics, *in* 'International Geophysics Series', Vol. 14, Academic Press, New York.

Röttger, J. (1980*a*), 'Reflection and scattering of VHF radar signals from atmospheric refractivity structures', *Radio Science* **15**(2), 259–276.

Röttger, J. (1980*b*), 'Structure and dynamics of the stratosphere and mesosphere revealed by VHF radar investigations', *Pure and Applied Geophysics* **118**, 494–527.

Röttger, J. (1981), 'Investigations of lower and middle atmosphere dynamics with spaced antenna drifts radars', *Journal of Atmospheric and Terrestrial Physics* **43**(4), 277–292.

Röttger, J. (1984), 'The MST radar technique', *Handbook for the Middle Atmosphere Program* **13**, 187–232. SCOSTEP Secretariat, University of Illinois, Urbana, IL, USA.

Röttger, J. (1989), 'The interpretation of MST radar echoes: T present knowledge of the scattering/reflection and the irregularity mechanism', *Handbook for the Middle Atmosphere Program* **28**, 68–82. SCOSTEP Secretariat, University of Illinois, Urbana, IL, USA.

Röttger, J. & Ierkic, H. M. (1985), 'Postset beam steering and interferometer applications of VHF radars to study winds, waves and turbulence in the lower and middle atmosphere', *Radio Science* **20**(6), 1461–1480.

Röttger, J., Liu, C. H., Chao, J. K., A. J. Chen, Y. H. C., Fu, I. J., Huang, C. M., Kiang, Y. W., Kuo, F. S., Lin, C. H. & Pan, C. J. (1990), 'The Chung–Li VHF radar: Technical layout and a summary of initial results', *Radio Science* **25**(4), 487–502.

Rüster, R., Czechowsky, P. & Schmidt, G. (1989), 'VHF radar observations of tides at polar latitudes in the summer mesosphere', *Journal of Atmospheric and Terrestrial Physics* **50**, 1041–1046.

Sander, K. F. & Reed, G. A. L. (1986), *Transmission and propagation of electromagnetic waves*, Cambridge University Press, London.

Sürücü, F., Franke, P. M. & Kudeki, E. (1992), 'On the use of software beam synthesis in multiple–receiver MF radar wind estimation', *Radio Science* **27**(6), 775–782.

VanBaelen, J. S. & Richmond, A. D. (1991a), 'Radar interferometry technique: three–dimensional wind measurement theory', *Radio Science* **26**, 1209–1218.

VanBaelen, J. S., Richmond, A. D., Tsuda, T., Avery, S. K., Kato, S., Fukao, S. & Yamamoto, M. (1991b), 'Radar interferometry technique and anisotropy of the echo power distribution: First results', *Radio Science* **26**, 1315–1326.

Vincent, R. A. (1972), 'Ionospheric irregularities in the E–region', *Journal of Atmospheric and Terrestrial Physics* **34**, 1881–1898.

Vincent, R. A. & Reid, I. M. (1983), 'HF Doppler measurements of mesospheric gravity wave momentum fluxes', *Journal of the Atmospheric Sciences* **40**, 1321–1333.

Vincent, R. A., May, P. T., Hocking, W. K., Elford, W. G., Candy, B. H. & Briggs, B. H. (1987), 'First results with the Adelaide VHF radar: Spaced antenna studies of tropospheric winds', *Journal of Atmospheric and Terrestrial Physics* **49**, 353–366.

Whitehead, J. D. & Monro, P. E. (1975), 'Phase and amplitude analysis of radio echoes from the ionosphere', *Journal of Atmospheric and Terrestrial Physics* **37**, 1427–1430.

Whitehead, J. D., From, W. R., Jones, K. L. & Monro, P. E. (1983), 'Measurement of movements in the ionosphere using radio reflections', *Journal of Atmospheric and Terrestrial Physics* **45**(5), 345–351.

Woodman, R. F. & Guillen, A. (1974), 'Radar observations of winds and turbulence in the stratosphere and mesosphere', *Journal of the Atmospheric Sciences* **31**, 493–505.

Errata

Section 1.2.1

The rate of decrease of temperature in the troposphere is also due to the effects of latent heat.
The peak abundance of ozone lies between 30 and 35 km.
The departure from radiative equilibrium of the Earth's atmosphere is not only due to breaking internal gravity waves, but also planetary waves.

Section 1.5.7

Franke et al., [1990] did not, in fact, use the NPD criterion to reject certain Doppler frequencies in their experiment.

Section 2.2

Pulse width: The half-power full-width of the transmitter pulse.

Section 3.6.1

Clearly, the NPD criterion must be identically zero when applied to individual spectral frequency estimates with only three antennae available.

Page 116, line 10

"Alhtough" should read "Although".

Page 153

The expression

$$\frac{\sin\theta}{\sin^2\theta_S} + \frac{\sin\theta\sin\theta_A}{\sin^2\theta_B} = 0$$

should read

$$\frac{\sin\theta}{\sin^2\theta_S} + \frac{\sin\theta - \sin\theta_A}{\sin^2\theta_B} = 0\,.$$

Section 4.4.3

"104.2 s time series" should read "102.4 s time series".

Page 165, line 11

"appled" should read "applied".

Page 169, line 23 - 25

The spaced antenna wind profiles were averaged using vector methods.

Section 5.2

"Functional smoothness" is invoked in the theoretical section in order to derive valid analytical expressions for spectral phases using the shift theorem of Fourier Transforms. In terms of smoothness of cross-spectra of experimental data, no mathematically rigorous criteria were applied.

Page 189, last line

"is" should read "it".

Page 191, line 6

Perturbation velocities in excess of 200 ms^{-1} are considered to be artifacts of the analysis. As stated in the same paragraph, any exclusion of large IDI velocities will tend to reduce the IDI velocity measured. As the study concluded that the IDI velocities were, in general, too large, such an exclusion is irrelevant to the conclusion.

Page 222, line 8

"recievers" should read "receivers".

Page 222, line 32

"ariel" should read "aerial".

Page 223, line 26

"Fakao" should read "Fukao".

Page 224, line 6

"jicamarca" should read "Jicamarca".

Page 226, line 13

"T" should read "The".